



# ScuDo

Scuola di Dottorato ~ Doctoral School

WHAT YOU ARE, TAKES YOU FAR

Doctoral Dissertation

Doctoral Program in Mechanical Engineering (34<sup>th</sup> cycle)

# Free vibration and post-buckling analyses of thin-walled beam and flexible plate structures through the Unified Formulation

By

**Ehsan Daneshkhah**

\*\*\*\*\*

**Supervisor(s):**

Prof. Erasmo Carrera

Prof. Alfonso Pagani

**Doctoral Examination Committee:**

Prof. Maria Cinefra, Referee, Politecnico di Bari, Italy

Prof. Sara Bagassi, Referee, Università degli Studi di Bologna, Italy

Politecnico di Torino

2022

## **Declaration**

I hereby declare that the contents and organization of this dissertation constitute my own original work and do not compromise in any way the rights of third parties, including those relating to the security of personal data.

Ehsan Daneshkhah

2022

\* This dissertation is presented in partial fulfillment of the requirements for **Ph.D. degree** in the Graduate School of Politecnico di Torino (ScuDo).

*I would like to dedicate this thesis to all my family and those who have taught me  
that affection is the only way of redemption*

## **Acknowledgements**

First and foremost, I would like to express my sincerest thanks to my supervisor Prof. Erasmo Carrera, for his invaluable support, advice and encouragement throughout this study. It has been a great pleasure and honor to work under the supervision of such a distinguished scholar.

I would like to thank Prof. Alfonso Pagani, Prof. Marco Petrolo, and Dr. Riccardo Augello for their continuous support and valuable comments during the Ph.D. period.

I would also like to thank all my teachers and professors who accompanied and motivated me in my whole life.

## **Abstract**

In this research, refined structural and nonlinear theories are used in order to investigate the free vibration and post-buckling response of thin-walled beam and flexible plate structures. In this regard, the Unified Formulation is employed to obtain nonlinear governing equations of the finite beam and plate elements.

Then, various assessments are conducted related to the thin-walled beam and flexible plate structures. The free vibration response of thin-walled isotropic and composite beams is accurately evaluated, and the Vibration Correlation Technique is used in order to investigate the variations of natural frequencies in thin-walled laminated isotropic and composite beam structures under compression. The physically and geometrically nonlinear analysis of thin-walled beams is also investigated using Newton–Raphson linearization scheme with the path-following method based on the arc-length constraint.

The large-deflection and post-buckling of isotropic and composite plates under axial, in-plane shear and combined loadings are analyzed considering different strain-displacement assumptions, and the corresponding equilibrium curves and stress distributions are presented.

Furthermore, the effects of load and displacement boundary conditions in the post-buckled laminated composite plates are investigated, and the effects of stiffeners are assessed. The results show that the present method based on the Unified Formulation can be efficiently used for accurate structural analysis, including the free vibration and post-buckling of the thin-walled beam and flexible plate structures.

# Contents

<b>List of Figures</b>	<b>xi</b>
<b>List of Tables</b>	<b>xxii</b>
<b>1 Introduction</b>	<b>1</b>
1.1 Motivation . . . . .	1
1.2 Carrera Unified Formulation . . . . .	2
1.3 Preliminary considerations . . . . .	3
1.4 Free vibration analysis based on the CUF . . . . .	4
1.5 Refined Taylor Expansion . . . . .	6
1.6 Refined Lagrange Expansion . . . . .	7
1.7 Shear locking . . . . .	9
<b>2 Nonlinear Governing Equations</b>	<b>11</b>
2.1 Introduction . . . . .	11
2.2 Geometrically nonlinear analysis based on the CUF . . . . .	12
2.3 Newton-Raphson linearization with path-following constraint . . . . .	13
2.4 Secant stiffness matrix . . . . .	16
2.4.1 FN of the secant stiffness matrix for finite beam element . . . . .	18
2.4.2 FN of the secant stiffness matrix for finite plate element . . . . .	21
2.5 Tangent stiffness matrix . . . . .	26

---

2.5.1	FN of the tangent stiffness matrix for finite beam element . . . . .	29
2.5.2	FN of the tangent stiffness matrix for finite plate element . . . . .	30
2.6	Different strain-displacement assumptions . . . . .	30
<b>3</b>	<b>Higher-order vibration modes of thin-walled beam structures</b>	<b>34</b>
3.1	Introduction . . . . .	34
3.2	Description of the Chen benchmark . . . . .	36
3.3	Convergence study . . . . .	37
3.4	Shear locking treatments . . . . .	43
3.5	Higher-order modes detection via various models . . . . .	46
3.5.1	Validation case-cruciform beam . . . . .	46
3.5.2	Beam 1- C-shaped cross-section . . . . .	49
3.5.3	Beam 2- T-shaped cross-section . . . . .	57
3.5.4	Beam 3- Arbitrary cross-section . . . . .	60
3.5.5	Beam 4- Arbitrary cross-section . . . . .	63
3.6	Conclusions . . . . .	67
<b>4</b>	<b>Virtual Vibration Correlation Technique for thin-walled beam structures</b>	<b>68</b>
4.1	Introduction . . . . .	68
4.2	Cruciform isotropic beam . . . . .	71
4.3	Thin cruciform isotropic beam . . . . .	80
4.4	Arbitrary cross-section isotropic beam (I) . . . . .	84
4.5	Arbitrary cross-section isotropic beam (II) . . . . .	88
4.6	Symmetric [90/0/0/90] square beam . . . . .	91
4.7	Unsymmetric [0/ $\theta$ ] square beam . . . . .	92
4.8	Box composite beam . . . . .	95
4.9	I-shaped composite beam . . . . .	99

4.10	Channel-shaped composite beam . . . . .	102
4.11	Channel-shaped composite beam with transverse stiffeners . . . . .	106
4.12	Conclusions . . . . .	112
<b>5</b>	<b>Physically and geometrically nonlinear analysis of thin-walled beam structures</b>	<b>114</b>
5.1	Introduction . . . . .	114
5.2	The von Mises model for elastoplasticity . . . . .	115
5.3	Square beam . . . . .	117
5.4	C-shaped beam . . . . .	124
5.5	T-shaped beam . . . . .	128
5.6	Conclusions . . . . .	133
<b>6</b>	<b>Large-deflection and post-buckling analysis of flexible plates</b>	<b>135</b>
6.1	Introduction . . . . .	135
6.2	Large-deflection response of square isotropic plates . . . . .	137
6.3	Post-buckling analysis of slender isotropic plates . . . . .	144
6.3.1	Validation . . . . .	144
6.3.2	Post-buckling of slender plates with the (movable simply-supported)-free-(movable simply-supported)-free ( $S_1FS_1F$ ) edge conditions . . . . .	145
6.3.3	Post-buckling of slender plates with all edges simply-supported ( $S_1S_2S_1S_2$ ) . . . . .	148
6.4	Large-deflection of composite plates subjected to transverse pressure	149
6.4.1	Cross-ply $[0/90]_s$ laminate with different edge conditions . . .	149
6.4.2	$[45/-45/0/0/45/-45/90/90]_s$ laminate with clamped edge conditions . . . . .	152
6.4.3	Cross-ply $[0/90]$ and $[0/90]_3$ laminates with clamped edge conditions . . . . .	154



---

6.5	Post-buckling of composite plates under in-plane compressive loads	157
6.5.1	Cross-ply $[0/90]_2$ rectangular laminate with simply-supported edge conditions . . . . .	157
6.5.2	Cross-ply $[0/90]_n$ square laminates with simply-supported edge conditions . . . . .	161
6.5.3	Angle-ply $[45/-45]_s$ laminate with simply-supported edge conditions . . . . .	164
6.5.4	Cross-ply $[0/90]$ square laminate with different edge conditions	167
6.6	Conclusions . . . . .	170
<b>7</b>	<b>Stiffeners and boundary conditions effects on the compressed flexible plates</b>	<b>172</b>
7.1	Introduction . . . . .	172
7.2	Square composite plate with SFSF edge conditions . . . . .	174
7.2.1	Evaluation of different stiffeners . . . . .	174
7.2.2	Convergence analysis . . . . .	176
7.2.3	Lamination angles and equilibrium curves . . . . .	177
7.2.4	Geometrically nonlinear assumptions and equilibrium curves	178
7.2.5	Geometrically nonlinear assumptions and stress distributions	179
7.3	Square composite plate with SSSS edge conditions . . . . .	181
7.3.1	Evaluations of different stiffeners . . . . .	182
7.3.2	Convergence analysis . . . . .	184
7.3.3	Lamination angles and equilibrium curves . . . . .	185
7.3.4	Geometrically nonlinear assumptions and equilibrium curves	186
7.3.5	Geometrically nonlinear assumptions and stress distributions	187
7.4	Angle-ply lamintaed composite plate with SSSS edge conditions . .	190
7.4.1	Evaluation of different stiffeners . . . . .	190
7.4.2	Geometrically nonlinear assumptions and equilibrium curves	191

---

7.5	Conclusions . . . . .	192
<b>8</b>	<b>Modeling in-plane shear and combined loadings in flexible plates</b>	<b>194</b>
8.1	Introduction . . . . .	194
8.2	Modeling technique . . . . .	195
8.2.1	The surrounding area . . . . .	196
8.2.2	The stiffeners . . . . .	197
8.2.3	Validation of models . . . . .	198
8.3	Pure shear loading . . . . .	201
8.4	Shear and biaxial compressive loading . . . . .	204
8.5	Shear and biaxial tensile loading . . . . .	208
8.6	Comparison of loading conditions . . . . .	209
8.7	Conclusions . . . . .	210
<b>9</b>	<b>Conclusions and perspectives</b>	<b>213</b>
9.1	Summary . . . . .	213
9.2	Concluding remarks . . . . .	214
9.3	Future directions . . . . .	216
	<b>References</b>	<b>218</b>

# List of Figures

1.1	Some generalized displacement variables derived from the linear TE model for a schematic beam under bending around the $z$ axis . . . . .	7
1.2	schematic depiction of pure displacement variables according to the Lagrange model (L4) for an example beam subjected to bending around $z$ axis . . . . .	8
1.3	Nine-node Lagrange polynomials in the actual and normalized geometries . . . . .	9
2.1	Different incremental techniques based on the load control, displacement control, and path-following methods . . . . .	14
2.2	The details of implemented incremental method . . . . .	15
2.3	Main geometrically nonlinear assumptions for the von Kármán nonlinear plate . . . . .	32
3.1	The schematic view and material properties of the investigated benchmark beam problems . . . . .	36
3.2	Different Cross-sectional discretization of the beam-1 based on the LE	39
3.3	Different Cross-sectional discretization of the beam-2 based on the LE	40
3.4	Different Cross-sectional discretization of the beam-3 based on the LE	41
3.5	Different Cross-sectional discretization of the beam-4 based on the LE	41
3.6	The comparison of convergence analyses of vertical displacements and axial stresses for the beam 1 based on the DOF of beam structure	43

3.7	Shear locking effects on the vertical displacements of the investigated beam 1 . . . . .	44
3.8	Schematic view of the cruciform beam . . . . .	47
3.9	The comparison of free vibration mode shapes of ABQ shell and CUF 20B4-25L9 models . . . . .	48
3.10	The comparison of free vibration mode shapes of ABQ shell and CUF 20B4-22L9 models . . . . .	49
3.11	MAC analysis for the comparison of free vibration modes for the beam 1 . . . . .	56
4.1	Schematic view of the cruciform beam with the length of 670 mm . . . . .	71
4.2	The MAC analysis for the comparison of free vibration mode shapes of the cruciform beams with 20B4 elements . . . . .	76
4.3	The comparison of the first five natural frequencies in the cruciform beam under progressive compressive loads . . . . .	77
4.4	The comparison of the first five natural frequencies in the cruciform beam under progressive compressive loads based on the Taylor model order 1 and CUF model with 105 Lagrange points . . . . .	78
4.5	The variations of fundamental frequencies in the cruciform beam under progressive compressive loads based on the different CUF 1D models(a) effect of the structural theory (b) effect of FE discretization . . . . .	79
4.6	Critical buckling loads and the fundamental frequencies versus the applied progressive compressive loads in the cruciform beam according to the Ref. and the CUF 1D model . . . . .	80
4.7	Schematic view of the thin cruciform beam . . . . .	81
4.8	The comparison of free vibration modes using the MAC analysis for the cruciform beams with 20B4 elements based on different structural theories versus the Lagrange model with 153 points . . . . .	84
4.9	The comparison of the first five natural frequencies in the thin cruciform beam under progressive compressive loads based on the Taylor model order 1 and CUF model with 105 Lagrange points . . . . .	84

---

4.10	Schematic view of the arbitrary cross-section beam (I) . . . . .	85
4.11	The comparison of the first five natural frequencies of the arbitrary cross-section beam (I) under progressive compressive loads . . . . .	87
4.12	Schematic view of the arbitrary cross-section beam (II) . . . . .	88
4.13	The comparison of the first five natural frequencies in the arbitrary cross-section beam (II) under progressive compressive loads . . . . .	90
4.14	The variations of natural frequencies with the axial loads for the square composite beam . . . . .	94
4.15	The variations of natural frequencies with the axial loads for the square composite beam . . . . .	94
4.16	Geometry of thin-walled box beam (dimensions in mm) . . . . .	95
4.17	The variations of natural frequencies with the axial loads for the composite box beam based on the CUF 1D model with LE, ABQ shell, and the available literature . . . . .	99
4.18	Geometry of thin-walled I-shaped beam (dimensions in mm) . . . . .	100
4.19	The variations of fundamental frequencies with the axial loads for the I-shaped composite beam based on the CUF 1D model with LE, ABQ shell model, and the available literature . . . . .	102
4.20	Geometry of thin-walled channel-shaped composite beam (dimensions in mm) . . . . .	103
4.21	The variations of natural frequencies with the axial loads for the channel-shaped composite beam based on the CUF 1D model with LE and ABQ shell model . . . . .	106
4.22	Geometry of thin-walled channel-shaped composite beam with transverse stiffeners (dimensions in mm) . . . . .	107
4.23	The comparison of natural frequencies variations for the channel-shaped beam without stiffener and with one stiffener . . . . .	111
4.24	The comparison of natural frequencies variations for the channel-shaped beam with three and five stiffeners . . . . .	111
5.1	Schematic view of the square beam . . . . .	117

5.2	Convergence analysis of equilibrium curves for the square beam with elastic behavior (a) effect of the structural theory (b) effect of the FE discretization . . . . .	118
5.3	Equilibrium curves for the square beam based on various structural theories (a) elastic material (b) elastoplastic material . . . . .	119
5.4	Effect of plasticity on equilibrium curves for the square beam (a) complete view (b) detailed view of plasticity initiation . . . . .	120
5.5	The axial stress at $F=1100$ N, $x=0$ , $y=75$ mm of the square beam considering (a) elastic behavior of material (b) elastoplastic behavior of material . . . . .	121
5.6	The transverse shear stress at $F=1100$ N, $x=0$ , $y=75$ mm of the square beam considering (a) elastic behavior of material (b) elastoplastic behavior of material . . . . .	121
5.7	2D contour plots of $\sigma_{yy}$ (Pa) with $F=1100$ N and $y=75$ mm of the square beam for the elastoplastic material based on (a) CUF 1D (LE-16L9) (b) ABQ-3D refined models . . . . .	122
5.8	2D contour plots of $\sigma_{yz}$ (Pa) with $F=1100$ N and $y=75$ mm of the square beam for the elastoplastic material based on (a) CUF 1D (LE-16L9) (b) ABQ-3D refined models . . . . .	122
5.9	Schematic view of the C-shaped beam, all dimensions are in cm . . . . .	124
5.10	The comparison of equilibrium curves of the C-shaped beam with different material behaviors . . . . .	125
5.11	3D contour plots of the displacement for the elastoplastic material, C-shaped beam based on (a) CUF 1D (LE-13L9) (b) ABQ-3D refined models . . . . .	126
5.12	The axial stress at $x=0$ , $y=75$ cm for $u_z=100$ cm, C-shaped beam, considering (a) elastic material (b) elastoplastic material . . . . .	126
5.13	The transverse shear stress at $x=0$ , $y=75$ cm for $u_z=100$ cm, C-shaped beam, considering (a) elastic material (b) elastoplastic material . . . . .	127

5.14	2D contour plots of $\sigma_{yy}$ for $u_z=100$ cm, at $y=75$ cm, elastoplastic material, C-shaped beam based on (a) CUF 1D (LE-13L9) (b) ABQ-3D refined models . . . . .	127
5.15	2D contour plots of $\sigma_{yz}$ for $u_z=100$ cm, at $y=75$ cm, elastoplastic material, C-shaped beam based on (a) CUF 1D (LE-13L9) (b) ABQ-3D refined models . . . . .	128
5.16	Schematic view of the T-shaped beam, all dimensions are in mm . . . . .	129
5.17	Equilibrium curves obtained from the CUF 1D (LE-9L9) model considering elastic and elastoplastic material behavior . . . . .	130
5.18	Detailed view of the plasticity initiation for the T-shaped beam (a) force-vertical displacement ( $u_z$ ) curve (b) force-lateral displacement ( $u_x$ ) curve . . . . .	131
5.19	3D contour plots of the displacement at the load of 3400 N for elastoplastic material based on (a) CUF 1D (LE-9L9) (b) ABQ-3D refined models . . . . .	132
5.20	2D contour plots of $\sigma_{yy}$ (Pa) at the load of 3400 N near the clamped edge ( $y=100$ mm) for the elastoplastic material based on (a) CUF 1D (LE-9L9) (b) ABQ-3D refined models . . . . .	132
5.21	2D contour plots of $\sigma_{yz}$ (Pa) at the load of 3400 N near the clamped edge ( $y=100$ mm) for the elastoplastic material based on (a) CUF 1D (LE-9L9) (b) ABQ-3D refined models . . . . .	133
6.1	Square plate subjected to uniform pressure . . . . .	138
6.2	Convergence analysis for the CCCC moderately thick plate . . . . .	138
6.3	Large-deflection equilibrium curves of CCCC square plates based on different nonlinear strain-displacement assumptions . . . . .	139
6.4	Effect of nonlinear strain-displacement relations on the equilibrium curves in the case of CCCC moderately thick square plate under uniform pressure . . . . .	140
6.5	The distributions of the dimensionless transverse shear stress through the thickness of CCCC moderately thick square plate at the point ( $x = a/6, y = b/2$ ) and fixed load of $\frac{P_z a^4}{Eh^4} = 200$ . . . . .	141

- 
- 6.6 The distributions of the dimensionless in-plane normal stress through the thickness of CCCC moderately thick square plate at the middle point ( $x = a/2, y = b/2$ ) and fixed load of  $\frac{P_z a^4}{Eh^4} = 200$  . . . . . 141
- 6.7 The distributions of the dimensionless transverse shear stress through the thickness of moderately thick square plate at the point ( $x = a/6, y = b/2$ ) and fixed load of  $\frac{P_z a^4}{Eh^4} = 200$  . . . . . 142
- 6.8 The distributions of the dimensionless in-plane normal stress through the thickness of CCCC moderately thick square plate at the middle point ( $x = a/2, y = b/2$ ) and fixed displacement of  $\frac{u_z}{h} = 1.5$  . . . . . 143
- 6.9 The distributions of the dimensionless transverse shear stress through the thickness of CCCC moderately thick square plate at the point ( $x = a/6, y = b/2$ ) and fixed displacement of  $\frac{u_z}{h} = 1.5$  . . . . . 143
- 6.10 Post-buckling equilibrium curves for slender plates subjected to an in-plane compressive point load  $P$  based on plate and beam models . 145
- 6.11 Post-buckling equilibrium curves of  $S_1FS_1F$  slender plates under the in-plane compressive point loads based on the different geometrically nonlinear CUF plate models . . . . . 146
- 6.12 The distributions of the dimensionless in-plane normal stress through the thickness of  $S_1FS_1F$  slender plate at the point ( $x = a/4, y = b/4$ ) and fixed load of  $\frac{Pa^2}{\pi^2El_b} = 1.1$  . . . . . 147
- 6.13 The distributions of the dimensionless transverse shear stress through the thickness of  $S_1FS_1F$  slender plate at the point ( $x = a/4, y = b/4$ ) and fixed load of  $\frac{Pa^2}{\pi^2El_b} = 1.1$  . . . . . 147
- 6.14 Post-buckling equilibrium curves of slender plates with all edges simply-supported ( $S_1S_2S_1S_2$ ) under the in-plane compressive line loads based on the different geometrically nonlinear CUF plate models 148
- 6.15 Convergence analysis for a 4-layer  $[0/90]_s$  composite plate under uniform transverse pressure with clamped edge conditions at the center of the composite plate . . . . . 150
- 6.16 The equilibrium curves for a 4-layer composite plate under uniform transverse pressure with different edge conditions . . . . . 151



6.17	Schematic view of a 16-layer $[45/-45/0/0/45/-45/90/90]_s$ composite plate . . . . .	152
6.18	Convergence analysis for a 16-layer $[45/-45/0/0/45/-45/90/90]_s$ composite plate under uniform transverse pressure with clamped edge conditions . . . . .	153
6.19	The equilibrium curves for the 16-layer composite plate based on the CUF 2D and the available literature . . . . .	154
6.20	Convergence analysis for a 2-layer $[0/90]$ composite plate under uniform transverse pressure with clamped edge conditions . . . . .	155
6.21	The equilibrium curves for 2-layer and 6-layer composite plates under uniform transverse pressure with clamped edge conditions . . . . .	156
6.22	Convergence analysis for a cross-ply $[0/90]_2$ laminate under in-plane compressive line loads in the $x$ -axis direction with simply-supported edge conditions . . . . .	158
6.23	The comparison of equilibrium curves for the cross-ply $[0/90]_2$ laminate based on the CUF 2D full nonlinear model ( $20 \times 5Q9-LD1$ ), ABQ 2D NL model ( $60 \times 15 S8R$ ) and ABQ 3D NL model ( $60 \times 15 \times 4 C3D20R$ ) . . . . .	159
6.24	The comparison of displacement contours at the fixed load of $\frac{N_x b a}{E_2 h^3} = 300$ for a cross-ply $[0/90]_2$ laminate based on (a) CUF 2D full nonlinear $20 \times 5Q9-LD1$ model, (b) ABQ 2D NL $60 \times 15 S8R$ model and (c) ABQ 3D NL $60 \times 15 \times 4 C3D20R$ model . . . . .	160
6.25	Convergence analysis of the in-plane mesh approximation for a cross-ply $[0/90]$ laminate under in-plane compressive line loads in the $y$ -axis direction with simply-supported edge conditions . . . . .	162
6.26	The equilibrium curves for different cross-ply laminated plates under in-plane compressive line loads . . . . .	163
6.27	Combined loading of a laminated composite plate: negative in-plane shear, in-plane compression, and the uniform transverse pressure [240]	164
6.28	Convergence analysis for an angle-ply $[45/-45]_s$ laminate under the combined loading with simply-supported edge conditions . . . . .	165

6.29	The equilibrium curves based on the values of loading factor $\lambda$ for an angle-ply $[45/-45]_s$ laminate under different combined loadings with simply-supported edge conditions . . . . .	165
6.30	The equilibrium curves for an angle-ply $[45/-45]_s$ laminate under different combined loadings with simply-supported edge conditions	166
6.31	Convergence analysis of the in-plane mesh approximation for a cross-ply $[0/90]$ laminate under in-plane compressive loads in the $x$ axis direction with simply-supported edge conditions . . . . .	168
6.32	The equilibrium curves for a cross-ply $[0/90]$ laminate under in-plane compressive line loads in the $x$ -axis direction with different edge conditions based on CUF 2D full nonlinear $12 \times 12Q9$ -LD1 model .	168
6.33	The equilibrium curves for a cross-ply $[0/90]$ laminate under in-plane compressive line loads in the $y$ -axis direction with different edge conditions based on CUF 2D full nonlinear $12 \times 12Q9$ -LD1 model .	169
7.1	The effects of attachments on the boundary conditions of a panel in the sample wing structure . . . . .	173
7.2	The comparison of equilibrium curves for the composite plate $[0/90/0/90]$ with different load and displacement boundary conditions based on the full nonlinear CUF plate model $12 \times 12Q9$ -LD1 . . . . .	175
7.3	Convergence analysis of the in-plane mesh size for SFSF composite plate based on the full nonlinear CUF plate model . . . . .	176
7.4	The comparison of equilibrium curves for SFSF composite plates with different lamination angles based on the full nonlinear CUF plate model . . . . .	178
7.5	The comparison of equilibrium curves for the composite plate $[0/90/0/90]$ with SFSF edge conditions with different geometrically nonlinear assumptions of Table 2.3 based on the $12 \times 12Q9$ -LD1 model . . . .	179
7.6	The distributions of dimensionless in-plane normal stress through the thickness of plate at the point $(x = 0.5a, y = 0.7b)$ of SFSF $[0/90/0/90]$ square composite plate at the fixed displacement of $\frac{u_z}{h} = 20180$	

7.7	The distributions of dimensionless transverse shear stress through the thickness of plate at the point $(x = 0.5a, y = 0.7b)$ of SFSSF [0/90/0/90] square composite plate at the fixed displacement of $\frac{u_z}{h} = 20$	181
7.8	The comparison of equilibrium curves for the composite plate [0/90/0/90] with SSSS edge conditions with different load and displacement boundary conditions based on the full nonlinear CUF plate model 12×12Q9-LD1 . . . . .	182
7.9	Convergence analysis of the in-plane mesh size for SSSS composite plate based on the full nonlinear CUF plate model . . . . .	184
7.10	The comparison of equilibrium curves for the composite plate [0/90/0/90] with SSSS edge conditions with different geometrically nonlinear assumptions of Table 2.3 based on the 12×12Q9-LD1 model . . . .	186
7.11	The comparison of equilibrium curves for the composite plate [0/90/0/90] with SSSS edge conditions with different geometrically nonlinear assumptions of Table 2.3 based on the 12×12Q9-LD1 model . . . .	187
7.12	The distributions of dimensionless in-plane normal stress through the thickness of plate at the point $(x = 0.5a, y = 0.7b)$ of SSSS [0/90/0/90] square composite plate at the fixed load of $\frac{N_y a^2}{E_2 h^3} = 400$ .	189
7.13	The distributions of dimensionless transverse shear stress through the thickness of plate at the point $(x = 0.5a, y = 0.7b)$ of SSSS [0/90/0/90] square composite plate at the fixed load of $\frac{N_y a^2}{E_2 h^3} = 400$ .	190
7.14	The comparison of equilibrium curves for the composite plate [45/-45/45/-45] with SSSS edge conditions with different load and displacement boundary conditions based on the full nonlinear CUF plate model 12×12Q9-LD1 . . . . .	191
7.15	The comparison of equilibrium curves for the composite plate [45/-45/45/-45] with SSSS edge conditions with different geometrically nonlinear assumptions of Table 2.3 based on the 12×12Q9-LD1 model	192
8.1	The effect of material properties of surrounding area on the equilibrium curves for [45/-45] <sub>s</sub> composite plates without stiffeners subjected to negative pure shear loading conditions based on the 12x12Q9-LD1 model . . . . .	197

8.2	The effect of material properties of the stiffeners on the equilibrium curves for $[45/-45]_s$ composite plates with stiffeners subjected to negative pure shear loading conditions based on the 12x12Q9-LD1 model . . . . .	198
8.3	The comparison of equilibrium curves for Baron Epoxy composite plates subjected to pure shear loading . . . . .	199
8.4	The comparison of equilibrium curves for Carbon Epoxy composite plates subjected to pure negative shear loading . . . . .	200
8.5	The comparison of equilibrium curves for composite plates without stiffeners subjected to pure shear loading based on the 12x12Q9-LD1 model (a) prebuckling and buckling (b) post-buckling in large deflections . . . . .	202
8.6	The comparison of equilibrium curves for composite plates with stiffeners subjected to pure shear loading based on the 12x12Q9-LD1 model (a) prebuckling and buckling (b) post-buckling in large deflections . . . . .	203
8.7	The comparison of equilibrium curves for composite plates without stiffeners subjected to pure shear and biaxial compressive loading based on the 12x12Q9-LD1 model (a) prebuckling and buckling (b) post-buckling in large deflections . . . . .	205
8.8	The comparison of equilibrium curves for composite plates with stiffeners subjected to pure shear and biaxial compressive loading based on the 12x12Q9-LD1 model (a) prebuckling and buckling (b) post-buckling in large deflections . . . . .	207
8.9	The comparison of equilibrium curves for composite plates $[45/-45]_s$ with stiffeners subjected to pure shear and biaxial tensile loading based on the 12x12Q9-LD1 model (a) prebuckling and buckling (b) post-buckling in large deflections . . . . .	208
8.10	The comparison of equilibrium curves for composite plates without stiffeners subjected to different loading conditions based on the 12x12Q9-LD1 model (a) prebuckling and buckling (b) post-buckling in large deflections . . . . .	210

---

8.11 The comparison of equilibrium curves for composite plates with stiffeners subjected to different loading conditions based on the 12x12Q9-LD1 model (a) prebuckling and buckling (b) post-buckling in large deflections . . . . .	210
---	-----

# List of Tables

1.1	Normalized coordinates of L9 element . . . . .	9
2.1	A schematic description of the CUF and FE approximation for the beam structures . . . . .	18
2.2	A schematic description of the CUF and FE approximation for the plate structures . . . . .	21
2.3	Different geometrically nonlinear assumptions based on the Green-Lagrange nonlinear strains . . . . .	33
3.1	The convergence analysis of vertical displacements and axial stresses for the beam 1- effect of FE . . . . .	37
3.2	The convergence analysis of vertical displacements and axial stresses for the beam 2- effect of FEs . . . . .	38
3.3	The convergence analysis of vertical displacements and axial stresses for the beam 3- effect of FEs . . . . .	38
3.4	The convergence analysis of vertical displacements and axial stresses for the beam 4- effect of FEs . . . . .	39
3.5	The convergence analysis of vertical displacements and axial stresses for the beam 1- effect of structural theory . . . . .	40
3.6	The convergence analysis of vertical displacements and axial stresses for the beam 2- effect of structural theory . . . . .	40
3.7	The convergence analysis of vertical displacements and axial stresses for the beam 3- effect of structural theory . . . . .	41

---

3.8	The convergence analysis of vertical displacements and axial stresses for the beam 4- effect of structural theory . . . . .	42
3.9	Shear locking effects on the values of vertical displacements in the investigated beam 1 . . . . .	45
3.10	Shear locking effects on the values of vertical displacements in the investigated beam 2 . . . . .	46
3.11	The details of ABQ shell and CUF 1D models employed for the cruciform beam . . . . .	47
3.12	The first ten natural frequencies of cruciform beam with doubly clamped edge conditions based on the used ABQ shell and CUF 1D models . . . . .	48
3.13	The comparison of first ten natural frequencies of the cruciform beam with the available literature . . . . .	48
3.14	The details of ABQ shell models employed for the beam 1 . . . . .	49
3.15	Natural frequencies of beam 1 with clamped-free edge conditions based on different structural theories . . . . .	50
3.16	The first forty mode shapes of beam 1, 20B4,TE=1 model with clamped-free edge conditions . . . . .	51
3.17	The first forty mode shapes of beam 1, 20B4,TE=10 model with clamped-free edge conditions . . . . .	52
3.18	The first forty mode shapes of beam 1, 20B4-22L9 model with clamped-free edge conditions . . . . .	53
3.19	Natural frequencies of beam 1 with clamped-free edge conditions based on different structural theories for the corresponding mode shapes by the MAC (see Table 3.15 for comparison) . . . . .	55
3.20	The details of ABQ shell models employed for the beam 2 . . . . .	57
3.21	Natural frequencies of beam 2 with clamped-free edge conditions based on different structural theories for the corresponding mode shapes by the MAC . . . . .	58

3.22	The first forty mode shapes of beam 2, 20B4-23L9 model with clamped-free edge conditions . . . . .	59
3.23	The details of ABQ shell models employed for the beam 3 . . . . .	60
3.24	Natural frequencies of beam 3 with clamped-free edge conditions based on different structural theories for the corresponding mode shapes by the MAC . . . . .	61
3.25	The first forty mode shapes of beam 3, 20B4-25L9 model with clamped-free edge conditions . . . . .	62
3.26	The details of ABQ shell models employed for the beam 4 . . . . .	63
3.27	The first forty mode shapes of beam 4, 20B4-26L9 model with clamped-free edge conditions . . . . .	64
3.28	Natural frequencies of beam 4 with clamped-free edge conditions based on different structural theories for the corresponding mode shapes by the MAC . . . . .	65
3.29	The comparison of ABQ shell and CUF 1D models employed for the investigated beam structures . . . . .	66
4.1	Isotropic material properties of the cruciform beam . . . . .	71
4.2	The first ten vibration mode shapes of the cruciform beam based on the model with 105 Lagrange points and 20B4 elements . . . . .	72
4.3	Middle cross-sectional view of the first ten vibration mode shapes in the cruciform beam based on the model with 105 Lagrange points and 20B4 elements . . . . .	73
4.4	The first ten buckling modes and the corresponding critical axial displacements of the cruciform beam based on the model with 105 Lagrange points and 20B4 elements . . . . .	74
4.5	The first nine natural frequencies of the unloaded cruciform beam based on the CUF 1D models and the literature . . . . .	74
4.6	The corresponding vibration mode shapes of the cruciform beam obtained by the MAC for the Taylor model order 1 and Lagrange model with 153 points (See Fig 4.2a) . . . . .	76



---

4.7	Evaluation of fundamental frequencies in the cruciform beam under progressive compressive loads based on the CUF 1D model with 105 Lagrange points and the literature . . . . .	78
4.8	The first ten vibration mode shapes of thin cruciform beam based on the model with 105 Lagrange points and 20B4 elements (See table 4.2 for comparison) . . . . .	81
4.9	Middle cross-sectional view of the first ten vibration mode shapes in the thin cruciform beam based on the model with 105 Lagrange points and 20B4 elements . . . . .	82
4.10	The first nine natural frequencies of the unloaded thin cruciform beam based on the CUF 1D Lagrange model and the thin ABQ shell model . . . . .	82
4.11	The comparison of free vibration mode shapes of the thin cruciform beam based on the CUF 1D Lagrange model and the thin ABQ shell model . . . . .	83
4.12	Isotropic material properties of the arbitrary cross-section beam (I) .	85
4.13	The first ten vibration mode shapes of the arbitrary cross-section beam (I) based on the model with 129 Lagrange points and 20B4 elements . . . . .	86
4.14	Middle cross-sectional view of the first ten vibration mode shapes in the arbitrary cross-section beam (I) based on the model with 129 Lagrange points and 20B4 elements . . . . .	86
4.15	The first ten buckling modes and the corresponding critical axial displacements of the arbitrary cross-section beam (I) based on the model with 129 Lagrange points and 20B4 elements . . . . .	87
4.16	The variations of frequencies versus the applied axial displacements in the arbitrary cross-section beam (I) under progressive compressive loads based on the CUF 1D models and Ref. . . . .	88
4.17	Isotropic material properties of the arbitrary cross-section beam (II)	88
4.18	The first ten vibration mode shapes of the arbitrary cross-section beam (II) based on the model with 117 Lagrange points and 20B4 elements . . . . .	89

4.19	Middle cross-sectional view of the first ten vibration mode shapes in the arbitrary cross-section beam (II) based on the model with 117 Lagrange points and 20B4 elements . . . . .	90
4.20	The variations of frequencies versus the applied axial displacements in the arbitrary cross-section beam (II) under progressive compressive loads based on the CUF 1D models and Ref. . . . .	91
4.21	Material properties of the 4-layer composite beam with simply-supported edge conditions . . . . .	92
4.22	The first five natural frequencies of the square composite beam [90/0/0/90] with simply-supported edge conditions based on the CUF 1D models and the literature . . . . .	92
4.23	The first three buckling loads of the square composite beam [90/0/0/90] beam with simply-supported edge conditions based on the CUF 1D models and the literature ( $\times 10^6$ N/m) . . . . .	92
4.24	The first five natural frequencies of the square composite beam [0/θ] with clamped-free edge conditions based on the different structural models and the literature . . . . .	93
4.25	The first six natural frequencies of the composite box beam with simply-supported edge conditions based on the different structural models and the literature . . . . .	96
4.26	The comparison of vibration mode shapes for the composite box beam with simply-supported edge conditions based on the CUF 1D with LE and ABQ shell models . . . . .	97
4.27	The first nine mode shapes of the composite box beam with simply-supported edge conditions based on the CUF 1D model with LE . . . . .	98
4.28	Material properties of the thin-walled I-shaped composite beam with clamped-free edge conditions . . . . .	100
4.29	The first ten natural frequencies of the I-shaped composite beam with clamped-free edge conditions based on the different structural models and the literature . . . . .	100

4.30	The first nine mode shapes of the I-shaped composite beam with [30] lamination and clamped-free edge conditions based on the CUF 1D model with LE . . . . .	101
4.31	Material properties of the channel-shaped composite beam with clamped-clamped edge conditions . . . . .	103
4.32	The first ten natural frequencies of the channel-shaped composite beam with clamped-clamped edge conditions based on the different models and the literature . . . . .	103
4.33	The first ten natural frequencies of the channel-shaped composite beam with clamped-clamped edge conditions based on the different models and the literature . . . . .	104
4.34	The first nine mode shapes of the channel-shaped composite beam with clamped-clamped edge conditions based on the CUF 1D model with LE . . . . .	105
4.35	The comparison of ABQ shell and CUF 1D models employed for the investigated beam structures . . . . .	106
4.36	Material properties of the channel-shaped composite beam with transverse stiffeners and simply-supported edge conditions . . . . .	107
4.37	The first ten natural frequencies of the channel-shaped composite beam with different number of transverse stiffeners based on the CUF 1D model with LE . . . . .	108
4.38	The first nine mode shapes of the channel-shaped composite beam with simply-supported edge conditions based on the CUF 1D model with LE . . . . .	110
5.1	Material properties of the square beam . . . . .	117
5.2	Computational size of the investigated models for the square beam . . . . .	119
5.3	The values of $u_z$ at the tip point of the square beam (0, 1000, -10), $\sigma_{yy}$ at (0, 75, 10), and $\sigma_{yz}$ at (0, 75, 0), with $F=1100$ N . . . . .	123
5.4	Material properties of the C-shaped beam . . . . .	124
5.5	Computational size of the investigated models for the C-shaped beam . . . . .	125

5.6	The values of $\sigma_{yy}$ at (0, 75, 15), and $\sigma_{yz}$ at (0, 75, 0), for the C-shaped beam based on various structural theories and 3D FE discretizations for $u_z=100$ cm . . . . .	128
5.7	Material properties of the T-shaped beam . . . . .	129
5.8	Computational size of the investigated models for the T-shaped beam	130
5.9	The values of $u_z$ at (0, 1200, 30), $\sigma_{yy}$ at (0, 100, 33), and $\sigma_{yz}$ at (0, 100, 0), T-shaped beam based at the load of 3400 N . . . . .	133
6.1	Material properties of the investigated 4-layer composite plate . . .	149
6.2	Equilibrium points of nonlinear response curves of a 4-layer [0/90] <sub>s</sub> composite plate under transverse pressure with clamped edge conditions . . . . .	150
6.3	The comparison of displacement values for the 4-layer [0/90] <sub>s</sub> composite plates under transverse pressure at the fixed load of $\frac{P_z a^4}{E_2 h^4} = 100$ with clamped edge conditions, and at the fixed load of $\frac{P_z a^4}{E_2 h^4} = 25$ with simply-supported edge conditions . . . . .	151
6.4	Material properties of the investigated 16-layer composite plate . . .	152
6.5	Equilibrium points of nonlinear response curves of a 16-layer [45/-45/0/0/45/-45/90/90] <sub>s</sub> composite plate under uniform transverse pressure with clamped edge conditions . . . . .	153
6.6	Material properties of the investigated 2-layer composite plate . . .	154
6.7	Equilibrium points of nonlinear response curves of a 2-layer [0/90] composite plate under uniform transverse pressure with clamped edge conditions . . . . .	155
6.8	The displacement values based on different methods at the fixed load of $\frac{P_z a^4}{E_2 h^4} = 500$ for the 2-layer [0/90] composite plate, and at the fixed load of $\frac{P_z a^4}{E_2 h^4} = 1500$ for the 6-layer [0/90] <sub>3</sub> composite plate . . . . .	157
6.9	Material properties of a 4-layer [0/90] <sub>2</sub> composite plate . . . . .	158
6.10	Equilibrium points of nonlinear response curves of a cross-ply [0/90] <sub>2</sub> laminate under in-plane compressive line loads in the $x$ -axis direction with simply-supported edge conditions . . . . .	159

6.11	The comparison of displacement values at the fixed load of $\frac{N_x b a}{E_2 h^3} = 300$ and the normalized linear buckling loads for a cross-ply $[0/90]_2$ laminate . . . . .	161
6.12	Material properties of the investigated composite plate . . . . .	161
6.13	Equilibrium points of nonlinear response curves of a cross-ply $[0/90]$ laminate under in-plane compressive line loads in the y-axis direction with simply-supported edge conditions . . . . .	162
6.14	Material properties of the investigated 4-layer composite plate . . . . .	164
6.15	Material properties of the investigated 2-layer composite plate . . . . .	167
7.1	Material properties of the investigated composite plate . . . . .	174
7.2	Equilibrium points for different in-plane mesh size in SFSF composite plate based on the full nonlinear CUF plate model . . . . .	177
7.3	Equilibrium points for SFSF composite plate based on the different geometrically nonlinear assumptions of Table 2.3 . . . . .	179
7.4	The deformation contour plots of composite plate $[0/90/0/90]$ with SSSS edge conditions with different load and displacement boundary conditions based on the full nonlinear CUF plate model $12 \times 12Q9-LD1$ . . . . .	183
7.5	Equilibrium points for different in-plane mesh size in SSSS composite plate based on the full nonlinear CUF plate model . . . . .	185
7.6	Equilibrium points for SSSS composite plate based on the different geometrically nonlinear assumptions of Table 2.3 . . . . .	187
8.1	Material properties of the investigated composite plates . . . . .	196
8.2	Equilibrium points for Baron Epoxy composite plates subjected to pure shear loading based on the $12 \times 12Q9-LD1$ CUF model and the available literature . . . . .	199
8.3	Equilibrium points for Carbon Epoxy composite plates subjected to pure negative shear loading based on the $12 \times 12Q9-LD1$ CUF model and the available literature . . . . .	200

---

8.4	The deformation contour plots based on Fig. 8.5(b) for composite plates without stiffeners subjected to pure shear loading . . . . .	202
8.5	Equilibrium points for composite plates without stiffeners subjected to pure shear loading based on the 12x12Q9-LD1 model . . . . .	202
8.6	The deformation contour plots based on Fig. 8.6(b) for composite plates with stiffeners subjected to pure shear loading . . . . .	204
8.7	Equilibrium points for composite plates with stiffeners subjected to pure shear loading based on the 12x12Q9-LD1 model . . . . .	204
8.8	The deformation contour plots based on Fig. 8.7(b) for composite plates without stiffeners subjected to pure shear and biaxial compressive loading . . . . .	205
8.9	Equilibrium points for composite plates without stiffeners subjected to pure shear and biaxial compressive loading based on the 12x12Q9-LD1 model . . . . .	206
8.10	The deformation contour plots based on Fig. 8.8(b) for composite plates with stiffeners subjected to pure shear and biaxial compressive loading . . . . .	207
8.11	Equilibrium points for composite plates with stiffeners subjected to pure shear and biaxial compressive loading based on the 12x12Q9-LD1 model . . . . .	207
8.12	The deformation contour plots based on Fig. 8.9(b) for composite plates [45/-45] <sub>s</sub> with stiffeners subjected to pure shear and biaxial tensile loading . . . . .	209

# Chapter 1

## Introduction

### 1.1 Motivation

Nowadays, thin-walled beam and flexible plate structures are extensively used in many engineering applications such as mechanical components, aerospace, and civil industries. In addition, many high-performance goods and spare parts of automobiles and airplanes are made of fiber-reinforced composite materials because of the desired characteristics of high stiffness-to-weight ratio and corrosion resistance. The use of efficient computational methods for the analysis of the thin-walled beam and flexible plate structures made of composite materials has always been of primary importance for engineers and designers. In the present work, the Carrera Unified Formulation (CUF) is employed in order to solve the different structural problems of thin-walled beam and flexible plate structures. The large-deflection and post-buckling of isotropic and composite plates are investigated using the CUF and Newton–Raphson linearization scheme with the path-following method based on the arc-length constraint. The effects of different nonlinear theories and strain-displacement assumptions on the equilibrium curves and stress distributions are evaluated. The benchmarks for free vibration response of different thin-walled beams are presented, and the Vibration Correlation Technique is used for the assessment of vibrations under compressive loads. Using the efficient CUF-based framework, the following points will be addressed precisely in the present research:

- Free vibration response of thin-walled beams due to the cross-sectional deformations (Chapter 3)

- Vibrations of thin-walled beams under compression and the use of Virtual Correlation Technique for thin-walled beam structures under compression (Chapter 4)
- Physically and geometrically nonlinear analysis of thin-walled beam structures (Chapter 5)
- Large-deflection and post-buckling analysis of flexible plates and evaluation of geometrically nonlinear terms in the post-buckling of flexible plates (Chapter 6)
- Investigation of stiffeners and surroundings effects on the nonlinear response of flexible plates (Chapter 7)
- Buckling and post-buckling of flexible plates under in-plane shear and combined loadings (Chapter 8)

## 1.2 Carrera Unified Formulation

The CUF was introduced as an accurate and cost-effective method for the solution of different engineering problems related to the beam, plate, and shell structures. The free vibration analysis of plate and shell structure can be found in [1–4]. A hierarchical finite element (FE) was developed for the free vibration analysis of beam structures. In this regard, the matrices of stiffness and mass were formulated based on the Fundamental Nucleus (FN) [5]. The free vibration analysis of beam structures with different cross-sections was presented by Carrera et al. [6] by employing the CUF. The free vibration response of the beams with bridge-like cross-sections was investigated in [7]. A formulation of exact dynamic stiffness was developed by using the higher-order kinematic fields in order to evaluate the free vibration response of thin-walled structures [8]. The free vibration analysis of thin-walled structures considering the influence of nonstructural localized inertia was analyzed by Pagani et al. [9]. The free vibration of beam structures made of composite materials was investigated by employing higher-order beam theories [10]. Higher-order expansions based on Chebyshev polynomials were used for the free vibration analysis of composite beam structures [11]. Refined dynamic stiffness elements were studied for the free vibration response of composite beams [12]. Radial basis



functions were used in order to evaluate the free vibration response of thin-walled beam structures [13]. The beam structures with simply-supported edge conditions were focused [14]. Exact solutions were presented for the free vibration response of box and sandwich composite beams [15]. The mode changes and frequencies of beams with geometrical nonlinearities were analyzed by Pagani et al. [16]. Carrera et al. [17] investigated the effects of large displacements and rotations on the vibration response of composite beams. The Lagrange polynomial expansion for thin-walled beams of various cross-sections was used by Xu et al. [18] in order to develop an FE approach based on the CUF. A thorough investigation of free vibration analysis for thin-walled beams was studied by Xu et al. [19]. The method based on the framework of CUF for the vibration of isotropic and composite beams under compression was further studied in [20, 21].

### 1.3 Preliminary considerations

Here, a beam structure can be assumed in such a way that the cross-section domain  $S$  is located in the  $x - z$  plane, and the axis of the beam is located along the  $y$  axis. As a result, the vectorial forms for the displacement, stress, and strain could be expressed as follows:

$$\begin{aligned}\mathbf{u}(x, y, z; t) &= \{u_x \ u_y \ u_z\}^T \\ \boldsymbol{\sigma} &= \{\sigma_{xx} \ \sigma_{yy} \ \sigma_{zz} \ \sigma_{xz} \ \sigma_{yz} \ \sigma_{xy}\}^T \\ \boldsymbol{\varepsilon} &= \{\varepsilon_{xx} \ \varepsilon_{yy} \ \varepsilon_{zz} \ \varepsilon_{xz} \ \varepsilon_{yz} \ \varepsilon_{xy}\}^T\end{aligned}\tag{1.1}$$

By the assumption of small displacements and rotations, the following relationship between the strains and displacements can be obtained. This geometrical relation in the matrix form is:

$$\boldsymbol{\varepsilon} = \mathbf{D}\mathbf{u}\tag{1.2}$$

where  $\mathbf{D}$  is the linear differential operators expressed as:

$$\mathbf{D} = \begin{bmatrix} \partial_x & 0 & 0 \\ 0 & \partial_y & 0 \\ 0 & 0 & \partial_z \\ \partial_z & 0 & \partial_x \\ 0 & \partial_z & \partial_y \\ \partial_y & \partial_x & 0 \end{bmatrix}, \quad (1.3)$$

where  $\partial_x = \frac{\partial(\cdot)}{\partial x}$ ,  $\partial_y = \frac{\partial(\cdot)}{\partial y}$ , and  $\partial_z = \frac{\partial(\cdot)}{\partial z}$  are partial derivative operators.

The stress-strain relationship according to the Hook's law is:

$$\boldsymbol{\sigma} = \mathbf{C} \boldsymbol{\varepsilon} \quad (1.4)$$

For the orthotropic material, the matrix  $\mathbf{C}$  is:

$$\mathbf{C} = \begin{bmatrix} C_{11} & C_{12} & C_{13} & 0 & 0 & C_{16} \\ C_{12} & C_{22} & C_{23} & 0 & 0 & C_{26} \\ C_{13} & C_{23} & C_{33} & 0 & 0 & C_{36} \\ 0 & 0 & 0 & C_{44} & C_{45} & 0 \\ 0 & 0 & 0 & C_{45} & C_{55} & 0 \\ C_{16} & C_{26} & C_{36} & 0 & 0 & C_{66} \end{bmatrix} \quad (1.5)$$

where  $C_{ij}$  coefficients are functions of the elastic moduli along the longitudinal and transverse directions, the shear moduli, and the Poisson's ratios [22]. Interested readers are referred to [23] for more information about the explicit form of the material matrix  $\mathbf{C}$ .

## 1.4 Free vibration analysis based on the CUF

In the CUF framework, the three-dimensional displacement field for the beam structures is defined as follows [24]:

$$\mathbf{u}(x, y, z; t) = F_\tau(x, z) \mathbf{u}_\tau(y; t), \quad \tau = 0, 1, \dots, N, \quad (1.6)$$

where  $F_\tau$  is the set of cross-section functions and  $\mathbf{u}_\tau$  is the generalized displacement vector. It should be noted that  $\tau$  is expansion function index, and varies from 1 to  $N$ , where  $N$  refers to the number of polynomial terms in the cross-section expansion function. As it is obvious in Eq. (1.6), using the CUF allows us to select any expansion orders over the beam cross-section. As a result, various structural theories and kinematics assumptions can be efficiently implemented and employed. In this study, Taylor and Lagrange cross-section functions are used. Note that the refined Taylor and Lagrange expansions will be further described in the next sections of this chapter. If we use the FE approximation, the vector of displacement  $\mathbf{u}_\tau$  according to the nodal parameters  $\mathbf{u}_{\tau i}$  and shape functions  $N_i$  can be expressed as:

$$\mathbf{u}_\tau(y;t) = N_i(y) \mathbf{u}_{\tau i}(t), \quad i = 1, 2, \dots, p + 1, \quad (1.7)$$

where  $N_i$  is the  $i$ -th shape function,  $p$  is related to the order of the shape functions, and  $\mathbf{u}$  is the vector of nodal unknowns. Note that the choice of the axial shape functions  $N_i$  is independent of the choice of the cross-sectional expansion functions  $F_\tau$ , resulting in the significant flexibility in the structural modeling. Interested readers are referred to [25] for more information about the Lagrange polynomials and shape functions. As a result of employing the FE approximation and the CUF, the following displacement field is obtained:

$$\mathbf{u}(x, y, z; t) = N_i(y) F_\tau(x, z) \mathbf{u}_{\tau i}(t) \quad (1.8)$$

Based on the the Principle of Virtual Displacements (PVD), one can notice that:

$$\delta L_{int} + \delta L_{ine} = \delta L_{ext} \quad (1.9)$$

where  $L_{int}$ ,  $L_{ine}$ , and  $L_{ext}$  denote the strain energy, the work of inertial loadings, and the work of external loadings. In the case of free vibration analysis, the work of external loadings is zero, hence:

$$\delta L_{int} + \delta L_{ine} = 0 \quad (1.10)$$

As a result, the following equations are obtained for the virtual variations of strain energy and the inertial work.

$$\begin{aligned}\delta L_{\text{int}} &= \int_V \delta \boldsymbol{\varepsilon}^T \boldsymbol{\sigma} dV = \delta \mathbf{u}_{sj}^T \left( \int_V F_s(x, z) N_j(y) \mathbf{D}^T \mathbf{C} \mathbf{D} N_i(y) F_\tau(x, z) dV \right) \mathbf{u}_{\tau i} = \delta \mathbf{u}_{sj}^T \mathbf{K}^{ij\tau s} \mathbf{u}_{\tau i} \\ \delta L_{\text{ine}} &= \int_V \delta \mathbf{u}^T \rho \ddot{\mathbf{u}} dV = \delta \mathbf{u}_{sj}^T \left( \int_V F_s(x, z) N_j(y) \rho N_i(y) F_\tau(x, z) dV \right) \ddot{\mathbf{u}}_{\tau i} = \delta \mathbf{u}_{sj}^T \mathbf{M}^{ij\tau s} \ddot{\mathbf{u}}_{\tau i}\end{aligned}\quad (1.11)$$

where  $\mathbf{K}^{ij\tau s}$  and  $\mathbf{M}^{ij\tau s}$  are the FNs of stiffness and mass matrices. For a given  $i, j$  pair, these  $3 \times 3$  matrices are independent of the structure's order, and have a fixed form. All combinations of  $i, j, \tau$ , and  $s$  indices are taken into account to get the global matrices. Interested readers are referred to [24, 26] for additional information on the FN formulation and its explicit forms.

The PVD might be expressed as follows if the virtual variations of strain energy and the inertial work from Eqs. (1.11) are substituted into Eq. (1.10):

$$\delta \mathbf{u}_{sj}^T (\mathbf{K}^{ij\tau s} \mathbf{u}_{\tau i} + \mathbf{M}^{ij\tau s} \ddot{\mathbf{u}}_{\tau i}) = 0 \quad (1.12)$$

That could be expressed as:

$$\mathbf{M}^{ij\tau s} \ddot{\mathbf{u}}_{\tau i} + \mathbf{K}^{ij\tau s} \mathbf{u}_{\tau i} = 0 \quad (1.13)$$

Because the problem is linear, by using harmonic solutions, we can find the natural frequencies that allows us to find the solution of the eigenvalues problem.

$$(-\omega_k^2 \mathbf{M} + \mathbf{K}) \mathbf{u}_k = 0 \quad (1.14)$$

where  $\omega_k$  are the natural frequencies, and  $\mathbf{u}_k$  is the  $k$  th eigenvector.

## 1.5 Refined Taylor Expansion

Polynomial expansions of the kind  $x^m z^n$  are used as cross-section functions  $F_\tau$  in Taylor Expansion (TE) models. The integers  $m$  and  $n$  are both positive. The beam's structural theory is represented by the TE model's order (N), which is specified by

the user.  $N = 2$  is the second-order displacement field in this example:

$$\begin{aligned} u_x &= u_{x_1} + xu_{x_2} + zu_{x_3} + x^2u_{x_4} + xzu_{x_5} + z^2u_{x_6} \\ u_y &= u_{y_1} + xu_{y_2} + zu_{y_3} + x^2u_{y_4} + xzu_{y_5} + z^2u_{y_6} \\ u_z &= u_{z_1} + xu_{z_2} + zu_{z_3} + x^2u_{z_4} + xzu_{z_5} + z^2u_{z_6} \end{aligned} \quad (1.15)$$

In the above equation, there are eighteen generalized displacement variables from  $u_{x_1}$  to  $u_{z_6}$ . Fig. 1.1 schematically depicts some of these variables for the linear TE model ( $N = 1$ ), where the beam example is subjected to bending around  $z$  axis. It can be observed in this figure that for the given beam example, the unknowns  $u_{x_1}$ ,  $u_{y_1}$ , and  $u_{z_1}$  are axis displacements of the beam. The other unknowns are  $u_{x_2}$ ,  $u_{y_2}$ ,  $u_{z_2}$ ,  $u_{x_3}$ ,  $u_{y_3}$ , and  $u_{z_3}$  which correspond to the rotations with respect to the axes. The two classical beam theories of Timoshenko beam theory (TBT) and Euler–Bernoulli beam theory (EBBT) are derived from the linear TE model [24]. When it comes to the displacement field, for example, the TBT only considers these terms:

$$\begin{aligned} u_x &= u_{x_1} \\ u_y &= u_{y_1} + xu_{y_2} + zu_{y_3} \\ u_z &= u_{z_1} \end{aligned} \quad (1.16)$$

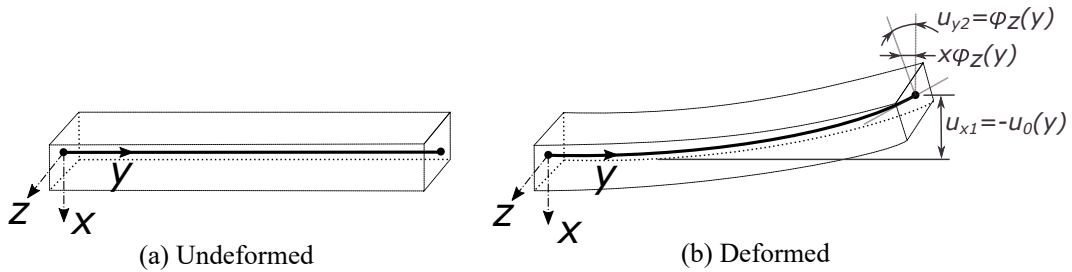


Fig. 1.1 Some generalized displacement variables derived from the linear TE model for a schematic beam under bending around the  $z$  axis

## 1.6 Refined Lagrange Expansion

The effectiveness of Lagrange Expansions (LE) has been proved in a variety of applications, including aerospace and civil constructions [27–29]. The unknown variables in the LE models are pure displacements (refer to Fig. 1.2). For the

expansion function over the cross-section, four-node Lagrange polynomials (L4) and nine-node Lagrange polynomials (L9) are used in this study. The displacement field when using L9 polynomials is quadratic and could be written in the following form:

$$\begin{aligned} u_x(x, y, z; t) &= F_1(x, z)u_{x_1}(y; t) + F_2(x, z)u_{x_2}(y; t) + \dots + F_9(x, z)u_{x_9}(y; t) \\ u_y(x, y, z; t) &= F_1(x, z)u_{y_1}(y; t) + F_2(x, z)u_{y_2}(y; t) + \dots + F_9(x, z)u_{y_9}(y; t) \\ u_z(x, y, z; t) &= F_1(x, z)u_{z_1}(y; t) + F_2(x, z)u_{z_2}(y; t) + \dots + F_9(x, z)u_{z_9}(y; t) \end{aligned} \quad (1.17)$$

where  $u_{x_1}, \dots, u_{z_9}$  denote the displacements of the cross-sectional elements' points and  $F_1, \dots, F_9$  denote functions of the cross-sectional coordinates which are the first nine Lagrange polynomials of order three [17]. More information regarding the beam models with LE may be found in the book by Carrera et al. [24], which is recommended for interested readers.

Eqs. (1.18) and Table 1.1 report the interpolation functions and point coordinates for the L9 Lagrange polynomials using the isoparametric formulation for beams with arbitrary cross-sections. The actual and normalized geometries of the L9 Lagrange elements are shown in Fig. 1.3. For a schematic beam subjected to bending around the  $z$  axis, pure displacement variables according to the Lagrange model (L4) are illustrated in Fig. 1.2.

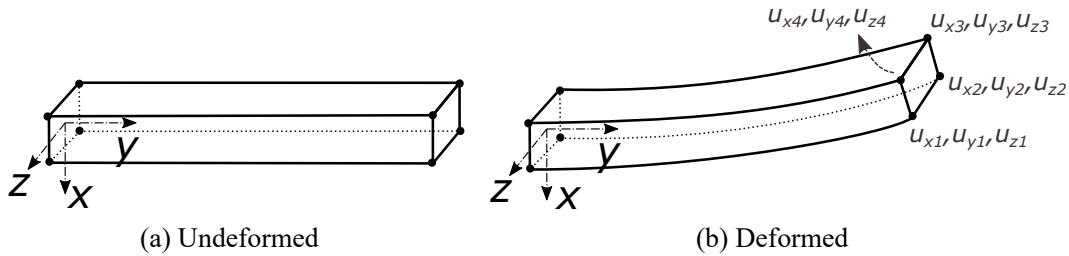


Fig. 1.2 schematic depiction of pure displacement variables according to the Lagrange model (L4) for an example beam subjected to bending around  $z$  axis

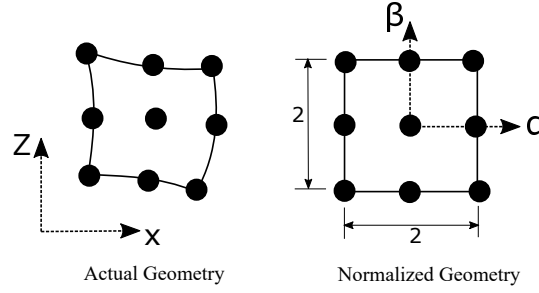


Fig. 1.3 Nine-node Lagrange polynomials in the actual and normalized geometries

$$\begin{aligned}
 F_{\tau} &= \frac{1}{4}(\alpha^2 + \alpha\alpha_{\tau})(\beta^2 + \beta\beta_{\tau}), & \tau = 1, 3, 5, 7 \\
 F_{\tau} &= \frac{1}{2}\beta_{\tau}^2(\beta^2 + \beta\beta_{\tau})(1 - \alpha^2) + \frac{1}{2}\alpha_{\tau}^2(\alpha^2 + \alpha\alpha_{\tau})(1 - \beta^2), & \tau = 2, 4, 6, 8 \\
 F_{\tau} &= (1 - \alpha^2)(1 - \beta^2), & \tau = 9
 \end{aligned} \tag{1.18}$$

Table 1.1 Normalized coordinates of L9 element

Points	1	2	3	4	5	6	7	8	9
$\alpha_{\tau}$	-1	0	1	1	1	0	-1	-1	0
$\beta_{\tau}$	-1	-1	-1	0	1	1	1	0	0

## 1.7 Shear locking

Shear locking [30, 31] is a numerical phenomenon that can occur when the thickness of beams or plates decreases. In fact, this is due to the overestimation of the shear stiffness of the structures, which tends to be infinite as the thickness approaches zero [24]. This problem may be addressed using the techniques such as reduced integration, selective integration, and Mixed Interpolation of Tensorial Components (MITC).

To lessen the stiffness of displacement-based elements, Zienkiewicz [32, 33] presented the reduced integration approach that suggests reducing the order of numerical integration in some terms of the stiffness matrix. Another method according

to the reduced integration for transverse shear terms is selective integration [34, 35]. For the other stiffness matrix terms, a full quadrature is taken into account when using the selective integration approach. A reduced Gauss integration of the terms of the stiffness matrix that are connected to the shear is the basis of this method. Hence, the structure's shear stiffness is decreased as a result of the reduction in the number of Gauss points.

Furthermore, the MITC method for reducing the shear locking problem has been successful [36, 37]. In the MITC formulation, the FE approximation for the transverse shear strains is brought into the element domain. The phenomenon of transverse shear locking is thus eliminated as a result of this procedure. For the transverse shear terms and, finally, membrane terms of the stiffness matrix of FEs, this method relies on the usage of assumed strain distributions [38]. Refer to [38] for further information on the formulation and the development of the MITC technique for higher-order beam theories.



# Chapter 2

## Nonlinear Governing Equations

### 2.1 Introduction

By employing refined structural models, nonlinear analysis can be made more affordable without affecting their accuracy or reliability. In recent years, the CUF has been extended to nonlinear structural problems, allowing to generate of any order structural theory [39–42, 22, 43]. A refined beam model based on the CUF was developed by Pagani and Carrera to address geometrically nonlinear structural problems [40, 44]. They employed a path-following method in conjunction with the Newton-Raphson linearization scheme. By using the layer-wise approach [45, 46] based on the LE, interface compatibility conditions could be easily imposed between different layers, and the expansions along the thickness could be chosen of any order. The CUF and layer-wise theory were used to study the large-deflection and post-buckling in composite beam structures [39]. Petrolo et al. [41] proposed a CUF-based global-local technique that considered physical nonlinearities to study elastoplastic structures. The isotropically work-hardening von Mises constitutive model for material nonlinearity was implemented by Carrera et al.[42] to conduct nonlinear analysis on the elastoplastic structures. Based on the one-dimensional component-wise CUF models, Kaleel et al. [47] developed a computational framework for predicting the delamination of laminated structures. For the delamination problems of composite structures with von Mises plasticity and cohesive interface modeling, the influence of kinematic enrichment was evaluated [48]. The elastoplastic contact problems of metallic structures were investigated by Nagaraj et al. [49]. Petrolo

et al. [50] analyzed the nonlinear response and stress distributions for the beam structures with geometrical and physical nonlinearities. Using the refined beam and plate models in the framework of CUF with a total Lagrangian scenario, nonlinear theories based on the different strain-displacement assumptions were evaluated [51–53]. In the same framework, Carrera et al. [54] studied the large-deflection and post-buckling equilibrium states of plate structures subjected to different loading conditions. The nonlinear analyses of two-dimensional isotropic and composite shell structures based on the CUF are provided in [55–57].

## 2.2 Geometrically nonlinear analysis based on the CUF

An elastic system that is in the equilibrium state, subjected to external forces and prescribed geometrical constraints is assumed. According to the principle of virtual work, the sum of all the virtual work which is done by the internal and external forces in the system is zero in any arbitrary infinitesimal virtual displacements satisfying the geometrical constraints [58]. Hence:

$$\delta L_{\text{int}} - \delta L_{\text{ext}} = 0 \quad (2.1)$$

where  $L_{\text{int}}$  is the strain energy,  $L_{\text{ext}}$  is the work of external loadings, and  $\delta$  represents the variation.

In the analysis of elastic systems, the Large deflection leads to complex nonlinear differential equations for the problem. The analytical solutions for these problems are rarely available and only in a limited number of applications. A broader range of geometrically nonlinear problems can be analyzed if the FE method is used. In this regard, a system of nonlinear algebraic equations can be used to define the equilibrium state of the structure. By employing the framework of CUF (Eq. (1.6)) along with Eqs. (1.7) and (2.1), the equilibrium conditions and the corresponding FE arrays could be expressed as follows:

$$\mathbf{K}_S^{ij\tau s} \mathbf{q}_{sj} - \mathbf{p}_{sj} = 0 \quad (2.2)$$

where  $\mathbf{p}_{sj}$  and  $\mathbf{K}_S^{ij\tau s}$  denote the FNs of the vector of the nodal loadings and the secant stiffness matrix, respectively, refer to [59] for more information about the derivation of the loading vector's FN. Moreover, the detailed formulation of the FNs of the secant stiffness matrix for the beam and plate structures are discussed in sections 2.4.1 and 2.4.2, respectively.

Using the indexes  $\tau, s = 1, \dots, M$  and  $i, j = 1, \dots, p + 1$ , and expanding Eq. (2.2), the following FE governing equations can be obtained:

$$\mathbf{K}_S \mathbf{q} - \mathbf{p} = 0 \quad (2.3)$$

where  $\mathbf{K}_S$ ,  $\mathbf{q}$ , and  $\mathbf{p}$  denote global, assembled FE arrays of the structure.

## 2.3 Newton-Raphson linearization with path-following constraint

Eq. (2.3) constitutes the starting point for FE calculation of geometrically nonlinear systems, and it is usually solved through an incremental linearized scheme, typically the Newton-Raphson method (or *tangent method*).

The Newton-Raphson approach or tangent method commonly used to incrementally linearize Eq. (2.3) as the starting point for FE calculations of geometrically nonlinear problems. Based on the Newton-Raphson method, Eq. (2.3) is expressed as [60]:

$$\varphi_{res} \equiv \mathbf{K}_S \mathbf{q} - \mathbf{p} = 0 \quad (2.4)$$

where  $\varphi_{res}$  denotes the vector of residual nodal forces. Therefore, Eq. (2.4) could be linearized by Taylor's series expanding  $\varphi_{res}$  about a known solution  $(\mathbf{q}, \mathbf{p})$ . By removing the second-order terms, the following equation are obtained:

$$\varphi_{res}(\mathbf{q} + \delta\mathbf{q}, \mathbf{p} + \delta\mathbf{p}) = \varphi_{res}(\mathbf{q}, \mathbf{p}) + \frac{\partial \varphi_{res}}{\partial \mathbf{q}} \delta\mathbf{q} + \frac{\partial \varphi_{res}}{\partial \mathbf{p}} \delta\lambda \mathbf{p}_{ref} = 0 \quad (2.5)$$

where  $\frac{\partial \varphi_{res}}{\partial \mathbf{q}} = \mathbf{K}_T$  represents the tangent stiffness matrix, and  $-\frac{\partial \varphi_{res}}{\partial \mathbf{p}}$  is equal to the unit matrix  $\mathbf{I}$ . One can obtain  $\lambda, \mathbf{p} = \lambda \mathbf{p}_{ref}$  under the assumption that the load varies directly with the vector of reference loadings  $\mathbf{p}_{ref}$  and has a rate of variations

equal to the load parameter. Thus, Eq. (2.5) can be rewritten in the following form:

$$\mathbf{K}_T \delta \mathbf{q} = \delta \lambda \mathbf{p}_{ref} - \boldsymbol{\varphi}_{res} \quad (2.6)$$

Because  $\lambda$  is a load-scaling variable, another governing equation is required, i.e. constraint relationship  $c(\delta \mathbf{q}, \delta \lambda)$ , as a result:

$$\begin{cases} \mathbf{K}_T \delta \mathbf{q} = \delta \lambda \mathbf{p}_{ref} - \boldsymbol{\varphi}_{res} \\ c(\delta \mathbf{q}, \delta \lambda) = 0 \end{cases} \quad (2.7)$$

Different incremental techniques can be implemented in accordance with the constraint equation, for instance, in the case of constraint equation  $c(\delta \mathbf{q}, \delta \lambda) = \delta \lambda = 0$ , one can note that Eq. (2.7) represents the load-control method.  $c(\delta \mathbf{q}, \delta \lambda) = \delta \mathbf{q} = 0$ , on the other hand, refers to the displacement control approach. Fig. 2.1 illustrates the differences between the load control, displacement control, and path-following approaches. In this research, a path-following method based on the arc-length constraint is used in which the constraint equation is the function of both the displacement and load parameter variations. More information regarding different incremental methods can be found in [60–62].

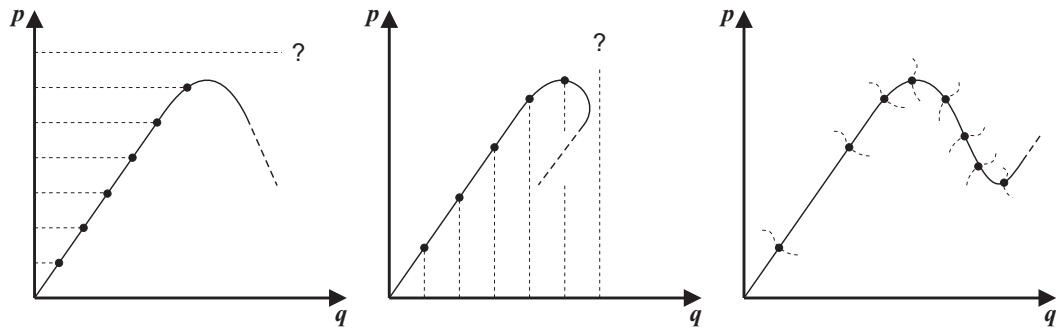


Fig. 2.1 Different incremental techniques based on the load control, displacement control, and path-following methods [40]

Fig. 2.2 shows the details of incremental method implemented here. In this figure,  $\delta_m^n(\cdot)$  represents the finite variations,  $m = 1, 2, \dots$  refers to the global variations of load-step, and  $n = 0, 1, 2, \dots$  refers to the local iteration within the load-step  $m$ , where  $\delta_m^n(\cdot) = (\cdot)_m^n - (\cdot)_m^{n-1}$ ,  $(\cdot)_m = (\cdot)_{m-1} + \sum_n \delta_m^n(\cdot)$ . Therefore,  $n = 0$ , and  $\delta_m^0 \mathbf{q}$  correspond to the initial solution;  $\delta_m^0 \lambda$  is the initial increment of load parameter. Furthermore,  $\mathbf{q}_{m-1}$  and  $\lambda_{m-1} \mathbf{p}_{ref}$  refer to the displacement and load vectors at the

previous load-step, respectively; and finally,  $\varphi_{m_{res}}^n$  is the residual force vector of the current iteration. According to Eq. (2.7) and Fig. 2.2, the equilibrium iterates (solid dots) are provided by the intersection of the linearized governing equations and the constraint equation  $c(\delta \mathbf{q}, \delta \lambda) = 0$ , which is depicted as a series of arcs. At each iteration,  $\mathbf{t}_m^n = \mathbf{t}_m^{n-1} + \delta_m^n \mathbf{t} = \mathbf{t}_m^{n-1} + (\delta_m^n \mathbf{q} + \delta_m^n \lambda \mathbf{p}_{ref})$  refers to the vector connecting the current equilibrium iterates to the solution at the previous load-step.

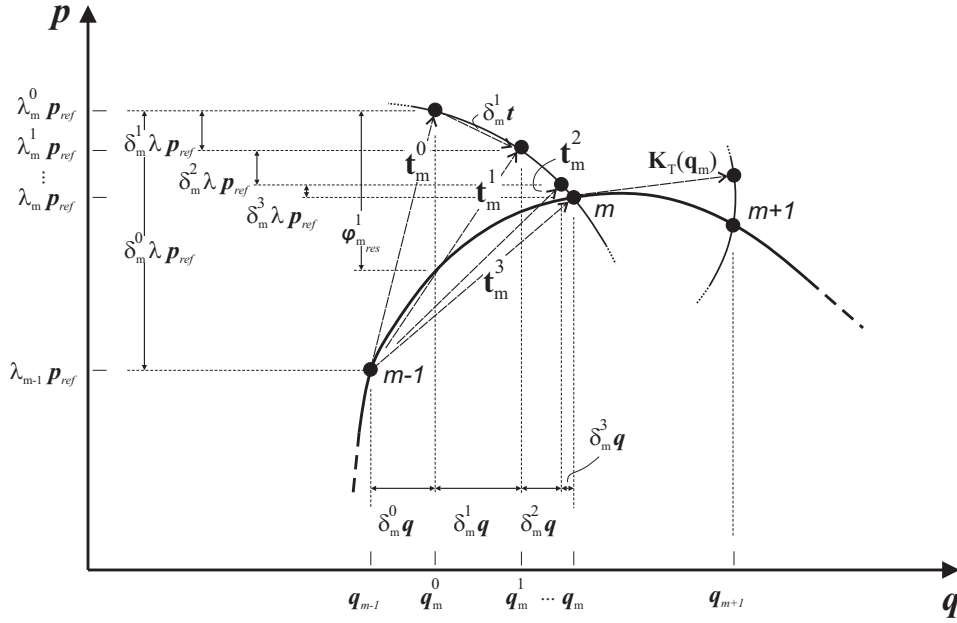


Fig. 2.2 The details of implemented incremental method [40]

According to the strategy proposed by Batoz and Dhatt [63], the incremental displacement vector at the current iteration could be rewritten in the following form:

$$\delta_m^n \mathbf{q} = \delta_m^n \lambda \bar{\mathbf{q}}_m^n + \delta_m^n \hat{\mathbf{q}} \quad (2.8)$$

where  $\bar{\mathbf{q}}_m^n$  and  $\delta_m^n \hat{\mathbf{q}}$  are the solutions of the following linear systems:

$$\begin{cases} \mathbf{K}_T \bar{\mathbf{q}}_m^n = \mathbf{p}_{ref} \\ \mathbf{K}_T \delta_m^n \hat{\mathbf{q}} = -\varphi_{m_{res}}^n \end{cases} \quad (2.9)$$

Therefore, based on the arc-length method proposed by Crisfield [64, 65], the following quadratic constraint equation is obtained:

$$a(\delta_m^n \lambda)^2 + 2b \delta_m^n \lambda + c = 0 \quad (2.10)$$

where

$$\begin{aligned} a &= \bar{\mathbf{q}}_m^{nT} \bar{\mathbf{q}}_m^n + \mathbf{p}_{ref}^T \mathbf{p}_{ref} \\ b &= (\mathbf{q}_m^{n-1} - \mathbf{q}_{m-1})^T \bar{\mathbf{q}}_m^n + \bar{\mathbf{q}}_m^{nT} \delta_m^n \hat{\mathbf{q}} + (\lambda_m^{n-1} - \lambda_{m-1}) \mathbf{p}_{ref}^T \mathbf{p}_{ref} \\ c &= ((\mathbf{q}_m^{n-1} - \mathbf{q}_{m-1}) + \delta_m^n \hat{\mathbf{q}})^T ((\mathbf{q}_m^{n-1} - \mathbf{q}_{m-1}) + \delta_m^n \hat{\mathbf{q}}) + \\ &\quad (\lambda_m^{n-1} - \lambda_{m-1})^2 \mathbf{p}_{ref}^T \mathbf{p}_{ref} - (\Delta l_m^0)^2 \end{aligned} \quad (2.11)$$

In this research, a full Newton-Raphson method is used in such a way that an updated tangent stiffness matrix at each iteration is utilized. The tangent stiffness matrix  $\mathbf{K}_T$  is calculated from the linearization of the constitutive equations and geometrical relations. Readers are referred to [66–68] for more information about other linearization methods. Based on the total Lagrangian formulation, the expressions of both  $\mathbf{K}_S$  and  $\mathbf{K}_T$  are given in the following sections for the beam and plate structures. These matrices are provided in terms of FNs, and the use of CUF gives the possibility to engender the element matrices of any arbitrary refined theories.

## 2.4 Secant stiffness matrix

The secant stiffness matrix  $\mathbf{K}_S$  can be obtained from the virtual variation of the strain energy  $\delta L_{int}$ :

$$\delta L_{int} = \langle \delta \boldsymbol{\varepsilon}^T \boldsymbol{\sigma} \rangle \quad (2.12)$$

where  $\langle (\cdot) \rangle = \int_V (\cdot) dV$ , where  $V$  is the initial volume of the structure.

By using the strain-displacement relations, the Green-Lagrange strain vector  $\boldsymbol{\varepsilon}$  is calculated as:

$$\boldsymbol{\varepsilon} = \boldsymbol{\varepsilon}_l + \boldsymbol{\varepsilon}_{nl} = (\mathbf{b}_l + \mathbf{b}_{nl}) \mathbf{q} \quad (2.13)$$

where  $\mathbf{b}_l$  and  $\mathbf{b}_{nl}$  represent the  $6 \times 3$  linear and nonlinear differential operators as follows:

$$\mathbf{b}_l = \begin{bmatrix} 0 & \partial_y & 0 \\ \partial_x & 0 & 0 \\ 0 & 0 & \partial_z \\ \partial_z & 0 & \partial_x \\ 0 & \partial_z & \partial_y \\ \partial_y & \partial_x & 0 \end{bmatrix}, \quad \mathbf{b}_{nl} = \begin{bmatrix} \frac{1}{2}(\partial_y)^2 & \frac{1}{2}(\partial_y)^2 & \frac{1}{2}(\partial_y)^2 \\ \frac{1}{2}(\partial_x)^2 & \frac{1}{2}(\partial_x)^2 & \frac{1}{2}(\partial_x)^2 \\ \frac{1}{2}(\partial_z)^2 & \frac{1}{2}(\partial_z)^2 & \frac{1}{2}(\partial_z)^2 \\ \partial_x \partial_z & \partial_x \partial_z & \partial_x \partial_z \\ \partial_y \partial_z & \partial_y \partial_z & \partial_y \partial_z \\ \partial_x \partial_y & \partial_x \partial_y & \partial_x \partial_y \end{bmatrix}, \quad (2.14)$$

in which  $\partial_x = \partial(\cdot)/\partial x$ ,  $\partial_y = \partial(\cdot)/\partial y$ , and  $\partial_z = \partial(\cdot)/\partial z$ .

The strain vector  $\boldsymbol{\varepsilon}$  can be written in terms of the generalized nodal unknowns  $\mathbf{q}_{sj}$  by employing the CUF and FE approximation as:

$$\boldsymbol{\varepsilon} = (\mathbf{B}_l^{sj} + \mathbf{B}_{nl}^{sj})\mathbf{q}_{sj} \quad (2.15)$$

Similar to Eq. (2.15), the virtual variation of the strain vector  $\delta\boldsymbol{\varepsilon}$  can be written in terms of nodal unknowns as:

$$\delta\boldsymbol{\varepsilon} = \delta((\mathbf{B}_l^{\tau i} + \mathbf{B}_{nl}^{\tau i})\mathbf{q}_{\tau i}) = (\mathbf{B}_l^{\tau i} + 2\mathbf{B}_{nl}^{\tau i})\delta\mathbf{q}_{\tau i} \quad (2.16)$$

Therefore,

$$\delta\boldsymbol{\varepsilon}^T = \delta\mathbf{q}_{\tau i}^T (\mathbf{B}_l^{\tau i} + 2\mathbf{B}_{nl}^{\tau i})^T \quad (2.17)$$

By substituting the constitutive relations, Eqs. (2.15), and (2.17) into Eq. (2.12), we have:

$$\begin{aligned} \delta L_{\text{int}} &= \delta\mathbf{q}_{\tau i}^T \langle (\mathbf{B}_l^{\tau i} + 2\mathbf{B}_{nl}^{\tau i})^T \mathbf{C} (\mathbf{B}_l^{sj} + \mathbf{B}_{nl}^{sj}) \rangle \mathbf{q}_{sj} \\ &= \delta\mathbf{q}_{\tau i}^T \mathbf{K}_0^{ij\tau s} \mathbf{q}_{sj} + \delta\mathbf{q}_{\tau i}^T \mathbf{K}_{lnl}^{ij\tau s} \mathbf{q}_{sj} + \delta\mathbf{q}_{\tau i}^T \mathbf{K}_{nll}^{ij\tau s} \mathbf{q}_{sj} + \delta\mathbf{q}_{\tau i}^T \mathbf{K}_{nlnl}^{ij\tau s} \mathbf{q}_{sj} \\ &= \delta\mathbf{q}_{\tau i}^T \mathbf{K}_S^{ij\tau s} \mathbf{q}_{sj} \end{aligned} \quad (2.18)$$

in which the secant stiffness matrix is  $\mathbf{K}_S^{ij\tau s} = \mathbf{K}_0^{ij\tau s} + \mathbf{K}_{lnl}^{ij\tau s} + \mathbf{K}_{nll}^{ij\tau s} + \mathbf{K}_{nlnl}^{ij\tau s}$ . In Eq. (2.18),  $\mathbf{K}_0^{ij\tau s}$  is referred to as linear stiffness matrix and contains the linear component of  $\mathbf{K}_S$ ,  $\mathbf{K}_{lnl}^{ij\tau s}$  and  $\mathbf{K}_{nll}^{ij\tau s}$  are related to nonlinear contributions of order one, and  $\mathbf{K}_{nlnl}^{ij\tau s}$  corresponds to nonlinearities of order two. The following equations can be used for the calculation of these matrices:

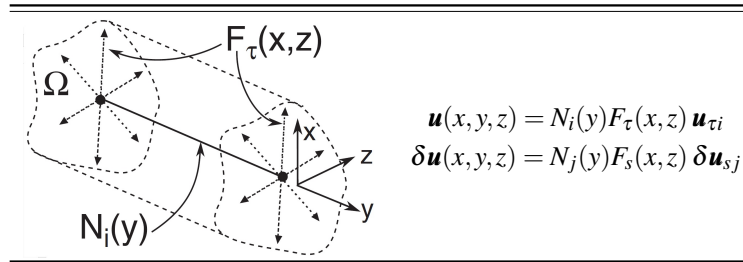
$$\begin{aligned} \mathbf{K}_0^{ij\tau s} &= \langle (\mathbf{B}_l^{\tau i})^T \mathbf{C} \mathbf{B}_l^{sj} \rangle & \mathbf{K}_{lnl}^{ij\tau s} &= \langle (\mathbf{B}_l^{\tau i})^T \mathbf{C} \mathbf{B}_{nl}^{sj} \rangle \\ \mathbf{K}_{nll}^{ij\tau s} &= 2 \langle (\mathbf{B}_{nl}^{\tau i})^T \mathbf{C} \mathbf{B}_l^{sj} \rangle & \mathbf{K}_{nlnl}^{ij\tau s} &= 2 \langle (\mathbf{B}_{nl}^{\tau i})^T \mathbf{C} \mathbf{B}_{nl}^{sj} \rangle \end{aligned} \quad (2.19)$$

In sections 2.4.1 and 2.4.2, the expressions for the FNs of  $\mathbf{K}_0^{ij\tau s}$ ,  $\mathbf{K}_{lnl}^{ij\tau s}$ ,  $\mathbf{K}_{nll}^{ij\tau s}$ , and  $\mathbf{K}_{nlnl}^{ij\tau s}$  matrices are provided for the sake of completeness. These are  $3 \times 3$  matrices that, given the expansion functions and the shape functions, can be expanded by using the indexes  $\tau, s = 1, \dots, M$  and  $i, j = 1, \dots, p + 1$  in order to obtain the element secant stiffness matrix of any arbitrarily refined model. Then, the element secant stiffness matrix can be assembled based on the classical FE methods (see [24]).

### 2.4.1 FN of the secant stiffness matrix for finite beam element

A schematic description of the CUF and FE approximation for the beam structures is shown in Table 2.1. Therefore, the two matrices of  $\mathbf{B}_l^{sj}$  and  $\mathbf{B}_{nl}^{sj}$  for the beam structures are obtained as follows:

Table 2.1 A schematic description of the CUF and FE approximation for the beam structures [24]





$$\mathbf{B}_l^{sj} = \mathbf{b}_l(F_s N_j) = \begin{bmatrix} F_{s,x} N_j & 0 & 0 \\ 0 & F_s N_{j,y} & 0 \\ 0 & 0 & F_{s,z} N_j \\ F_{s,z} N_j & 0 & F_{s,x} N_j \\ 0 & F_{s,z} N_j & F_s N_{j,y} \\ F_s N_{j,y} & F_{s,x} N_j & 0 \end{bmatrix} \quad (2.20)$$

and

$$\mathbf{B}_{nl}^{sj} = \frac{1}{2} \begin{bmatrix} u_{x,x} F_{s,x} N_j & u_{y,x} F_{s,x} N_j & u_{z,x} F_{s,x} N_j \\ u_{x,y} F_s N_{j,y} & u_{y,y} F_s N_{j,y} & u_{z,y} F_s N_{j,y} \\ u_{x,z} F_{s,z} N_j & u_{y,z} F_{s,z} N_j & u_{z,z} F_{s,z} N_j \\ u_{x,x} F_{s,z} N_j + u_{x,z} F_{s,x} N_j & u_{y,x} F_{s,z} N_j + u_{y,z} F_{s,x} N_j & u_{z,x} F_{s,z} N_j + u_{z,z} F_{s,x} N_j \\ u_{x,y} F_{s,z} N_j + u_{x,z} F_s N_{j,y} & u_{y,y} F_{s,z} N_j + u_{y,z} F_s N_{j,y} & u_{z,y} F_{s,z} N_j + u_{z,z} F_s N_{j,y} \\ u_{x,x} F_s N_{j,y} + u_{x,y} F_{s,x} N_j & u_{y,x} F_s N_{j,y} + u_{y,y} F_{s,x} N_j & u_{z,x} F_s N_{j,y} + u_{z,y} F_{s,x} N_j \end{bmatrix} \quad (2.21)$$

where  $\mathbf{B}_l$  and  $\mathbf{B}_{nl}$  represent linear and nonlinear geometrical matrices, and commas denote partial derivatives. Accordingly, if we consider  $r$  as the row number ( $r = 1, 2, 3$ ) and  $c$  as the column number ( $c = 1, 2, 3$ ), the nine components of the  $3 \times 3$  FN of linear stiffness matrix in the form of  $\mathbf{K}_0^{ij\tau s}[r, c]$  could be expressed as follows:

$$\begin{aligned} \mathbf{K}_0^{ij\tau s}[1, 1] &= \langle C_{11} F_{\tau,x} F_{s,x} N_i N_j \rangle + \langle C_{44} F_{\tau,z} F_{s,z} N_i N_j \rangle \\ &+ \langle C_{66} F_{\tau} F_s N_{i,y} N_{j,y} \rangle \end{aligned}$$

$$\mathbf{K}_0^{ij\tau s}[1, 2] = \langle C_{66} F_{\tau} F_{s,x} N_{i,y} N_j \rangle + \langle C_{12} F_{\tau,x} F_s N_i N_{j,y} \rangle$$

$$\mathbf{K}_0^{ij\tau s}[1, 3] = \langle C_{13} F_{\tau,x} F_{s,z} N_i N_j \rangle + \langle C_{44} F_{\tau,z} F_{s,x} N_i N_j \rangle$$

$$\mathbf{K}_0^{ij\tau s}[2, 1] = \langle C_{12} F_{\tau} F_{s,x} N_{i,y} N_j \rangle + \langle C_{66} F_{\tau,x} F_s N_i N_{j,y} \rangle$$

$$\begin{aligned} \mathbf{K}_0^{ij\tau s}[2, 2] &= \langle C_{66} F_{\tau,x} F_{s,x} N_i N_j \rangle + \langle C_{55} F_{\tau,z} F_{s,z} N_i N_j \rangle \\ &+ \langle C_{22} F_{\tau} F_s N_{i,y} N_{j,y} \rangle \end{aligned}$$

$$\mathbf{K}_0^{ij\tau s}[2, 3] = \langle C_{23} F_{\tau} F_{s,z} N_{i,y} N_j \rangle + \langle C_{55} F_{\tau,z} F_s N_i N_{j,y} \rangle$$

$$\mathbf{K}_0^{ij\tau s}[3, 1] = \langle C_{44} F_{\tau,x} F_{s,z} N_i N_j \rangle + \langle C_{13} F_{\tau,z} F_{s,x} N_i N_j \rangle$$

$$\mathbf{K}_0^{ij\tau s}[3, 2] = \langle C_{55} F_{\tau} F_{s,z} N_{i,y} N_j \rangle + \langle C_{23} F_{\tau,z} F_s N_i N_{j,y} \rangle$$

$$\begin{aligned}
\mathbf{K}_0^{ij\tau s}[3,3] &= \langle C_{44} F_{\tau,x} F_{s,x} N_i N_j \rangle + \langle C_{33} F_{\tau,z} F_{s,z} N_i N_j \rangle \\
&+ \langle C_{55} F_{\tau} F_s N_{i,y} N_{j,y} \rangle
\end{aligned} \tag{2.22}$$

Similarly, the components of the FNs of the first-order nonlinear stiffness matrix  $\mathbf{K}_{nll}^{ij\tau s}$  are obtained as:

For  $c = 1$ :

$$\begin{aligned}
\mathbf{K}_{nll}^{ij\tau s}[r,c] &= \langle \mathbf{u}_{,x}[r] C_{11} F_{\tau,x} F_{s,x} N_i N_j \rangle + \langle \mathbf{u}_{,x}[r] C_{44} F_{\tau,z} F_{s,z} N_i N_j \rangle \\
&+ \langle \mathbf{u}_{,x}[r] C_{66} F_{\tau} F_s N_{i,y} N_{j,y} \rangle + \langle \mathbf{u}_{,y}[r] C_{66} F_{\tau,x} F_s N_i N_{j,y} \rangle \\
&+ \langle \mathbf{u}_{,x}[r] C_{12} F_{\tau} F_{s,x} N_{i,y} N_j \rangle + \langle \mathbf{u}_{,z}[r] C_{44} F_{\tau,x} F_{s,z} N_i N_j \rangle \\
&+ \langle \mathbf{u}_{,z}[r] C_{13} F_{\tau,z} F_{s,x} N_i N_j \rangle
\end{aligned}$$

For  $c = 2$ :

$$\begin{aligned}
\mathbf{K}_{nll}^{ij\tau s}[r,c] &= \langle \mathbf{u}_{,x}[r] C_{12} F_{\tau,x} F_s N_i N_{j,y} \rangle + \langle \mathbf{u}_{,x}[r] C_{66} F_{\tau} F_{s,x} N_{i,y} N_j \rangle \\
&+ \langle \mathbf{u}_{,y}[r] C_{66} F_{\tau,x} F_{s,x} N_i N_j \rangle + \langle \mathbf{u}_{,y}[r] C_{55} F_{\tau,z} F_{s,z} N_i N_j \rangle \\
&+ \langle \mathbf{u}_{,y}[r] C_{22} F_{\tau} F_s N_{i,y} N_{j,y} \rangle + \langle \mathbf{u}_{,z}[r] C_{23} F_{\tau,z} F_s N_i N_{j,y} \rangle \\
&+ \langle \mathbf{u}_{,z}[r] C_{55} F_{\tau} F_{s,z} N_{i,y} N_j \rangle
\end{aligned}$$

For  $c = 3$ :

$$\begin{aligned}
\mathbf{K}_{nll}^{ij\tau s}[r,c] &= \langle \mathbf{u}_{,x}[r] C_{13} F_{\tau,x} F_{s,z} N_i N_j \rangle + \langle \mathbf{u}_{,x}[r] C_{44} F_{\tau,z} F_{s,x} N_i N_j \rangle \\
&+ \langle \mathbf{u}_{,y}[r] C_{55} F_{\tau,z} F_s N_i N_{j,y} \rangle + \langle \mathbf{u}_{,y}[r] C_{23} F_{\tau} F_{s,z} N_{i,y} N_j \rangle \\
&+ \langle \mathbf{u}_{,z}[r] C_{44} F_{\tau,x} F_{s,x} N_i N_j \rangle + \langle \mathbf{u}_{,z}[r] C_{33} F_{\tau,z} F_{s,z} N_i N_j \rangle \\
&+ \langle \mathbf{u}_{,z}[r] C_{55} F_{\tau} F_s N_{i,y} N_{j,y} \rangle
\end{aligned} \tag{2.23}$$

Based on Eq. (2.19), it is proved that  $(\mathbf{K}_{lnl}^{ij\tau s})^T = \frac{1}{2} \mathbf{K}_{nll}^{ij\tau s}$ . Therefore, the components of  $\mathbf{K}_{lnl}^{ij\tau s}$  are not provided here for the sake of brevity. The component  $[r,c]$  of the

matrix  $\mathbf{K}_{nlnl}^{ij\tau s}$  is expressed as follows:

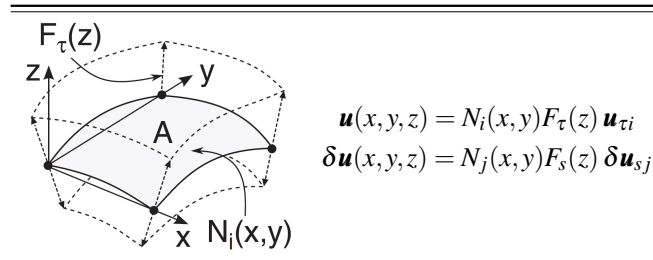
$$\begin{aligned}
2 \times \mathbf{K}_{nlnl}^{ij\tau s}[r, c] = & \langle \mathbf{u}_{,x}[r] \mathbf{u}_{,x}[c] C_{11} F_{\tau,x} F_{s,x} N_i N_j \rangle + \langle \mathbf{u}_{,x}[r] \mathbf{u}_{,x}[c] C_{44} F_{\tau,z} F_{s,z} N_i N_j \rangle \\
& + \langle \mathbf{u}_{,x}[r] \mathbf{u}_{,x}[c] C_{66} F_{\tau} F_s N_{i,y} N_{j,y} \rangle + \langle \mathbf{u}_{,y}[r] \mathbf{u}_{,y}[c] C_{66} F_{\tau,x} F_{s,x} N_i N_j \rangle \\
& + \langle \mathbf{u}_{,y}[r] \mathbf{u}_{,y}[c] C_{55} F_{\tau,z} F_{s,z} N_i N_j \rangle + \langle \mathbf{u}_{,y}[r] \mathbf{u}_{,y}[c] C_{22} F_{\tau} F_s N_{i,y} N_{j,y} \rangle \\
& + \langle \mathbf{u}_{,z}[r] \mathbf{u}_{,z}[c] C_{44} F_{\tau,x} F_{s,x} N_i N_j \rangle + \langle \mathbf{u}_{,z}[r] \mathbf{u}_{,z}[c] C_{33} F_{\tau,z} F_{s,z} N_i N_j \rangle \\
& + \langle \mathbf{u}_{,z}[r] \mathbf{u}_{,z}[c] C_{55} F_{\tau} F_s N_{i,y} N_{j,y} \rangle + \langle \mathbf{u}_{,x}[r] \mathbf{u}_{,y}[c] C_{12} F_{\tau,x} F_s N_i N_{j,y} \rangle \\
& + \langle \mathbf{u}_{,x}[r] \mathbf{u}_{,y}[c] C_{66} F_{\tau} F_{s,x} N_{i,y} N_j \rangle + \langle \mathbf{u}_{,y}[r] \mathbf{u}_{,x}[c] C_{12} F_{\tau} F_{s,x} N_{i,y} N_j \rangle \\
& + \langle \mathbf{u}_{,y}[r] \mathbf{u}_{,x}[c] C_{66} F_{\tau,x} F_s N_i N_{j,y} \rangle + \langle \mathbf{u}_{,x}[r] \mathbf{u}_{,z}[c] C_{13} F_{\tau,x} F_{s,z} N_i N_j \rangle \\
& + \langle \mathbf{u}_{,x}[r] \mathbf{u}_{,z}[c] C_{44} F_{\tau,z} F_{s,x} N_i N_j \rangle + \langle \mathbf{u}_{,z}[r] \mathbf{u}_{,x}[c] C_{13} F_{\tau,z} F_{s,x} N_i N_j \rangle \\
& + \langle \mathbf{u}_{,z}[r] \mathbf{u}_{,x}[c] C_{44} F_{\tau,x} F_{s,z} N_i N_j \rangle + \langle \mathbf{u}_{,y}[r] \mathbf{u}_{,z}[c] C_{23} F_{\tau} F_{s,z} N_{i,y} N_j \rangle \\
& + \langle \mathbf{u}_{,y}[r] \mathbf{u}_{,z}[c] C_{55} F_{\tau,z} F_s N_i N_{j,y} \rangle + \langle \mathbf{u}_{,z}[r] \mathbf{u}_{,y}[c] C_{55} F_{\tau} F_{s,z} N_{i,y} N_j \rangle \\
& + \langle \mathbf{u}_{,z}[r] \mathbf{u}_{,y}[c] C_{23} F_{\tau,z} F_s N_i N_{j,y} \rangle
\end{aligned} \tag{2.24}$$

In the expressions above,  $\mathbf{u}_{,x}[r]$  denotes the  $r$ -th component of the vector  $\frac{\partial \mathbf{u}}{\partial x}$ ; for instance,  $\mathbf{u}_{,x}[2] = u_{y,x}$ . Similarly,  $\mathbf{u}_{,y}[c]$  is the  $c$ -th component of the vector  $\frac{\partial \mathbf{u}}{\partial y}$ , etc.

## 2.4.2 FN of the secant stiffness matrix for finite plate element

A schematic description of the CUF and FE approximation for the plate structures is shown in Table 2.2. Therefore, the two matrices of  $\mathbf{B}_l^{sj}$  and  $\mathbf{B}_{nl}^{sj}$  for the plate structures are obtained as follows:

Table 2.2 A schematic description of the CUF and FE approximation for the plate structures [24]



$$\mathbf{B}_l^{sj} = \mathbf{b}_l(F_s N_j) = \begin{bmatrix} F_s N_{j,x} & 0 & 0 \\ 0 & F_s N_{j,y} & 0 \\ 0 & 0 & F_{s,z} N_j \\ F_{s,z} N_j & 0 & F_s N_{j,x} \\ 0 & F_{s,z} N_j & F_s N_{j,y} \\ F_s N_{j,y} & F_s N_{j,x} & 0 \end{bmatrix}, \quad (2.25)$$

and

$$\mathbf{B}_{nl}^{sj} = \frac{1}{2} \begin{bmatrix} u_{x,x} F_s N_{j,x} & u_{y,x} F_s N_{j,x} & u_{z,x} F_s N_{j,x} \\ u_{x,y} F_s N_{j,y} & u_{y,y} F_s N_{j,y} & u_{z,y} F_s N_{j,y} \\ u_{x,z} F_{s,z} N_j & u_{y,z} F_{s,z} N_j & u_{z,z} F_{s,z} N_j \\ u_{x,x} F_{s,z} N_j + u_{x,z} F_s N_{j,x} & u_{y,x} F_{s,z} N_j + u_{y,z} F_s N_{j,x} & u_{z,x} F_{s,z} N_j + u_{z,z} F_s N_{j,x} \\ u_{x,y} F_{s,z} N_j + u_{x,z} F_s N_{j,y} & u_{y,y} F_{s,z} N_j + u_{y,z} F_s N_{j,y} & u_{z,y} F_{s,z} N_j + u_{z,z} F_s N_{j,y} \\ u_{x,x} F_s N_{j,y} + u_{x,y} F_s N_{j,x} & u_{y,x} F_s N_{j,y} + u_{y,y} F_s N_{j,x} & u_{z,x} F_s N_{j,y} + u_{z,y} F_s N_{j,x} \end{bmatrix}, \quad (2.26)$$

where  $\mathbf{B}_l$  and  $\mathbf{B}_{nl}$  represent linear and nonlinear geometrical matrices, and commas denote partial derivatives. Accordingly, if we consider  $r$  as the row number ( $r = 1, 2, 3$ ) and  $c$  as the column number ( $c = 1, 2, 3$ ), the nine components of the  $3 \times 3$  FN of linear stiffness matrix in the form of  $\mathbf{K}_0^{ij\tau s}[r, c]$  could be expressed as follows:

$$\begin{aligned} \mathbf{K}_0^{ij\tau s}[1, 1] &= \langle C_{11} F_\tau F_s N_{i,x} N_{j,x} \rangle + \langle C_{44} F_{\tau,z} F_{s,z} N_i N_j \rangle \\ &+ \langle C_{66} F_\tau F_s N_{i,y} N_{j,y} \rangle + \langle C_{16} F_\tau F_s N_{i,y} N_{j,x} \rangle \\ &+ \langle C_{16} F_\tau F_s N_{i,x} N_{j,y} \rangle, \end{aligned}$$

$$\begin{aligned} \mathbf{K}_0^{ij\tau s}[1, 2] &= \langle C_{66} F_\tau F_s N_{i,y} N_{j,x} \rangle + \langle C_{12} F_\tau F_s N_{i,x} N_{j,y} \rangle \\ &+ \langle C_{45} F_{\tau,z} F_{s,z} N_i N_j \rangle + \langle C_{16} F_\tau F_s N_{i,x} N_{j,x} \rangle \\ &+ \langle C_{26} F_\tau F_s N_{i,y} N_{j,y} \rangle, \end{aligned}$$

$$\begin{aligned} \mathbf{K}_0^{ij\tau s}[1, 3] &= \langle C_{13} F_\tau F_{s,z} N_{i,x} N_j \rangle + \langle C_{44} F_{\tau,z} F_s N_i N_{j,x} \rangle \\ &+ \langle C_{45} F_{\tau,z} F_s N_i N_{j,y} \rangle + \langle C_{36} F_\tau F_{s,z} N_{i,y} N_j \rangle, \end{aligned}$$

$$\begin{aligned}
\mathbf{K}_0^{ij\tau s}[2, 1] &= \langle C_{12} F_\tau F_s N_{i,y} N_{j,x} \rangle + \langle C_{66} F_\tau F_s N_{i,x} N_{j,y} \rangle \\
&+ \langle C_{45} F_{\tau,z} F_{s,z} N_i N_j \rangle + \langle C_{16} F_\tau F_s N_{i,x} N_{j,x} \rangle \\
&+ \langle C_{26} F_\tau F_s N_{i,y} N_{j,y} \rangle, \\
\mathbf{K}_0^{ij\tau s}[2, 2] &= \langle C_{66} F_\tau F_s N_{i,x} N_{j,x} \rangle + \langle C_{55} F_{\tau,z} F_{s,z} N_i N_j \rangle \\
&+ \langle C_{22} F_\tau F_s N_{i,y} N_{j,y} \rangle + \langle C_{26} F_\tau F_s N_{i,x} N_{j,y} \rangle \\
&+ \langle C_{26} F_\tau F_s N_{i,y} N_{j,x} \rangle, \\
\mathbf{K}_0^{ij\tau s}[2, 3] &= \langle C_{23} F_\tau F_{s,z} N_{i,y} N_j \rangle + \langle C_{55} F_{\tau,z} F_s N_i N_{j,y} \rangle \\
&+ \langle C_{45} F_{\tau,z} F_s N_i N_{j,x} \rangle + \langle C_{36} F_\tau F_{s,z} N_{i,x} N_j \rangle, \\
\mathbf{K}_0^{ij\tau s}[3, 1] &= \langle C_{44} F_\tau F_{s,z} N_{i,x} N_j \rangle + \langle C_{13} F_{\tau,z} F_s N_i N_{j,x} \rangle \\
&+ \langle C_{45} F_\tau F_{s,z} N_{i,y} N_j \rangle + \langle C_{36} F_{\tau,z} F_s N_i N_{j,y} \rangle, \\
\mathbf{K}_0^{ij\tau s}[3, 2] &= \langle C_{55} F_\tau F_{s,z} N_{i,y} N_j \rangle + \langle C_{23} F_{\tau,z} F_s N_i N_{j,y} \rangle \\
&+ \langle C_{45} F_\tau F_{s,z} N_{i,x} N_j \rangle + \langle C_{36} F_{\tau,z} F_s N_i N_{j,x} \rangle, \\
\mathbf{K}_0^{ij\tau s}[3, 3] &= \langle C_{44} F_\tau F_s N_{i,x} N_{j,x} \rangle + \langle C_{33} F_{\tau,z} F_{s,z} N_i N_j \rangle \\
&+ \langle C_{55} F_\tau F_s N_{i,y} N_{j,y} \rangle + \langle C_{45} F_\tau F_s N_{i,y} N_{j,x} \rangle \\
&+ \langle C_{45} F_\tau F_s N_{i,x} N_{j,y} \rangle.
\end{aligned}$$

(2.27)

Similarly, the components of the FNs of the first-order nonlinear stiffness matrix  $\mathbf{K}_{nll}^{ij\tau s}$  are derived:

For  $c = 1$ :

$$\begin{aligned} \mathbf{K}_{nll}^{ij\tau s}[r, 1] = & \langle \mathbf{u}_{,x}[r] C_{11} F_{\tau} F_s N_{i,x} N_{j,x} \rangle + \langle \mathbf{u}_{,x}[r] C_{44} F_{\tau,z} F_{s,z} N_i N_j \rangle \\ & + \langle \mathbf{u}_{,x}[r] C_{66} F_{\tau} F_s N_{i,y} N_{j,y} \rangle + \langle \mathbf{u}_{,x}[r] C_{16} F_{\tau} F_s N_{i,y} N_{j,x} \rangle \\ & + \langle \mathbf{u}_{,x}[r] C_{16} F_{\tau} F_s N_{i,x} N_{j,y} \rangle + \langle \mathbf{u}_{,y}[r] C_{66} F_{\tau} F_s N_{i,x} N_{j,y} \rangle \\ & + \langle \mathbf{u}_{,y}[r] C_{12} F_{\tau} F_s N_{i,y} N_{j,x} \rangle + \langle \mathbf{u}_{,y}[r] C_{45} F_{\tau,z} F_{s,z} N_i N_j \rangle \\ & + \langle \mathbf{u}_{,y}[r] C_{16} F_{\tau} F_s N_{i,x} N_{j,x} \rangle + \langle \mathbf{u}_{,y}[r] C_{26} F_{\tau} F_s N_{i,y} N_{j,y} \rangle \\ & + \langle \mathbf{u}_{,z}[r] C_{44} F_{\tau} F_{s,z} N_{i,x} N_j \rangle + \langle \mathbf{u}_{,z}[r] C_{13} F_{\tau,z} F_s N_i N_{j,x} \rangle \\ & + \langle \mathbf{u}_{,z}[r] C_{45} F_{\tau} F_{s,z} N_{i,y} N_j \rangle + \langle \mathbf{u}_{,z}[r] C_{36} F_{\tau,z} F_s N_i N_{j,y} \rangle, \end{aligned}$$

For  $c = 2$ :

$$\begin{aligned} \mathbf{K}_{nll}^{ij\tau s}[r, 2] = & \langle \mathbf{u}_{,x}[r] C_{12} F_{\tau} F_s N_{i,x} N_{j,y} \rangle + \langle \mathbf{u}_{,x}[r] C_{66} F_{\tau} F_s N_{i,y} N_{j,x} \rangle \\ & + \langle \mathbf{u}_{,x}[r] C_{45} F_{\tau,z} F_{s,z} N_i N_j \rangle + \langle \mathbf{u}_{,x}[r] C_{16} F_{\tau} F_s N_{i,x} N_{j,x} \rangle \\ & + \langle \mathbf{u}_{,x}[r] C_{26} F_{\tau} F_s N_{i,y} N_{j,y} \rangle + \langle \mathbf{u}_{,y}[r] C_{66} F_{\tau} F_s N_{i,x} N_{j,x} \rangle \\ & + \langle \mathbf{u}_{,y}[r] C_{55} F_{\tau,z} F_{s,z} N_i N_j \rangle + \langle \mathbf{u}_{,y}[r] C_{22} F_{\tau} F_s N_{i,y} N_{j,y} \rangle \\ & + \langle \mathbf{u}_{,y}[r] C_{26} F_{\tau} F_s N_{i,y} N_{j,x} \rangle + \langle \mathbf{u}_{,y}[r] C_{26} F_{\tau} F_s N_{i,x} N_{j,y} \rangle \\ & + \langle \mathbf{u}_{,z}[r] C_{23} F_{\tau,z} F_s N_i N_{j,y} \rangle + \langle \mathbf{u}_{,z}[r] C_{55} F_{\tau} F_{s,z} N_{i,y} N_j \rangle \\ & + \langle \mathbf{u}_{,z}[r] C_{45} F_{\tau} F_{s,z} N_{i,x} N_j \rangle + \langle \mathbf{u}_{,z}[r] C_{36} F_{\tau,z} F_s N_i N_{j,x} \rangle, \end{aligned}$$

For  $c = 3$ :

$$\begin{aligned} \mathbf{K}_{nll}^{ij\tau s}[r, 3] = & \langle \mathbf{u}_{,x}[r] C_{13} F_{\tau} F_{s,z} N_{i,x} N_j \rangle + \langle \mathbf{u}_{,x}[r] C_{44} F_{\tau,z} F_s N_i N_{j,x} \rangle \\ & + \langle \mathbf{u}_{,x}[r] C_{45} F_{\tau,z} F_s N_i N_{j,y} \rangle + \langle \mathbf{u}_{,x}[r] C_{36} F_{\tau} F_{s,z} N_{i,y} N_j \rangle \\ & + \langle \mathbf{u}_{,y}[r] C_{55} F_{\tau,z} F_s N_i N_{j,y} \rangle + \langle \mathbf{u}_{,y}[r] C_{23} F_{\tau} F_{s,z} N_{i,y} N_j \rangle \\ & + \langle \mathbf{u}_{,y}[r] C_{45} F_{\tau,z} F_s N_i N_{j,x} \rangle + \langle \mathbf{u}_{,y}[r] C_{36} F_{\tau} F_{s,z} N_{i,x} N_j \rangle \\ & + \langle \mathbf{u}_{,z}[r] C_{44} F_{\tau} F_s N_{i,x} N_{j,x} \rangle + \langle \mathbf{u}_{,z}[r] C_{33} F_{\tau,z} F_{s,z} N_i N_j \rangle \\ & + \langle \mathbf{u}_{,z}[r] C_{55} F_{\tau} F_s N_{i,y} N_{j,y} \rangle + \langle \mathbf{u}_{,z}[r] C_{45} F_{\tau} F_s N_{i,x} N_{j,y} \rangle \\ & + \langle \mathbf{u}_{,z}[r] C_{45} F_{\tau} F_s N_{i,y} N_{j,x} \rangle. \end{aligned} \tag{2.28}$$

The nine components of  $\mathbf{K}_{lnl}^{ij\tau s}$  can be easily obtained from Eq. (2.19) as  $(\mathbf{K}_{lnl}^{ij\tau s})^T = \mathbf{K}_{nll}^{jis\tau}/2$ . The nine components of the matrix  $\mathbf{K}_{nlnl}^{ij\tau s}[r, c]$  are given in the following:

$$\begin{aligned}
2 \times \mathbf{K}_{nlnl}^{ij\tau s}[r, c] = & \langle \mathbf{u}_{,x}[r] \mathbf{u}_{,x}[c] C_{11} F_{\tau} F_s N_{i,x} N_{j,x} \rangle + \langle \mathbf{u}_{,x}[r] \mathbf{u}_{,x}[c] C_{44} F_{\tau,z} F_{s,z} N_i N_j \rangle \\
& + \langle \mathbf{u}_{,x}[r] \mathbf{u}_{,x}[c] C_{66} F_{\tau} F_s N_{i,y} N_{j,y} \rangle + \langle \mathbf{u}_{,x}[r] \mathbf{u}_{,x}[c] C_{16} F_{\tau} F_s N_{i,x} N_{j,y} \rangle \\
& + \langle \mathbf{u}_{,x}[r] \mathbf{u}_{,x}[c] C_{16} F_{\tau} F_s N_{i,y} N_{j,x} \rangle + \langle \mathbf{u}_{,y}[r] \mathbf{u}_{,y}[c] C_{66} F_{\tau} F_s N_{i,x} N_{j,x} \rangle \\
& + \langle \mathbf{u}_{,y}[r] \mathbf{u}_{,y}[c] C_{55} F_{\tau,z} F_{s,z} N_i N_j \rangle + \langle \mathbf{u}_{,y}[r] \mathbf{u}_{,y}[c] C_{22} F_{\tau} F_s N_{i,y} N_{j,y} \rangle \\
& + \langle \mathbf{u}_{,y}[r] \mathbf{u}_{,y}[c] C_{26} F_{\tau} F_s N_{i,x} N_{j,y} \rangle + \langle \mathbf{u}_{,y}[r] \mathbf{u}_{,y}[c] C_{26} F_{\tau} F_s N_{i,y} N_{j,x} \rangle \\
& + \langle \mathbf{u}_{,z}[r] \mathbf{u}_{,z}[c] C_{44} F_{\tau} F_s N_{i,x} N_{j,x} \rangle + \langle \mathbf{u}_{,z}[r] \mathbf{u}_{,z}[c] C_{33} F_{\tau,z} F_{s,z} N_i N_j \rangle \\
& + \langle \mathbf{u}_{,z}[r] \mathbf{u}_{,z}[c] C_{55} F_{\tau} F_s N_{i,y} N_{j,y} \rangle + \langle \mathbf{u}_{,z}[r] \mathbf{u}_{,z}[c] C_{45} F_{\tau} F_s N_{i,x} N_{j,y} \rangle \\
& + \langle \mathbf{u}_{,z}[r] \mathbf{u}_{,z}[c] C_{45} F_{\tau} F_s N_{i,y} N_{j,x} \rangle + \langle \mathbf{u}_{,x}[r] \mathbf{u}_{,y}[c] C_{12} F_{\tau} F_s N_{i,x} N_{j,y} \rangle \\
& + \langle \mathbf{u}_{,x}[r] \mathbf{u}_{,y}[c] C_{66} F_{\tau} F_s N_{i,y} N_{j,x} \rangle + \langle \mathbf{u}_{,x}[r] \mathbf{u}_{,y}[c] C_{45} F_{\tau,z} F_{s,z} N_i N_j \rangle \\
& + \langle \mathbf{u}_{,x}[r] \mathbf{u}_{,y}[c] C_{16} F_{\tau} F_s N_{i,x} N_{j,x} \rangle + \langle \mathbf{u}_{,x}[r] \mathbf{u}_{,y}[c] C_{26} F_{\tau} F_s N_{i,y} N_{j,y} \rangle \\
& + \langle \mathbf{u}_{,y}[r] \mathbf{u}_{,x}[c] C_{12} F_{\tau} F_s N_{i,y} N_{j,x} \rangle + \langle \mathbf{u}_{,y}[r] \mathbf{u}_{,x}[c] C_{66} F_{\tau} F_s N_{i,x} N_{j,y} \rangle \\
& + \langle \mathbf{u}_{,y}[r] \mathbf{u}_{,x}[c] C_{45} F_{\tau,z} F_{s,z} N_i N_j \rangle + \langle \mathbf{u}_{,y}[r] \mathbf{u}_{,x}[c] C_{16} F_{\tau} F_s N_{i,x} N_{j,x} \rangle \\
& + \langle \mathbf{u}_{,y}[r] \mathbf{u}_{,x}[c] C_{26} F_{\tau} F_s N_{i,y} N_{j,y} \rangle + \langle \mathbf{u}_{,x}[r] \mathbf{u}_{,z}[c] C_{13} F_{\tau} F_{s,z} N_{i,x} N_j \rangle \\
& + \langle \mathbf{u}_{,x}[r] \mathbf{u}_{,z}[c] C_{44} F_{\tau,z} F_s N_i N_{j,x} \rangle + \langle \mathbf{u}_{,x}[r] \mathbf{u}_{,z}[c] C_{45} F_{\tau,z} F_s N_i N_{j,y} \rangle \\
& + \langle \mathbf{u}_{,x}[r] \mathbf{u}_{,z}[c] C_{36} F_{\tau} F_{s,z} N_{i,y} N_j \rangle + \langle \mathbf{u}_{,z}[r] \mathbf{u}_{,x}[c] C_{13} F_{\tau,z} F_s N_i N_{j,x} \rangle \\
& + \langle \mathbf{u}_{,z}[r] \mathbf{u}_{,x}[c] C_{44} F_{\tau} F_{s,z} N_{i,x} N_j \rangle + \langle \mathbf{u}_{,z}[r] \mathbf{u}_{,x}[c] C_{45} F_{\tau} F_{s,z} N_{i,y} N_j \rangle \\
& + \langle \mathbf{u}_{,z}[r] \mathbf{u}_{,x}[c] C_{36} F_{\tau,z} F_s N_i N_{j,y} \rangle + \langle \mathbf{u}_{,y}[r] \mathbf{u}_{,z}[c] C_{23} F_{\tau} F_{s,z} N_{i,y} N_j \rangle \\
& + \langle \mathbf{u}_{,y}[r] \mathbf{u}_{,z}[c] C_{55} F_{\tau,z} F_s N_i N_{j,y} \rangle + \langle \mathbf{u}_{,y}[r] \mathbf{u}_{,z}[c] C_{45} F_{\tau,z} F_s N_i N_{j,x} \rangle \\
& + \langle \mathbf{u}_{,y}[r] \mathbf{u}_{,z}[c] C_{36} F_{\tau} F_{s,z} N_{i,x} N_j \rangle + \langle \mathbf{u}_{,z}[r] \mathbf{u}_{,y}[c] C_{55} F_{\tau} F_{s,z} N_{i,y} N_j \rangle \\
& + \langle \mathbf{u}_{,z}[r] \mathbf{u}_{,y}[c] C_{23} F_{\tau,z} F_s N_i N_{j,y} \rangle + \langle \mathbf{u}_{,z}[r] \mathbf{u}_{,y}[c] C_{45} F_{\tau} F_{s,z} N_{i,x} N_j \rangle \\
& + \langle \mathbf{u}_{,z}[r] \mathbf{u}_{,y}[c] C_{36} F_{\tau,z} F_s N_i N_{j,x} \rangle
\end{aligned} \tag{2.29}$$

In the above-mentioned formulation,  $\mathbf{u}_{,x}[r]$  denotes the  $r$ -th component of the vector  $\partial \mathbf{u} / \partial x$  (e.g.  $\mathbf{u}_{,x}[2] = u_{y,x}$ ). Similarly,  $\mathbf{u}_{,y}[c]$  denotes the  $c$ -th component of the vector  $\partial \mathbf{u} / \partial y$ , etc.

## 2.5 Tangent stiffness matrix

The FN of the tangent stiffness matrix  $\mathbf{K}_T^{ij\tau s}$  can be obtained via the linearization of equilibrium equations [69] (see Eq. (2.5)). Under the assumption that the loading is conservative, the linearization of the virtual variation of the external loads is zero ( $\delta(\delta L_{\text{ext}}) = 0$ ). Therefore, the tangent stiffness matrix can be derived from the linearization of the virtual variation of strain energy as follows:

$$\begin{aligned}
 \delta(\delta L_{\text{int}}) &= \langle \delta(\delta \boldsymbol{\varepsilon}^T \boldsymbol{\sigma}) \rangle \\
 &= \langle \delta \boldsymbol{\varepsilon}^T \delta \boldsymbol{\sigma} \rangle + \langle \delta(\delta \boldsymbol{\varepsilon}^T) \boldsymbol{\sigma} \rangle \\
 &= \delta \mathbf{q}_{\tau i}^T (\mathbf{K}_0^{ij\tau s} + \mathbf{K}_{T_1}^{ij\tau s} + \mathbf{K}_{\sigma}^{ij\tau s}) \delta \mathbf{q}_{s j} \\
 &= \delta \mathbf{q}_{\tau i}^T \mathbf{K}_T^{ij\tau s} \delta \mathbf{q}_{s j}
 \end{aligned} \tag{2.30}$$

In the following, each nonlinear contribution  $\mathbf{K}_{T_1}^{ij\tau s}$  and  $\mathbf{K}_{\sigma}^{ij\tau s}$  in Eq. (2.30) will be discussed separately. The first term,  $\langle \delta \boldsymbol{\varepsilon}^T \delta \boldsymbol{\sigma} \rangle$ , needs the linearization of the constitutive relations. based on Eq. (2.16), and under the assumption that the material coefficients are constant ( $\delta \mathbf{C} = 0$ ), the following equations are obtained:

$$\delta \boldsymbol{\sigma} = \delta(\mathbf{C}\boldsymbol{\varepsilon}) = \mathbf{C}\delta \boldsymbol{\varepsilon} = \mathbf{C}(\mathbf{B}_l^{s j} + 2\mathbf{B}_{nl}^{s j})\delta \mathbf{q}_{s j} \tag{2.31}$$

Therefore, according to Eqs. (2.17) and (2.31), we have:

$$\begin{aligned}
 \langle \delta \boldsymbol{\varepsilon}^T \delta \boldsymbol{\sigma} \rangle &= \delta \mathbf{q}_{\tau i}^T \langle (\mathbf{B}_l^{\tau i} + 2\mathbf{B}_{nl}^{\tau i})^T \mathbf{C} (\mathbf{B}_l^{s j} + 2\mathbf{B}_{nl}^{s j}) \rangle \delta \mathbf{q}_{s j} \\
 &= \delta \mathbf{q}_{\tau i}^T \mathbf{K}_0^{ij\tau s} \delta \mathbf{q}_{s j} + \delta \mathbf{q}_{\tau i}^T (2\mathbf{K}_{lnl}^{ij\tau s}) \delta \mathbf{q}_{s j} + \delta \mathbf{q}_{\tau i}^T \mathbf{K}_{nll}^{ij\tau s} \delta \mathbf{q}_{s j} + \delta \mathbf{q}_{\tau i}^T (2\mathbf{K}_{nlnl}^{ij\tau s}) \delta \mathbf{q}_{s j} \\
 &= \delta \mathbf{q}_{\tau i}^T (\mathbf{K}_0^{ij\tau s} + \mathbf{K}_{T_1}^{ij\tau s}) \delta \mathbf{q}_{s j}
 \end{aligned} \tag{2.32}$$

where  $\mathbf{K}_{T_1}^{ij\tau s} = 2\mathbf{K}_{lnl}^{ij\tau s} + \mathbf{K}_{nll}^{ij\tau s} + 2\mathbf{K}_{nlnl}^{ij\tau s}$  is the nonlinear contribution of the FN of the tangent stiffness matrix which is stemmed from the linearization of the Hooke's law.  $\mathbf{K}_0^{ij\tau s}$ ,  $\mathbf{K}_{lnl}^{ij\tau s}$ ,  $\mathbf{K}_{nll}^{ij\tau s}$ , and  $\mathbf{K}_{nlnl}^{ij\tau s}$  are the same  $3 \times 3$  FNs as expressed in Eq. (2.19).

The linearization of nonlinear geometrical relations is required for the second contribution of Eq. (2.30), ( $\langle \delta(\delta \boldsymbol{\varepsilon}^T) \boldsymbol{\sigma} \rangle$ ). Therefore, based on the Crisfield [62], Eqs. (1.2) and (1.3), we have:



$$\delta(\delta\boldsymbol{\varepsilon}) = \left\{ \begin{array}{l} (\delta u_{x,x})_v \delta u_{x,x} + (\delta u_{y,x})_v \delta u_{y,x} + (\delta u_{z,x})_v \delta u_{z,x} \\ (\delta u_{x,y})_v \delta u_{x,y} + (\delta u_{y,y})_v \delta u_{y,y} + (\delta u_{z,y})_v \delta u_{z,y} \\ (\delta u_{x,z})_v \delta u_{x,z} + (\delta u_{y,z})_v \delta u_{y,z} + (\delta u_{z,z})_v \delta u_{z,z} \\ [(\delta u_{x,x})_v \delta u_{x,z} + \delta u_{x,x} (\delta u_{x,z})_v] + [(\delta u_{y,x})_v \delta u_{y,z} + \delta u_{y,x} (\delta u_{y,z})_v] + [(\delta u_{z,x})_v \delta u_{z,z} + \delta u_{z,x} (\delta u_{z,z})_v] \\ [(\delta u_{x,y})_v \delta u_{x,z} + \delta u_{x,y} (\delta u_{x,z})_v] + [(\delta u_{y,y})_v \delta u_{y,z} + \delta u_{y,y} (\delta u_{y,z})_v] + [(\delta u_{z,y})_v \delta u_{z,z} + \delta u_{z,y} (\delta u_{z,z})_v] \\ [(\delta u_{x,x})_v \delta u_{x,y} + \delta u_{x,x} (\delta u_{x,y})_v] + [(\delta u_{y,x})_v \delta u_{y,y} + \delta u_{y,x} (\delta u_{y,y})_v] + [(\delta u_{z,x})_v \delta u_{z,y} + \delta u_{z,x} (\delta u_{z,y})_v] \end{array} \right\} \quad (2.33)$$

where the subscript “v” represents the variations. By using Eq. (2.33), the CUF, and the FE approximation for both the linearized variables ( $\delta\mathbf{u} = F_s N_j \delta\mathbf{q}_{s_j}$ ) and the variations ( $(\delta\mathbf{u})_v = F_\tau N_i \delta\mathbf{q}_{\tau i}$ ), the following forms can be used for the relations:

$$\delta(\delta\boldsymbol{\varepsilon}) = \mathbf{B}_{nl}^* \left\{ \begin{array}{l} \delta q_{x\tau i} \delta q_{x_s j} \\ \delta q_{y\tau i} \delta q_{y_s j} \\ \delta q_{z\tau i} \delta q_{z_s j} \end{array} \right\} \quad (2.34)$$

and

$$\delta(\delta\boldsymbol{\varepsilon}^T) = \left\{ \begin{array}{l} \delta q_{x\tau i} \delta q_{x_s j} \\ \delta q_{y\tau i} \delta q_{y_s j} \\ \delta q_{z\tau i} \delta q_{z_s j} \end{array} \right\}^T (\mathbf{B}_{nl}^*)^T \quad (2.35)$$

where  $\mathbf{B}_{nl}^*$  will be provided according to the CUF for the beam and plate structures in the sections 2.5.1 and 2.5.2.

Employing Eq. (2.35), and after simple manipulations, the following equations are obtained:

$$\begin{aligned}
\langle \delta(\delta\boldsymbol{\varepsilon}^T)\boldsymbol{\sigma} \rangle &= \left\langle \begin{Bmatrix} \delta q_{u_{x\tau i}} & \delta q_{u_{xsj}} \\ \delta q_{u_{y\tau i}} & \delta q_{u_{ysj}} \\ \delta q_{u_{z\tau i}} & \delta q_{u_{zsj}} \end{Bmatrix}^T (\mathbf{B}_{nl}^*)^T \boldsymbol{\sigma} \right\rangle \\
&= \delta \mathbf{q}_{\tau i}^T \langle \text{diag}((\mathbf{B}_{nl}^*)^T \boldsymbol{\sigma}) \rangle \delta \mathbf{q}_{sj} \\
&= \delta \mathbf{q}_{\tau i}^T \langle \text{diag}((\mathbf{B}_{nl}^*)^T (\boldsymbol{\sigma}_l + \boldsymbol{\sigma}_{nl})) \rangle \delta \mathbf{q}_{sj} \\
&= \delta \mathbf{q}_{\tau i}^T (\mathbf{K}_{\sigma_l}^{ij\tau s} + \mathbf{K}_{\sigma_{nl}}^{ij\tau s}) \delta \mathbf{q}_{sj} \\
&= \delta \mathbf{q}_{\tau i}^T \mathbf{K}_{\sigma}^{ij\tau s} \delta \mathbf{q}_{sj}
\end{aligned} \tag{2.36}$$

where  $\text{diag}((\mathbf{B}_{nl}^*)^T \boldsymbol{\sigma})$  is the  $3 \times 3$  diagonal matrix, and the diagonal terms are the components of the vector  $(\mathbf{B}_{nl}^*)^T \boldsymbol{\sigma}$ . Based on Eqs. (1.4) and (1.2),  $\boldsymbol{\sigma}_l = \mathbf{C}\boldsymbol{\varepsilon}_l$  and  $\boldsymbol{\sigma}_{nl} = \mathbf{C}\boldsymbol{\varepsilon}_{nl}$ . The term in Eq. (2.36) represents a tangent term arising from the nonlinear form of the strain-displacement equations, and is often called the geometric stiffness [69], of which  $\mathbf{K}_{\sigma}^{ij\tau s} = \mathbf{K}_{\sigma_l}^{ij\tau s} + \mathbf{K}_{\sigma_{nl}}^{ij\tau s}$  is the FN. The explicit forms of  $\mathbf{K}_{\sigma}^{ij\tau s}$  for the beam and plate structures are provided in the following sections for the sake of completeness.

### 2.5.1 FN of the tangent stiffness matrix for finite beam element

Based on the CUF for the beam structures, the introduced matrix  $\mathbf{B}_{nl}^*$  in Eqs. (2.34) and (2.35) is as follows:

$$\mathbf{B}_{nl}^* = \begin{bmatrix} F_{\tau_x} F_{s,x} N_i N_j & F_{\tau_x} F_{s,x} N_i N_j & F_{\tau_x} F_{s,x} N_i N_j \\ F_{\tau_z} F_{s,z} N_i N_j & F_{\tau_z} F_{s,z} N_i N_j & F_{\tau_z} F_{s,z} N_i N_j \\ F_{\tau_y} F_{s,y} N_i N_j & F_{\tau_y} F_{s,y} N_i N_j & F_{\tau_y} F_{s,y} N_i N_j \\ F_{\tau_x} F_{s,z} N_i N_j + F_{\tau_z} F_{s,x} N_i N_j & F_{\tau_x} F_{s,z} N_i N_j + F_{\tau_z} F_{s,x} N_i N_j & F_{\tau_x} F_{s,z} N_i N_j + F_{\tau_z} F_{s,x} N_i N_j \\ F_{\tau_z} F_{s,y} N_i N_j + F_{\tau_y} F_{s,z} N_i N_j & F_{\tau_z} F_{s,y} N_i N_j + F_{\tau_y} F_{s,z} N_i N_j & F_{\tau_z} F_{s,y} N_i N_j + F_{\tau_y} F_{s,z} N_i N_j \\ F_{\tau_y} F_{s,x} N_i N_j + F_{\tau_x} F_{s,y} N_i N_j & F_{\tau_y} F_{s,x} N_i N_j + F_{\tau_x} F_{s,y} N_i N_j & F_{\tau_y} F_{s,x} N_i N_j + F_{\tau_x} F_{s,y} N_i N_j \end{bmatrix} \quad (2.37)$$

Accordingly, the explicit form of  $\mathbf{K}_{\sigma}^{ij\tau s}$  is derived as:

$$\begin{aligned} \mathbf{K}_{\sigma}^{ij\tau s} &= \left( \langle \sigma_{xx} F_{\tau_x} F_{s,x} N_i N_j \rangle + \langle \sigma_{yy} F_{\tau_y} F_{s,y} N_i N_j \rangle \right. \\ &+ \langle \sigma_{zz} F_{\tau_z} F_{s,z} N_i N_j \rangle + \langle \sigma_{xy} F_{\tau_x} F_{s,y} N_i N_j \rangle \\ &+ \langle \sigma_{xy} F_{\tau_y} F_{s,x} N_i N_j \rangle + \langle \sigma_{xz} F_{\tau_x} F_{s,z} N_i N_j \rangle \\ &+ \langle \sigma_{xz} F_{\tau_z} F_{s,x} N_i N_j \rangle + \langle \sigma_{yz} F_{\tau_y} F_{s,z} N_i N_j \rangle \\ &\left. + \langle \sigma_{yz} F_{\tau_z} F_{s,y} N_i N_j \rangle \right) \mathbf{I} \end{aligned} \quad (2.38)$$

where  $\mathbf{I}$  is the  $3 \times 3$  identity matrix. Employing Eq. (2.30), and the three matrices of  $\mathbf{K}_0^{ij\tau s}$ ,  $\mathbf{K}_{T_1}^{ij\tau s}$ ,  $\mathbf{K}_{\sigma}^{ij\tau s}$ , the FN of the tangent stiffness matrix  $\mathbf{K}_T^{ij\tau s}$  for the beam structures is calculated straightforwardly.

## 2.5.2 FN of the tangent stiffness matrix for finite plate element

Based on the CUF for the plate structures, the introduced matrix  $\mathbf{B}_{nl}^*$  in Eqs. (2.34) and (2.35) is as follows:

$$\mathbf{B}_{nl}^* = \begin{bmatrix} F_\tau F_s N_{i,x} N_{j,x} & F_\tau F_s N_{i,x} N_{j,x} & F_\tau F_s N_{i,x} N_{j,x} \\ F_\tau F_s N_{i,y} N_{j,y} & F_\tau F_s N_{i,y} N_{j,y} & F_\tau F_s N_{i,y} N_{j,y} \\ F_{\tau_z} F_{s_z} N_i N_j & F_{\tau_z} F_{s_z} N_i N_j & F_{\tau_z} F_{s_z} N_i N_j \\ F_\tau F_{s_z} N_{i,x} N_j + F_{\tau_z} F_s N_i N_{j,x} & F_\tau F_{s_z} N_{i,x} N_j + F_{\tau_z} F_s N_i N_{j,x} & F_\tau F_{s_z} N_{i,x} N_j + F_{\tau_z} F_s N_i N_{j,x} \\ F_{\tau_z} F_s N_{i,y} N_j + F_\tau F_{s_z} N_{i,y} N_j & F_{\tau_z} F_s N_{i,y} N_j + F_\tau F_{s_z} N_{i,y} N_j & F_{\tau_z} F_s N_{i,y} N_j + F_\tau F_{s_z} N_{i,y} N_j \\ F_\tau F_s N_{i,x} N_{j,y} + F_{\tau_z} F_s N_{i,y} N_{j,x} & F_\tau F_s N_{i,x} N_{j,y} + F_{\tau_z} F_s N_{i,y} N_{j,x} & F_\tau F_s N_{i,x} N_{j,y} + F_{\tau_z} F_s N_{i,y} N_{j,x} \end{bmatrix}. \quad (2.39)$$

Accordingly, the explicit form of  $\mathbf{K}_\sigma^{ij\tau s}$  is derived as:

$$\begin{aligned} \mathbf{K}_\sigma^{ij\tau s} &= \left( \langle \sigma_{xx} F_\tau F_s N_{i,x} N_{j,x} \rangle + \langle \sigma_{yy} F_\tau F_s N_{i,y} N_{j,y} \rangle \right. \\ &+ \langle \sigma_{zz} F_{\tau_z} F_{s_z} N_i N_j \rangle + \langle \sigma_{xy} F_\tau F_s N_{i,x} N_{j,y} \rangle \\ &+ \langle \sigma_{xy} F_\tau F_s N_{i,y} N_{j,x} \rangle + \langle \sigma_{xz} F_\tau F_{s_z} N_{i,x} N_j \rangle \\ &+ \langle \sigma_{xz} F_{\tau_z} F_s N_i N_{j,x} \rangle + \langle \sigma_{yz} F_{\tau_z} F_s N_i N_{j,y} \rangle \\ &\left. + \langle \sigma_{yz} F_\tau F_{s_z} N_{i,y} N_j \rangle \right) \mathbf{I}, \end{aligned} \quad (2.40)$$

where  $\mathbf{I}$  is the  $3 \times 3$  identity matrix. Employing Eq. (2.30), and the three matrices of  $\mathbf{K}_0^{ij\tau s}$ ,  $\mathbf{K}_{T_1}^{ij\tau s}$ ,  $\mathbf{K}_\sigma^{ij\tau s}$ , the FN of the tangent stiffness matrix  $\mathbf{K}_T^{ij\tau s}$  for the plate structures is calculated straightforwardly

## 2.6 Different strain-displacement assumptions

The linear and nonlinear differential operator matrices of  $\mathbf{b}_l$  and  $\mathbf{b}_{nl}$  in the strain-displacement relationship were previously defined in Eq. (2.14). Here, the parameters  $P_{ij}$  are employed as coefficients of nonlinear differential operator matrix to tune the

kinematics assumptions opportunely (see [70]):

$$\mathbf{b}_l = \begin{bmatrix} \partial_x & 0 & 0 \\ 0 & \partial_y & 0 \\ 0 & 0 & \partial_z \\ \partial_z & 0 & \partial_x \\ 0 & \partial_z & \partial_y \\ \partial_y & \partial_x & 0 \end{bmatrix}, \quad \mathbf{b}_{nl} = \begin{bmatrix} P_{11} \frac{1}{2} (\partial_x)^2 & P_{12} \frac{1}{2} (\partial_x)^2 & P_{13} \frac{1}{2} (\partial_x)^2 \\ P_{21} \frac{1}{2} (\partial_y)^2 & P_{22} \frac{1}{2} (\partial_y)^2 & P_{23} \frac{1}{2} (\partial_y)^2 \\ P_{31} \frac{1}{2} (\partial_z)^2 & P_{32} \frac{1}{2} (\partial_z)^2 & P_{33} \frac{1}{2} (\partial_z)^2 \\ P_{41} \partial_x \partial_z & P_{42} \partial_x \partial_z & P_{43} \partial_x \partial_z \\ P_{51} \partial_y \partial_z & P_{52} \partial_y \partial_z & P_{53} \partial_y \partial_z \\ P_{61} \partial_x \partial_y & P_{62} \partial_x \partial_y & P_{63} \partial_x \partial_y \end{bmatrix}, \quad (2.41)$$

in which  $\partial_x = \partial(\cdot)/\partial x$ ,  $\partial_y = \partial(\cdot)/\partial y$ ,  $\partial_z = \partial(\cdot)/\partial z$ , and  $P_{11}$  to  $P_{63}$  are the parameters used as coefficients of nonlinear differential operator matrix. As will be discussed in the following sections of this research, these parameters play an important role in the accuracy of problem's kinematic model, and define the assumed geometrically nonlinear theory.

The use of these parameters provides the possibility of opportunely tuning the kinematics assumptions and the nonlinear theory. For instance, in the case of well-known von Kármán theory [71], nonlinear geometric relations of the plate structures are defined as:

$$\begin{aligned} \epsilon_{xx_{nl}} &= \frac{1}{2} (u_{z,x})^2 \\ \epsilon_{yy_{nl}} &= \frac{1}{2} (u_{z,y})^2 \\ \epsilon_{xy_{nl}} &= u_{z,x} u_{z,y} \end{aligned} \quad (2.42)$$

As illustrated in Fig. 2.3, the Kármán strains approximation ignores all nonlinear quadratic components in Eq. (2.41) except for those corresponding to the in-plane partial derivatives of the transverse displacement. Thus, except for  $P_{13}$ ,  $P_{23}$ , and  $P_{63}$ , all of the parameters in Eq. (2.41) are zero for the Kármán nonlinear plate. The  $P_{ij}$  matrix using several nonlinear models is shown in Table 2.3. The von Kármán nonlinear theory and four modifications are assumed in here. In this regard, the notations  $\text{vK}_{+T}$ ,  $\text{vK}_{+S}$ ,  $\text{vK}_{+IN}$ , and  $\text{vK}_{+ALL}$  are employed. The first three notations respectively refer to Kármán nonlinear theory which considers the thickness stretching, shear deformations owing to transverse deflection, and in-plane displacement

components. Additionally,  $\text{vK}_{+\text{ALL}}$  corresponds to Kármán nonlinear theory with all of the previously described modifications. Also, it should be noted that the notation  $\text{FNL}_{-\text{vK}}$  represents the full nonlinear theory without von Kármán terms. The effect of adopting these geometrically nonlinear assumptions on the post-buckling equilibrium curves and stress distributions will be further investigated in Chapters 6 and 7. As will be highlighted in these chapters, selecting the appropriate model for strain-displacement relationship is critical for predicting a structure's nonlinear response that is both dependable and precise.

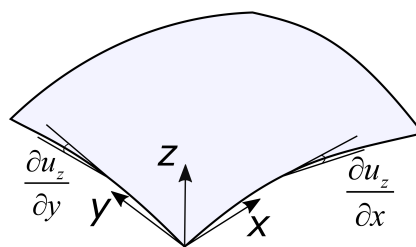


Fig. 2.3 Main geometrically nonlinear assumptions for the von Kármán nonlinear plate

Table 2.3 Different geometrically nonlinear assumptions based on the Green-Lagrange nonlinear strains

Theory	Description	Notation	Theory	Description	Notation
$\begin{pmatrix} \circ & \circ & \circ \\ \circ & \circ & \circ \\ \circ & \circ & \circ \\ \circ & \circ & \circ \\ \circ & \circ & \circ \\ \circ & \circ & \circ \end{pmatrix}$	<i>Linear</i>	Lin	$\begin{pmatrix} \circ & \circ & \bullet \\ \circ & \circ & \circ \\ \circ & \circ & \circ \\ \circ & \circ & \circ \\ \circ & \circ & \circ \\ \circ & \circ & \bullet \end{pmatrix}$	<i>von Kármán</i>	vK
$\begin{pmatrix} \circ & \circ & \bullet \\ \circ & \circ & \bullet \\ \circ & \circ & \bullet \\ \circ & \circ & \bullet \\ \circ & \circ & \bullet \\ \circ & \circ & \bullet \end{pmatrix}$	<i>von Kármán considering thickness stretching</i>	vK <sub>+T</sub>	$\begin{pmatrix} \circ & \circ & \bullet \\ \circ & \circ & \bullet \\ \circ & \circ & \bullet \\ \circ & \circ & \bullet \\ \circ & \circ & \bullet \\ \circ & \circ & \bullet \end{pmatrix}$	<i>von Kármán considering shear deformations due to the transverse deflection</i>	vK <sub>+S</sub>
$\begin{pmatrix} \bullet & \bullet & \bullet \\ \bullet & \bullet & \bullet \\ \bullet & \bullet & \bullet \\ \bullet & \bullet & \bullet \\ \bullet & \bullet & \bullet \\ \bullet & \bullet & \bullet \end{pmatrix}$	<i>von Kármán considering in-plane components of displacement</i>	vK <sub>+IN</sub>	$\begin{pmatrix} \bullet & \bullet & \bullet \\ \bullet & \bullet & \bullet \\ \bullet & \bullet & \bullet \\ \bullet & \bullet & \bullet \\ \bullet & \bullet & \bullet \\ \bullet & \bullet & \bullet \end{pmatrix}$	<i>von Kármán with all the mentioned considerations</i>	vK <sub>+ALL</sub>
$\begin{pmatrix} \bullet & \bullet & \circ \\ \bullet & \bullet & \circ \\ \bullet & \bullet & \circ \\ \bullet & \bullet & \circ \\ \bullet & \bullet & \circ \\ \bullet & \bullet & \circ \end{pmatrix}$	<i>Full Nonlinear without von Kármán terms</i>	FNL <sub>-vK</sub>	$\begin{pmatrix} \bullet & \bullet & \bullet \\ \bullet & \bullet & \bullet \\ \bullet & \bullet & \bullet \\ \bullet & \bullet & \bullet \\ \bullet & \bullet & \bullet \\ \bullet & \bullet & \bullet \end{pmatrix}$	<i>Full Nonlinear</i>	FNL

# Chapter 3

## Higher-order vibration modes of thin-walled beam structures

### 3.1 Introduction

Lightweight thin-walled beam structures with open sections are widely demanded by different engineering industries such as aerospace and construction. In general, a beam should have the capability to sustain extension, compression, transverse shear, bending, and twisting loads [72]. One-dimensional beam theories have been widely employed in order to take advantage of their simplicity and lower computational costs [73–76], and further by Vlasov for the thin-walled beams [77, 78].

Free vibration takes place after the initial excitation, once the system is left to vibrate on its own (without any external forces). There are several investigations devoted to analyzing the free vibration response of beam structures [79–81]. The free vibration response of stepped beams are studied in [82–85]. Considering the displacement of the beam as a combination of Fourier series and auxiliary polynomial function, Li [86] proposed an approach for the investigation of free vibration response in generally supported beams. Dey and Talukdar [87] studied the free vibration response of thin-walled channel section steel beams. An FE method for the coupled free vibration of thin-walled beams with open cross-sections was developed by Chen and Hsiao [88] with numerical examples from the literature [89–91]. Murin et al. analyzed the influence of torsional warping on the vibrations of thin-walled beams with functionally graded materials [92]. The Generalized Beam Theory



(GBT) [93] was further developed by Camotim and Silvestre [94–96] and was effectively employed for the vibrations analysis in thin-walled structures. In a compressed non-symmetric thin-walled beam with the cruciform cross-section, Piana et al. [97] presented a comparison of experimental and numerical results. They detected the frequencies by the Peak Picking technique employing PZT pickups or Laser sensors. For the free vibration analysis of thin-walled structures, Fazzolari [98] developed a Ritz formulation. Kugler et al. [99, 100] presented a novel GBT based on the reference beam problem for the slender prismatic structures. Jrad conducted a comprehensive study on the dynamic behavior of thin-walled beams using experimental, numerical and analytical approaches [101, 102]. Also, interested readers are referred to the books by Gorman [103], and Blevins [104] for more information and analyses.

In many cases, the beam and plate structures are subjected to high frequencies and large amplitude vibrations. Thus, the higher modes in the free vibration response of structures have been studied in some studies. For the high frequency vibrations of structures, a discrete singular convolution algorithm was developed by Wei et al. [105]. Langley and Bardell [106] worked on the alternative analysis methods for high frequency vibrations of aerospace structures. The displacements of trigonometric function were considered, and a theory for high frequency vibrations of rectangular beams was presented [107]. According to the classic Ritz method, Sudalagunta et al. [108] presented a framework for higher modes vibrations of one-dimensional structures. Wang [109] developed a discrete singular convolution algorithm in order to investigate the high frequency vibrations of structures. An energy FE formulation for the high frequency vibration of beam structures was proposed by Lin et al. [110].

This chapter investigates the higher vibration modes of thin-walled beams with complicated geometries using the CUF. The higher-order vibration modes are evaluated in a series of thin-walled beams that Chen offered as benchmark problems. We employ both classical and higher-order beam theories and study the influence of cross-sectional deformations on higher-order modes. The Modal Assurance Criterion (MAC) is used to assess free vibration modes. A detailed comparison is made between classical beam theories, refined beam theories based on the CUF, shell results from commercial FE software, and data from the literature. It is demonstrated that classical beam theories ignore several modes in favor of rigid-cross section modes that do not really exist. Additionally, it is demonstrated that when the CUF is used,

the results are not only cost-effective but also accurate and consistent with shell models with high computational costs.

### 3.2 Description of the Chen benchmark

This section is devoted to presenting a series of thin-walled beams with open cross-sections by Ref. [88] as benchmark problems. Beams with C-shaped and T-shaped cross-sections are discussed firstly, and then beams with arbitrary and complex cross-sections will be introduced. The schematic figures of the investigated beam examples as shown in Fig. 3.1 (dimensions in mm).

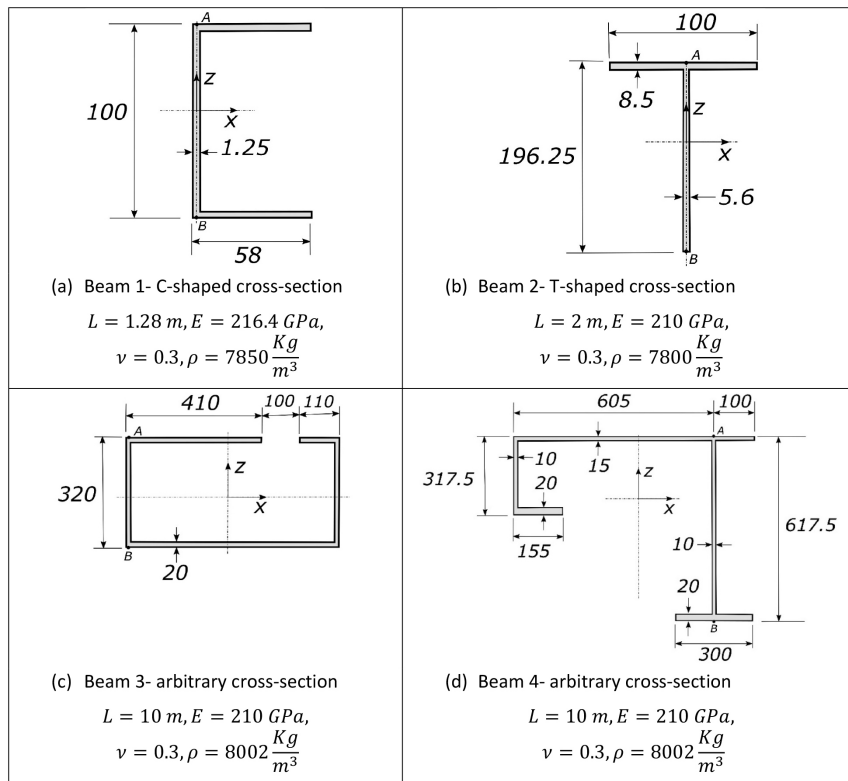


Fig. 3.1 The schematic view and material properties of the investigated benchmark beam problems

### 3.3 Convergence study

This section discusses the convergence analyses according to the displacements and axial stresses for cantilever beams under a point load at the free end. In this regard, the displacements at the beam's free end are determined, as well as the axial stresses at the beam's clamped edge. Four beams having C-shaped, T-shaped, and two arbitrary cross-sections are investigated here. All the beams are clamped at one end and subjected to downward tip forces of  $P$  applied at the free end of each beam (see points A in Fig. 3.1) with values 1000 N, 15000 N, 30000 N, and 90000 N, for the beams 1, 2, 3, and 4, respectively. In order to investigate the effect of FE discretization, convergence analyses are conducted for the displacements and stresses of the mentioned beam structures. Based on the models with different FE discretizations, the results of the vertical displacements and axial stresses at the bottom points B of Fig. 3.1 at  $y = L$  are reported in Tables 3.1, 3.2, 3.3, 3.4 for the beams 1, 2, 3, and 4, respectively. In addition, the Degree of Freedom (DOF) corresponding to each model is listed in the tables. Note that the results are presented for the beam elements with two nodes (B2), three nodes (B3), and four nodes (B4), respectively. In addition, it should be noted that the last columns of tables are devoted to the error values of displacements and axial stresses compared to the corresponding most refined model in the table.

Table 3.1 The convergence analysis of vertical displacements and axial stresses for the beam 1- effect of FE

Model	DOF	Displacement (mm)	Axial Stress (MPa)	Displacement Error %	Axial Stress Error %
5B2-14L9	1566	3.29	64.36	78.84	77.29
10B2-14L9	2871	6.48	87.13	58.32	69.26
20B2-14L9	5481	10.72	213.14	31.06	24.81
30B2-14L9	8091	12.80	235.51	17.68	16.92
50B2-14L9	13311	14.38	263.54	7.52	7.03
5B3-14L9	2871	15.10	139.42	2.89	50.81
10B3-14L9	5481	15.37	220.11	1.15	22.35
20B3-14L9	10701	15.49	272.46	0.38	3.88
30B3-14L9	15921	15.53	281.03	0.12	0.86
5B4-14L9	4176	15.36	187.63	1.22	33.81
10B4-14L9	8091	15.49	237.92	0.38	16.07
20B4-14L9	15921	15.55	283.48	0.00	0.00

Table 3.2 The convergence analysis of vertical displacements and axial stresses for the beam 2- effect of FEs

Model	DOF	Displacement (mm)	Axial Stress (MPa)	Displacement Error %	Axial Stress Error %
5B2-15L9	1674	10.84	228.88	57.10	53.57
10B2-15L9	3069	18.82	327.71	25.52	33.52
20B2-15L9	5859	23.20	474.24	8.19	3.79
30B2-15L9	8649	24.28	475.76	3.91	3.48
50B2-15L9	14229	24.90	486.85	1.46	1.23
5B3-15L9	3069	24.84	402.06	1.70	18.43
10B3-15L9	5859	25.10	441.04	0.67	10.53
20B3-15L9	11439	25.22	486.00	0.19	1.41
30B3-15L9	17019	25.26	489.21	0.03	0.76
5B4-15L9	4464	25.09	429.61	0.71	12.85
10B4-15L9	8649	25.22	467.26	0.19	5.21
20B4-15L9	17019	25.27	492.96	0.00	0.00

Table 3.3 The convergence analysis of vertical displacements and axial stresses for the beam 3- effect of FEs

Model	DOF	Displacement (mm)	Axial Stress (MPa)	Displacement Error %	Axial Stress Error %
5B2-16L9	1782	14.60	10.83	82.56	85.92
10B2-16L9	3267	33.92	27.51	59.48	64.25
20B2-16L9	6237	58.88	59.05	29.67	23.27
30B2-16L9	9207	70.00	66.13	16.39	14.07
50B2-16L9	15147	78.06	72.98	6.77	5.17
5B3-16L9	3267	82.13	39.04	1.91	49.27
10B3-16L9	6237	83.14	69.22	0.70	10.05
20B3-16L9	12177	83.56	74.97	0.20	2.58
30B3-16L9	18117	83.68	76.76	0.05	0.25
5B4-16L9	4752	83.10	47.93	0.75	37.72
10B4-16L9	9207	83.53	71.06	0.23	7.66
20B4-16L9	18117	83.73	76.96	0.00	0.00

Table 3.4 The convergence analysis of vertical displacements and axial stresses for the beam 4- effect of FEs

Model	DOF	Displacement (mm)	Axial Stress (MPa)	Displacement Error %	Axial Stress Error %
5B2-17L9	1890	32.65	73.62	72.07	61.45
10B2-17L9	3465	65.79	104.78	43.72	45.13
20B2-17L9	6615	95.65	179.66	18.17	5.92
30B2-17L9	9765	105.88	181.07	9.42	5.18
50B2-17L9	16065	112.54	188.63	3.72	1.23
5B3-17L9	3465	114.78	140.19	1.81	26.59
10B3-17L9	6615	116.09	159.44	0.69	16.51
20B3-17L9	12915	116.65	187.21	0.21	1.97
30B3-17L9	19215	116.83	189.48	0.05	0.78
5B4-17L9	5040	116.02	153.45	0.75	19.65
10B4-17L9	9765	116.62	165.39	0.23	13.39
20B4-17L9	19215	116.90	190.98	0.00	0.00

In order to evaluate the effect of structural theories, the convergence analyses are conducted for the displacements and stresses of the previously mentioned beam structures. Different discretizations over the beam cross-sections are schematically shown in Figs. 3.2, 3.3, 3.4, and 3.5 for the beams 1, 2, 3, and 4, respectively. The results of these convergence analyses are reported in Tables 3.5, 3.6, 3.7, and 3.8 for the beams 1, 2, 3, and 4, respectively. The results reveal that the classical and TE models of lower orders cannot present reliable displacements and axial stresses. For example, in most of the tables, TE=1 and TE=2 show significant errors compared to the most refined model of the corresponding table.

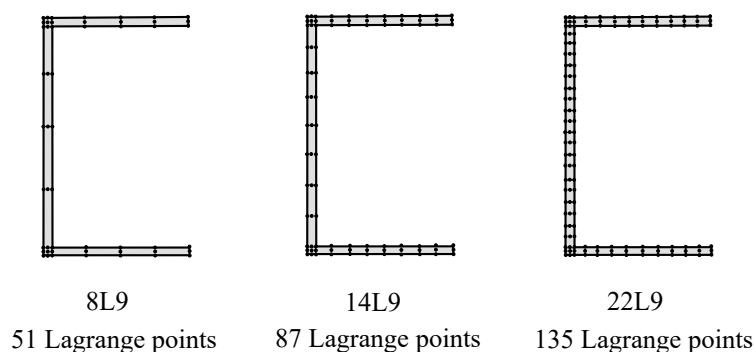


Fig. 3.2 Different Cross-sectional discretization of the beam-1 based on the LE

Table 3.5 The convergence analysis of vertical displacements and axial stresses for the beam 1- effect of structural theory

Model	DOF	Displacement (mm)	Axial Stress (MPa)	Displacement Error %	Axial Stress Error %
20B4,TE=1	549	7.24	127.98	53.44	54.88
20B4,TE=2	1098	7.18	128.60	53.82	54.66
20B4,TE=5	3843	8.31	155.63	46.55	45.13
20B4,TE=10	12078	14.63	267.55	5.91	5.67
20B4,TE=15	24888	15.33	277.15	1.41	2.29
20B4-8L9	933	15.54	283.29	0.06	0.12
20B4-14L9	15921	15.55	283.48	0.00	0.05
20B4-22L9	24705	15.55	283.65	0.00	0.00

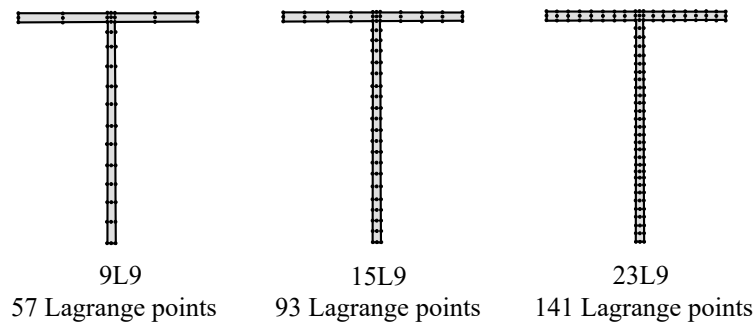


Fig. 3.3 Different Cross-sectional discretization of the beam-2 based on the LE

Table 3.6 The convergence analysis of vertical displacements and axial stresses for the beam 2- effect of structural theory

Model	DOF	Displacement (mm)	Axial Stress (MPa)	Displacement Error %	Axial Stress Error %
20B4,TE=1	549	25.18	488.11	0.35	0.90
20B4,TE=2	1098	25.09	489.93	0.71	0.53
20B4,TE=5	3843	25.25	491.95	0.07	0.12
20B4,TE=10	12078	25.27	492.54	0.07	0.00
20B4,TE=15	24888	25.27	492.58	0.00	0.00
20B4-9L9	10431	25.27	493.68	0.00	0.22
20B4-15L9	17019	25.27	492.96	0.00	0.08
20B4-23L9	25803	25.27	492.56	0.00	0.00

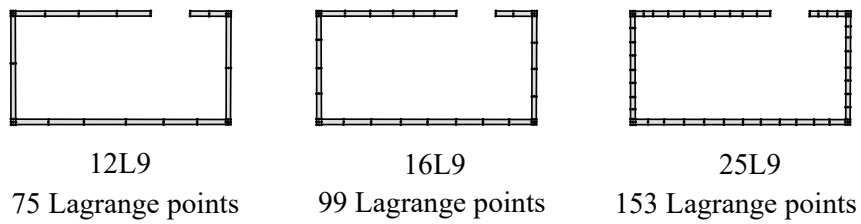


Fig. 3.4 Different Cross-sectional discretization of the beam-3 based on the LE

Table 3.7 The convergence analysis of vertical displacements and axial stresses for the beam 3- effect of structural theory

Model	DOF	Displacement (mm)	Axial Stress (MPa)	Displacement Error %	Axial Stress Error %
20B4,TE=1	549	81.82	73.67	2.31	4.32
20B4,TE=2	1098	81.46	74.16	2.74	3.68
20B4,TE=5	3843	81.89	74.22	2.23	3.61
20B4,TE=10	12078	82.11	74.36	1.96	3.42
20B4,TE=15	24888	82.23	74.46	1.82	3.29
20B4-12L9	13725	83.66	76.93	0.11	0.09
20B4-16L9	18117	83.73	76.96	0.03	0.05
20B4-25L9	27999	83.76	77.00	0.00	0.00

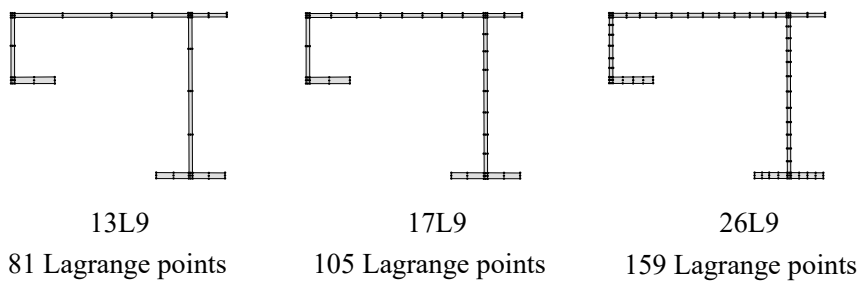


Fig. 3.5 Different Cross-sectional discretization of the beam-4 based on the LE

Table 3.8 The convergence analysis of vertical displacements and axial stresses for the beam 4- effect of structural theory

Model	DOF	Displacement (mm)	Axial Stress (MPa)	Displacement Error %	Axial Stress Error %
20B4,TE=1	549	104.94	173.54	10.25	9.33
20B4,TE=2	1098	104.30	173.89	10.80	9.15
20B4,TE=5	3843	105.52	174.07	9.75	9.05
20B4,TE=10	12078	111.47	184.58	4.66	3.56
20B4,TE=15	24888	116.03	190.21	0.76	0.62
20B4-13L9	14823	116.87	190.82	0.05	0.30
20B4-17L9	19215	116.90	190.98	0.02	0.22
20B4-26L9	29097	116.93	191.41	0.00	0.00

For the sake of completeness, based on the values of table 3.1, for the example beam 1 with a C-shaped cross-section, in Figs. 3.6a and 3.6b the displacements and axial stresses against the DOF of each model are plotted. In addition, the corresponding error values are indicated in Figs. 3.6c and 3.6d. The findings reveal that the convergence rate of B4 beam elements is much greater than that of B3 and B2 beam elements for both vertical displacements and axial stresses. Additionally, the calculated displacement values for B2 elements are not precise enough due to the model's requirement for shear refinements. This subject will be discussed in further detail in Section 3.4.



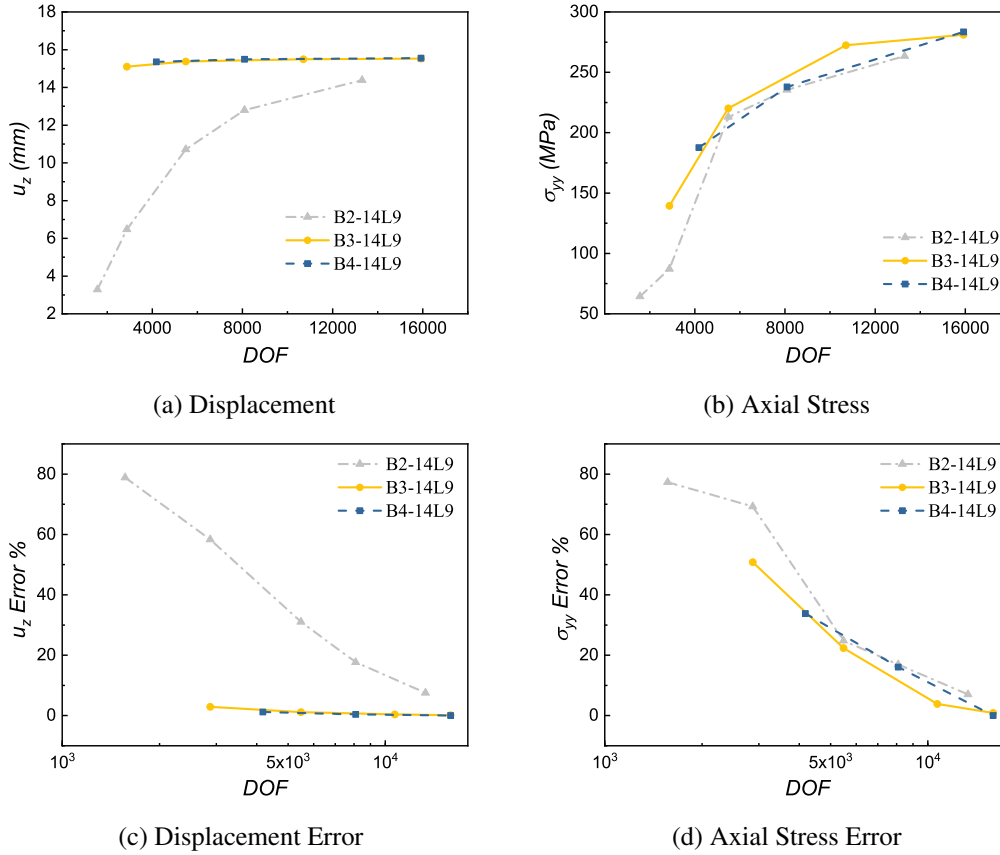


Fig. 3.6 The comparison of convergence analyses of vertical displacements and axial stresses for the beam 1 based on the DOF of beam structure

### 3.4 Shear locking treatments

The findings of displacements and axial stresses by various approaches for the elimination of shear locking are explored and compared in this section. As discussed in Section 1.7, the methods of full, selective, reduced integration, and MITC are considered here.

The C-shaped beam is used as the initial locking example. Fig. 3.7 illustrates displacement values based on the DOF by utilizing the full, selective, reduced, integration, and MITC methods. As can be seen clearly in this figure, when the full integration is used, the locking occurs for B2 linear beam elements. The displacements and axial stresses of B2, B3, and B4 elements are presented in Table 3.9. It

is worth noting that increasing the number of beam elements along the beam's axis lessens the impact of shear locking considerably.

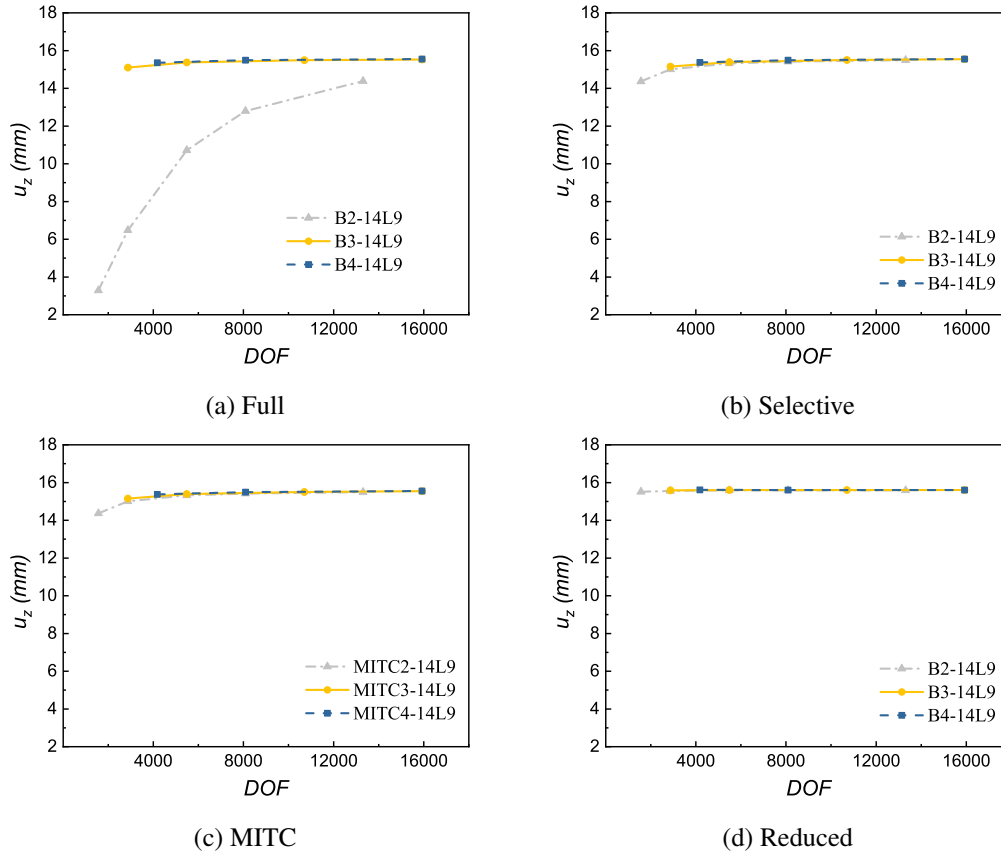


Fig. 3.7 Shear locking effects on the vertical displacements of the investigated beam 1

Table 3.9 Shear locking effects on the values of vertical displacements in the investigated beam 1

Models	DOF	Displacement (mm)				Axial Stress (MPa)			
		Selective	Reduced	MITC	Full	Selective	Reduced	MITC	Full
5B2-14L9	1566	14.37	15.51	14.37	3.29	283.35	281.55	283.35	64.36
10B2-14L9	2871	15.01	15.56	15.01	6.48	202.21	114.11	202.21	87.13
20B2-14L9	5481	15.32	15.59	15.32	10.72	299.06	490.46	299.06	213.14
30B2-14L9	8091	15.42	15.59	15.42	12.80	293.77	70.74	293.77	235.51
50B2-14L9	13311	15.49	15.59	15.49	14.38	291.40	38.77	291.40	263.54
5B3-14L9	2871	15.15	15.59	15.15	15.10	240.84	182.36	240.84	139.42
10B3-14L9	5481	15.39	15.60	15.39	15.37	338.22	469.27	338.22	220.11
20B3-14L9	10701	15.50	15.60	15.50	15.49	272.85	492.40	272.85	272.46
30B3-14L9	15921	15.54	15.60	15.54	15.53	268.20	512.63	268.20	281.03
5B4-14L9	4176	15.37	15.61	15.37	15.36	274.14	277.32	274.14	187.63
10B4-14L9	8091	15.49	15.60	15.49	15.49	256.18	100.80	256.18	237.92
20B4-14L9	15921	15.55	15.60	15.55	15.55	263.82	496.75	263.82	283.48

The T-shaped beam is considered to be the second example of shear locking evaluation. The displacements and axial stresses of B2, B3, and B4 elements are presented in Table 3.10. The same observations as in the preceding case might be made concerning the results obtained using the full integration approach when the shear locking phenomenon occurs for the case of linear elements. The findings emphasize the importance of high order FE in order to resolve this problem. When the CUF is used, shear locking has a negligible effect on the models. Moreover, when utilizing the full integration approach, particularly for linear FE, the shear locking effect should be carefully considered. It should be noted that the locking behavior for the other investigated beams in this chapter are almost similar, and are not presented here for the sake of brevity.

Table 3.10 Shear locking effects on the values of vertical displacements in the investigated beam 2

Models	DOF	Displacement (mm)				Axial Stress (MPa)			
		Selective	Reduced	MITC	Full	Selective	Reduced	MITC	Full
5B2-15L9	1674	23.94	25.14	57.10	10.84	496.93	493.63	496.93	228.88
10B2-15L9	3069	24.69	25.25	25.52	18.82	430.40	342.62	430.40	327.71
20B2-15L9	5859	25.04	25.30	8.19	23.20	494.21	671.25	494.21	474.24
30B2-15L9	8649	25.14	25.31	3.91	24.28	508.30	318.49	508.30	475.76
50B2-15L9	14229	25.22	25.31	1.46	24.90	495.95	331.88	495.95	486.85
5B3-15L9	3069	24.87	25.31	1.70	24.84	445.29	387.17	445.29	402.06
10B3-15L9	5859	25.11	25.32	0.67	25.10	509.26	629.58	509.26	441.04
20B3-15L9	11439	25.23	25.32	0.19	25.22	475.52	646.94	475.52	486.00
30B3-15L9	17019	25.26	25.32	0.03	25.26	485.29	644.23	485.29	489.21
5B4-15L9	4464	25.09	25.33	0.71	25.09	468.34	472.70	468.34	429.61
10B4-15L9	8649	25.22	25.32	0.19	25.22	507.72	377.02	507.72	467.26
20B4-15L9	17019	25.28	25.32	0.00	25.27	484.11	641.67	484.11	492.96

### 3.5 Higher-order modes detection via various models

The findings of free vibration analysis and higher mode detection with cross-sectional deformation are reported in this section for the mentioned beam structures in this chapter. To begin, the proposed method is validated by presenting the free vibration modes and natural frequencies of the beam with cruciform cross-section and comparing the results to experiments, other available data from the literature, and Abaqus (ABQ) shell models. Then, the mode shapes and natural frequencies of beam structures with C-shaped, T-shaped, and arbitrary cross-sections are investigated.

#### 3.5.1 Validation case-cruciform beam

To verify the suggested CUF-based approach, a 670 mm long doubly clamped cruciform beam is considered [97]. The dimensions of the beam's cross-section are provided in schematic Fig. 3.8 (dimensions in mm). This beam model considers the isotropic material properties of Young's modulus ( $E=70$  GPa), Poisson's ratio ( $\nu=0.3$ ), and density ( $\rho=2600$  kg/m<sup>3</sup>).

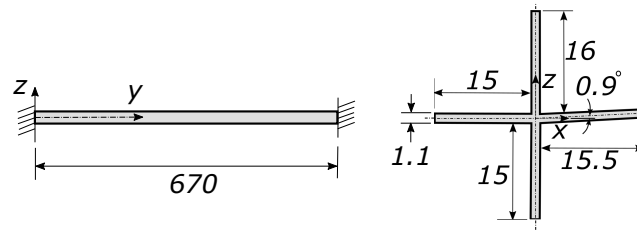


Fig. 3.8 Schematic view of the cruciform beam

The ABQ shell and CUF 1D models used to analyze this cruciform beam are described in Table 3.11. Additionally, Table 3.12 compares the first ten natural frequencies of this beam using the ABQ shell and CUF 1D models. The corresponding mode shapes 5 and 10 are also compared using the CUF 1D and ABQ shell models, as illustrated in Fig. 3.9. The contour plots of the mode shapes reveal that the CUF 1D results, which require much less computational effort, match well with costly ABQ shell models. Additionally, in Table 3.13, the natural frequencies of the experimental approach in [97] and the other relevant literature in [101] are compared to the suggested CUF 1D method. The findings demonstrate that the free vibration mode shapes and natural frequencies obtained by the CUF 1D method match well with experimental results. Note that small deviations of less than 6.5% could be due to many factors influencing different steps of experimental approach during the frequency extraction process, or the approximations introduced by the kinematics assumption or FEM method. Accordingly, the ABQ and CUF models employ different FEM formulations, and are based on different structural theories of shells and beam structures.

Table 3.11 The details of ABQ shell and CUF 1D models employed for the cruciform beam

Model	DOF	Number of elements	Element type	Section discretization	Time (Sec)
ABQ shell-coarse	6342	320	Quadratic S8R	8	25.16
ABQ shell-medium	24198	1280	Quadratic S8R	16	31.47
ABQ shell-fine	94470	5120	Quadratic S8R	32	53.89
CUF 1D-LE	2736	5B4	4-node beam	9L9	4.33
CUF 1D-LE	9765	10B4	4-node beam	17L9	11.48
CUF 1D-LE	27999	20B4	4-node beam	25L9	35.35

Table 3.12 The first ten natural frequencies of cruciform beam with doubly clamped edge conditions based on the used ABQ shell and CUF 1D models

Modes	ABQ shell-coarse	ABQ shell-medium	ABQ shell-fine	5B4-9L9	10B4-17L9	20B4-25L9
Mode 1	168.13	167.71	167.70	173.58	171.66	170.84
Mode 2	261.21	261.07	261.02	267.03	265.04	264.12
Mode 3	267.48	267.34	267.28	273.41	271.38	270.43
Mode 4	336.98	336.15	336.13	347.87	344.04	342.42
Mode 5	507.15	505.90	505.87	523.39	517.72	515.30
Mode 6	679.10	677.45	677.40	700.96	693.12	689.91
Mode 7	703.74	703.29	703.11	737.32	714.46	711.94
Mode 8	720.35	719.88	719.70	720.48	731.20	728.65
Mode 9	853.92	851.83	851.77	887.21	871.44	867.42
Mode 10	1031.8	1029.3	1029.2	1079.08	1052.84	1047.93

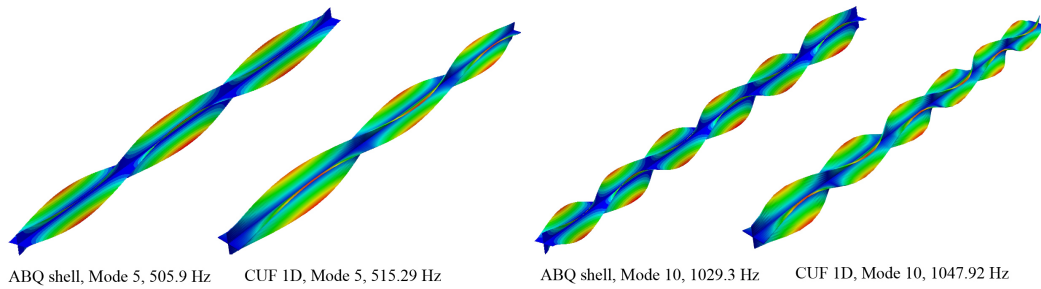


Fig. 3.9 The comparison of free vibration mode shapes of ABQ shell and CUF 20B4-25L9 models

Table 3.13 The comparison of first ten natural frequencies of the cruciform beam with the available literature

Modes	Experimental results [97]	Numerical results[97]	B3Dw[101]	ABQ-B31OS[101]	ABQ shell-fine	CUF 1D 20B4-25L9	CUF 1D difference with experiments (%)
Mode 1	161.87	165.66	165.56	166.05	167.70	170.84	5.25
Mode 2	275.47	263.75	266.97	265.38	261.02	264.12	4.30
Mode 3	284.18	269.90	273.34	271.63	267.28	270.43	5.08
Mode 4	325.43	331.69	331.17	332.16	336.13	342.42	4.96
Mode 5	486.13	499.17	496.79	498.28	505.87	515.30	5.66
Mode 6	667.84	667.49	662.34	664.31	677.40	689.91	3.20
Mode 7	741.30	716.75	734.71	725.23	703.11	711.94	4.12
Mode 8	767.30	733.04	752.20	742.02	719.70	728.65	5.30
Mode 9	813.39	838.93	827.96	830.47	851.77	867.42	6.23
Mode 10	-	-	-	-	1029.2	1047.93	-

### 3.5.2 Beam 1- C-shaped cross-section

The initial assessment of higher vibration modes in the presence of cross-sectional deformations is focused on the C-shaped beam with clamped-free edge conditions. In Table 3.15, the natural frequencies based on the different models using the proposed CUF 1D method and ABQ shell models are provided. In Figs. 3.16, 3.17, and 3.18, the first forty mode shapes of this beam are shown using the TE=1, TE=10, and 22L9 models with 20B4 FE beams. The details of ABQ shell models employed for this beam example are reported in Table 3.14. As seen in Fig. 3.10, the contour plots of mode shapes and natural frequencies for the corresponding modes number 40 are compared using the CUF 1D and ABQ shell models. The contour plots of the mode shapes reveal that the CUF 1D findings, which require much less computational effort, match well with the more costly ABQ shell model.

Table 3.14 The details of ABQ shell models employed for the beam 1

Model	DOF	Number of elements	Element type	Beam axis elements	Cross-Section discretization
Shell	27102	1440	Quadratic S8R	80	18

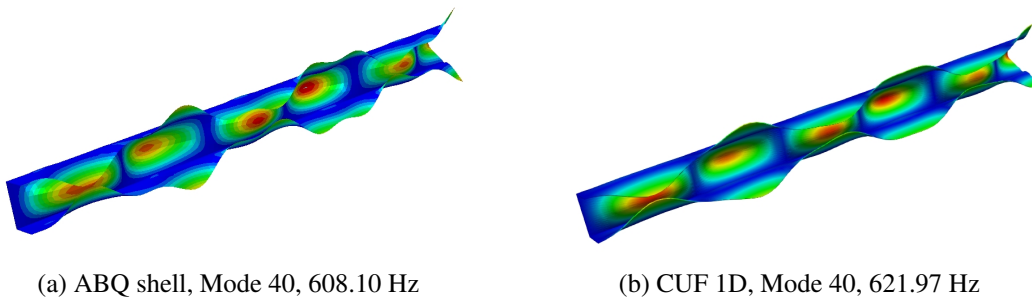


Fig. 3.10 The comparison of free vibration mode shapes of ABQ shell and CUF 20B4-22L9 models

Table 3.15 Natural frequencies of beam 1 with clamped-free edge conditions based on different structural theories

Modes	20B4-22L9	20B4,TE=1	20B4,TE=2	20B4,TE=5	20B4,TE=10	20B4-8L9	20B4-14L9	ABQ shell
Mode 1	25.10	33.59	33.84	33.63	26.39	25.12	25.11	25.00
Mode 2	33.57	73.00	73.33	53.09	33.57	33.58	33.57	33.51
Mode 3	96.19	208.23	209.15	110.72	96.56	96.32	96.22	96.07
Mode 4	135.58	435.55	436.06	203.13	141.18	137.72	136.05	134.61
Mode 5	151.31	573.27	480.15	206.62	160.67	152.83	151.63	150.51
Mode 6	156.40	624.08	573.55	419.71	169.17	158.10	156.72	155.20
Mode 7	166.95	650.22	1028.77	436.95	183.24	168.46	167.25	165.91
Mode 8	183.88	1097.31	1092.32	438.48	205.81	185.28	184.16	182.71
Mode 9	204.29	1139.50	1139.09	483.69	223.16	205.62	204.55	203.02
Mode 10	215.70	1762.99	1444.29	552.87	232.62	217.88	216.21	214.38
Mode 11	229.14	1872.25	1744.64	553.33	261.92	230.44	229.40	225.64
Mode 12	229.55	1950.34	2049.14	641.40	268.99	247.87	233.18	227.73
Mode 13	254.69	2055.96	2423.79	652.07	295.06	258.61	257.55	250.14
Mode 14	257.28	2549.61	2506.89	729.85	306.69	277.26	259.05	255.73
Mode 15	273.33	3249.50	3081.75	731.54	329.75	290.33	277.74	268.67
Mode 16	288.90	3115.53	3095.34	805.25	331.15	296.28	289.18	287.18
Mode 17	293.74	3120.41	3357.31	872.57	353.25	316.40	298.08	289.06
Mode 18	316.69	3437.52	3426.73	932.17	370.12	325.54	320.98	312.03
Mode 19	321.57	4266.07	4223.09	986.88	369.77	339.06	324.24	316.19
Mode 20	323.92	4409.07	4276.19	985.44	379.76	347.62	328.89	319.73
Mode 21	323.98	4368.58	4461.05	1027.46	383.12	352.11	327.49	322.03
Mode 22	344.40	4547.07	5119.94	1033.64	408.80	364.17	348.56	339.74
Mode 23	362.29	5449.09	5248.65	1076.31	411.87	366.25	362.66	360.20
Mode 24	374.97	5474.33	5390.34	1079.32	441.42	396.48	379.06	370.33
Mode 25	404.03	5616.75	5539.36	1121.52	456.46	406.26	404.47	401.74
Mode 26	409.21	5842.42	6258.72	1137.52	477.33	430.49	413.24	404.59
Mode 27	447.20	6544.88	6548.31	1164.09	503.81	451.81	449.66	442.62
Mode 28	449.12	6718.19	6690.49	1207.46	510.85	468.40	451.22	446.58
Mode 29	471.32	6864.92	7133.03	1216.18	516.69	500.86	484.71	464.38
Mode 30	488.90	7134.94	7299.74	1252.72	560.16	510.12	492.91	484.35
Mode 31	497.85	7686.00	7691.95	1265.32	554.52	524.70	498.53	495.07
Mode 32	534.25	7982.08	7904.82	1293.70	554.38	549.72	538.24	529.79
Mode 33	541.94	8113.12	8357.42	1304.41	585.74	553.70	544.43	539.89
Mode 34	549.83	8424.00	8849.89	1300.74	606.08	556.12	550.64	546.68
Mode 35	571.11	8864.03	9108.39	1338.04	608.12	581.46	578.92	558.61
Mode 36	578.16	9253.18	9141.08	1352.34	655.86	605.70	588.19	576.65
Mode 37	584.20	9361.35	9431.04	1372.11	660.99	610.00	601.73	580.09
Mode 38	600.87	9709.00	10025.34	1407.62	665.29	659.25	606.98	587.46
Mode 39	606.06	10072.19	10382.11	1408.09	705.34	670.05	636.62	602.08
Mode 40	621.98	10517.44	10509.69	1445.67	709.34	716.91	641.26	608.10



Table 3.16 The first forty mode shapes of beam 1, 20B4,TE=1 model with clamped-free edge conditions

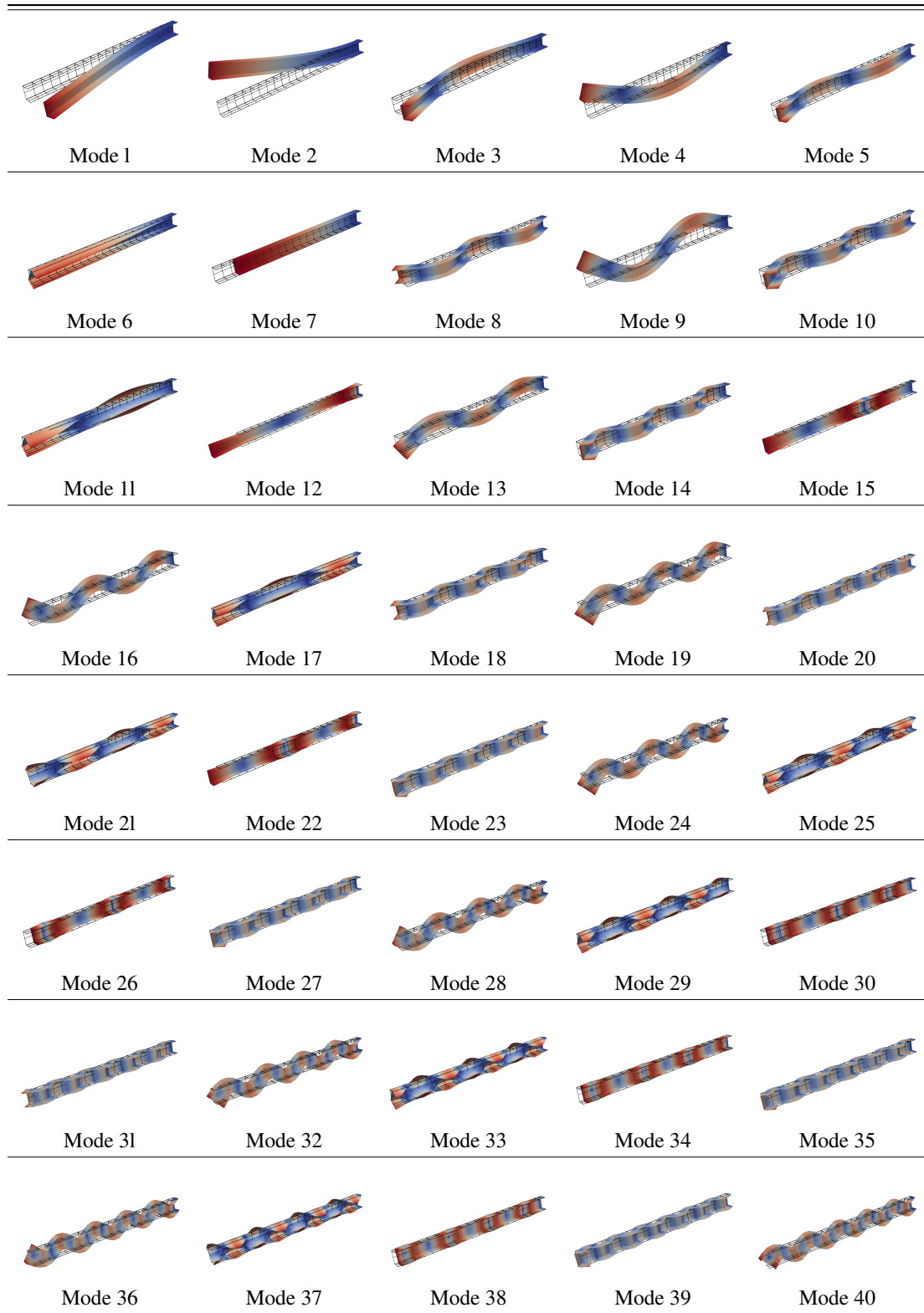
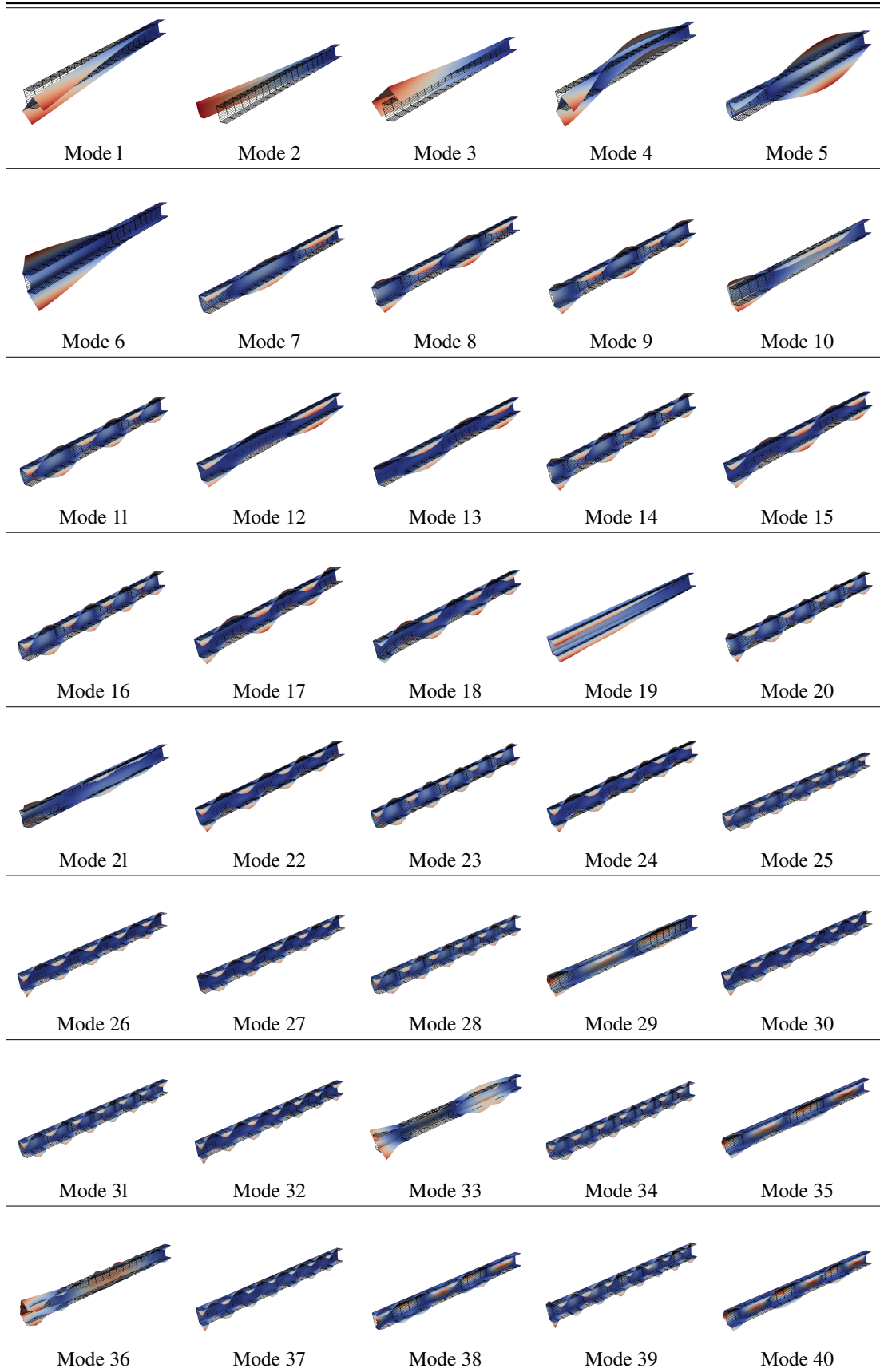


Table 3.17 The first forty mode shapes of beam 1, 20B4,TE=10 model with clamped-free edge conditions



Table 3.18 The first forty mode shapes of beam 1, 20B4-22L9 model with clamped-free edge conditions



Some comments could be made according to the results of Figs. 3.16, 3.17, 3.18, and Table 3.15 of the natural frequencies.

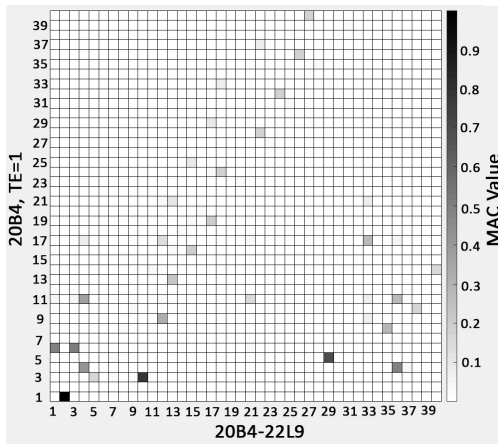
1. Classical beam theories and the linear TE of order one are unable to capture a large number of cross-sectional deformations associated with bending or torsion; instead, they exhibit rigid-cross section modes that do not exist.
2. In contrast to the TE=1 model, the TE=10 and 22L9 structural models have several corresponding mode shapes.
3. Natural frequency values determined using the CUF 1D (at a far lower computational cost) match pretty well with those obtained using the more costly ABQ shell models.
4. The contour plots of the mode shapes reveal that many of them do not correspond to one another. As a result, MAC analysis is required to study the corresponding modes associated with each theory.

The MAC is described as a scalar that measures the degree of consistency between two separate modal vectors using values ranging from 0 to 1. A MAC value of 0 indicates that the models do not correlate with each other. The MAC is calculated using the following equation [9, 111–113]:

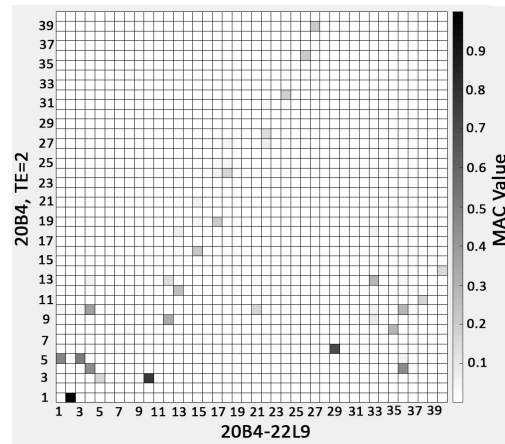
$$MAC_{ij} = \frac{|\{\varphi_{A_i}\}^T \{\varphi_{B_j}\}|^2}{\{\varphi_{A_i}\}^T \{\varphi_{A_i}\} \{\varphi_{B_j}\} \{\varphi_{B_j}\}^T} \quad (3.1)$$

where  $\varphi_{A_i}$  is the  $i$  th eigenvector of model A, and  $\varphi_{B_j}$  is the  $j$  th eigenvector of model B. In the following, by employing the MAC analysis (see Fig. 3.11), a comparison of the corresponding natural frequencies based on the different structural theories of the proposed CUF 1D method is presented in Table 3.19, where the natural frequencies of different CUF 1D models are compared to the ABQ shell results.

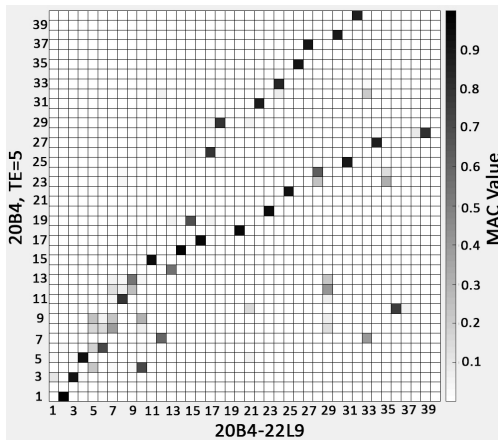




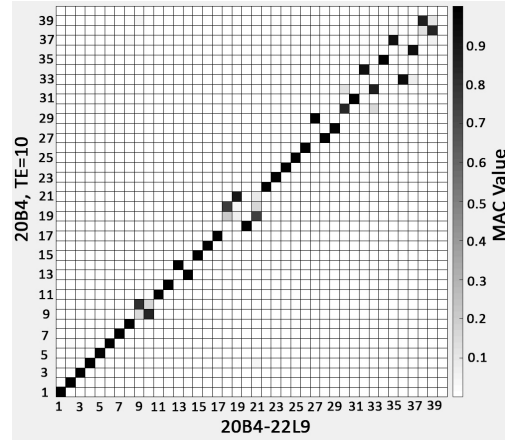
(a) 20B4, TE=1



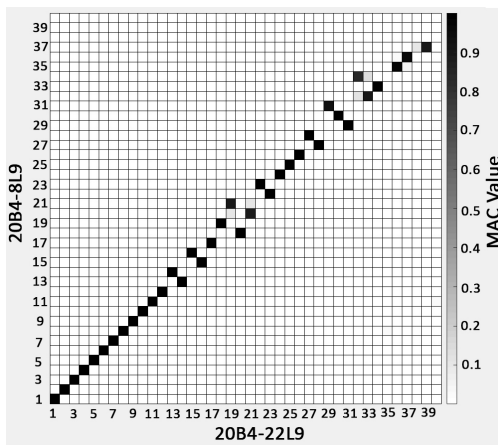
(b) 20B4, TE=2



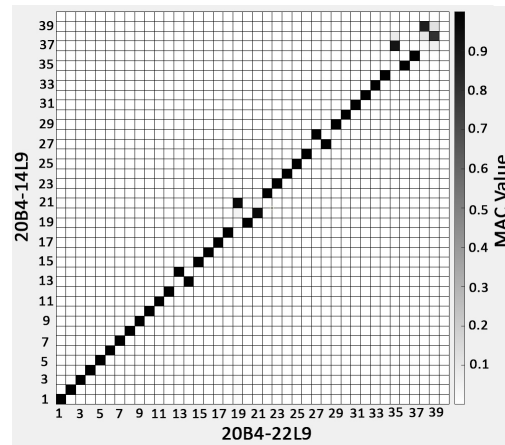
(c) 20B4, TE=5



(d) 20B4, TE=10



(e) 20B4-8L9



(f) 20B4-14L9

Fig. 3.11 MAC analysis for the comparison of free vibration modes for the beam 1

### 3.5.3 Beam 2- T-shaped cross-section

The second assessment of higher vibration modes with cross-sectional deformations is focused on the T-shaped beam with clamped-free edge conditions. Fig. 3.22 illustrates the first forty modes of this beam based on the 20B4-23L9 model. The ABQ shell model used to simulate the T-shaped beam is detailed in Table 3.20. The MAC analysis is used to compare the corresponding modes of different models based on the proposed CUF 1D method, and the corresponding natural frequencies are reported in Table 3.21.

Table 3.20 The details of ABQ shell models employed for the beam 2

Model	DOF	Number of elements	Element type	Beam axis elements	Cross-Section discretization
Shell	28554	1520	Quadratic S8R	80	19

Table 3.21 Natural frequencies of beam 2 with clamped-free edge conditions based on different structural theories for the corresponding mode shapes by the MAC

Modes	20B4-23L9	20B4,TE=1	20B4,TE=2	20B4,TE=5	20B4,TE=10	20B4-9L9	20B4-15L9	ABQ shell
Mode 1	12.54	-	-	-	12.93	12.57	12.55	12.43
Mode 2	27.50	-	-	48.28	30.33	27.71	27.59	27.09
Mode 3	45.42	-	-	-	45.43	45.42	45.42	45.27
Mode 4	54.68	-	-	-	60.23	55.14	54.89	53.99
Mode 5	88.32	-	-	-	96.35	89.01	88.61	87.18
Mode 6	124.21	-	-	-	130.59	124.84	124.48	122.58
Mode 7	130.74	-	-	-	141.13	131.57	131.07	128.97
Mode 8	166.59	-	-	240.45	179.65	167.87	167.07	164.26
Mode 9	205.85	-	-	279.77	219.39	207.32	206.37	203.12
Mode 10	250.20	-	-	-	264.02	251.83	250.75	247.08
Mode 11	263.02	272.56	271.49	264.22	263.46	263.17	263.06	261.84
Mode 12	298.44	-	-	-	-	300.11	298.98	295.04
Mode 13	315.93	-	-	-	319.22	316.37	316.05	312.55
Mode 14	354.59	-	-	427.15	368.44	356.52	355.19	350.82
Mode 15	415.57	-	-	486.95	429.36	417.65	416.19	411.51
Mode 16	459.32	-	-	-	478.93	462.10	460.11	453.70
Mode 17	482.26	-	-	-	496.67	484.66	482.98	477.57
Mode 18	487.54	-	-	-	511.15	490.55	488.48	482.23
Mode 19	525.06	-	-	-	541.66	528.18	526.05	520.31
Mode 20	553.70	-	-	-	-	556.73	554.69	548.26
Mode 21	560.24	-	-	-	-	563.11	561.13	555.21
Mode 22	628.34	-	-	-	662.19	632.78	629.89	622.36
Mode 23	639.20	-	-	705.85	-	641.79	639.93	634.02
Mode 24	649.55	-	-	649.66	649.58	649.57	649.55	649.13
Mode 25	662.35	715.18	769.26	670.59	665.68	663.84	662.69	658.32
Mode 26	677.64	-	-	-	717.97	682.37	679.44	669.76
Mode 27	725.15	-	-	-	-	728.39	726.15	719.34
Mode 28	732.66	-	-	-	779.94	739.58	734.87	726.48
Mode 29	816.96	-	-	-	-	-	819.10	809.46
Mode 30	823.29	-	-	-	-	-	824.91	816.58
Mode 31	902.95	-	-	-	963.75	913.63	906.19	893.08
Mode 32	923.70	-	-	-	935.53	927.05	924.58	916.21
Mode 33	965.36	-	-	-	1006.02	972.81	967.76	945.81
Mode 34	994.64	-	-	1363.44	1063.81	1007.73	998.38	982.57
Mode 35	1032.09	-	-	1096.39	1044.03	1035.54	1033.00	1022.73
Mode 36	1084.75	-	-	-	-	1099.84	1088.86	1060.54
Mode 37	1107.53	-	-	-	1263.43	1140.75	1115.41	1070.11
Mode 38	1120.25	-	-	-	-	-	1128.13	1073.57
Mode 39	1140.14	1294.36	1269.53	1171.98	1153.91	1147.42	1141.59	1097.15
Mode 40	1142.58	-	-	-	-	-	1147.82	1130.12



Table 3.22 The first forty mode shapes of beam 2, 20B4-23L9 model with clamped-free edge conditions



### 3.5.4 Beam 3- Arbitrary cross-section

This numerical example of higher vibration modes corresponds to the beam 3 (arbitrary cross-section) with clamped-free edge conditions. The first forty mode shapes of this beam are illustrated in Fig. 3.25 based on the 20B4-25L9 model. The details of the ABQ shell model for the beam 3 are listed in Table 3.23. By using the MAC analysis, a comparison of the corresponding natural frequencies based on the different models by the proposed CUF 1D method is presented in Table 3.24.

Table 3.23 The details of ABQ shell models employed for the beam 3

Model	DOF	Number of elements	Element type	Beam axis elements	Cross-section discretizations
Shell	64854	3520	Quadratic S8R	80	42

Table 3.24 Natural frequencies of beam 3 with clamped-free edge conditions based on different structural theories for the corresponding mode shapes by the MAC

Modes	20B4-25L9	20B4,TE=1	20B4,TE=2	20B4,TE=5	20B4,TE=10	20B4-12L9	20B4-16L9	ABQ shell
Mode 1	3.27	-	-	-	-	3.27	3.27	3.26
Mode 2	4.80	-	-	-	-	4.81	4.80	4.79
Mode 3	12.37	-	-	-	-	12.38	12.38	12.35
Mode 4	18.44	-	-	-	-	18.46	18.45	18.35
Mode 5	25.50	-	-	-	-	25.58	25.53	25.35
Mode 6	37.73	-	-	-	-	38.28	37.91	37.07
Mode 7	38.20	-	-	-	-	-	38.29	37.77
Mode 8	44.01	-	-	-	-	44.49	44.17	43.43
Mode 9	55.53	-	-	-	-	55.86	55.62	55.08
Mode 10	56.23	-	-	-	-	56.92	56.43	55.66
Mode 11	67.58	-	-	-	-	68.11	67.74	67.12
Mode 12	73.55	-	-	-	-	-	74.24	72.05
Mode 13	74.30	-	-	-	-	-	74.95	72.67
Mode 14	75.29	-	-	-	-	78.52	76.18	73.46
Mode 15	78.71	-	-	-	-	81.64	79.50	77.07
Mode 16	82.26	-	-	-	-	85.03	83.04	80.44
Mode 17	85.97	-	-	-	-	90.98	87.10	83.80
Mode 18	93.85	-	-	-	-	96.38	94.59	92.02
Mode 19	95.43	-	-	-	-	101.66	96.80	92.94
Mode 20	97.63	-	-	-	-	99.26	97.99	96.88
Mode 21	103.70	-	-	-	-	104.41	103.97	101.29
Mode 22	104.05	-	-	-	-	-	105.55	103.09
Mode 23	111.89	-	-	-	-	114.79	112.73	109.69
Mode 24	112.91	-	-	-	-	-	114.48	110.31
Mode 25	122.04	-	-	-	-	129.91	123.74	119.05
Mode 26	128.22	-	-	-	-	128.23	128.22	128.15
Mode 27	131.93	-	-	-	-	140.08	133.69	128.83
Mode 28	133.94	-	-	-	-	142.57	-	130.61
Mode 29	135.02	-	-	-	-	138.64	-	132.79
Mode 30	142.84	-	-	-	-	151.09	144.64	139.66
Mode 31	148.90	-	-	-	-	167.84	152.89	143.39
Mode 32	152.58	-	-	-	-	-	156.50	147.27
Mode 33	154.03	-	-	-	-	-	-	150.53
Mode 34	155.96	-	-	-	-	-	-	152.23
Mode 35	157.38	-	-	-	-	-	-	155.05
Mode 36	161.28	-	-	-	-	165.78	162.53	158.64
Mode 37	166.97	-	-	-	-	175.53	168.84	163.60
Mode 38	169.74	-	-	-	-	-	170.33	168.55
Mode 39	180.35	-	-	-	-	188.96	182.28	176.84
Mode 40	186.40	-	-	-	-	-	188.28	183.35

Table 3.25 The first forty mode shapes of beam 3, 20B4-25L9 model with clamped-free edge conditions



### 3.5.5 Beam 4- Arbitrary cross-section

The last assessment of higher vibration modes with cross-sectional deformations is focused on the beam 4 (arbitrary cross-section) with clamped-free edge conditions. Fig. 3.27 illustrates the first forty modes of this beam based on the 20B4-26L9 model. The ABQ shell model employed for this beam example is detailed in Table 3.26. The MAC analysis is used to compare the corresponding modes of different models based on the proposed CUF 1D method, and the corresponding natural frequencies are reported in Table 3.28. Moreover, for the sake of completeness, the comparison of ABQ shell and CUF 1D models employed for all the investigated beam structures are provided in Table 3.29.

Table 3.26 The details of ABQ shell models employed for the beam 4

Model	DOF	Number of elements	Element type	Beam axis elements	Cross-Section discretization
Shell	60498	3280	Quadratic S8R	80	41

Table 3.27 The first forty mode shapes of beam 4, 20B4-26L9 model with clamped-free edge conditions

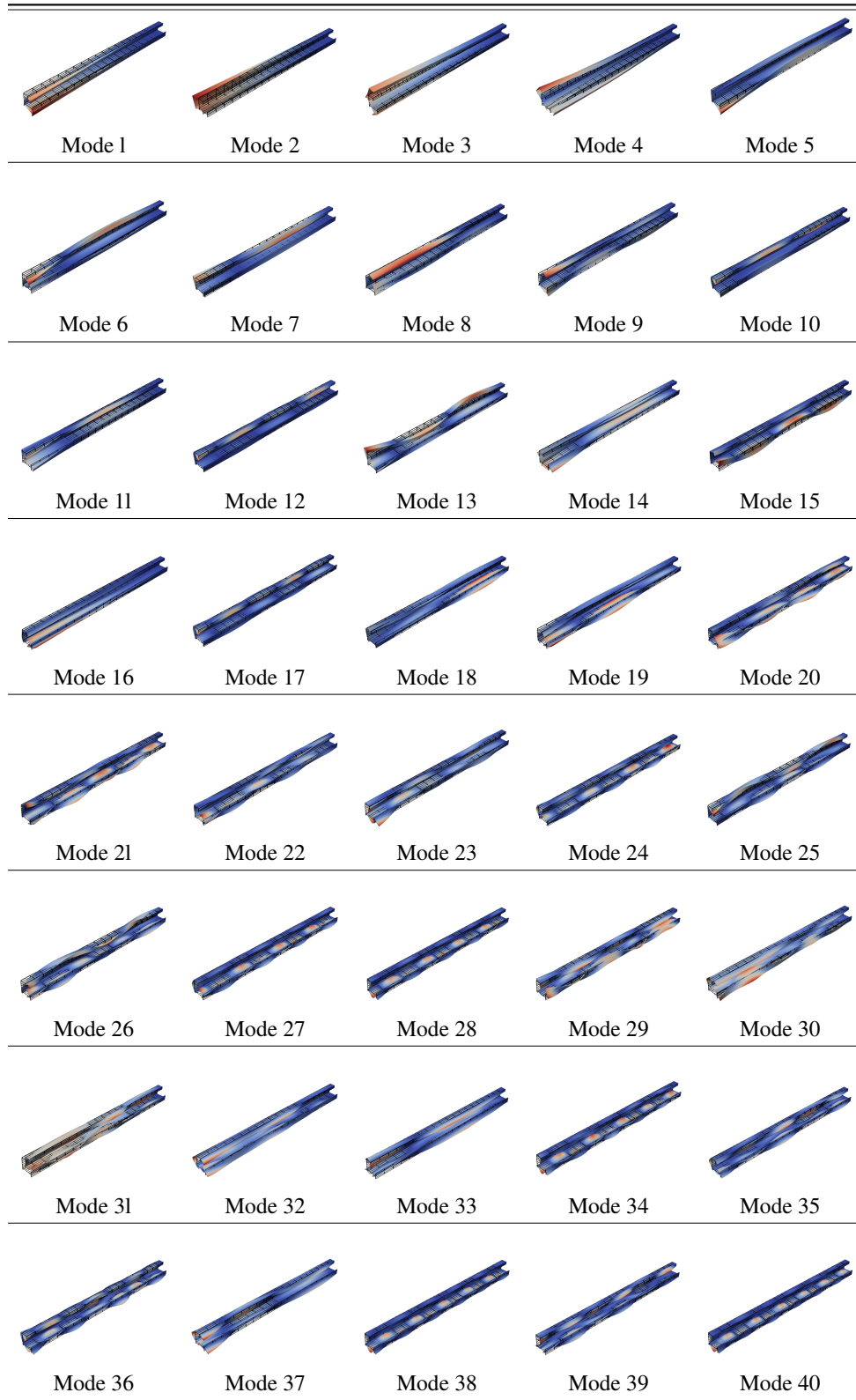


Table 3.28 Natural frequencies of beam 4 with clamped-free edge conditions based on different structural theories for the corresponding mode shapes by the MAC

Modes	20B4-26L9	20B4,TE=1	20B4,TE=2	20B4,TE=5	20B4,TE=10	20B4-13L9	20B4-17L9	ABQ shell
Mode 1	3.15	-	-	-	3.93	3.15	3.15	3.13
Mode 2	5.71	-	-	-	5.80	5.71	5.71	5.71
Mode 3	12.27	-	-	-	-	12.36	12.30	12.17
Mode 4	16.04	-	-	-	-	-	16.10	15.81
Mode 5	16.22	-	-	-	-	-	16.26	16.04
Mode 6	25.34	-	-	-	46.80	25.71	25.56	25.12
Mode 7	29.33	-	-	-	-	29.95	29.73	29.03
Mode 8	38.76	-	-	-	-	-	-	37.83
Mode 9	38.81	-	-	-	-	-	-	38.38
Mode 10	42.80	-	-	-	-	44.79	44.26	42.01
Mode 11	47.36	-	-	-	-	49.36	48.94	46.61
Mode 12	56.71	-	-	-	-	58.54	58.07	55.97
Mode 13	59.38	-	-	-	-	60.17	59.86	59.03
Mode 14	69.87	-	-	-	-	71.70	70.30	69.02
Mode 15	71.76	-	-	-	-	74.07	72.44	70.68
Mode 16	76.22	-	-	-	-	83.12	77.40	74.18
Mode 17	77.38	-	-	-	100.23	79.17	78.18	76.64
Mode 18	82.61	-	-	-	-	88.14	83.64	80.97
Mode 19	85.58	-	-	-	-	91.35	86.64	83.86
Mode 20	90.67	-	-	-	-	96.93	92.11	88.82
Mode 21	94.83	-	-	-	-	-	96.45	92.97
Mode 22	97.56	-	-	-	-	-	98.92	95.86
Mode 23	98.57	-	-	-	-	-	99.99	97.49
Mode 24	107.55	-	-	-	-	-	109.74	105.04
Mode 25	114.04	-	-	-	-	-	-	111.84
Mode 26	114.39	-	-	-	-	-	-	112.19
Mode 27	116.88	-	-	-	-	-	119.98	113.58
Mode 28	125.30	-	-	-	-	-	-	121.35
Mode 29	127.87	-	-	-	-	-	-	125.11
Mode 30	128.05	-	-	-	-	-	-	125.62
Mode 31	128.29	-	-	-	-	-	-	126.20
Mode 32	128.50	-	-	-	-	-	-	127.21
Mode 33	130.44	-	-	-	-	144.37	133.16	128.19
Mode 34	133.23	-	-	-	-	-	137.62	129.01
Mode 35	136.60	-	-	-	-	-	139.24	133.35
Mode 36	137.99	-	-	-	-	-	140.94	134.54
Mode 37	138.58	-	-	-	-	-	141.37	135.37
Mode 38	140.75	-	-	-	-	-	146.12	135.61
Mode 39	147.01	-	-	-	-	160.91	149.77	142.60
Mode 40	148.43	-	-	-	-	-	154.36	143.71

Table 3.29 The comparison of ABQ shell and CUF 1D models employed for the investigated beam structures

Model	DOF	Number of elements	Element type	Section discretization
ABQ shell-beam1	27102	1440	Quadratic S8R	18
ABQ shell-beam2	28554	1520	Quadratic S8R	19
ABQ shell-beam3	64854	3520	Quadratic S8R	42
ABQ shell-beam4	60498	3280	Quadratic S8R	41
CUF 1D-LE-beam1	15921	20B4	4-node beam	14L9
CUF 1D-LE-beam2	17019	20B4	4-node beam	15L9
CUF 1D-LE-beam3	18117	20B4	4-node beam	16L9
CUF 1D-LE-beam4	19215	20B4	4-node beam	17L9

The following comments could be made based on the mentioned results:

1. The influence of the structural theory that has been adopted is more apparent in the higher-order modes. Fig. 3.19 demonstrates, for example, how the MAC analysis reveals some discrepancies in the higher mode shapes (30-40) of the 20B4-8L9 and the 20B4-14L9 models.
2. The CUF-based method can predict the natural frequencies in good agreement with the more costly shell-2D models.
3. The acquired findings from the CUF refined models demonstrate that the suggested method accurately captures the structure's mode shapes considering the cross-sectional deformations.
4. As the complexity of the beam's cross-section is increased, the MAC analysis reveals that higher TE orders are required to accurately capture the mode shapes associated with cross-sectional deformations. For example, in the beam examples 3 and 4 with arbitrary sections, the majority of models with classical and low order TE were incapable of determining the precise mode shapes (See Tables 3.24 and 3.28)



## 3.6 Conclusions

The purpose of this chapter has been to evaluate higher-order vibration modes in a series of open-section thin-walled beams that had previously been offered as benchmark problems. CUF FEs based on the power of cross-sectional deformation coordinates ( $x, z$ ) have been implemented, as well as those based on Lagrangian polynomials. A detailed comparison has been made between the classical beam theories, refined ones based on the CUF, shell models obtained using commercial FE software, and data from the literature.

- The findings established the reliability and accuracy of the suggested CUF-based approach for the study of higher-order free vibrations in thin-walled beams with cross-sectional deformations. The natural frequencies and mode shapes found using the suggested efficient framework correlate well with those obtained using shell models, which require significantly more computational efforts.
- The importance of developing models capable of detecting cross-sectional deformations has been shown. Indeed, classical beam theories and the linear TE of order one were unable to capture a large number of cross-sectional deformations associated with bending or torsion; rather, they revealed rigid cross-section modes that did not exist in reality.
- Global vibration modes associated with stiff cross-sectional deformations, such as bending and torsion, have been determined using classical and shear refined theories. However, cross-sectional deformations have been seen at higher frequencies and have been mixed with the global modes.
- The MAC has been successfully used to compare the free vibration modes obtained by various structural theories. Additionally, the MAC analysis suggests that additional refinement is required for the TE when applied to the complicated cross-section geometries.
- It has been shown that the selected structural theory has a greater influence in higher-order modes.

# Chapter 4

## Virtual Vibration Correlation Technique for thin-walled beam structures

### 4.1 Introduction

Axial compression is frequently applied to thin-walled beam structures. Comprehensive prediction of these structures' vibration and buckling under compression is critical for secure and reliable structural engineering. The Vibration Correlation Technique (VCT) [114] was established as a non-destructive method for evaluating the buckling loads of structures subjected to progressive compressive loads. According to the VCT, compressive loads reduce the structure's natural frequencies. By assuming that the vibration modes are analogous to those associated with buckling, the critical buckling load may be extrapolated as the load that results in zero natural frequency [115]. Abramovich [116] conducted a comprehensive study of the literature on the applicability of the VCT for buckling load prediction in different structures such as columns, beams, plates, panels, and cylindrical shells.

In the case of small displacements and linear buckling, the tangent stiffness can be approximated as the sum of the linear stiffness ( $\mathbf{K}_0$ ) and the geometric stiffness ( $\mathbf{K}_\sigma$ ) contribution [115]:

$$\mathbf{K}_T \simeq \mathbf{K}_0 + \mathbf{K}_\sigma \quad (4.1)$$

Afterwards, by considering harmonic motion around quasi-static equilibrium states, the eigenvalues problem can be solved as follows:

$$(-\omega_k^2 \mathbf{M} + \mathbf{K}_T) \mathbf{u}_k = 0 \quad (4.2)$$

where  $\omega_k$  are the natural frequencies, and  $\mathbf{u}_k$  is the  $k$  th eigenvector.

The vibration and buckling of beam structures under compression have been assessed by many researchers [117–120]. By employing exact solutions, Prokic and Lukić [121] studied the flexure-torsion coupled vibrations of axially loaded thin-walled beams. Abramovich [122] investigated the natural frequencies in the Timoshenko beams under axial loads. Carpinteri et al. [123] analyzed the evolution of fundamental frequency in slender beams under axial displacements. Double-beam systems under compressive axial loads were focused in some research papers [124, 125]. Considering the warping effects, Piana et al. [126] conducted a study on the thin-walled beams with symmetric cross-sections. Zmuda [127] proposed a numerical method for axially-loaded cold-formed lipped channel section beams. Aquaro [128] investigated the torsional instabilities of thin-walled beams with stiffeners. By employing the CUF, Pagani et al. [129] studied the use of VCT for the geometrically nonlinear analysis of beam structures. A one-dimensional FE model for the forced nonlinear vibrations of thin-walled beams with open variable cross-sections was proposed by Elkaimbillah et al. [130].

Designers and researchers have always been concerned with accurately predicting the mechanical behavior of composite materials [131, 132]. As a result, in order to accurately model these structures, the use of refined FE models is necessary. Free vibration response of composite beam structures has been analyzed by many researchers [133–137]. Librescu [138] proposed a dynamic solution for composite beams with arbitrary cross-sections. The review of the buckling and free vibration of composite beams was presented in [139]. Karama et al. [140] employed discrete layer theory for the buckling and free vibration of composite beams. Khdeir and Reddy [141, 142] derived exact solutions for bending and buckling of laminated beams. Piovan [143] presented exact analytical solutions for the free vibration response of composite beams with shear flexibility. Cortínez and Piovan [144] developed a theoretical model incorporating shear flexibility and state of initial stresses for the vibration of thin-walled composite beams. The GBT was efficiently used for the vibration analysis of thin-walled composite structures [145, 146]. Sheikh

et al. [147] investigated the free vibration response of thin-walled composite beams based on the modeling technique for the transverse shear deformation and out of plane warping. Jun et al. [148–150] employed the dynamic stiffness method to analyze the free vibration response of composite beams under axial loads. Banerjee [151] developed the dynamic stiffness method for the free vibration analysis of composite Timoshenko beams under axial loads. By using shear deformation theory, Vo and Thai [152] analyzed the free vibration response of rectangular composite beams subjected to axial loads.

Thin-walled composite beams subjected to axial loads have been further investigated in [153, 154]. Vo and Lee [155] worked on 1D FE models to analyze the free vibration response of thin-walled composite box beams under axial loads. In this regard, they used the classical lamination theory accounting for structural couplings from material anisotropy. The same authors also developed a seven DOF FE model in order to evaluate the vibration and buckling of thin-walled composite beams with I-shaped cross-section [156, 157]. Kim et al. [158] employed the dynamic stiffness matrix for spatially coupled free vibration analysis of thin-walled composite beams. Some analytical models have been developed to investigate the buckling and vibration of thin-walled composite box beams considering the coupling of flexural and torsional modes [159–162].

This chapter is focused on the thin-walled isotropic and composite beam structures subjected to axial loads. For thin-walled beams with various cross-sections, an advanced refined FE based on the CUF is developed. The variations of natural frequencies under axial loads are studied using the VCT. A thorough comparison of the results with the implemented shell models and the available literature is presented in order to assess the suggested method's accuracy and efficiency. The necessity of employing refined FE models capable of accurately detecting cross-sectional deformations is highlighted. Additionally, the CUF 1D with LE is utilized to solve a more complicated structural problem of a channel-shaped composite beam with different number of transverse stiffeners that is subjected to compressive loads. It is demonstrated that the presented method can be used efficiently, and match well with the shell models, which are significantly more expensive in terms of computational cost.

## 4.2 Cruciform isotropic beam

Consider the first beam, which has a cruciform cross-section, and the length of 670 mm [97]. The beam is doubly clamped in such a way that except for the vertical displacements of the top edge of the beam along the beam axis ( $y$  direction), all translations and rotations of the beam cross-section are constrained. Refer to Fig. 4.1 for a schematic representation of this cruciform beam. It should be noted that all of the measurements in this figure are in mm. As seen in this figure, the thickness of the beam is 1.1 mm in thickness. When modeling this cruciform beam, the isotropic material characteristics of Table 4.1 are taken into consideration.

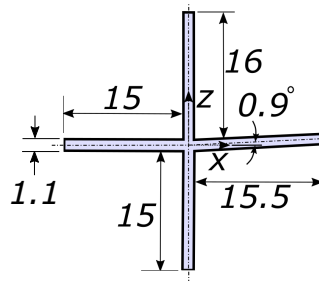


Fig. 4.1 Schematic view of the cruciform beam with the length of 670 mm

Table 4.1 Isotropic material properties of the cruciform beam

Material property	Value
Young's modulus	$E = 70 \text{ GPa}$
Poisson's ratio	$\nu = 0.3$
Density	$\rho = 2600 \frac{\text{kg}}{\text{m}^3}$

Table 4.2 shows the first ten cruciform beam vibration mode shapes according to the model with 105 Lagrange points and 20B4 elements. There are four different bending modes that may be observed in this table: the second, third, seventh, and eighth mode shapes, which respectively occur in the frequencies of 264.15, 270.47, 712.20, and 728.88 Hz. In Table. 4.3, the middle cross-sectional view of the first ten vibration mode shapes in the cruciform beam based on the model with 117 Lagrange points and 20B4 elements is shown. Because of the importance of cross-sectional deformations, it is necessary to employ structural theories that can correctly assess

such deformations. Table. 4.4 illustrates the first ten buckling modes and their associated critical axial displacements for the cruciform beam using a model with 105 Lagrange points and 20B4 elements. As the table indicates, the first buckling and vibration modes are analogous.

The first ten natural frequencies of an unloaded cruciform beam are evaluated in Table 4.5 using CUF 1D models and the available literature. The number of beam elements, Lagrange points, and DOF for various CUF 1D models are listed in this table using the TE and LE functions. The values of natural frequencies obtained from the existing literature [97] by utilizing experimental methods and three numerical approaches based on the thin shell, thick shell, and solid brick elements are provided in Table 4.5. The results demonstrate that the natural frequencies acquired by the CUF 1D with 20B4 and at least 57 Lagrange points are in good agreement with the values reported by the literature. This indicates the ability of cost-effective CUF 1D models to identify vibration modes and cross-sectional deformations in an open cross-section thin-walled beam. Note that the PZT pickups are used for the experimental natural frequencies of Ref. [97].

Table 4.2 The first ten vibration mode shapes of the cruciform beam based on the model with 105 Lagrange points and 20B4 elements

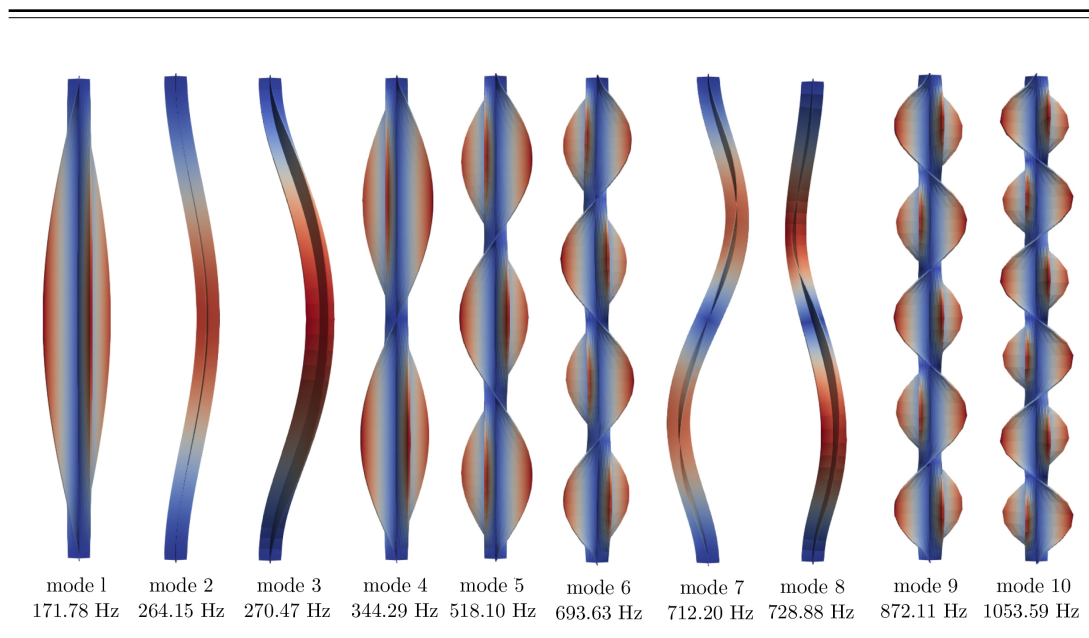
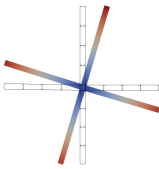
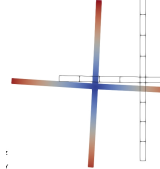
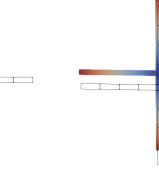
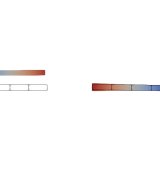
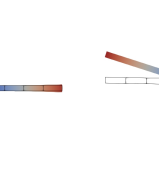
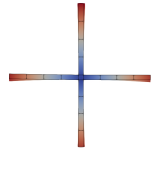
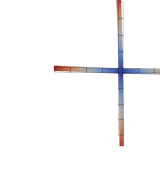
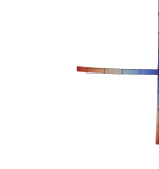
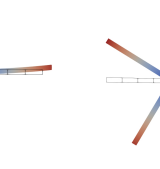
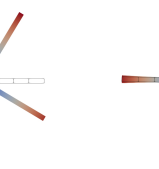


Table 4.3 Middle cross-sectional view of the first ten vibration mode shapes in the cruciform beam based on the model with 105 Lagrange points and 20B4 elements

---

---

				
mode 1 171.78 Hz	mode 2 264.15 Hz	mode 3 270.47 Hz	mode 4 344.29 Hz	mode 5 518.10 Hz
				
mode 6 693.63 Hz	mode 7 712.20 Hz	mode 8 728.88 Hz	mode 9 872.11 Hz	mode 10 1053.59 Hz

---

---

Table 4.4 The first ten buckling modes and the corresponding critical axial displacements of the cruciform beam based on the model with 105 Lagrange points and 20B4 elements

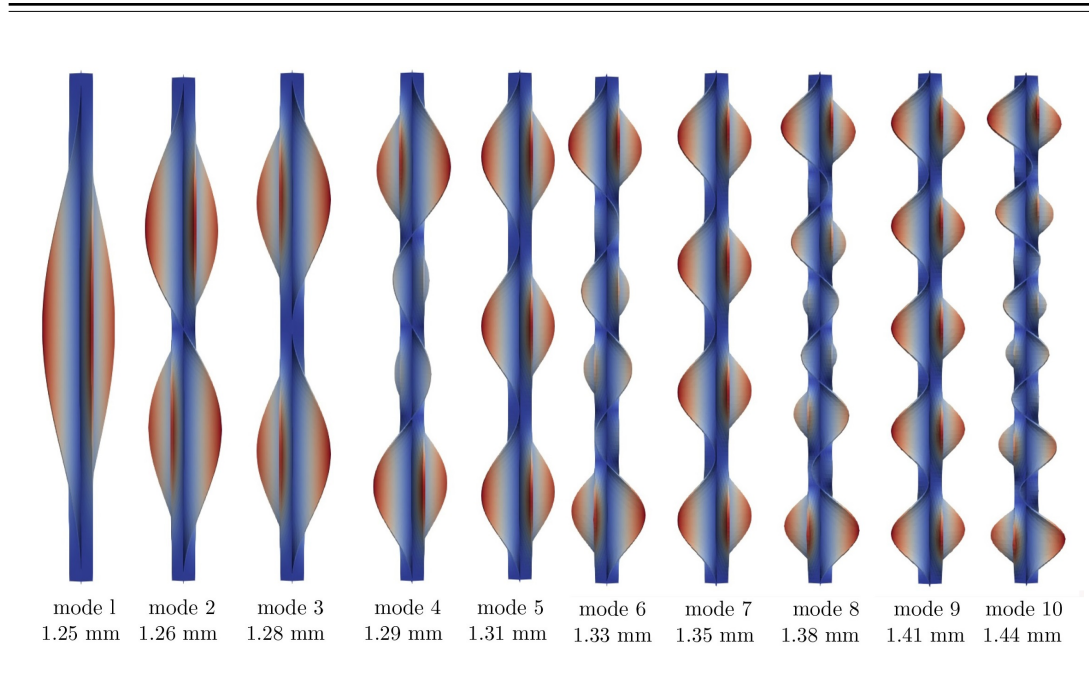


Table 4.5 The first nine natural frequencies of the unloaded cruciform beam based on the CUF 1D models and the literature

Model	Beam elements	Lag. Points	DOF	Buck. load	Natural Frequency (Hz)								
					Mode 1	Mode 2	Mode 3	Mode 4	Mode 5	Mode 6	Mode 7	Mode 8	Mode 9
Lag.(25L9)	5B4	153	7344	5.07	175.77	267.19	273.56	352.38	531.41	714.84	721.24	737.90	915.89
Lag.(25L9)	10B4	153	14229	8.45	172.27	265.07	271.40	345.26	519.57	695.75	714.49	731.24	875.24
Tay. order 1	20B4	-	549	8.94	265.09	271.68	724.47	742.17	1437.72	1404.21	2288.81	2341.88	2401.44
Tay. order 2	20B4	-	1098	9.05	273.12	266.51	728.32	746.05	1411.60	1445.13	2300.75	2353.79	2400.70
Tay. order 10	20B4	-	12078	8.82	264.20	270.96	326.25	648.65	717.66	733.41	970.92	1288.23	1367.62
Lag.(5L9)	20B4	33	6039	8.81	176.13	264.35	270.66	353.01	531.17	730.94	715.03	710.24	893.86
Lag.(9L9)	20B4	57	10431	8.76	173.65	264.22	270.53	348.04	523.73	701.02	712.89	729.46	881.52
Lag.(17L9)	20B4	105	19215	8.68	171.78	264.16	270.47	344.30	518.11	693.63	712.20	728.89	872.11
Lag.(25L9)	20B4	153	27999	8.65	171.06	264.14	270.45	342.85	515.95	690.78	712.01	728.72	868.52
Thin shell [97]					165.54	278.43	284.99	331.75	499.22	668.52	749.31	766.7	840.35
Thick shell [97]					163.86	278.43	284.99	328.4	494.22	661.87	749.32	766.71	832.09
Solid brick [97]					160.91	270.75	281.59	329.69	484.58	676.69	749.29	765.76	816.26
Experiment [97]					161.87	275.47	284.18	325.43	486.13	667.84	741.30	767.53	813.39



The given values in Table 4.5 should be interpreted in view of the fact that many of the mode shapes derived from various structural theories do not correlate to one another. As a result, the MAC analysis needs to be conducted in order to explore the corresponding modes of each model. As explained in the previous chapter, the MAC is defined as a scalar that indicates the degree of consistency between two separate modal vectors in such a manner that the values change from 0 to 1. The MAC value of zero indicates that there is no correspondence between the models. In Fig. 4.2, the free vibration modes for cruciform beams with 20B4 elements based on various structural theories are compared to the Lagrange model with 153 points using the MAC analysis. As this figure indicates, the number of corresponding modes for classical models such as Taylor order one is fewer than those of other Lagrange models. Indeed, classical beam theories obliterate several modes in favor of rigid cross-section modes that do not exist. The four black squares in Fig. 4.2a indicate that the Taylor modes 2, 3, 4, and 9 correspond to the Lagrange modes 3, 7, 8, and 1, respectively. Table 4.6 illustrates these mode shapes for the Taylor order 1 model and the Lagrange model with 153 points. It is worth noting that, although some modes may correspond to one another according to the MAC analysis, the values of natural frequencies calculated using the two models may exhibit major differences. For example, in Table 4.6, the two torsional modes of Taylor mode 9 and Lagrange mode 1 are corresponded, despite the fact that the natural frequencies derived by these two models are different. The necessity of selecting a structural theory capable of accurately identifying the structural problem's eigenvalues and eigenvectors should be emphasized.

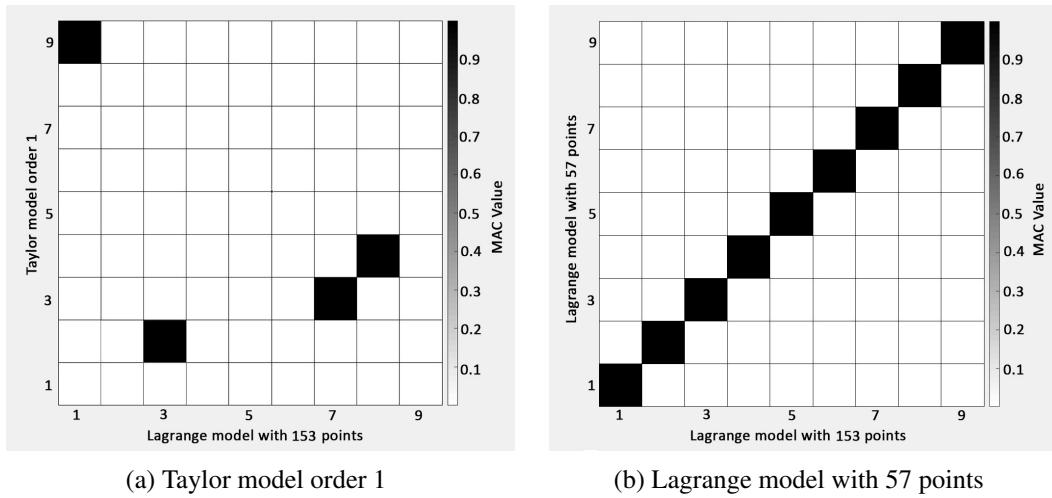


Fig. 4.2 The MAC analysis for the comparison of free vibration mode shapes of the cruciform beams with 20B4 elements

Table 4.6 The corresponding vibration mode shapes of the cruciform beam obtained by the MAC for the Taylor model order 1 and Lagrange model with 153 points (See Fig 4.2a)

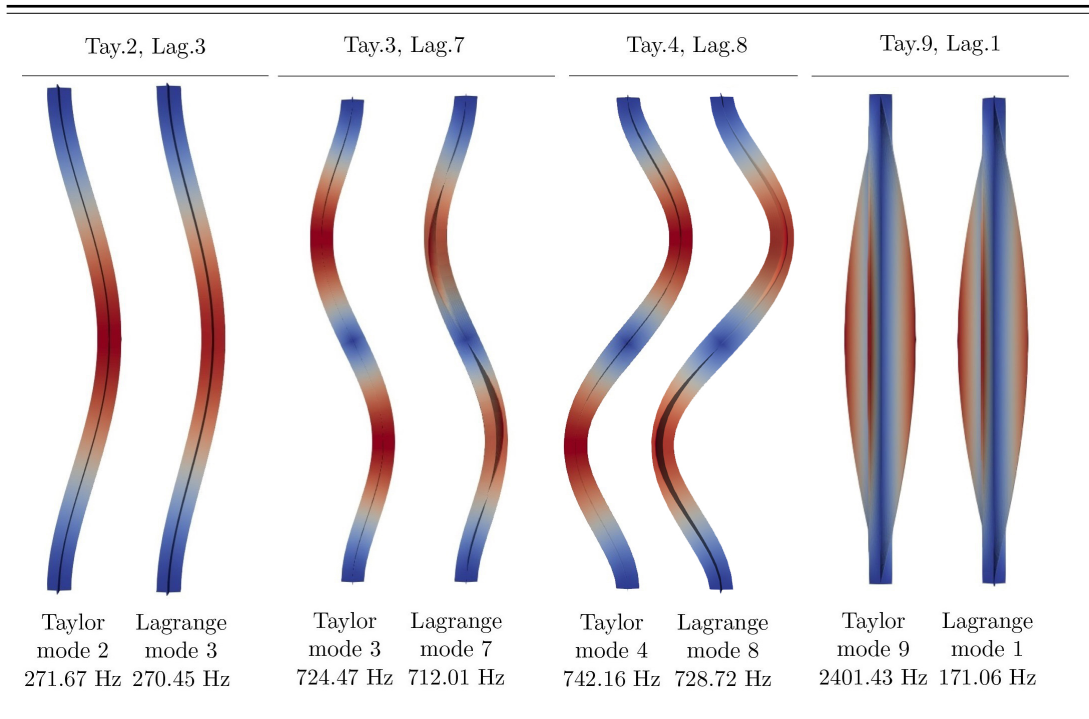


Fig. 4.3 compares the first five natural frequencies in the cruciform beam under progressive compressive loads based on the CUF model with 153 Lagrange points

and Ref. [97]. As can be seen in the graph, the natural frequencies of the beam structure are decreased as a result of the compressive loads. This is due to the reduction in the stiffness of the beam structure caused by the compressive loads. Notably, the natural frequencies derived by the efficient CUF 1D models given here are consistent with the experimental findings reported in Ref. [97]. Using the CUF 1D model with 153 Lagrange points, the fundamental frequencies in the cruciform beam under progressive compressive loads are reported in Table 4.7, where the first two columns show the fundamental frequencies obtained by the Laser and PZT sensors for the experimental method in [97].

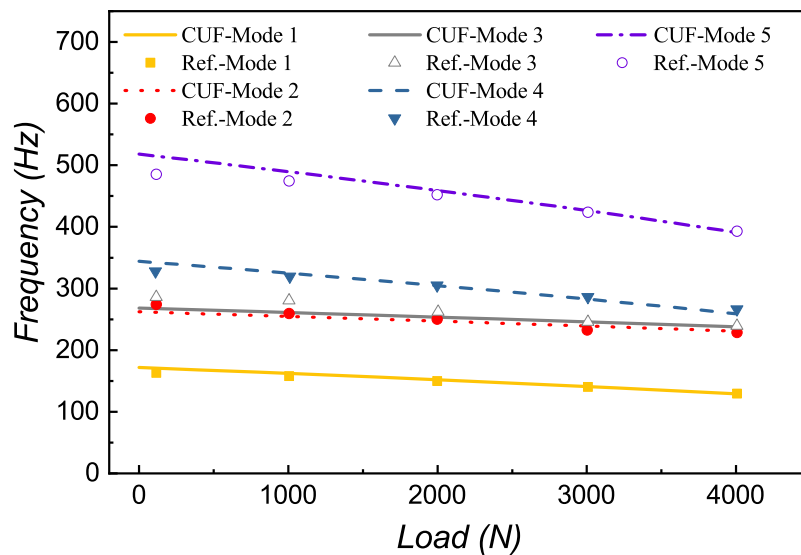


Fig. 4.3 The comparison of the first five natural frequencies in the cruciform beam under progressive compressive loads based on the CUF model with 105 Lagrange points and the available literature [97]

Table 4.7 Evaluation of fundamental frequencies in the cruciform beam under progressive compressive loads based on the CUF 1D model with 105 Lagrange points and the literature

Load (KN)	Frequency (Hz)-Laser [97]	Frequency (Hz)-PZT [97]	Frequency (Hz)-CUF 1D
0.00	161.73	161.87	171.78
0.24	156.88	159.12	171.08
0.49	154.08	156.42	168.27
1.00	150.04	151.69	162.55
1.41	146.60	149.22	157.95
2.02	142.44	145.42	151.10
2.46	139.60	142.33	146.16
2.98	135.94	138.24	140.32
3.43	132.33	134.61	135.27
3.95	130.96	131.33	129.43

In Fig. 4.4, the first five natural frequencies in the cruciform beam under progressive compressive loads are compared using the CUF model with 105 Lagrange points and Taylor model order 1. As indicated in this figure, the influence of compressive loads on the natural frequency variations is more apparent when refined theories based on LE are used. Additionally, it should be emphasized that certain modes are ignored by classical models; for example, the Taylor order 1 model does not identify the first torsional mode.

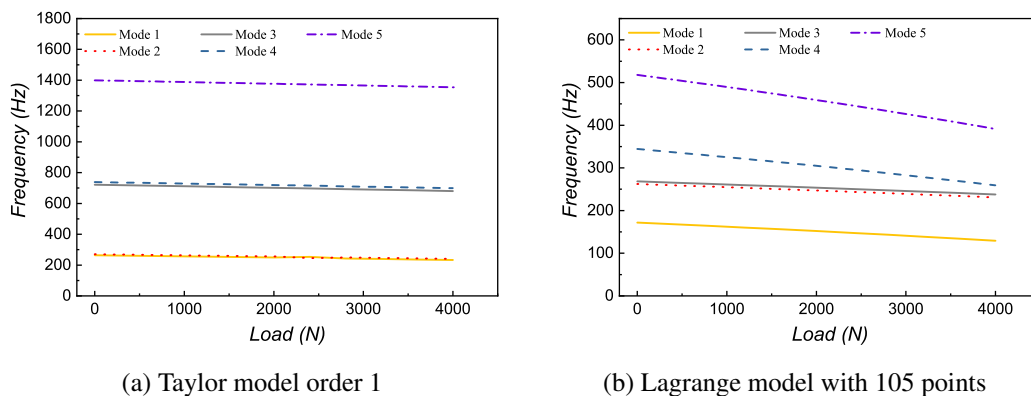


Fig. 4.4 The comparison of the first five natural frequencies in the cruciform beam under progressive compressive loads based on the Taylor model order 1 and CUF model with 105 Lagrange points

In Fig. 4.5, the effects of structural theory and FE discretization on the fundamental frequencies of the cruciform beam subjected to progressive compressive loads are studied. In this figure, the values of the fundamental frequency are displayed against the applied compressive stresses. As can be clearly seen, all of the provided Lagrange models exhibit good convergence except for the model with just five B4 elements. The critical buckling loads and fundamental frequencies related to the applied progressive compressive loads in the cruciform beam are shown in Fig. 4.6 using CUF 1D models. The CUF 1D results indicate that the critical buckling load and natural frequency variations with progressive loads are in agreement with the existing literature [97], and that the suggested approach can be utilized effectively to explore the natural frequencies of loaded beams under compression.

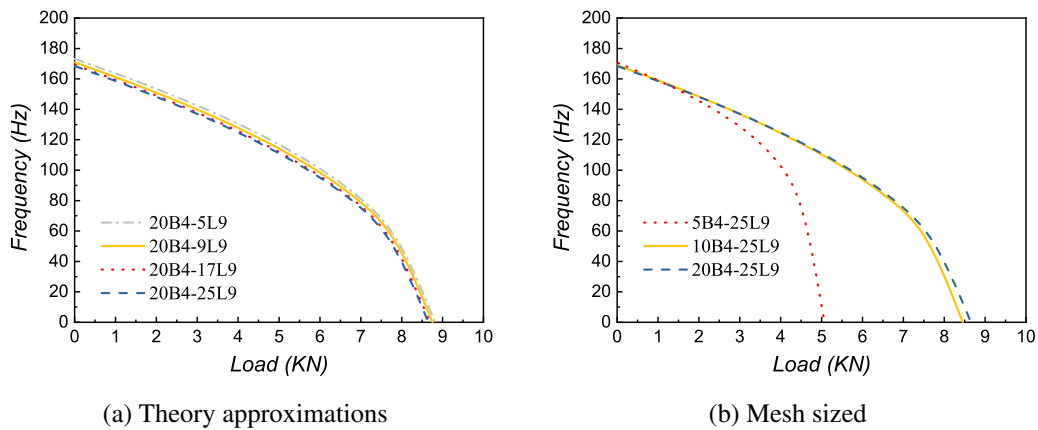


Fig. 4.5 The variations of fundamental frequencies in the cruciform beam under progressive compressive loads based on the different CUF 1D models (a) effect of the structural theory (b) effect of FE discretization

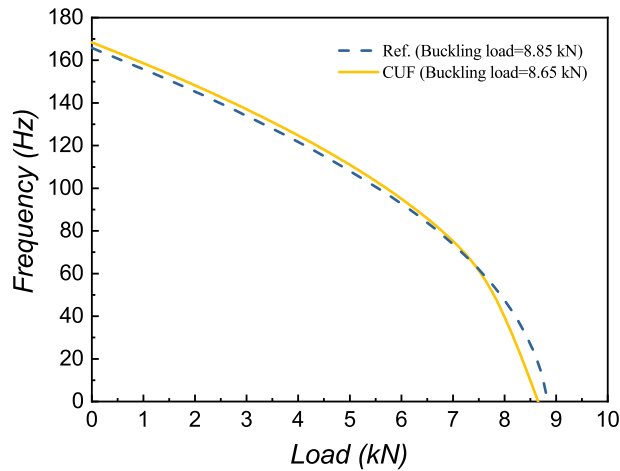


Fig. 4.6 Critical buckling loads and the fundamental frequencies versus the applied progressive compressive loads in the cruciform beam according to the Ref. [97] and the CUF 1D model

### 4.3 Thin cruciform isotropic beam

A thinner cruciform beam with a thickness of 0.2 mm is assumed here. The length of the beam is 670 mm, and the boundary conditions are doubly clamped except for the vertical displacements of the top edge (similar to the previous beam example). In Fig. 4.7, the schematic view of this thin cruciform beam is indicated (dimensions in mm). Table 4.1 lists the isotropic material properties of this beam example.

Table 4.8 depicts the first ten vibration mode shapes of the thin cruciform beam based on the model with 105 Lagrange points and 20B4 elements. A further illustration is provided in Table 4.9, which shows the middle cross-sectional view of the first ten vibration mode shapes in the thin cruciform beam obtained by employing a model with 105 Lagrange points and 20B4 elements. As can be seen in Table 4.8, the first seven modes for the thin cruciform beam are torsional, and then two bending modes, mode numbers 8 and 9, occur at frequencies of 250.00 and 256.39 Hz, respectively. When comparing Tables 4.2 and 4.8, it can be seen that for this beam with a thinner cross-section, the torsional modes with cross-sectional deformations occur before the other bending modes.

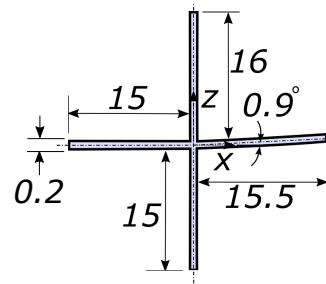


Fig. 4.7 Schematic view of the thin cruciform beam

Table 4.8 The first ten vibration mode shapes of thin cruciform beam based on the model with 105 Lagrange points and 20B4 elements (See table 4.2 for comparison)

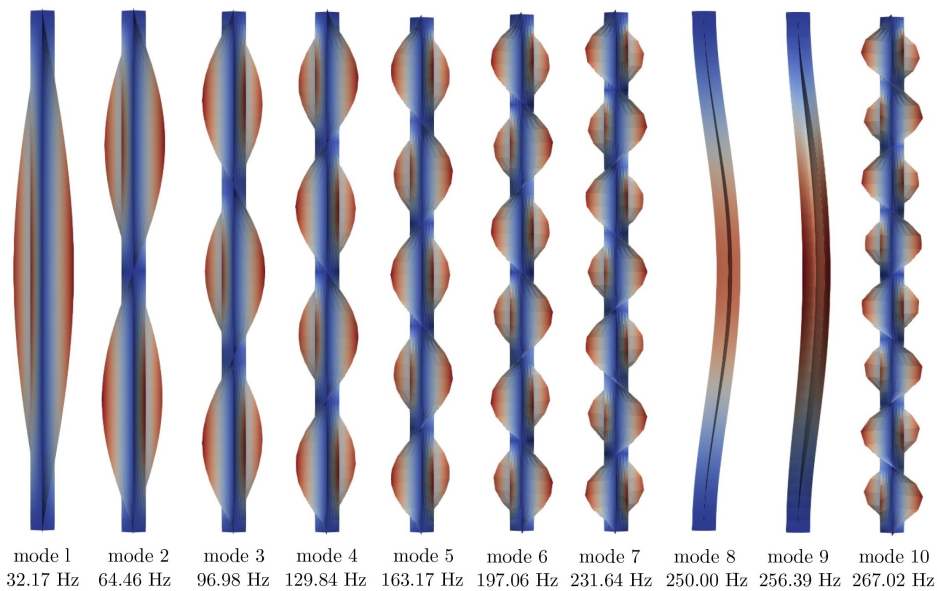
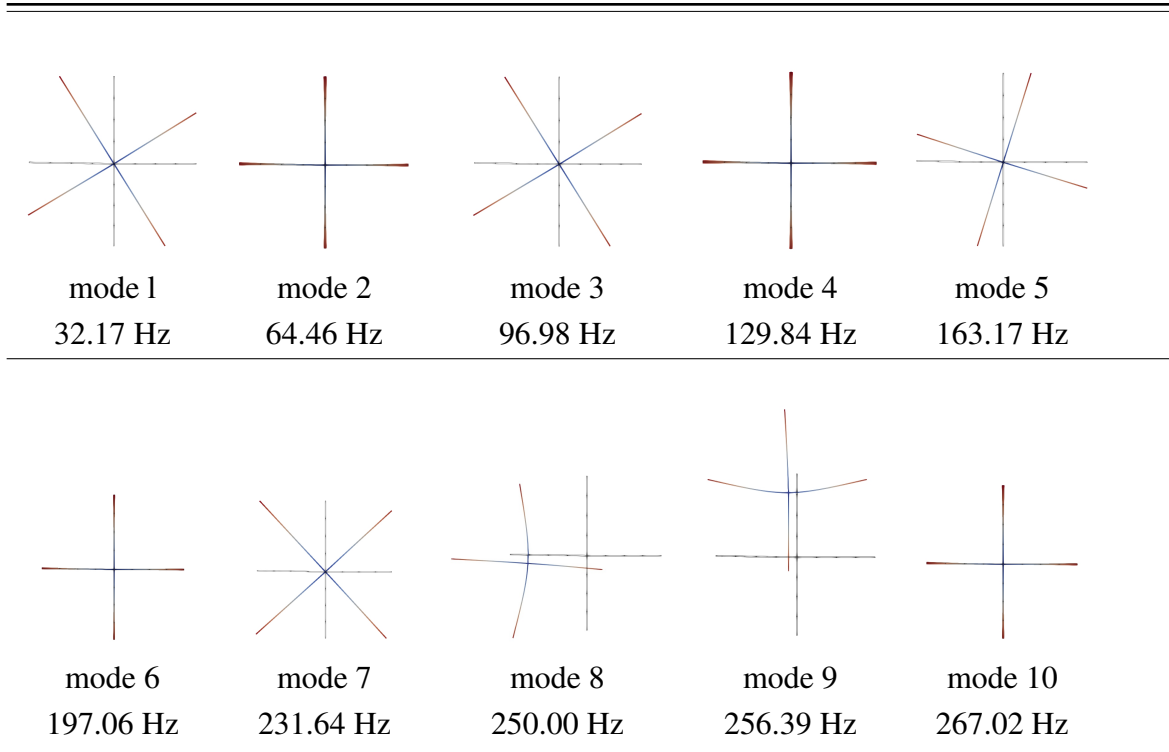


Table 4.9 Middle cross-sectional view of the first ten vibration mode shapes in the thin cruciform beam based on the model with 105 Lagrange points and 20B4 elements



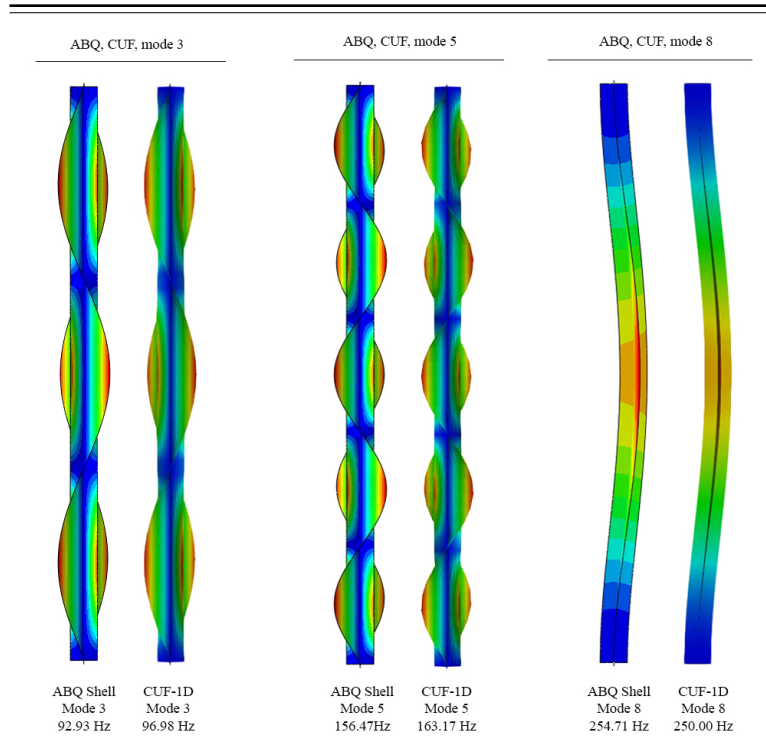
The first nine natural frequencies of the unloaded thin cruciform beam are compared in Table 4.10 using the CUF 1D Lagrange model and the thin ABQ shell model. Additionally, Table 4.11 illustrates the corresponding free vibration mode shapes. Not only the mode shapes, but also the natural frequencies obtained using the CUF 1D Lagrange model agree well with those found using the thin ABQ shell model. In comparison with costly shell models, the CUF has much fewer DOF and uses significantly less processing power.

Table 4.10 The first nine natural frequencies of the unloaded thin cruciform beam based on the CUF 1D Lagrange model and the thin ABQ shell model

Model	Number of elements	Lag. Points	DOF	Natural Frequency (Hz)								
				Mode 1	Mode 2	Mode 3	Mode 4	Mode 5	Mode 6	Mode 7	Mode 8	Mode 9
CUF 1D (Lag.)	20 B4	105	19215	32.17	64.46	96.98	129.84	163.17	197.06	231.64	250.00	256.39
Thin ABQ shell	1680 S8R	-	52396	30.82	61.76	92.93	124.47	156.47	189.05	222.32	254.71	261.08



Table 4.11 The comparison of free vibration mode shapes of the thin cruciform beam based on the CUF 1D Lagrange model and the thin ABQ shell model



The MAC analysis is used to compare the free vibration modes of thin cruciform beams with 20B4 elements based on various structural theories against the model with 153 Lagrange points. As can be seen in Fig. 4.8, the number of comparable modes for classical models such as Taylor order 1 is much fewer than that of other Lagrange models. Additionally, it is noted that for the cruciform beam with a thinner cross-section, the need to use refined theories is considerable. The first five natural frequencies in a thin cruciform beam subjected to progressive compressive loads are compared in Fig. 4.9 using the CUF model with 105 Lagrange points and Taylor model order 1. As indicated in this figure, the influence of compressive loads on natural frequency variations is more apparent when refined theories based on LE are used. Additionally, one may see how the classical theories do not identify the majority of the first seven torsional modes.

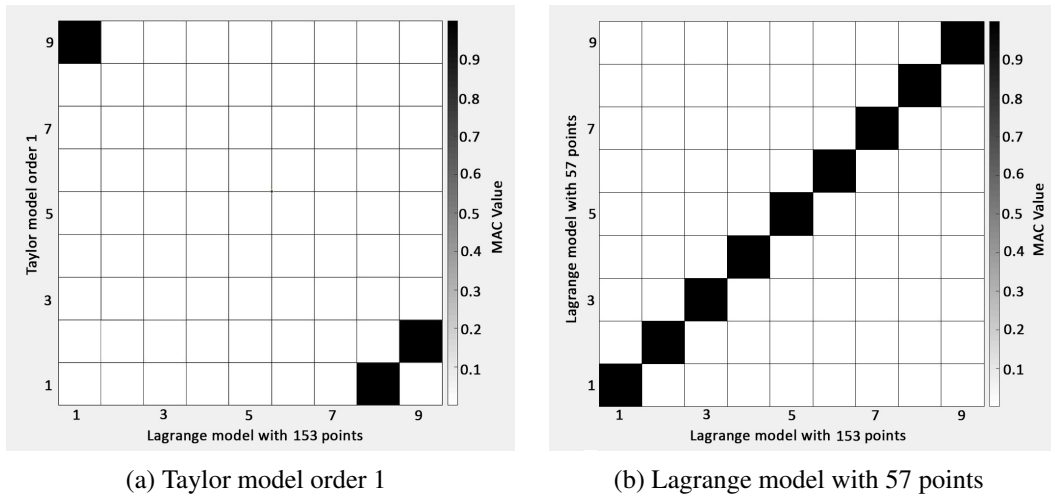


Fig. 4.8 The comparison of free vibration modes using the MAC analysis for the cruciform beams with 20B4 elements based on different structural theories versus the Lagrange model with 153 points

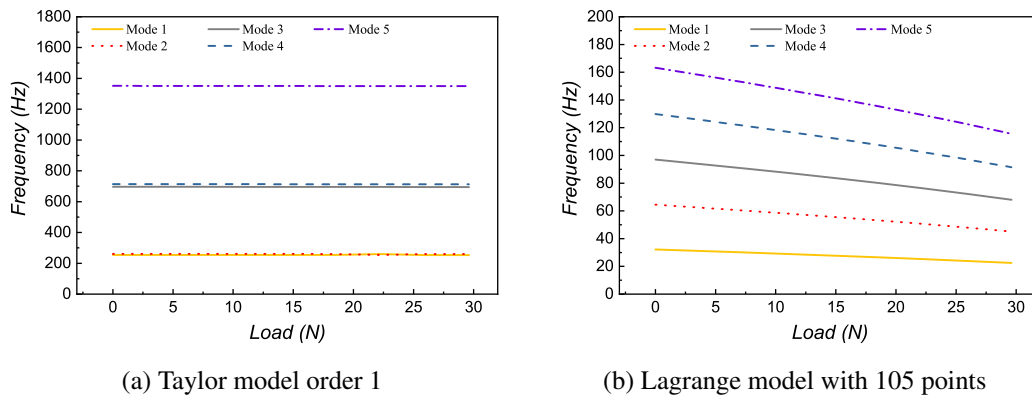


Fig. 4.9 The comparison of the first five natural frequencies in the thin cruciform beam under progressive compressive loads based on the Taylor model order 1 and CUF model with 105 Lagrange points

#### 4.4 Arbitrary cross-section isotropic beam (I)

The third beam problem of this chapter corresponds to an arbitrary cross-section beam with a length of 950 mm [119]. For this doubly clamped beam, all the translations and rotations are restrained for the bottom and top edges of the beam cross-section except for the vertical displacements of the top edge along the beam

axis. The schematic view of this beam is shown in Fig. 4.10 (dimensions in mm). The isotropic material properties of Table 4.12 are assumed for this beam example.

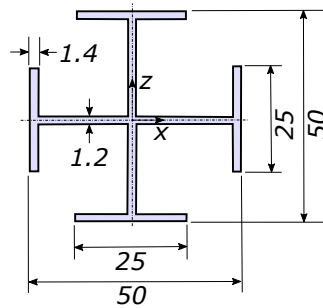


Fig. 4.10 Schematic view of the arbitrary cross-section beam (I)

Table 4.12 Isotropic material properties of the arbitrary cross-section beam (I)

Material property	Value
Young's modulus	$E = 69 \text{ GPa}$
Poisson's ratio	$\nu = 0.3$
Density	$\rho = 2600 \frac{\text{kg}}{\text{m}^3}$

Table 4.13 shows the first ten vibration mode shapes of the arbitrary cross-section beam (I) according to the model with 129 Lagrange points and 20B4 elements. The middle cross-sectional views of the first ten vibration mode shapes in this beam are provided in Table 4.14. Note that the obtained results are based on the model with 129 Lagrange points and 20B4 elements. The first ten buckling modes and associated critical axial displacements of the arbitrary cross-section beam (I) are shown in Table 4.15 using the model with 129 Lagrange points and 20B4 elements. As can be seen in this table, the first buckling and vibration modes are identical.

In Fig. 4.11, the first five natural frequencies in the arbitrary cross-section beam (I) subjected to progressive compressive loads are compared using the CUF model with 129 Lagrange points and Ref. [119]. The exhibited values in this figure demonstrate that compressive loads reduce natural frequencies, and their values agree well with the experimental data reported in Ref.[119]. The first three frequencies in the arbitrary cross-section beam (I) subjected to progressive compressive loads are

presented in Table 4.16 using the CUF 1D model with 129 Lagrange points and Ref. [119].

Table 4.13 The first ten vibration mode shapes of the arbitrary cross-section beam (I) based on the model with 129 Lagrange points and 20B4 elements

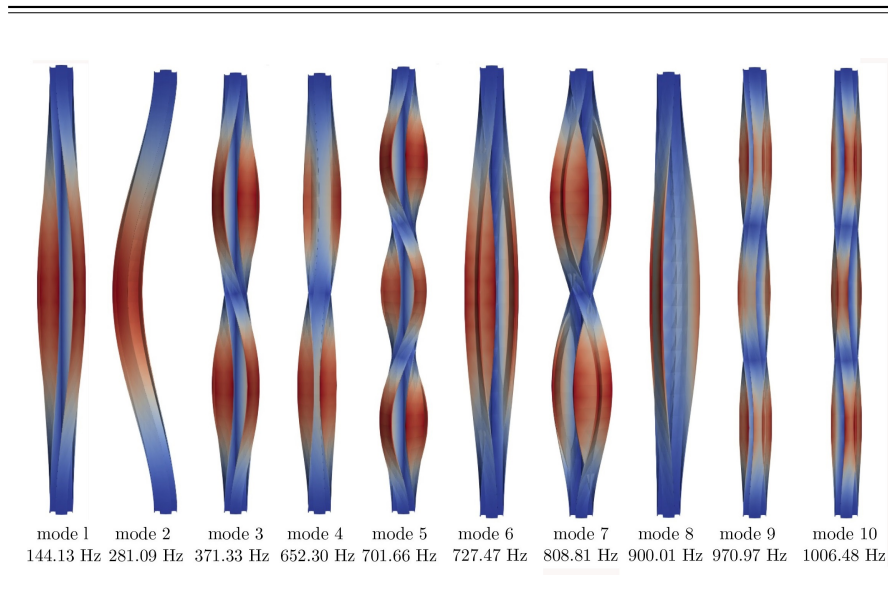


Table 4.14 Middle cross-sectional view of the first ten vibration mode shapes in the arbitrary cross-section beam (I) based on the model with 129 Lagrange points and 20B4 elements

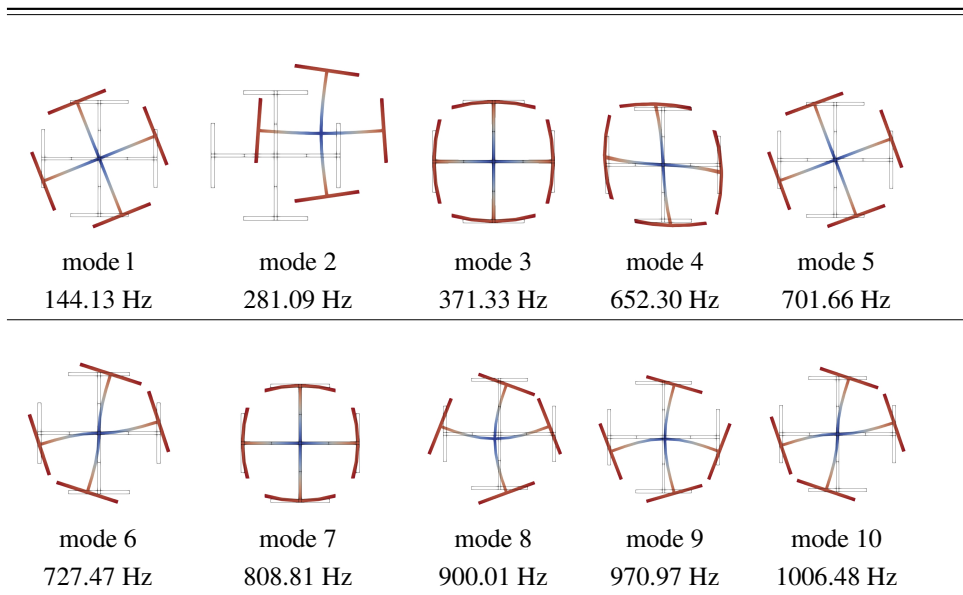


Table 4.15 The first ten buckling modes and the corresponding critical axial displacements of the arbitrary cross-section beam (I) based on the model with 129 Lagrange points and 20B4 elements

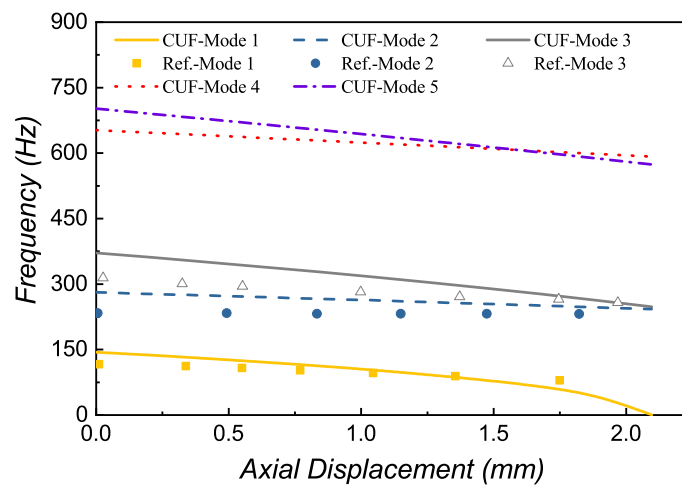
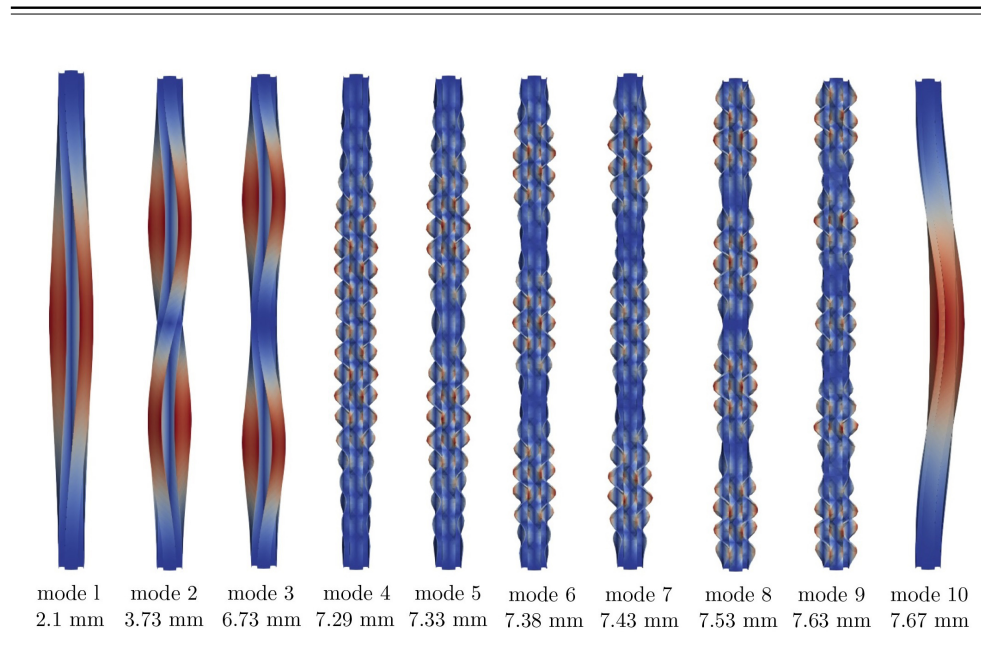


Fig. 4.11 The comparison of the first five natural frequencies of the arbitrary cross-section beam (I) under progressive compressive loads based on the CUF model with 129 Lagrange points and the available literature [119]

Table 4.16 The variations of frequencies versus the applied axial displacements in the arbitrary cross-section beam (I) under progressive compressive loads based on the CUF 1D models and Ref. [119]

Axial Displacement (mm)	Frequency (Hz)- CUF			Frequency (Hz)-Ref. [119]		
	Mode 1	Mode 2	Mode 3	Mode 1	Mode 2	Mode 3
0.25	134.91	275.74	359.76	113.61	233.14	302.96
0.50	125.44	272.19	346.75	108.88	233.14	295.86
0.75	115.98	267.46	332.54	102.96	231.95	288.76
1.00	104.14	262.72	318.34	97.04	231.95	281.66
1.25	92.31	259.17	304.14	91.12	231.95	273.37
1.50	76.92	253.25	288.76	85.21	231.95	268.64
1.75	60.36	249.70	272.19	79.29	231.95	265.09

## 4.5 Arbitrary cross-section isotropic beam (II)

For this assessment case, the beam has an arbitrary cross-section, as shown in Fig. 4.12, and the length of 9 m [127]. Similar to the previous examples of this chapter, the beam is doubly clamped. The isotropic material properties of Table 4.17 are assumed for this beam example.

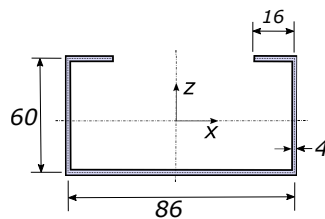


Fig. 4.12 Schematic view of the arbitrary cross-section beam (II)

Table 4.17 Isotropic material properties of the arbitrary cross-section beam (II)

Material property	Value
Young's modulus	$E = 210 \text{ GPa}$
Poisson's ratio	$\nu = 0.3$
Density	$\rho = 7850 \frac{\text{kg}}{\text{m}^3}$

The first ten vibration mode shapes of the arbitrary cross-section beam (II) are provided in Table 4.18 according to the model with 117 Lagrange points and 20B4 elements. The middle cross-sectional view of the first ten vibration mode shapes in this beam is given in Table 4.19. In Fig. 4.13, the first five natural frequencies in the arbitrary cross-section beam (II) under progressive compressive loads are compared using the CUF model with 117 Lagrange points and numerical data from the literature. The figure demonstrates that the results obtained using the suggested efficient CUF 1D models match well with those obtained using the costly shell models in Ref. [127]. The values of the first three frequencies in the arbitrary cross-section beam (II) under progressive compressive loads are provided in Table 4.20 by employing the CUF 1D model with 117 Lagrange points and Ref. [127].

Table 4.18 The first ten vibration mode shapes of the arbitrary cross-section beam (II) based on the model with 117 Lagrange points and 20B4 elements

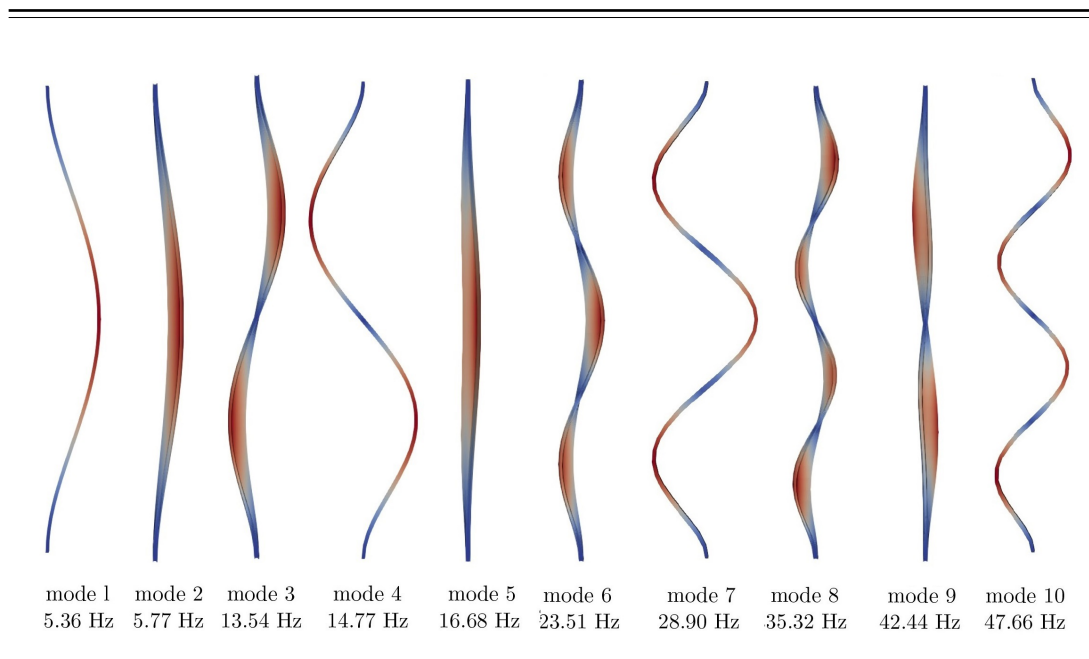


Table 4.19 Middle cross-sectional view of the first ten vibration mode shapes in the arbitrary cross-section beam (II) based on the model with 117 Lagrange points and 20B4 elements

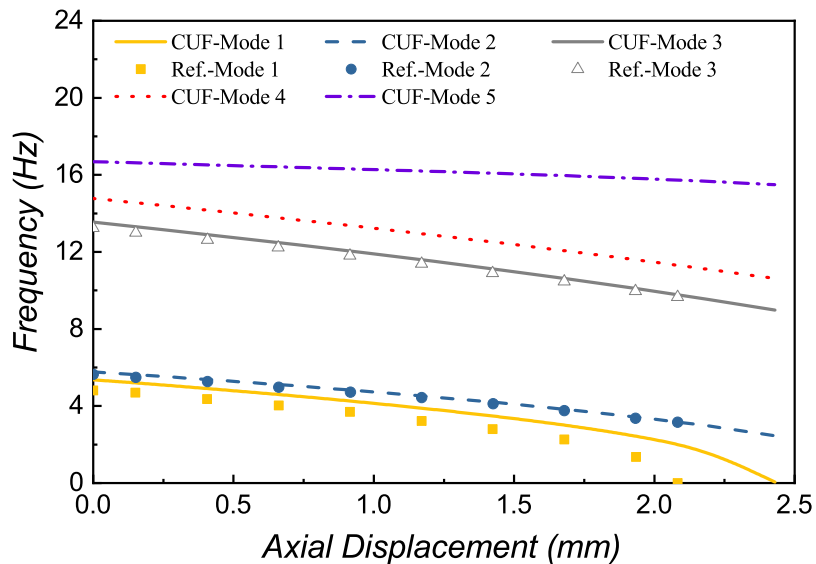
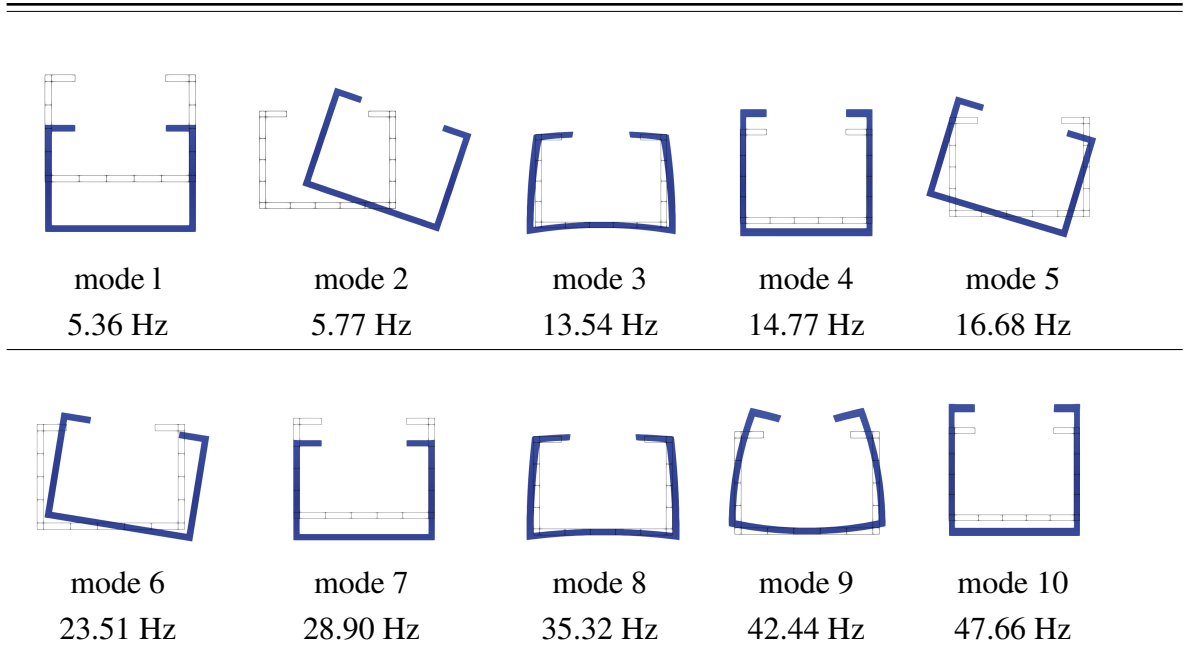


Fig. 4.13 The comparison of the first five natural frequencies in the arbitrary cross-section beam (II) under progressive compressive loads based on the CUF model with 117 Lagrange points and the available literature [127]



Table 4.20 The variations of frequencies versus the applied axial displacements in the arbitrary cross-section beam (II) under progressive compressive loads based on the CUF 1D models and Ref. [127]

Axial Displacement (mm)	Frequency (Hz)- CUF			Frequency (Hz)-Ref. [127]		
	Mode 1	Mode 2	Mode 3	Mode 1	Mode 2	Mode 3
0.25	5.10	5.53	13.09	4.57	5.40	12.89
0.50	4.80	5.27	12.68	4.24	5.17	12.48
0.75	4.50	5.02	12.28	3.92	4.87	12.08
1.00	4.14	4.72	11.88	3.54	4.62	11.68
1.25	3.77	4.42	11.43	3.09	4.35	11.23
1.50	3.37	4.09	10.98	2.66	4.02	10.78
1.75	2.86	3.74	10.50	2.06	3.64	10.32

## 4.6 Symmetric [90/0/0/90] square beam

An example of a [90/0/0/90] composite beam with a square cross-section is investigated in this section. The beam measures  $l = 6.35$  m and  $a = 27.94$  cm in width and length, and it is simply-supported at both ends. Table 4.21 displays the composite beam's material properties. Table 4.22 reports the values of natural frequencies of the beam structure based on the CUF 1D beam models with LE functions (briefly indicated as CUF-LE in the table) and classical beam theories (EBBT and TBT). As can be seen in Table 4.23, the reported values are also compared to those found in the literature for higher-order beam theories. In this regard, the terms FSDBT, ESDBT, and TSDBT respectively correspond to first-order, exponential, and trigonometric shear deformation beam theories. It is noticed that the natural frequencies and buckling loads derived by the CUF and all other higher-order beam theories in the literature are very consistent. On the other hand, as a result of the kinematic approximation provided by the EBBT, the natural frequencies and buckling loads associated with this theory are greater than the ones obtained by the other beam theories.

Table 4.21 Material properties of the 4-layer [90/0/0/90] composite beam [140] with simply-supported edge conditions

$E_1$ (GPa)	$E_2 = E_3$ (GPa)	$G_{12} = G_{13}$ (GPa)	$G_{23}$ (GPa)	$\nu_{12} = \nu_{13}$	$\rho$ ( $\frac{kg}{m^3}$ )
241.5	18.98	5.18	3.45	0.24	2015

Table 4.22 The first five natural frequencies of the square composite beam [90/0/0/90] with simply-supported edge conditions based on the CUF 1D models and the literature

Mode number	EBBT	TBT	CUF-LE	FSDBT [148]	ABQ[140]	TSDBT [149]
Mode 1	15.13	15.00	14.87	14.9	14.95	14.97
Mode 2	60.36	58.41	56.49	58.1	57.6	57.83
Mode 3	135.23	126.10	117.97	124.5	122.8	123.40
Mode 4	238.89	212.78	192.35	208.6	204.2	205.54
Mode 5	370.15	314.06	295.81	304.8	296.6	298.80

Table 4.23 The first three buckling loads of the square composite beam [90/0/0/90] beam with simply-supported edge conditions based on the CUF 1D models and the literature ( $*10^6$  N/m)

Mode number	EBBT	TBT	CUF-LE	FSDBT [148]	ESDBT [149]	TSDBT [149]
Mode 1	20.71	20.43	20.02	20.44	20.38	20.39
Mode 2	82.70	77.67	73.06	77.07	76.23	76.34
Mode 3	185.44	161.42	150.18	158.23	154.81	155.23

## 4.7 Unsymmetric [0/ $\theta$ ] square beam

In this section, a [0/ $\theta$ ] cantilever beam with a square cross-section is assumed. The beam has the length of  $l = 1$  m and width of  $b = t = 0.1$  m, respectively. The following material properties are considered for this composite beam structure [152]:

$$\frac{E_1}{E_2} = 40, \quad \frac{G_{12}}{E_2} = 0.6, \quad \frac{G_{23}}{E_2} = 0.5, \quad \nu_{12} = 0.25 \quad (4.3)$$

The values of natural frequencies for composite beams with [0/45] and [0/75] laminations are given in Table 4.24. In this table, natural frequencies are obtained

based on the EBBT, TBT, CUF 1D model with LE, ABQ-3D solid model, and other higher-order beam theories from [152] that incorporate coupled solutions (axial, bending, and shear components). As seen in this table, the natural frequencies based on the CUF-LE model closely match the values found using the ABQ 3D solid model and Ref. [152]. Nevertheless, those derived from classical theories exhibit certain discrepancies.

Table 4.24 The first five natural frequencies of the square composite beam [0/θ] with clamped-free edge conditions based on the different structural models and the literature

Mode number	[0/45]lamination					[0/75]lamination				
	EBBT	TBT	CUF-LE	ABQ	Ref. [152]	EBBT	TBT	CUF-LE	ABQ	Ref. [152]
Mode 1	4.66	4.59	4.29	4.30	4.32	4.71	4.62	4.18	4.19	4.26
Mode 2	15.57	13.90	12.13	12.96	-	15.76	13.96	11.19	11.27	-
Mode 3	28.83	27.50	20.18	21.57	20.02	42.88	33.65	18.77	20.02	19.73
Mode 4	36.01	34.29	36.62	37.98	-	70.78	35.33	33.64	33.85	-
Mode 5	67.45	45.12	42.89	44.92	44.05	77.96	46.40	42.33	43.66	43.22

The variations of natural frequencies with the axial loads for the prior composite beam with [0/45] and [0/75] laminations are further investigated in Figs. 4.14 and 4.15 to show the advantages of the proposed method based on the CUF. In these figures, the non-dimensional axial forces and natural frequencies are considered as follows [152]:

$$\bar{P} = \frac{P l^2}{b^3 t E_2}, \quad \bar{w} = \frac{w l^2}{b} \sqrt{\frac{\rho}{E_2}} \quad (4.4)$$

Due to the existence of axial loads, the natural frequencies are reduced dramatically. The critical buckling load may be defined as the load that causes the natural frequency to be zero. The findings obtained using the CUF 1D method correlate well with the coupled solution found using higher-order beam theories in [152]. As accurately stated in [152] and seen in the diagrams of Figs. 4.14 and 4.15, the uncoupled reference solution is no longer applicable for unsymmetrically laminated beams, and triply coupled vibration (axial, bending, and shear components) should be regarded. This is taken into account automatically when the proposed CUF 1D models with efficient LE are employed.

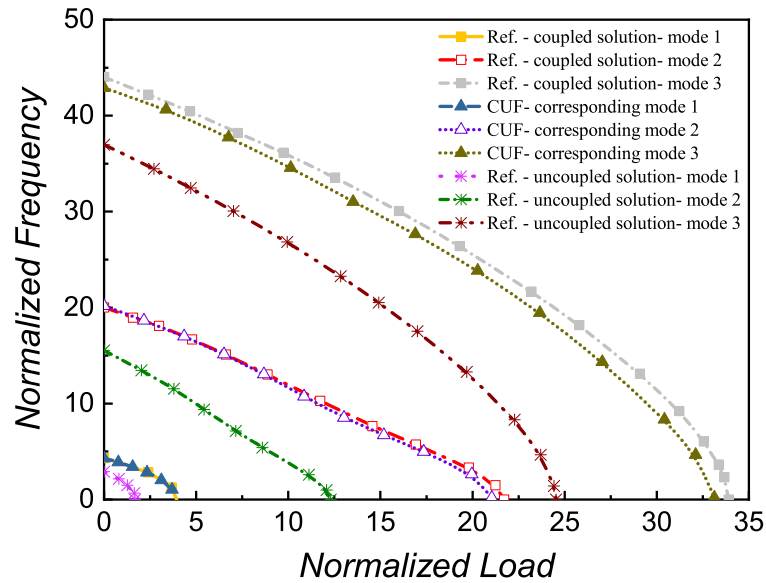


Fig. 4.14 The variations of natural frequencies with the axial loads for the square composite beam with [0/45] lamination based on the CUF 1D model with LE and the available literature [152]

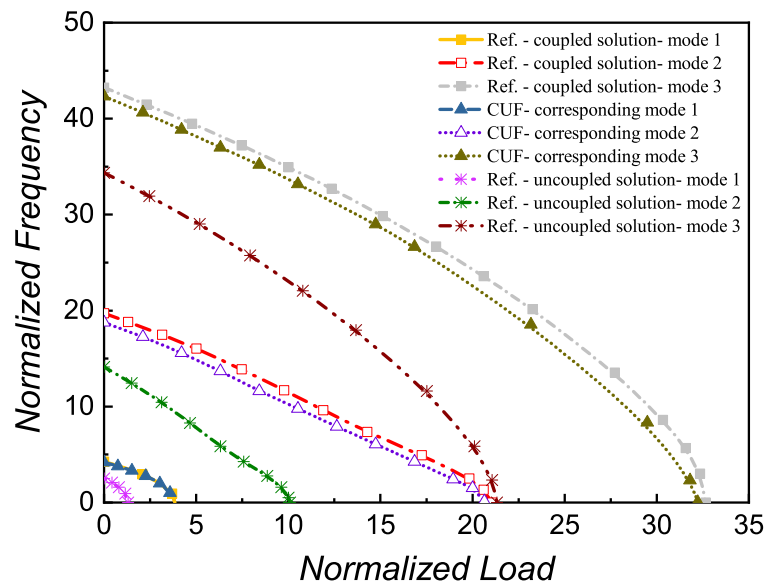


Fig. 4.15 The variations of natural frequencies with the axial loads for the square composite beam with [0/75] lamination based on the CUF 1D model with LE and the available literature [152]

## 4.8 Box composite beam

This section analyzes a thin-walled composite box beam with a length of  $l = 8$  m and geometries provided in Fig. 4.16. The edge conditions for this beam example are simply-supported, and Eqs. (4.4) are employed to normalize axial loads and natural frequencies. This composite beam's material properties are as follows [155]:

$$\frac{E_1}{E_2} = 25, \quad \frac{G_{12}}{E_2} = 0.6, \quad \nu_{12} = 0.25 \quad (4.5)$$

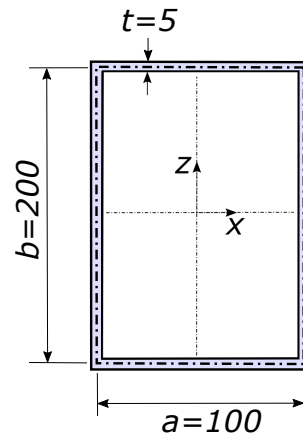


Fig. 4.16 Geometry of thin-walled box beam (dimensions in mm)

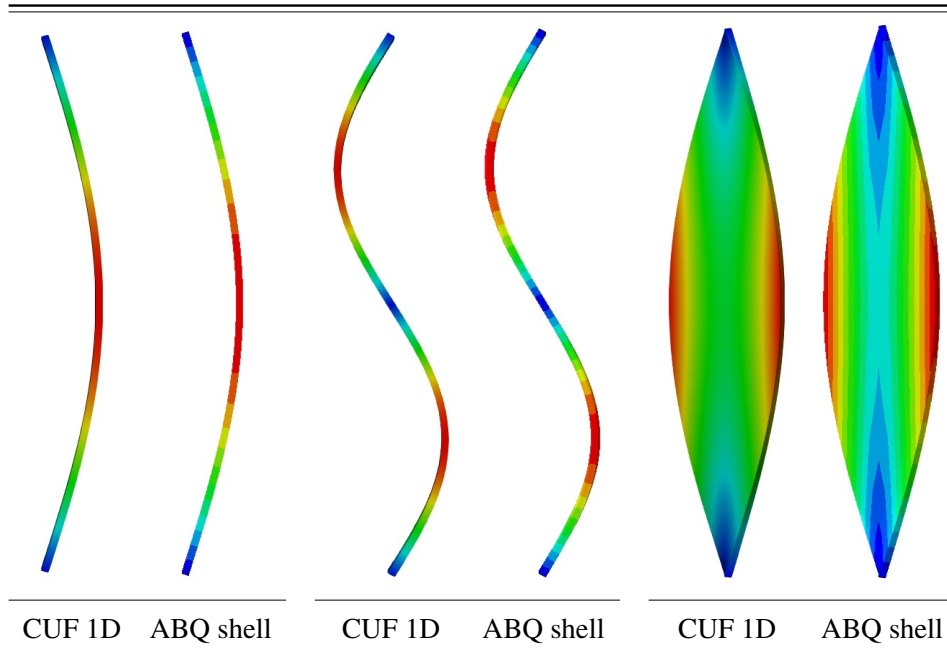
The values of natural frequencies based on the classical theories, CUF 1D, ABQ shell, and Ref. [155] are reported in Table 4.25 for the composite box beams with [0] and [30/-30] laminations. A good agreement is seen between the results obtained by the CUF 1D, ABQ shell, and higher-order beam theories of Ref. [155]. Furthermore, in Fig. 4.26, the vibration modes of this composite beam obtained by the CU-1D models with LE are compared with the ABQ shell models. Although the CUF 1D models require much less computational effort in comparison with expensive shell ones, the natural frequencies and vibration modes obtained by the two methods match well. Therefore, the present proposed method can be used efficiently for the evaluation of the dynamic response of these structures. For the sake of completeness, the first nine mode shapes of this composite box beam with [0] lamination based on the CUF 1D model with LE are displayed in Table 4.27.

Natural frequencies for composite box beams with [0] and [30/-30] laminations are presented in Table 4.25 using classical theories, CUF 1D, ABQ shell, and Ref. [155]. There is strong agreement between the CUF 1D, ABQ shell, and higher-order beam theories of Ref. [155]. Additionally, in Fig. 4.26, the vibration modes of this composite beam are compared to those derived using CU-1D models with LE and ABQ shell models. While the CUF 1D models demand far less computational effort than the more costly shell models, the natural frequencies and vibration mode shapes produced by the two methods are quite similar. As a result, the suggested technique may be utilized effectively to assess the dynamic response of these structures. Table 4.27 displays the first nine mode shapes of this composite box beam with [0] lamination based on the CUF 1D model with LE.

Table 4.25 The first six natural frequencies of the composite box beam with simply-supported edge conditions based on the different structural models and the literature

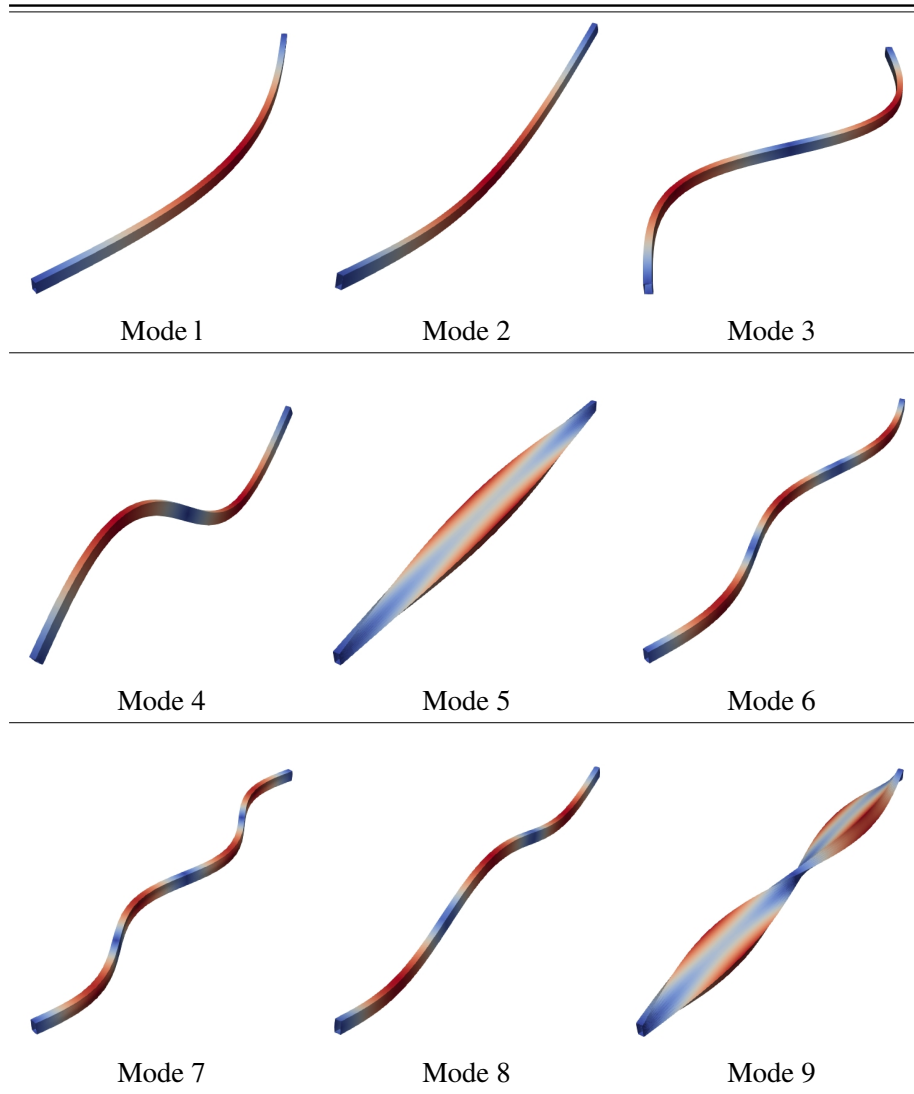
Mode number	[0]lamination					[30/-30] lamination in the webs				
	EBBT	TBT	CUF-LE	ABQ shell	Ref. [155]	EBBT	TBT	CUF-LE	ABQ shell	Ref. [155]
Mode 1	10.89	10.82	10.62	10.59	10.88	6.68	6.68	5.21	4.97	6.68
Mode 2	18.39	18.07	17.89	17.87	18.39	15.49	15.29	14.48	14.38	15.49
Mode 3	43.53	42.49	39.61	39.04	45.54	26.71	26.62	20.55	18.44	26.70
Mode 4	73.45	68.75	66.34	66.08	-	60.06	59.61	45.15	40.59	-
Mode 5	-	-	76.11	69.68	-	61.86	58.97	55.00	56.28	-
Mode 6	97.86	92.81	80.76	77.11	-	106.67	105.26	77.71	71.82	-

Table 4.26 The comparison of vibration mode shapes for the composite box beam with simply-supported edge conditions based on the CUF 1D with LE and ABQ shell models



To evaluate the effect of axial loads on the natural frequencies of thin-walled composite box beams, the results calculated using CUF 1D models with LE, higher-order beam theories, ABQ shell models, and Ref. [155] are compared in Fig. 4.17. It is clear that the CUF 1D findings are consistent with those obtained using the ABQ shell and the literature. In these graphs, for the third mode of Ref. [155], which employs higher-order beam theories, some discrepancies with the CUF and ABQ shell results can be seen. This could be explained by the fact that the difference between different structural theories becomes more important in higher modes. In fact, many structural models could miss some of the cross-sectional deformations that results in the stiffer structure and higher approximation of natural frequency. The suggested CUF 1D approach, on the other hand, is efficient in higher-order modes and corresponds well with the ABQ shell findings.

Table 4.27 The first nine mode shapes of the composite box beam with simply-supported edge conditions based on the CUF 1D model with LE





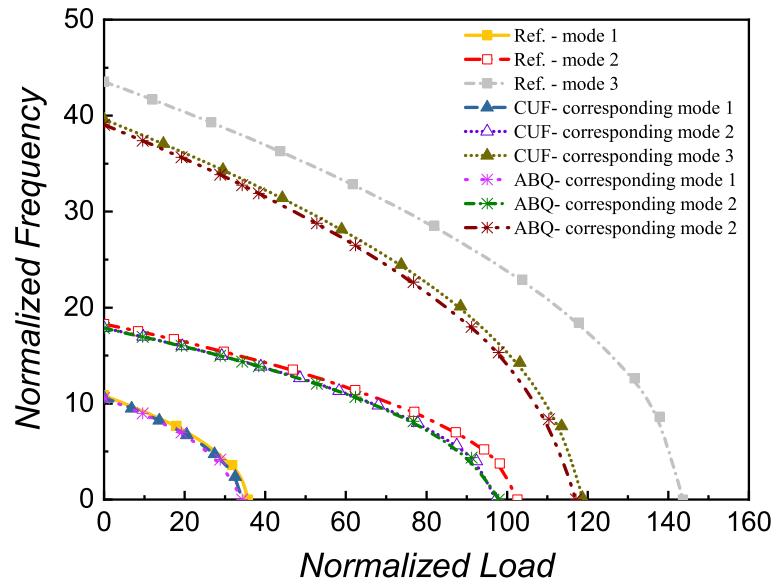


Fig. 4.17 The variations of natural frequencies with the axial loads for the composite box beam based on the CUF 1D model with LE, ABQ shell, and the available literature [155]

## 4.9 I-shaped composite beam

This numerical example deals with a thin-walled cantilever beam with an I-shaped cross-section. The beam edge conditions are clamped-free, and the beam length is  $l = 1$  m. Other cross-sectional dimensions of this beam example are schematically provided in Fig. 4.18. Table 4.28 lists the material properties of this composite beam. Natural frequencies for this composite beam with [0] and [60] laminations are given in Table 4.29 utilizing a variety of structural beam models as well as ABQ shell models. It is observed that the natural frequency values found using the CUF 1D and higher-order beam theories from the literature [153] match well with those predicted using ABQ shell models. However, the natural frequencies based on EBBT and TBT are greater than the others due to the kinematic approximation offered by these theories. Additionally, these classical beam theories do not account for some modes with cross-sectional deformations. This indicates the critical necessity of using precise refined FE models to analyze the dynamic behavior of thin-walled beam structures. Table 4.30 shows the first nine mode shapes of this composite beam with [30] lamination based on the CUF 1D model with LE.

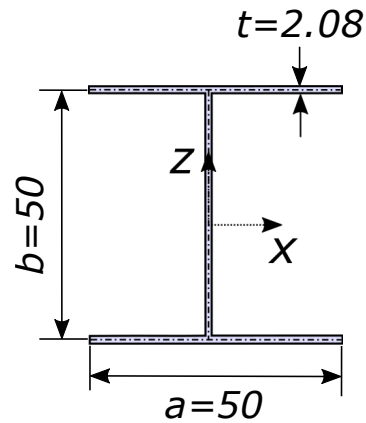


Fig. 4.18 Geometry of thin-walled I-shaped beam (dimensions in mm)

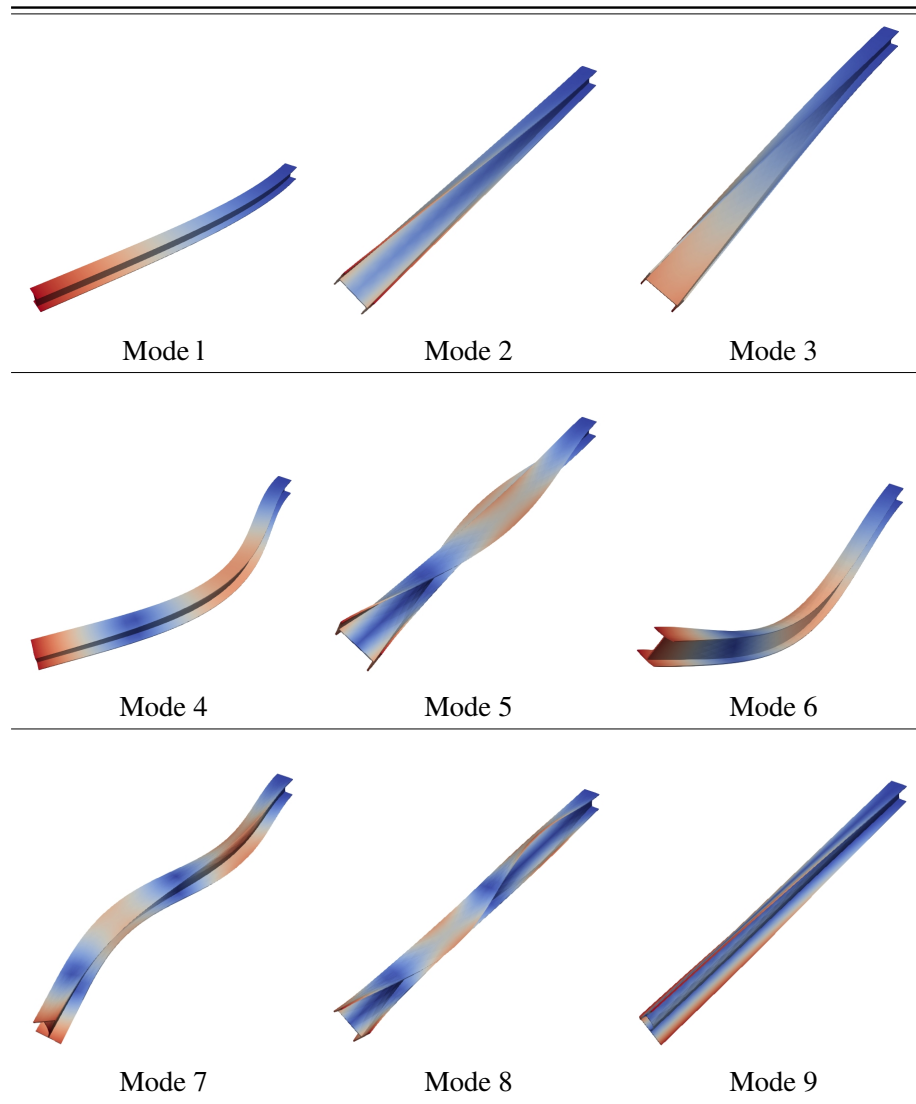
Table 4.28 Material properties of the thin-walled I-shaped composite beam [153] with clamped-free edge conditions

$E_1$ (GPa)	$E_2$ (GPa)	$G_{12}$ (GPa)	$\nu_{12}$	$\rho$ ( $\frac{kg}{m^3}$ )
53.78	17.93	8.96	0.25	1968.9

Table 4.29 The first ten natural frequencies of the I-shaped composite beam with clamped-free edge conditions based on the different structural models and the literature

Mode number	[0]lamination					[60] lamination				
	EBBT	TBT	CUF-LE	ABQ shell	Ref. [153]	EBBT	TBT	CUF-LE	ABQ shell	Ref. [153]
Mode 1	34.71	34.64	34.61	34.36	34.34	21.04	21.03	20.83	20.68	20.84
Mode 2	-	-	48.45	47.78	-	38.99	38.55	38.30	38.41	-
Mode 3	64.32	63.89	62.98	63.03	-	-	-	40.91	41.21	-
Mode 4	217.11	214.21	211.38	209.75	-	131.61	130.94	129.38	128.52	-
Mode 5	-	-	230.05	228.05	-	-	-1	62.26	162.57	-
Mode 6	400.39	383.06	348.77	347.48	-	242.71	236.60	228.31	230.35	-
Mode 7	-	-	512.89	505.47	-	367.35	363.03	353.61	353.79	-
Mode 8	-	-	522.66	512.18	-	-	-	387.17	386.31	-
Mode 9	-	-	547.02	536.28	-	-	-	538.53	600.26	-
Mode 10	-	-	570.67	562.32	-	-	-	559.06	660.61	-

Table 4.30 The first nine mode shapes of the I-shaped composite beam with [30] lamination and clamped-free edge conditions based on the CUF 1D model with LE



Similar to the previous numerical examples, the variations of natural frequencies with the axial loads are shown in the graphs of Fig. 4.19 for this thin-walled beam based on the different structural models. Three different laminations of [0], [30], and [60] are focused here. Due to the fact that for the case of [0] lamination, the fibers are located in the axial direction of the beam, this case shows higher natural frequencies and buckling strength compared to the other investigated laminations. As can be obviously seen in Fig. 4.19, the results obtained by the proposed cost-effective

CUF 1D method match well with the more expensive ABQ shell models for all the cases. The graphs in Fig. 4.19 illustrate the variations in natural frequencies against the axial loads for this thin-walled beam structure. Three laminations of [0], [30], and [60] are evaluated in this section. In the case of [0] lamination, due to the fact that the fibers are placed in the axial direction of the beam, higher natural frequencies and buckling strength are observed.

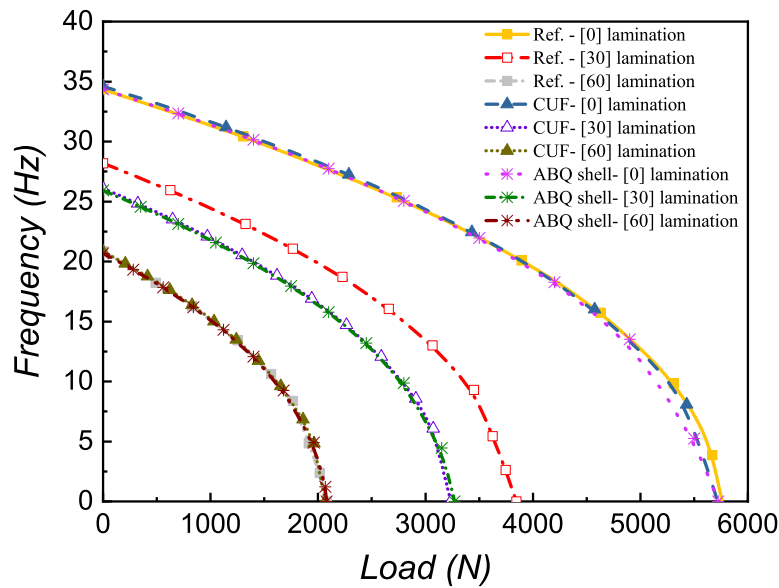


Fig. 4.19 The variations of fundamental frequencies with the axial loads for the I-shaped composite beam based on the CUF 1D model with LE, ABQ shell model, and the available literature [153]

### 4.10 Channel-shaped composite beam

In this section, a thin-walled channel-shaped composite beam as shown in Fig. 4.20 with a length of 2 m and clamped-clamped edge conditions is investigated. Table 4.31 reports the material properties for this composite beam example. For the cases of [0], [30], [60], and [90] laminations, in Tables 4.32 and 4.33, the values of natural frequencies based on different models and higher-order beam theories from [147] are compared. It is indicated that the results obtained by the different methods agree well. In Table 4.34, the first nine mode shapes of this beam using the CUF 1D model with LE are displayed.

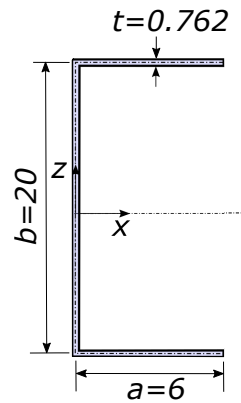


Fig. 4.20 Geometry of thin-walled channel-shaped composite beam (dimensions in mm)

Table 4.31 Material properties of the channel-shaped composite beam [147] with clamped-clamped edge conditions

$E_1$ (GPa)	$E_2$ (GPa)	$G_{12} = G_{13}$ (GPa)	$G_{23}$ (GPa)	$\nu_{12}$	$\rho$ ( $\frac{kg}{m^3}$ )
141.9	9.78	6.13	4.8	0.42	1445

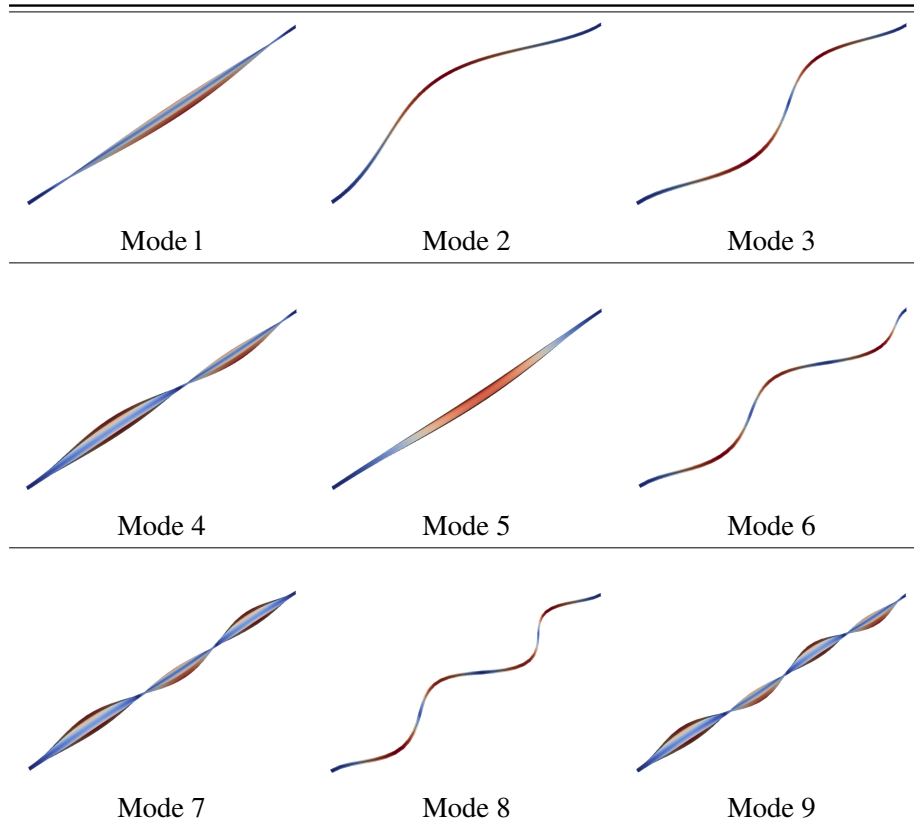
Table 4.32 The first ten natural frequencies of the channel-shaped composite beam with clamped-clamped edge conditions based on the different models and the literature

Mode number	[0]lamination				[30] lamination			
	CUF-LE	ABQ shell	Ansys shell [147]	HOBT [147]	CUF-LE	ABQ shell	Ansys shell [147]	HOBT [147]
Mode 1	15.93	15.90	15.90	15.93	6.82	6.75	6.75	8.39
Mode 2	31.11	32.40	34.80	32.69	18.79	18.60	18.61	23.13
Mode 3	43.78	43.70	43.71	43.89	26.30	27.53	27.75	37.27
Mode 4	68.68	71.03	72.93	71.64	36.82	36.46	36.47	45.32
Mode 5	72.27	72.65	75.53	73.10	50.61	50.48	56.31	55.81
Mode 6	85.47	85.34	-	-	60.85	60.30	-	-
Mode 7	116.24	119.31	-	-	63.61	71.72	-	-
Mode 8	140.52	140.34	-	-	90.86	89.95	-	-
Mode 9	175.39	178.83	-	-	93.22	107.39	-	-
Mode 10	193.81	195.43	-	-	103.72	125.12	-	-

Table 4.33 The first ten natural frequencies of the channel-shaped composite beam with clamped-clamped edge conditions based on the different models and the literature

Mode number	[60]lamination				[90] lamination			
	CUF-LE	ABQ shell	Ansys shell [147]	HOBT [147]	CUF-LE	ABQ shell	Ansys shell [147]	HOBT [147]
Mode 1	4.57	4.53	4.54	4.65	4.20	4.18	4.19	4.18
Mode 2	12.60	12.49	12.50	12.81	11.59	11.53	11.54	11.53
Mode 3	18.47	18.59	18.77	19.37	17.12	17.03	17.12	17.06
Mode 4	24.69	24.48	24.51	25.12	22.71	22.60	22.62	22.62
Mode 5	33.24	36.21	40.48	36.93	31.43	30.99	32.48	31.38
Mode 6	40.81	40.46	-	-	37.54	37.36	-	-
Mode 7	47.86	49.01	-	-	44.61	44.23	-	-
Mode 8	60.97	60.42	-	-	56.08	55.79	-	-
Mode 9	71.06	76.01	-	-	66.81	66.10	-	-
Mode 10	82.84	84.39	-	-	78.32	76.83	-	-

Table 4.34 The first nine mode shapes of the channel-shaped composite beam with clamped-clamped edge conditions based on the CUF 1D model with LE



The influence of axial loads on the variations of natural frequencies in a channel-shaped composite beam with [0] lamination is evaluated in Fig. 4.21 by comparing the results obtained using the proposed CUF 1D approach with LE to those obtained using ABQ shell models. In the presented graphs, the variations of natural frequencies with axial loads are compared to ABQ shell models for the first five modes of this channel-shaped beam. It can be clearly noticed that the mentioned approaches get identical results for the first five modes, and based on the VCT, the critical buckling load may be determined as the load that causes the natural frequency to be zero. For the sake of completeness, The DOF and element types of ABQ shell and CUF 1D models employed for the box, I-shaped, and channel-shaped beams are compared in Table 4.35.

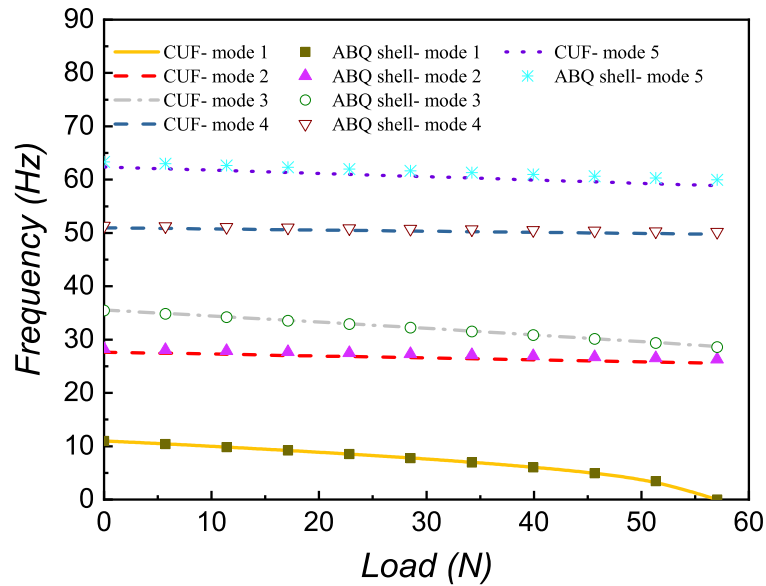


Fig. 4.21 The variations of natural frequencies with the axial loads for the channel-shaped composite beam based on the CUF 1D model with LE and ABQ shell model

Table 4.35 The comparison of ABQ shell and CUF 1D models employed for the investigated beam structures

Model	DOF	Number of elements	Element type
ABQ shell-box beam	32832	1800	Quadratic S8R
ABQ shell-I-shaped bam	26748	1400	Quadratic S8R
ABQ shell-Channel-shaped beam	28572	1500	Quadratic S8R
CUF 1D-LE-box beam	18117	20B4	4-node beam
CUF 1D-LE-I-shaped bam	17019	20B4	4-node beam
CUF 1D-LE-Channel-shaped beam	15921	20B4	4-node beam

## 4.11 Channel-shaped composite beam with transverse stiffeners

The preceding sections demonstrated the reliability and correctness of the proposed CUF-based approach by showing several numerical evaluations and comparisons to the existing literature and shell models for various thin-walled beams. To completely



illustrate the CUF 1D method's capability with the efficient LE, the final numerical study is conducted on a channel-shaped beam with transverse stiffeners. The dimensions of the web and flanges of this channel-shaped beam are all  $a = b = 0.6$  m. The edge conditions of the beam structure are simply-supported at both ends. This beam example measures  $l = 6$  m and  $t = 0.03$  m in length and thickness, respectively (see Fig. 4.22). Table 4.36 summarizes the material properties of the investigated composite beam.

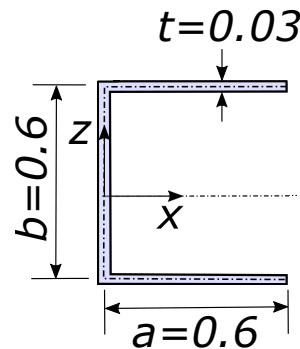


Fig. 4.22 Geometry of thin-walled channel-shaped composite beam (dimensions in mm)

Table 4.36 Material properties of the channel-shaped composite beam [144] with transverse stiffeners and simply-supported edge conditions

$E_1$ (GPa)	$E_2$ (GPa)	$G_{12} = G_{13}$ (GPa)	$G_{23}$ (GPa)	$\nu_{12} = \nu_{13}$	$\nu_{23}$	$\rho$ ( $\frac{kg}{m^3}$ )
144	9.65	4.14	3.45	0.3	0.5	1389

The first ten natural frequencies of the channel-shaped composite beam with different number of transverse stiffeners based on the CUF 1D model with LE are reported in Table 4.37. Moreover, Table 4.38 shows the corresponding first nine mode shapes of this beam. It should be noted that due to the presence of transverse stiffeners, the complexity of this beam structure is increased remarkably. Therefore, many analytical models based on the beam theories fail to predict the dynamic response accurately. However, by employing the present CUF-based method with efficient LE, the values of natural frequencies and vibration mode shapes can be assessed carefully. The first ten natural frequencies of a channel-shaped composite beam with different number of transverse stiffeners are presented in Table 4.37. Additionally, Table 4.38 illustrates the beam's first three mode shapes. As can be

seen in the mode shapes of this figure, the localized deformation along the length of the beam are decreased as the number of stiffeners are increased. In fact, the presence of stiffeners imposes some limitations for the localized deformations along the beam that leads to the increase of buckling strength and natural frequency. For instance, as will be further discussed in the following, the second and third modes of the case with five stiffeners show highest buckling loads and natural frequencies. Note that the existence of transverse stiffeners increases the complexity of this problem remarkably. As a result, many analytical models based on beam theories fail to effectively determine the dynamic response. However, by utilizing the current CUF-based approach with efficient LE, it is possible to thoroughly calculate the values of natural frequencies and assess vibration mode shapes.

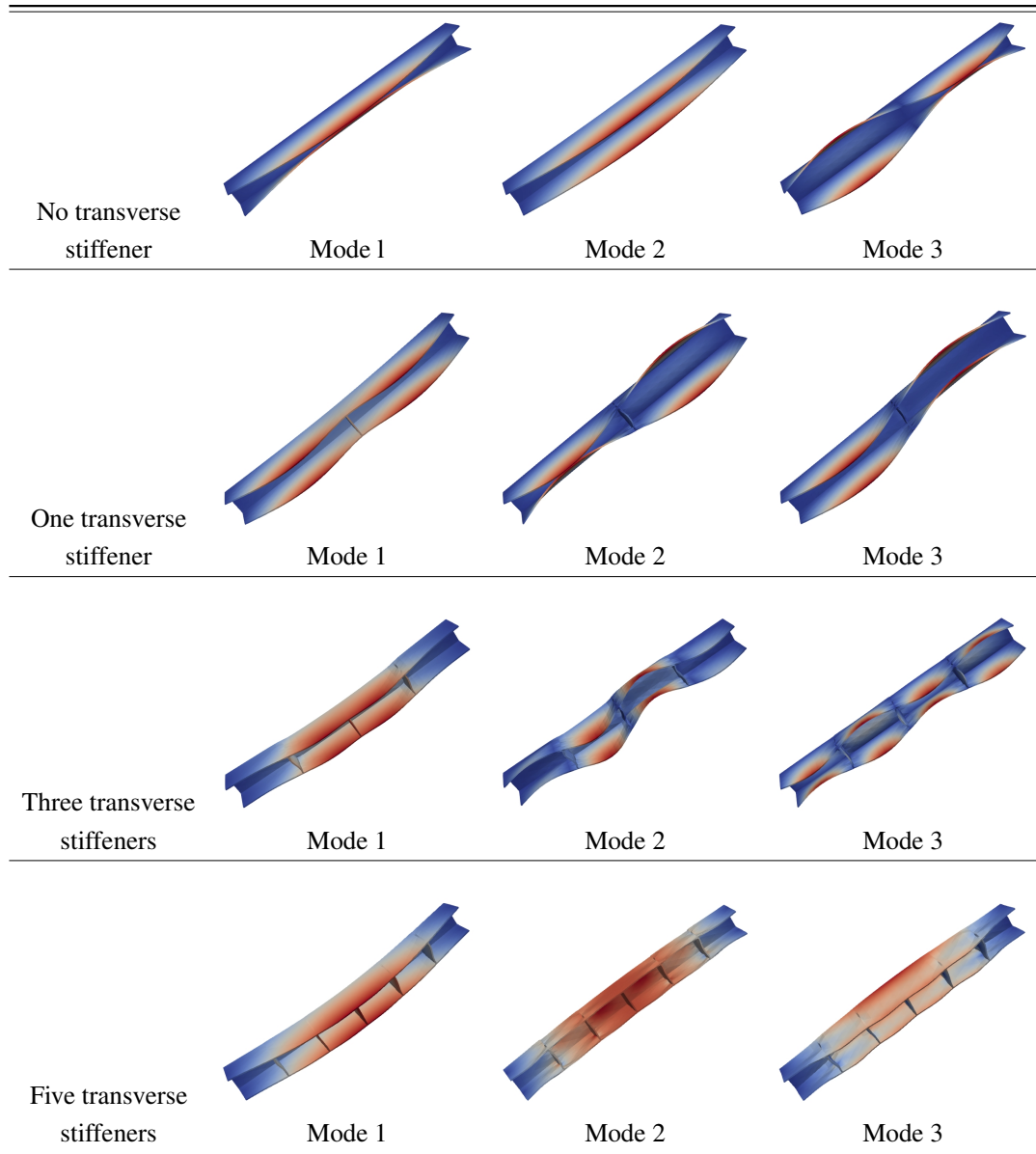
Table 4.37 The first ten natural frequencies of the channel-shaped composite beam with different number of transverse stiffeners based on the CUF 1D model with LE

Mode number	No stiffener	One stiffener	Three stiffeners	Five stiffeners
Mode 1	22.42	29.43	28.58	35.52
Mode 2	24.01	30.68	55.00	81.94
Mode 3	30.06	33.01	67.57	96.92
Mode 4	35.63	35.86	69.36	101.67
Mode 5	46.42	58.13	71.29	122.28
Mode 6	50.70	68.67	72.02	143.92
Mode 7	66.19	71.03	78.83	185.75
Mode 8	68.25	72.67	89.01	156.66
Mode 9	71.54	86.66	101.83	166.02
Mode 10	74.57	60.79	129.55	166.51

The final evaluations of the effects of axial loads on the variations of the first three natural frequencies are given in Figs. 4.23 and 4.24 for the channel-shaped beam with transverse stiffeners and [0] lamination. Note that Eqs. (4.4) are used in these figures in order to normalize axial loads and natural frequencies. The beam without any stiffener is compared to the beam with one stiffener in Fig. 4.23. Analogously, Fig. 4.24 compares beams with three and five stiffeners. These figures illustrate how the number of transverse stiffeners affects the buckling behavior and natural frequencies of this beam structure. The third mode of the case with five stiffeners has the highest natural frequency. It is worth mentioning that adding stiffeners alters the

mode shapes and natural frequencies of the beam structure remarkably. As a result, a mode-by-mode comparison may not be possible for the models with different number of stiffeners. As seen in Fig. 4.23, the third mode of the model with one stiffener has the highest natural frequency in the unloaded condition. However, it has a substantially lower buckling strength than the second mode of the beam without stiffener. Also, other examples from Fig. 4.24 could be the second and third modes of the beam with five stiffeners, with the former exhibiting the highest buckling strength and the latter exhibiting the highest natural frequency in the unloaded state.

Table 4.38 The first nine mode shapes of the channel-shaped composite beam with simply-supported edge conditions based on the CUF 1D model with LE



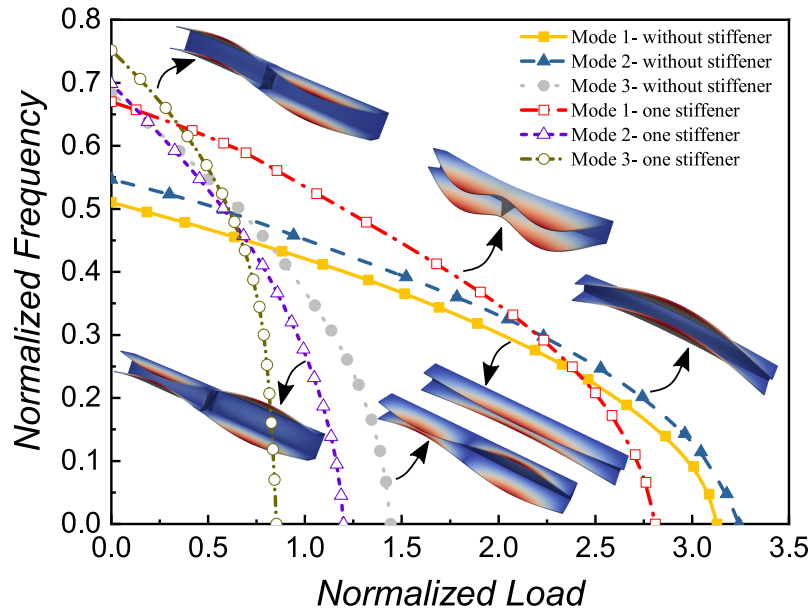


Fig. 4.23 The comparison of natural frequencies variations for the channel-shaped beam without stiffener and with one stiffener

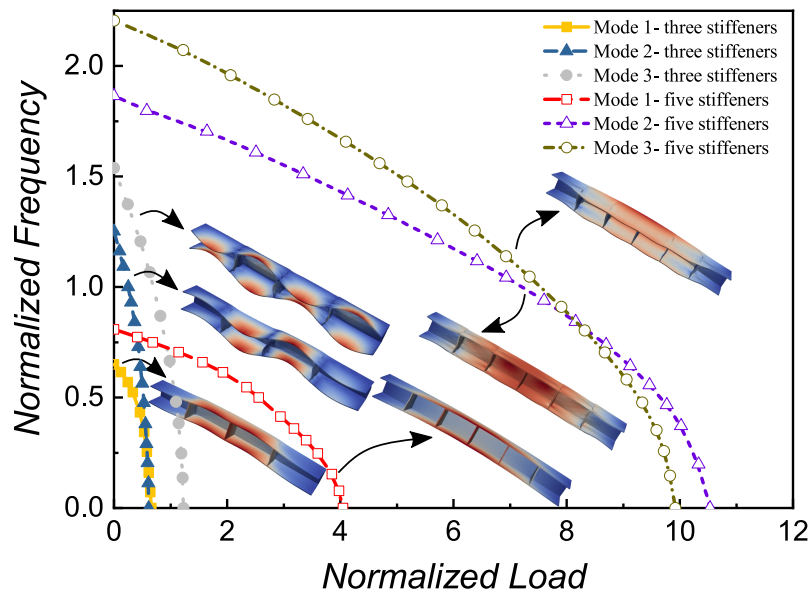


Fig. 4.24 The comparison of natural frequencies variations for the channel-shaped beam with three and five stiffeners

## 4.12 Conclusions

In this chapter, an efficient CUF-based method to evaluate the vibrations and buckling of thin-walled isotropic and composite beams under compression with different open cross-sections has been presented. The effects of axial loads on the variations of the beam structure's natural frequencies have been evaluated. In order to demonstrate the capabilities of the presented method, numerous comparisons of the CUF 1D results with higher-order beam theories in the available literature and shell FE models have been presented, and the consistency of results for both isotropic and composite beams have been demonstrated. The following comments could be made according to the results:

- The MAC analysis revealed that the number of related modes for classical models such as Taylor order 1 is much less than that for other Lagrange models. Indeed, classical beam theories eliminate a large number of modes in favor of never-existing rigid cross-section modes.
- Although certain modes may seem to be identical in the MAC analysis, the natural frequencies determined by using the two models may display significant deviations. Therefore, it is very important to consider a structural theory that is capable of assessing the problem's eigenvalues and eigenvectors precisely.
- Many cross-sectional deformations can be detected only by using higher-order and refined beam theories. In addition, the influence of compressive loads on the variations of natural frequencies could be more significant by employing the refined theories.
- As long as the initial buckling and vibration modes are similar; the VCT may be used to estimate buckling loads based on the decrease in the natural frequencies of the beam under progressive compressive loads.
- The advantages of the CUF 1D method with efficient LE were shown for a more complex structural problem involving a channel-shaped composite beam subjected to compression with different number of transverse stiffeners.
- It was shown that adding transverse stiffeners alters the mode shapes and natural frequencies of the beam structure significantly. It was indicated that

---

some models with higher natural frequencies in the unloaded condition of the VCT graph did not necessarily exhibit high buckling strength.

# Chapter 5

## Physically and geometrically nonlinear analysis of thin-walled beam structures

### 5.1 Introduction

This chapter discusses two types of nonlinearity that are frequently encountered: geometrical and material. The former is related to nonlinear strain-displacement relationships, whereas the latter is owing to the nonlinear constitutive equations of the material of the system. Several examples of plates and shells with nonlinearities may be found in [163–166]. Many studies have been focused on the elastoplastic analyses of beam-like structures [167–169]. Saje et al. [170] worked on the kinematically exact FE model for elastoplastic arbitrarily curved beams. A three-dimensional elastoplastic shear flexible beam element was presented by Park and Lee [171] in order to analyze geometrically nonlinear problems. By using thermodynamically consistent three-dimensional constitutive laws for describing the material behavior, Mata et al. [172] conducted an analysis of the beam structures with nonlinear geometric and constitutive behavior. Pajunen [173] employed kinematically exact finite beam element according to Reissner's stress resultant theory in order to solve large-deflection of elastoplastic beams. Battini and Pacoste [174] evaluated the plastic instabilities of the beams with arbitrary cross-sections. In this regard, they developed a formulation for the three-dimensional co-rotational elastic beam elements



with warping effects. Challamel et al. [175] focused on the plasticity collapse of hardening-softening beams. The GBT was successfully used to assess the nonlinear behavior of thin-walled structures [176, 177]. Abambres et al. conducted a structural analysis of elastoplastic thin-walled members [178, 179]. The same authors [180] developed a GBT-based formulation for the physically nonlinear response of thin-walled structures with isotropic hardening. The large deflection of elastoplastic frame structures was studied in [181–184].

This chapter combines geometrical and material nonlinearities. The results are shown for the beam structures with different cross-sections such as square, C-shaped, and T-shaped. Equilibrium curves for C-shaped and T-shaped beams are compared with the available literature. Additionally, the stress distributions obtained by various structural theories using TE and LE are compared with three-dimensional FE models. The isotropically work-hardening von Mises constitutive model is used for the implementation of elastoplasticity theory, and the assumed material behavior is represented by employing the labels *elastic* and *elastoplastic*. It is demonstrated that although the DOF and the computational costs of the problems are reduced significantly using the current method, the equilibrium curves and the stress distributions of the structure are predicted accurately and precisely.

## 5.2 The von Mises model for elastoplasticity

In this section, the von Mises model implemented for the nonlinear framework of metallic elastoplastic materials is provided [42, 185]. Based on the isotropic work-hardening von Mises constitutive model, the stress-strain relation is given by:

$$\boldsymbol{\sigma} = \mathbf{C}^{cep} \boldsymbol{\varepsilon}^e \quad (5.1)$$

where  $\boldsymbol{\varepsilon}^e$  is the elastic component of the strain tensor, and the consistent tangent elastoplastic operator  $\mathbf{C}^{cep}$  is a fourth-order tensor that describes the elastoplastic nature of the material and relates the current values of stress and strain such that:

$$\mathbf{C}^{cep} = \frac{\partial \boldsymbol{\sigma}_{n+1}}{\partial \boldsymbol{\varepsilon}_{n+1}} \quad (5.2)$$

In the current implementation of the model, a piece-wise linear hardening can be prescribed by providing a set of stress-strain points past the initial yield point.

If the elastic stress exceeds the yield limit  $\sigma_y$ , the following scalar nonlinear equation could be solved:

$$\bar{f}(\Delta\gamma) = q_{n+1}^{trial} - 3G\Delta\gamma - \sigma_y(\bar{\epsilon}_n^p + \Delta\gamma) \quad (5.3)$$

where  $q_{n+1}^{trial}$  is the trial von Mises stress at the increment  $t_{n+1}$ ,  $G$  is the shear modulus,  $\Delta\gamma$  is the unknown,  $\sigma_y$  is the yield stress,  $\bar{\epsilon}_n^p$  is the isotropic hardening parameter at the increment  $t_n$  and  $f$  is the von Mises yield locus, expressed as:

$$f = q(\boldsymbol{\sigma}) - \sigma_y(\bar{\epsilon}_p) \quad (5.4)$$

where

$$q(\boldsymbol{\sigma}) = \sqrt{\frac{1}{2}[(\sigma_{xx} - \sigma_{yy})^2 + (\sigma_{yy} - \sigma_{zz})^2 + (\sigma_{zz} - \sigma_{xx})^2 + 6(\sigma_{xy}^2 + \sigma_{xz}^2 + \sigma_{yz}^2)]} \quad (5.5)$$

Eq. (5.3) is solved using Newton-Raphson method and, with solution  $\Delta\gamma$  at hand, the stress and strain are updated:

$$\begin{aligned} \mathbf{S}_{n+1} &= \mathbf{S}_{n+1}^{trial} \left[ 1 - \frac{\Delta\gamma 3G}{q_{n+1}^{trial}} \right] \\ \boldsymbol{\sigma}_{n+1} &= \mathbf{S}_{n+1} + P_n^{trial} \mathbf{I} \\ \boldsymbol{\epsilon}_{n+1}^e &= \frac{1}{2G} \mathbf{S}_{n+1} + \frac{1}{3} \boldsymbol{\epsilon}_v^{e\, trial} \mathbf{I} \\ \bar{\epsilon}_{n+1}^p &= \bar{\epsilon}_n^p + \Delta\gamma \end{aligned} \quad (5.6)$$

where  $P_n^{trial} \mathbf{I}$  is the volumetric stress at increment  $t_n$ , and  $\frac{1}{3} \boldsymbol{\epsilon}_v^{e\, trial} \mathbf{I}$  is the volumetric component of the elastic trial strain. Interested readers are referred to [41, 185] for more details on the method of implementation.

### 5.3 Square beam

In this section, a square cantilever beam is considered with a length of 1000 mm. The beam is clamped at one end and subjected to an upward tip force at the free end. The schematic figure of the edge and loading conditions of the square beam is shown in Fig. 5.1. Note that all the dimensions in this figure are in mm. Furthermore, the properties of the material for this case are mentioned in Table 5.1, where  $\sigma_0$  and  $E_t$  refer to the yield stress and tangent modulus of the material with bilinear stress-strain relations, respectively.

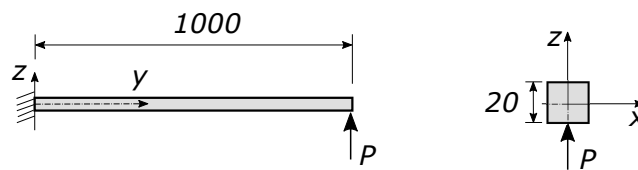


Fig. 5.1 Schematic view of the square beam

Table 5.1 Material properties of the square beam

Material property	Value
Young's modulus	$E=75$ GPa
Tangent modulus	$E_t=E/10$
Poisson's ratio	$\nu=0.33$
Yield stress	$\sigma_y=500$ MPa

In Fig. 5.2, the convergence analysis of equilibrium curves is provided. In this figure, the applied force is plotted versus the vertical displacement of the tip end of the square beam with the coordinate of (0,1000,-10). As illustrated in this figure, for the first analysis case, 20B4 elements are used along the beam axis, while 2L4, 1L9, and 4L9 Lagrange elements are used over the cross-section of the beam. For the second analysis case, the expansion over the cross-section is 1L9, while the beam axis discretization is changing from 2B4 to 20B4. Due to the fact that 20B4 ensures convergence, the remaining study focuses on the influence of structural theories on the equilibrium curves and stress distributions, while maintaining a constant FE mesh.

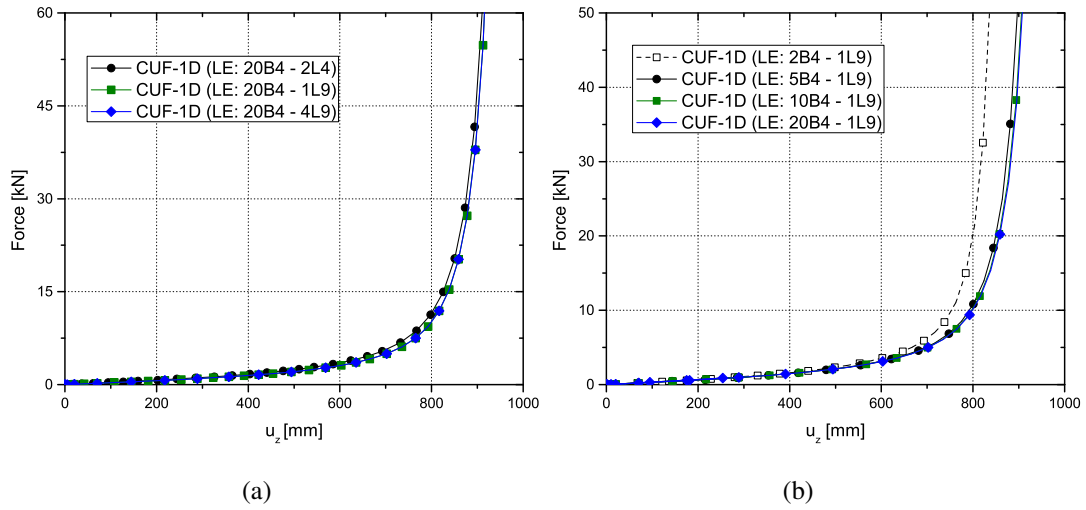


Fig. 5.2 Convergence analysis of equilibrium curves for the square beam with elastic behavior (a) effect of the structural theory (b) effect of the FE discretization

For the evaluations of stress distributions and equilibrium curves in the square beam, different 3D FE models with coarse, medium, and fine meshes of solid quadratic elements and CUF 1D beam models are considered. The degrees of freedom (DOF) and computational time corresponding to each model are shown in Table 5.2. The equilibrium curves of the square beam based on the different structural theories are compared in Fig. 5.3 for the elastic and elastoplastic cases. In Fig. 5.4 the two cases are compared in order to show the effect of plasticity on the curves. Furthermore, a detailed view of plasticity initiation is illustrated in Fig. 5.4 which shows the force-displacement curves based on the CUF 1D and ABQ-3D models with different material behaviors.

Table 5.2 Computational size of the investigated models for the square beam

Model	DOF	Computational time (s)
ABQ-3D Coarse	1869	83
ABQ-3D Medium	11001	194
ABQ-3D Refined	44085	546
CUF 1D (LE-4L9)	4575	56
CUF 1D (LE-9L9)	8967	101
CUF 1D (LE-16L9)	14823	171
CUF 1D (TE: N=1)	549	138
CUF 1D (TE: N=2)	1098	483
CUF 1D (TE: N=3)	1830	2125

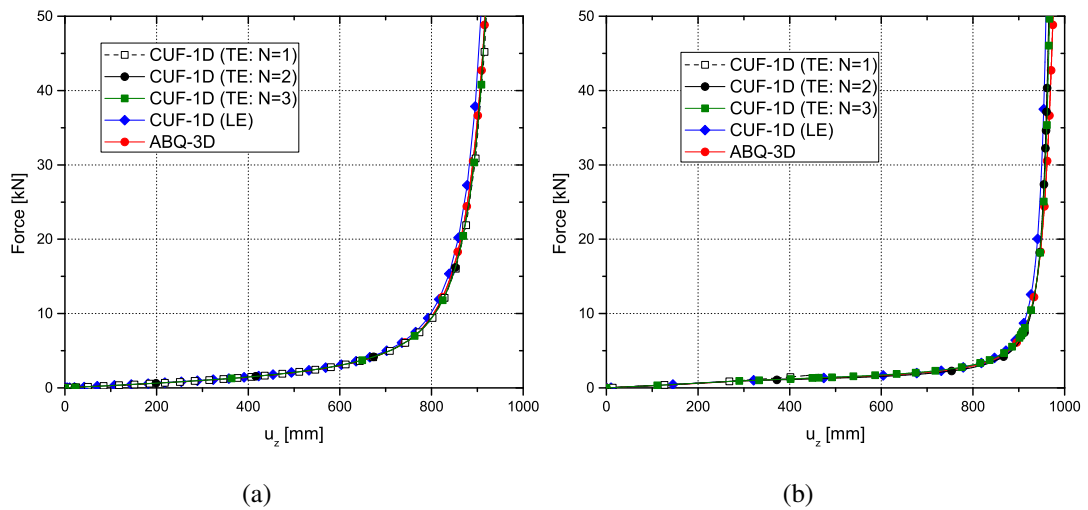


Fig. 5.3 Equilibrium curves for the square beam based on various structural theories (a) elastic material (b) elastoplastic material

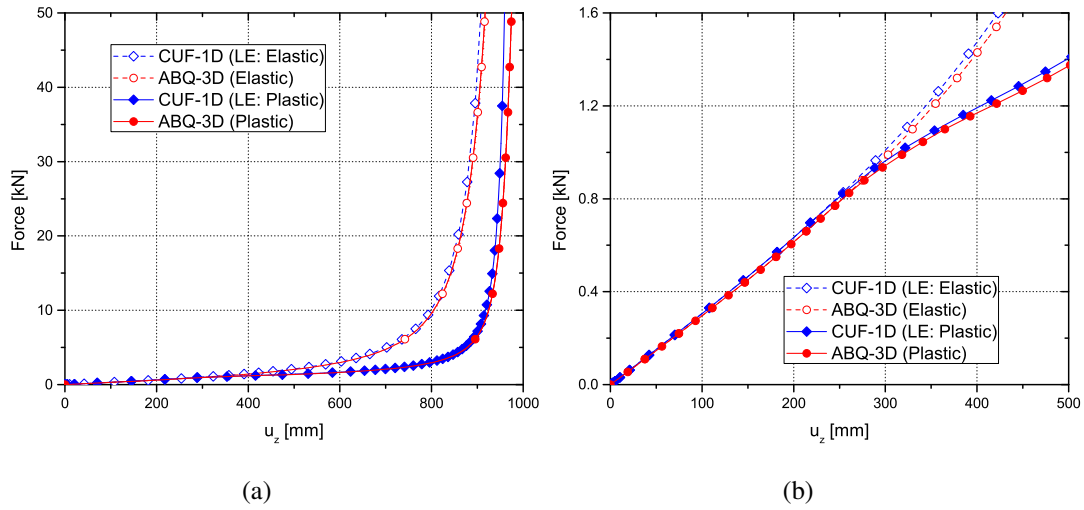


Fig. 5.4 Effect of plasticity on equilibrium curves for the square beam (a) complete view (b) detailed view of plasticity initiation

The axial stress at the load of 1100 N along the middle line of the cross-section ( $x=0$ ) near the clamped edge ( $y=75$  mm) is plotted in Fig. 5.5 based on either elastic or elastoplastic behavior of the material. Moreover, the 2D contour plots of axial stress for the corresponding cross-section are shown in Fig. 5.7 for the elastoplastic material. The transverse shear stress at the load of 1100 N along the middle line of a cross-section ( $x=0$ ) near the clamped edge ( $y=75$  mm) is plotted in Fig. 5.6 based on either elastic or elastoplastic behavior of the material. Moreover, the 2D contour plots of transverse shear stress for the corresponding cross-section are illustrated in Fig. 5.8 for the elastoplastic material. Table 5.3 shows the corresponding vertical displacement  $u_z$  at the tip point of the beam (0,1000,-10), the axial stress  $\sigma_{yy}$  at the point of (0,75,10), and the transverse shear stress  $\sigma_{yz}$  at the point of (0,75,0), for each model of Table 5.2 at the load of 1100 N.

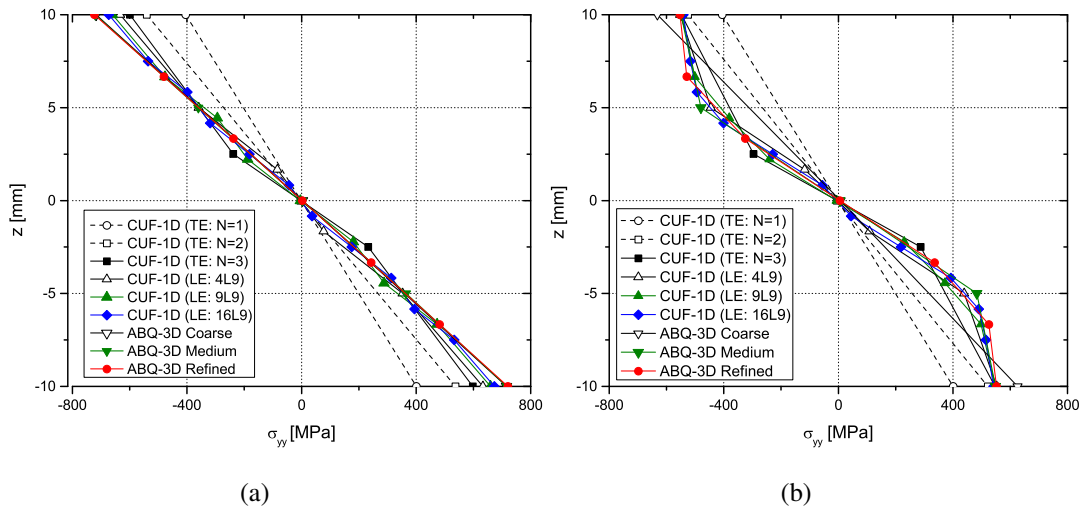


Fig. 5.5 The axial stress at  $F=1100$  N,  $x=0$ ,  $y=75$  mm of the square beam considering (a) elastic behavior of material (b) elastoplastic behavior of material

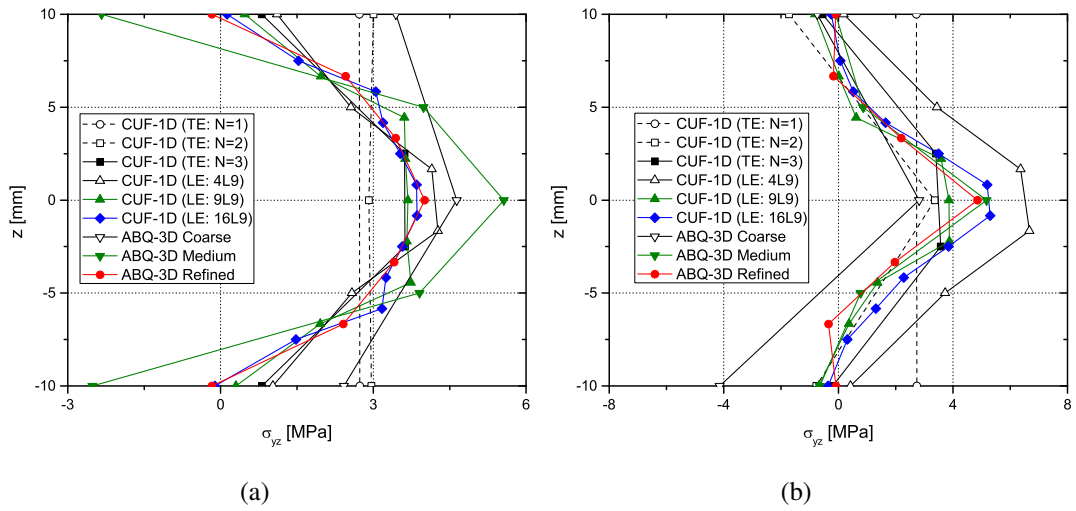


Fig. 5.6 The transverse shear stress at  $F=1100$  N,  $x=0$ ,  $y=75$  mm of the square beam considering (a) elastic behavior of material (b) elastoplastic behavior of material

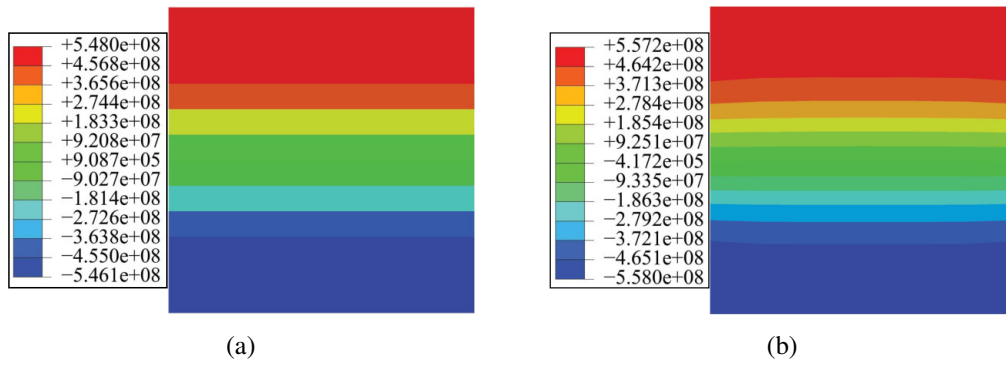


Fig. 5.7 2D contour plots of  $\sigma_{yy}$  (Pa) with  $F=1100$  N and  $y=75$  mm of the square beam for the elastoplastic material based on (a) CUF 1D (LE-16L9) (b) ABQ-3D refined models

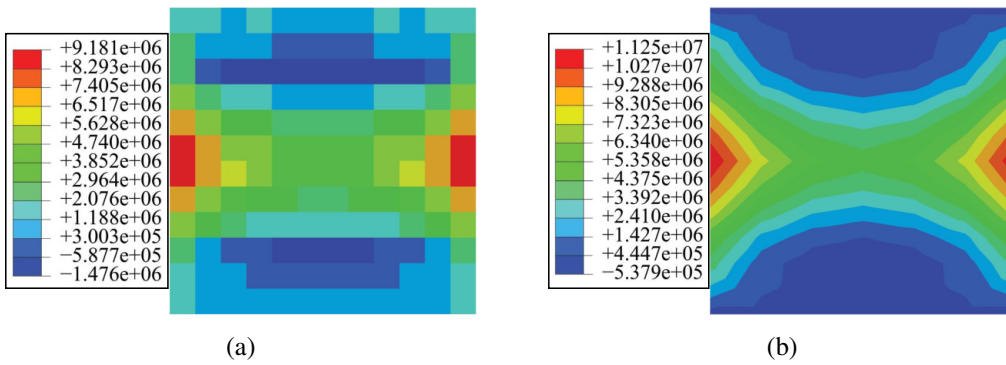


Fig. 5.8 2D contour plots of  $\sigma_{yz}$  (Pa) with  $F=1100$  N and  $y=75$  mm of the square beam for the elastoplastic material based on (a) CUF 1D (LE-16L9) (b) ABQ-3D refined models



Table 5.3 The values of  $u_z$  at the tip point of the square beam (0, 1000, -10),  $\sigma_{yy}$  at (0, 75, 10), and  $\sigma_{yz}$  at (0, 75, 0), with  $F=1100$  N

Model	Elastic			Elastoplastic		
	$u_z$ (mm)	$\sigma_{yy}$ (MPa)	$\sigma_{yz}$ (MPa)	$u_z$ (mm)	$\sigma_{yy}$ (MPa)	$\sigma_{yz}$ (MPa)
ABQ-3D Coarse	328.4	-717.3	4.6	366.0	-632.0	2.8
ABQ-3D Medium	325.5	-719.9	5.5	363.4	-548.9	5.1
ABQ-3D Refined	324.5	-723.1	4.0	361.2	-553.0	4.8
CUF 1D (LE-4L9)	321.6	-633.0	4.2	356.9	-552.1	6.5
CUF 1D (LE-9L9)	321.7	-660.1	3.6	357.5	-544.9	3.8
CUF 1D (LE-16L9)	321.7	-672.9	3.8	357.8	-541.0	5.2
CUF 1D (TE: N=1)	323.8	-404.5	2.7	331.1	-405.2	2.7
CUF 1D (TE: N=2)	322.5	-540.6	2.9	370.6	-524.9	3.3
CUF 1D (TE: N=3)	322.0	-599.5	3.6	359.8	-547.7	3.5

The following comments can be made according to the results of this section:

1. The convergence analysis for the equilibrium curves reveals that at least 10B4 and 1L9 are essential for the force-displacement curves.
2. Despite the fact that CUF needs less DOF than 3D solid models, the equilibrium curves based on CUF 1D LE models are very consistent with the results obtained using 3D FE models.
3. All of the LE and TE models are capable of predicting the large displacements of the compact square beam in the elastic range. Lower-order TE models (N = 1, 2), on the other hand, are not precise enough when the load reaches the yield limit.
4. Between the axial stress distributions obtained from lower-order models or coarse 3D meshes and those obtained from refined models, there is a significant difference around the bottom and top surfaces of the beam cross-sections. Furthermore, such discrepancies seem to be more considerable in the elastoplastic case, which could be owing to the existence of local plasticity, and that necessitates the use of more refined kinematics models. In fact, the importance of employing refined structural theories for the elastoplastic material is

higher in comparison with the elastic one. Such requirements are even more significant for the transverse shear stress evaluation.

## 5.4 C-shaped beam

In this section, a channel-shaped cantilever beam is considered with a length of 900 cm [168]. The beam is clamped at one end and subjected to an upward tip force at the free end. The schematic figure of the edge and loading conditions of the channel-shaped beam is shown in Fig. 5.9 (dimensions in cm). Moreover, the properties of the material for this case are mentioned in Table 5.4, where  $\sigma_0$  refers to the yield stress of elastic-perfectly plastic material [174].

Table 5.4 Material properties of the C-shaped beam

Material property	Value
Young's modulus	$E=210$ GPa
Poisson's ratio	$\nu=0.3$
Yield stress	$\sigma_y=360$ MPa

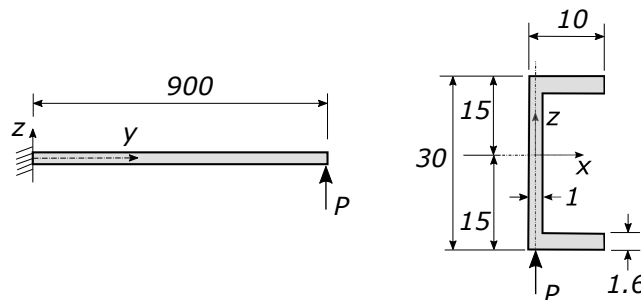


Fig. 5.9 Schematic view of the C-shaped beam, all dimensions are in cm

In Table 5.5 different numerical models employed for this beam example are presented. It should be noted that for thin-walled structures with local deformation, the use of TE models requires very high orders [24]. Therefore, LE is preferred here for the expansion function over the beam cross-section. The transverse displacement was assessed at the point (0, 900, -15) in order to plot the equilibrium curves. The equilibrium curves for elastic and elastoplastic cases are compared in Fig. 5.10. The

results in this figure are obtained from the CUF 1D model and reference numerical results from the available literature [174]. The 3D contour plots of displacement magnitude predicted by CUF 1D and 3D FE models for the elastoplastic case are illustrated in Fig. 5.11.

Table 5.5 Computational size of the investigated models for the C-shaped beam

Model	DOF	Computational time (s)
ABQ-3D Coarse	9867	419
ABQ-3D Medium	125814	1193
ABQ-3D Refined	245049	2911
CUF 1D (LE-5L9)	6039	322
CUF 1D (LE-8L9)	9333	421
CUF 1D (LE-13L9)	14823	730

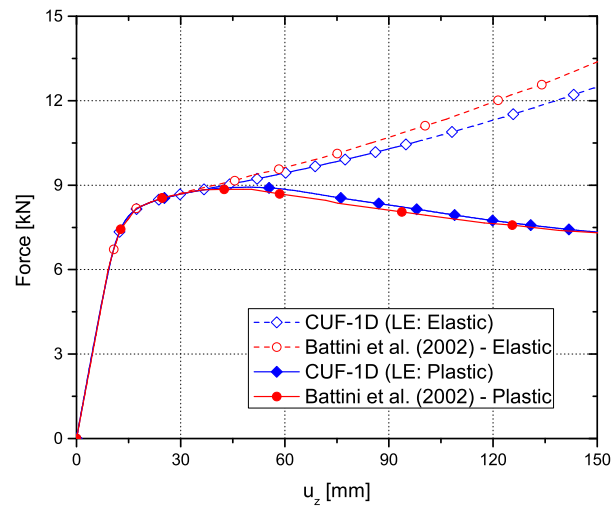


Fig. 5.10 The comparison of equilibrium curves of the C-shaped beam with different material behaviors and the available literature [174]

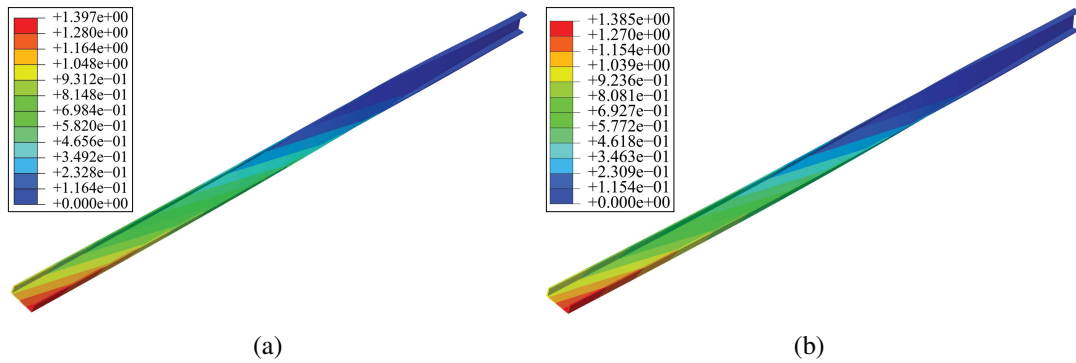


Fig. 5.11 3D contour plots of the displacement for the elastoplastic material, C-shaped beam based on (a) CUF 1D (LE-13L9) (b) ABQ-3D refined models

The axial and transverse shear stresses at the fixed tip displacement of 100 cm ( $u_z=100$  cm) along the middle line of the beam web section ( $x=0$ ) near the clamped edge ( $y=75$  cm) are plotted in Figs. 5.12 and 5.13, respectively. Furthermore, for the elastoplastic material, the 2D contour plots of axial and transverse shear stresses for the corresponding cross-section are shown in Figs. 5.14 and 5.15, respectively. Table 5.6 reports the axial stress  $\sigma_{yy}$  at the point of (0,75,15), and the transverse shear stress  $\sigma_{yz}$  at the point of (0,75,0), for each model of Table 5.5 at the fixed tip displacement of 100 cm ( $u_z=100$  cm).

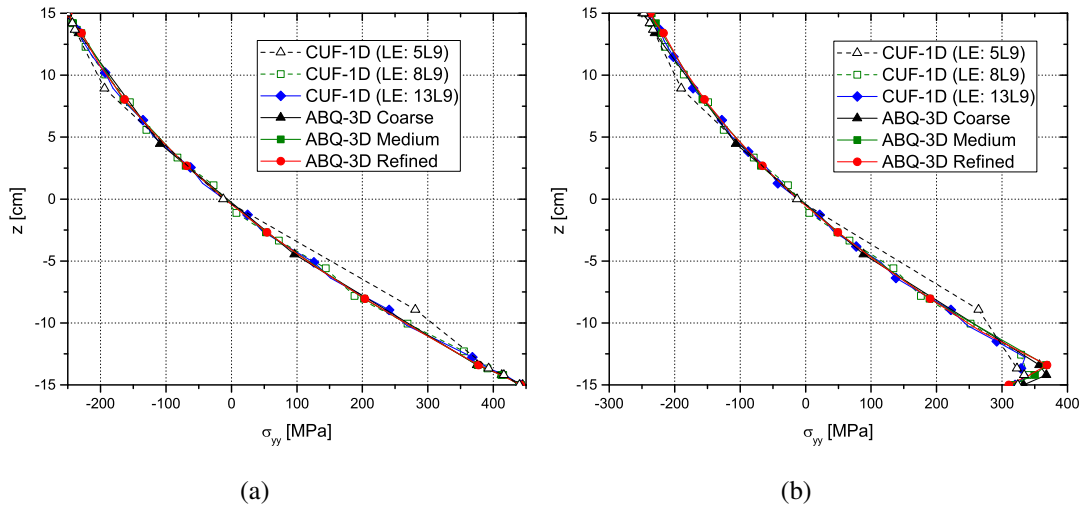


Fig. 5.12 The axial stress at  $x=0$ ,  $y=75$  cm for  $u_z=100$  cm, C-shaped beam, considering (a) elastic material (b) elastoplastic material

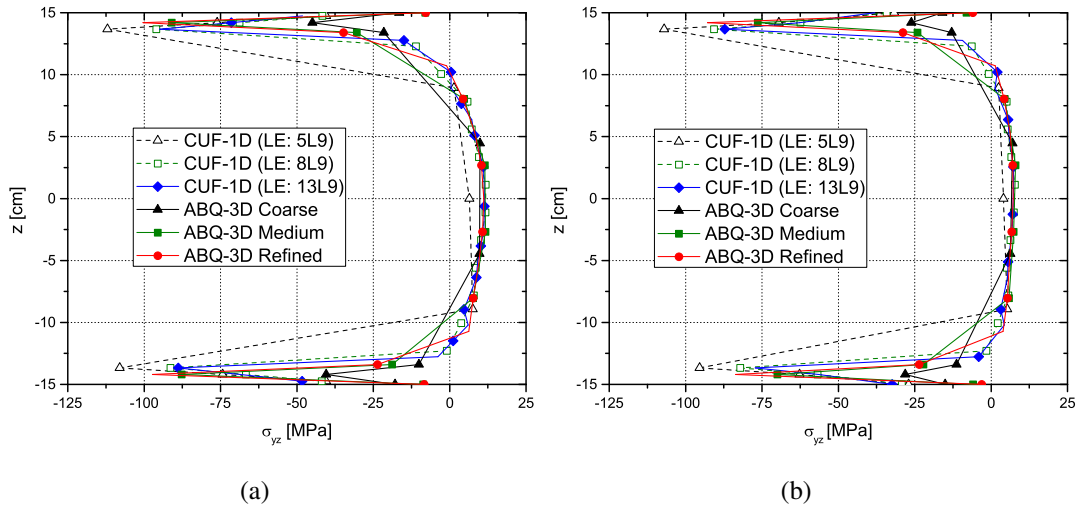


Fig. 5.13 The transverse shear stress at  $x=0$ ,  $y=75$  cm for  $u_z=100$  cm, C-shaped beam, considering (a) elastic material (b) elastoplastic material

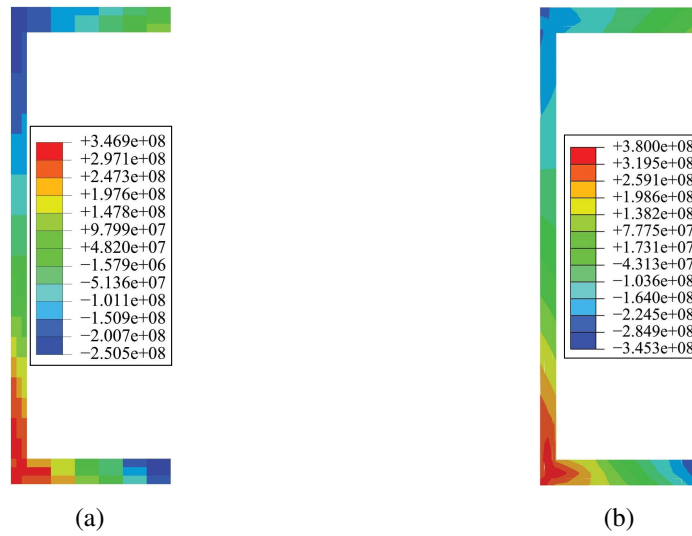


Fig. 5.14 2D contour plots of  $\sigma_{yy}$  for  $u_z=100$  cm, at  $y=75$  cm, elastoplastic material, C-shaped beam based on (a) CUF 1D (LE-13L9) (b) ABQ-3D refined models

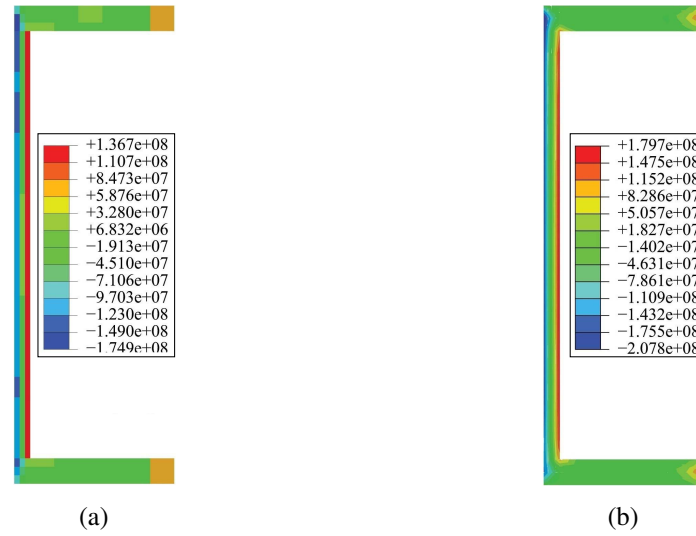


Fig. 5.15 2D contour plots of  $\sigma_{yz}$  for  $u_z=100$  cm, at  $y=75$  cm, elastoplastic material, C-shaped beam based on (a) CUF 1D (LE-13L9) (b) ABQ-3D refined models

Table 5.6 The values of  $\sigma_{yy}$  at  $(0, 75, 15)$ , and  $\sigma_{yz}$  at  $(0, 75, 0)$ , for the C-shaped beam based on various structural theories and 3D FE discretizations for  $u_z=100$  cm

Model	Elastic		Elastoplastic	
	$\sigma_{yy}$ (MPa)	$\sigma_{yz}$ (MPa)	$\sigma_{yy}$ (MPa)	$\sigma_{yz}$ (MPa)
ABQ-3D Coarse	-254.5	9.8	-249.2	6.6
ABQ-3D Medium	-249.5	11.6	-235.1	7.6
ABQ-3D Refined	-249.3	11.1	-236.9	7.1
CUF 1D (LE-5L9)	-251.1	6.4	-247.1	4.0
CUF 1D (LE-8L9)	-249.9	11.7	-242.0	7.6
CUF 1D (LE-13L9)	-251.0	11.4	-238.0	7.2

## 5.5 T-shaped beam

For the last assessment in this section, a T-shaped cantilever beam is assumed with a length of 1200 mm [174]. As can be seen in Fig. 5.16, a transverse force ( $P$ ) and a lateral load  $F=P/1000$  are applied to the free tip. In Table 5.7, the material properties for this beam example are reported, where  $\sigma_0$  and  $E_t$  refer to the yield stress and

tangent modulus of the material with a bilinear stress-strain relation, respectively [174].

Table 5.7 Material properties of the T-shaped beam

Material property	Value
Young's modulus	$E=70$ GPa
Tangent modulus	$E_t=E/10$
Poisson's ratio	$\nu=0.33$
Yield stress	$\sigma_y=500$ MPa

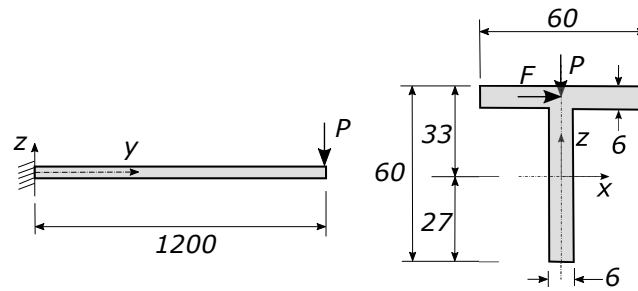


Fig. 5.16 Schematic view of the T-shaped beam, all dimensions are in mm

In Table 5.8, the DOF and computational size of the models considered for this beam example are listed. Three CUF models with 5L9, 7L9, and 9L9 over the cross-section are considered, and the 20B4 discretization is selected along the beam axis. In Fig. 5.17, the equilibrium curve obtained by the CUF model with 9L9 along with reference numerical results from [174] are plotted. A detailed view of the equilibrium curve is provided in Fig. 5.18. It can be understood that the findings for the T-shaped model show characteristics that are comparable to those for the C-shaped beam. Also, the graphs in the figures show the fact that the transverse and lateral displacements are accurately predicted for the very large displacements and rotations.

Table 5.8 Computational size of the investigated models for the T-shaped beam

Model	DOF	Computational time (s)
ABQ-3D Coarse	9393	241
ABQ-3D Medium	18453	477
ABQ-3D Refined	60549	1459
CUF 1D (LE-5L9)	6039	142
CUF 1D (LE-7L9)	8235	364
CUF 1D (LE-9L9)	10431	484

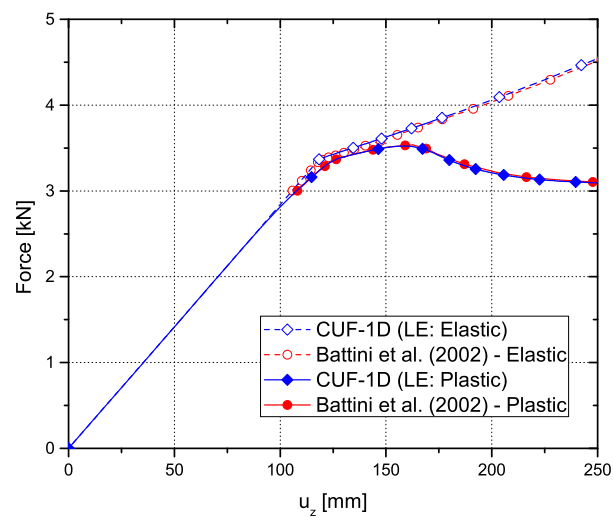


Fig. 5.17 Equilibrium curves obtained from the CUF 1D (LE-9L9) model considering elastic and elastoplastic material behavior. Reference numerical results from [174]



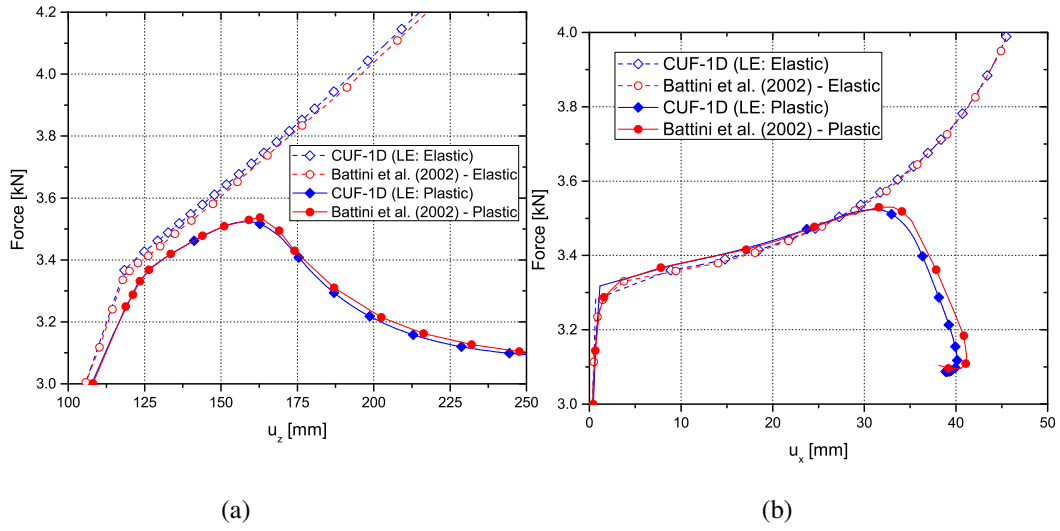


Fig. 5.18 Detailed view of the plasticity initiation for the T-shaped beam (a) force-vertical displacement ( $u_z$ ) curve (b) force-lateral displacement ( $u_x$ ) curve

For a load value of 3400 N, the 3D contour plots of the displacement are indicated in Fig. 5.19. In addition, for the same load value, the 2D contour plots of axial and shear stress components through the beam cross-section near the clamped edge ( $y=100$  mm) are shown in Figs. 5.20 and 5.21, respectively. Table 5.9 reports the transverse displacement  $u_z$  at the free tip of the beam (0, 1200, 30), the axial stress  $\sigma_{yy}$  at (0, 100, 33), and the shear stress  $\sigma_{yz}$  at (0, 100, 0), for a load value of 3400 N. It should be noted that as a result of the significant gradients in stress distributions over the cross-section, proper modeling of shear stress, in particular, necessitates the use of fine 3D meshes or refined CUF 1D LE models.

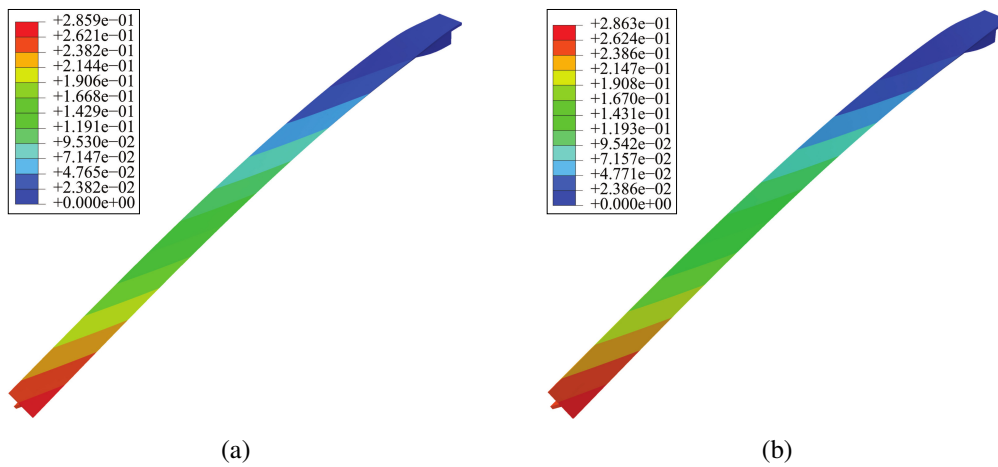


Fig. 5.19 3D contour plots of the displacement at the load of 3400 N for elastoplastic material based on (a) CUF 1D (LE-9L9) (b) ABQ-3D refined models

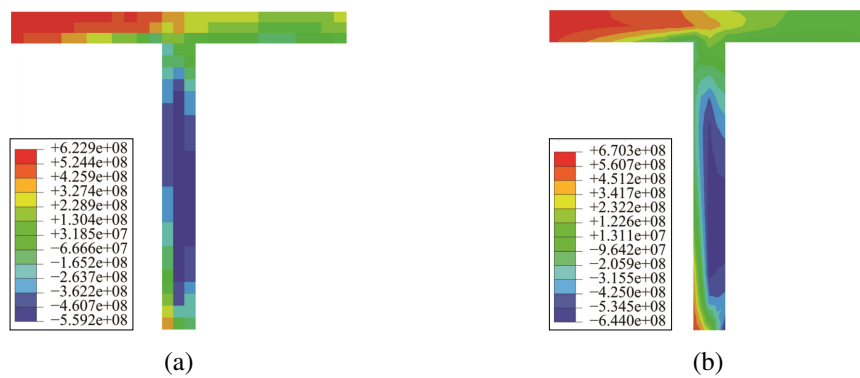


Fig. 5.20 2D contour plots of  $\sigma_{yy}$  (Pa) at the load of 3400 N near the clamped edge ( $y=100$  mm) for the elastoplastic material based on (a) CUF 1D (LE-9L9) (b) ABQ-3D refined models

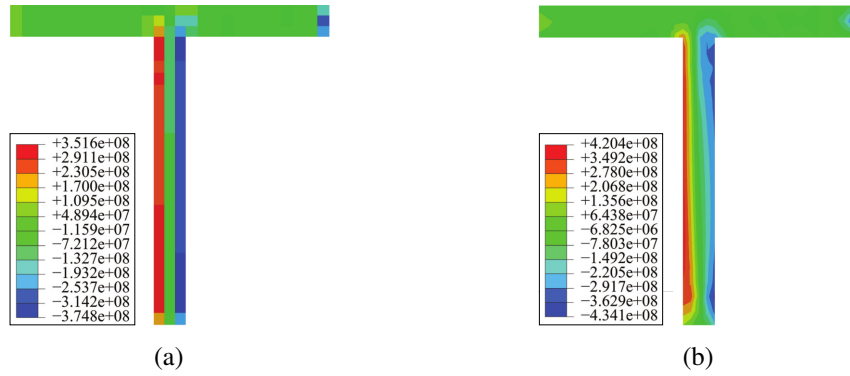


Fig. 5.21 2D contour plots of  $\sigma_{yz}$  (Pa) at the load of 3400 N near the clamped edge ( $y=100$  mm) for the elastoplastic material based on (a) CUF 1D (LE-9L9) (b) ABQ-3D refined models

Table 5.9 The values of  $u_z$  at (0, 1200, 30),  $\sigma_{yy}$  at (0, 100, 33), and  $\sigma_{yz}$  at (0, 100, 0), T-shaped beam based at the load of 3400 N

Model	Elastic			Elastoplastic		
	$u_z$ (mm)	$\sigma_{yy}$ (MPa)	$\sigma_{yz}$ (MPa)	$u_z$ (mm)	$\sigma_{yy}$ (MPa)	$\sigma_{yz}$ (MPa)
ABQ-3D Coarse	122.2	264.7	-9.8	131.9	279.7	-10.7
ABQ-3D Medium	123.9	270.3	-10.4	133.4	286.9	-11.0
ABQ-3D Refined	126.5	279.5	-10.9	135.4	298.8	-12.4
CUF 1D (LE-5L9)	121.7	259.9	-10.5	128.8	281.7	-10.8
CUF 1D (LE-7L9)	123.0	261.5	-10.9	129.3	282.9	-12.1
CUF 1D (LE-9L9)	124.1	267.9	-11.4	130.6	285.4	-12.5

## 5.6 Conclusions

In this chapter, the CUF 1D model in combination with a Newton–Raphson linearization scheme based on the path-following method with arc-length constraint has been used to solve physically and geometrically nonlinear beam problems. Numerical results have been presented for square, channel-shaped, and T-shaped beam structures with elastic and elastoplastic materials subjected to large deformations and rotations. Two types of TE and LE cross-section functions have been used to model the structure. The von Mises constitutive model as described in Section 5.2 has been used for the implementation of elastoplasticity theory.

### **134** Physically and geometrically nonlinear analysis of thin-walled beam structures

- It has been demonstrated that for the beams with different cross-sections, the equilibrium curves obtained by CUF 1D elastic and elastoplastic LE models match well with the results of available literature and 3D solid models.
- The stress distributions have been investigated based on the different LE models, and the results have been compared with 3D FE models.
- For the elastoplastic material, the plastic zones have been initiated near the top and bottom surfaces of the beam near the clamped edge, where the values of equivalent plastic strain have been increased due to the larger load factor values.
- Although the DOF and the computational costs of the problems have been reduced significantly using the current method, it can predict the equilibrium curves and the stress distributions of the structure accurately and precisely.

# Chapter 6

## Large-deflection and post-buckling analysis of flexible plates

### 6.1 Introduction

Plate structures are widely employed in a variety of engineering fields; for example, rectangular cantilever plates in nano-resonators, thin circular plates in computer hard disk drives, thin circular nano-plates of graphene in nano-devices [186]. Many studies have been conducted on the large deflection of plates [187–190]. Turvey and Osman [191] investigated the large deflection of Mindlin plates using the Dynamic Relaxation method. The large deflection of variable-thickness plates was analyzed [192]. Theoretical analyses for the large deflection of plates were proposed by Levy [193, 194]. In order to predict the correct thickness stretching, Alijani and Amabili [195] developed a numerical framework for nonlinear bending and vibration of plates. Amabili et al. [196] carried out a study by higher-order shell theory with thickness deformation as an independent parameter. Alijani and Amabili analyzed the effect of thickness deformation in functionally graded rectangular plates [197]. Comprehensive reports on the buckling and post-buckling response of composite plates were presented in [198, 199]. Librescu and Chang [200] worked on the imperfection sensitivity and post-buckling of composite doubly-curved shallow panels.

As a result of the availability of new components and manufacturing methods, the usage of composite laminated structures has grown significantly, and they are

now routinely employed in the fields of aeronautics, aerospace, automotive, and construction engineering [201]. When made thin enough, composite laminates may be designed to sustain substantial elastic displacements and rotations [202]. In this context, new research trends are emerged for characterizing the geometrically nonlinear response of composite structures [203–207]. Carrera and Kröplin [208] used higher-order shear deformation theories for the large-deflection of composite plates. Considering transverse shear and large rotations, Dash and Singh [209] developed a formulation for the nonlinear bending of laminated plates. Shukla and Nath [210] derived analytical solutions for composite plates with geometrically nonlinear boundary value problems. A review of recent developments in FE analysis of laminated plate structures was presented by Zhang and Yang [211]. Zhang and Kim [212] conducted a nonlinear analysis of different laminated structures by employing FSDT and a displacement-based three-node triangular plate element. Han et al. [213] developed a hierarchical FE method for geometrically nonlinear analysis of composite plates. Zhang and Kim [214] presented a displacement-based four-node quadrilateral element in order to analyze the geometrically nonlinear response of laminated plates. Sridhar and Rao [215] used the four-node quadrilateral composite shell FE in order to investigate circular composite plates in large displacements. A numerical method based on isogeometric analysis and the higher-order shear deformation theory was proposed by Tran et al. [216]. Alijani and Amabili [217] assessed geometrically nonlinear parametric instability of functionally graded plates. Liew et al. [218] used a kp-Ritz method for the nonlinear flexural analysis of plates. Reddy et al. [219] evaluated the influence of various geometrical and loading parameters on the bending analysis of laminated composite plates. Based on a discrete singular convolution approach, nonlinear analysis of thick composite plates resting on nonlinear elastic foundations was presented in [220]. Coda et al. [221, 222] developed FE formulation in order to study nonlinear response and correct stress fields of laminated plates and shells. Nonlinear vibrations and stability of shell and plate structures were investigated thoroughly by Amabili [223]. Interested readers are referred to [224–226] for more information on the nonlinear response of composite plates with the large displacements and rotations.

The post-buckling response of composite plates, which is one of the concerns characterized by the geometrically nonlinear response, merits particular consideration. This is the issue that has been addressed by many researchers [227–230]. For instance, Leissa [231] reviewed the two-dimensional methods for the buckling analy-

sis of laminated composite plates. In addition, Turvey and Marshal [232] presented comprehensive studies on buckling and post-buckling of composite plates. A geometrically nonlinear theory of isotropic symmetrically laminated plates was formulated [233]. By developing an eight-node isoparametric plate FE, Sundaresan et al. [234] analyzed the buckling and post-buckling response of typically two-dimensional thick laminated plates. The influence of material nonlinearity on the post-buckling of composite plates and shells was evaluated [235]. Amabili and Tajahmadi [236] conducted a post-buckling analysis of isotropic and composite plate structures subjected to thermal variations. A Ritz method was presented by Liew et al. [237] in order to study the post-buckling response of two-dimensional laminated structures. Dash and Singh [238] presented buckling and post-buckling analyses of laminated plates with random system properties. Employing the finite strip method, the post-buckling analysis of two-dimensional composite plates subjected to combined compressive and shear loadings was presented [239].

The geometrically nonlinear response of isotropic and composite plates is investigated in this chapter by using the CUF and arc-length approach with path-following constraint. The nonlinear response and post-buckling of plates with high displacements/rotations are studied in this context. As a result of using nonlinear CUF, we are able to take into account various Green-Lagrange strain tensor components. The Newton-Raphson linearization scheme is used to solve the large-deflection and post-buckling problems for various symmetric and antisymmetric composite plates. To show the effectiveness of the present CUF-based method, comprehensive comparisons with existing literature or traditional FE solutions are presented.

## 6.2 Large-deflection response of square isotropic plates

This section makes use of the nonlinear strain-displacement equations found in Table 2.3 of Chapter 2. In this context, the first case is the isotropic square plate. The plate dimensions are  $a=b=1.2$  m, with a thickness-to-width ratio of  $h/a=0.02$  and  $h/a=0.1$  (thin and moderately thick plates). The plate is subjected to the large deflections by a transverse uniform pressure, and the edges are fully clamped (CCCC). The material is isotropic, with Young's modulus of  $E=75$  GPa and Poisson's ratio of  $\nu=0.3$ , respectively. Fig. 6.1 illustrates the loading status and support conditions in this example.

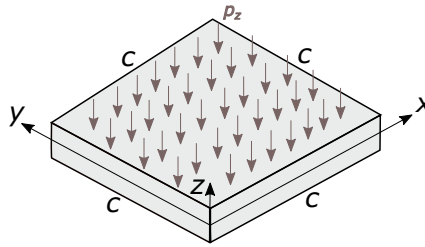


Fig. 6.1 Square plate subjected to uniform pressure

The convergence analysis in this paper takes into account different mesh sizes and expansion functions along the thickness direction. To begin, the number of plate elements is set to 12x12 Q9, and the analysis is conducted to determine the theory order through the thickness direction. The second analysis maintains the fixed order of theory approximation (LD2) while varying the number of FEs. The findings are shown in Fig. 6.2, which illustrates the vertical displacement at the centroid of a moderately thick plate under various pressure loading conditions. According to the results presented in this figure, for the subsequent analyses, 12x12 Q9 elements with the LD2 CUF plate model are employed.

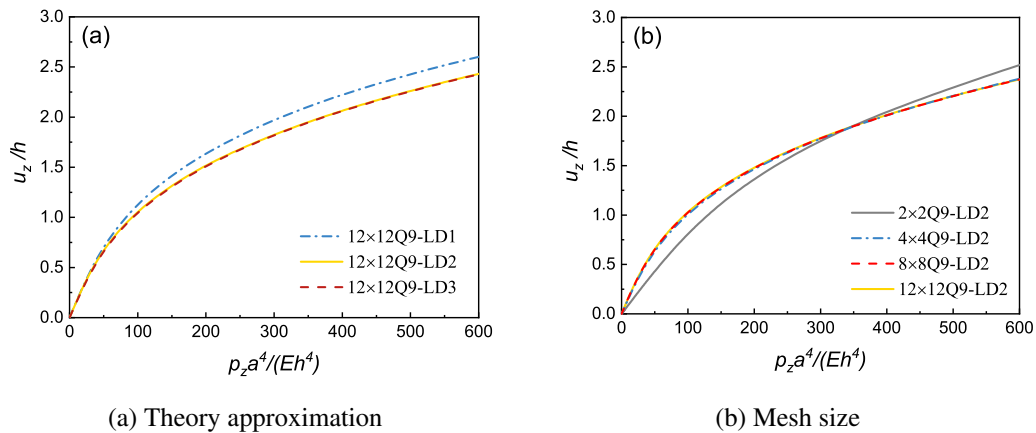


Fig. 6.2 Convergence analysis for the CCCC moderately thick plate

In Fig. 6.3, the large-deflection equilibrium curves of a square plate exposed to uniform pressure are presented using the full nonlinear, von Kármán, and linear CUF plate models. Additionally, the findings are compared to those found in the literature [191]. Fig. 6.3 illustrates the equilibrium curves for both the thin plate ( $h/a = 0.02$ ) and the moderately thick plate ( $h/a = 0.1$ ). The findings indicate that the model provided in this work is capable of reliably predicting large-deflection



equilibrium curves. Additionally, by comparing the two depicted graphs, it is clear that the influence of any geometrically nonlinear strain-displacement relations other than von Kármán theory is negligible for thin plates. As a result, using von Kármán theory in the large-deflection analysis of thin plates could be reliable. However, for moderately thick plates, the inconsistencies between von Kármán theory and the full nonlinear model are more considerable.

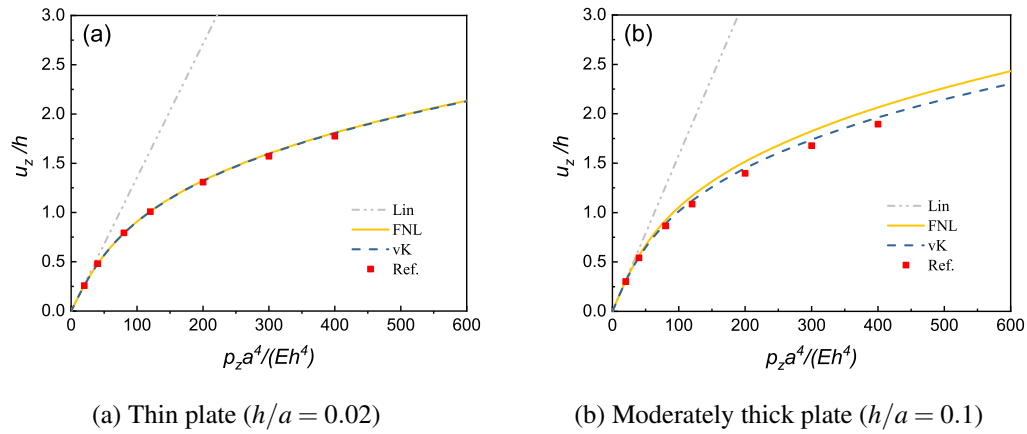


Fig. 6.3 Large-deflection equilibrium curves of CCCC square plates based on different nonlinear strain-displacement assumptions and the available literature [191]

To examine the impact of various nonlinear strain-displacement relations on the equilibrium curves in more detail, nonlinear analysis is conducted using the  $P_{ij}$  parameters established in the Chapter 2. The findings are displayed in Fig. 6.4. This figure demonstrates that the Linear theory (Lin) and the full nonlinear theory (FNL<sub>-vK</sub>) have the most substantial discrepancies when compared to other studied theories. Indeed, the distinction between the von Kármán theory (vK), the full nonlinear theory (FNL), and the various modifications that contain the von Kármán terms (vK<sub>+T</sub>, vK<sub>+S</sub>, vK<sub>+IN</sub>, and vK<sub>+ALL</sub>) is not significant for the case of a plate under bending.

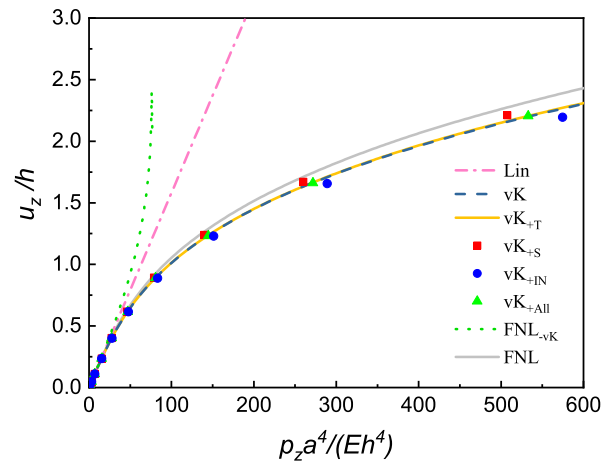


Fig. 6.4 Effect of nonlinear strain-displacement relations on the equilibrium curves in the case of CCCC moderately thick square plate under uniform pressure

Moreover, for the aforementioned problem of bending a moderately thick plate, the stress distributions are examined using several nonlinear theories. This comparison is presented for two fixed load and fixed displacement states in order to have a better understanding of the influence of nonlinear strain-displacement relationships on the axial and shear stress distributions. To begin, we study the through-the-thickness distributions of the dimensionless transverse shear stress  $\sigma_{xz}a^2/(Eh^2)$  at the location  $(x = a/6, y = b/2)$  of CCCC square plates using several full nonlinear plate models under a fixed load of  $\frac{P_z a^4}{Eh^4} = 200$ . As seen in Fig. 6.5, the LD1 and LD2 models are less accurate than the investigated nonlinear theories. Indeed, the LD1 and LD2 full nonlinear CUF plate models are incapable of predicting a physically acceptable shear stress distribution; however, the other higher-order CUF plate models can accurately describe the quadratic shear stress distribution. Note that the prefixes before LD in this figure refer to the number of elements in the thickness direction of plate structure.

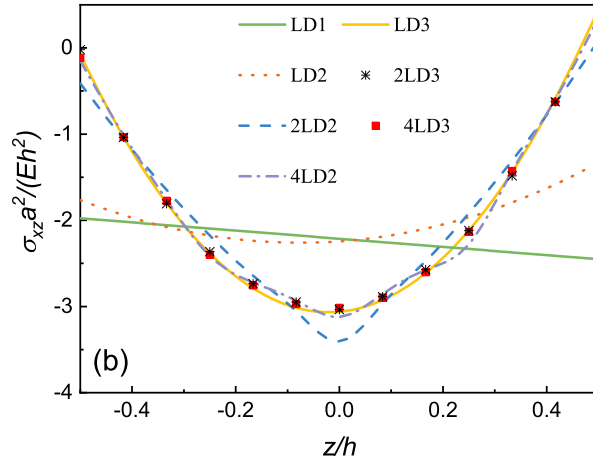


Fig. 6.5 The distributions of the dimensionless transverse shear stress through the thickness of CCCC moderately thick square plate at the point  $(x = a/6, y = b/2)$  and fixed load of  $\frac{P_z a^4}{Eh^4} = 200$

The thickness distributions of the dimensionless in-plane normal stress  $\sigma_{xx}a^2/(Eh^2)$  at the middle point  $(x = a/2, y = b/2)$  of CCCC square plates based on different geometrically nonlinear plate models at a fixed load of  $\frac{P_z a^4}{Eh^4} = 200$  are shown in Fig. 6.6 for LD2 and LD3 plate models. The findings indicate that the difference in axial stress predictions between the analyzed nonlinear theories is not substantial in the case of a plate subjected to bending. As a consequence, both the LD2 and LD3 plate models may provide valid findings for any theories that use von Kármán terms.

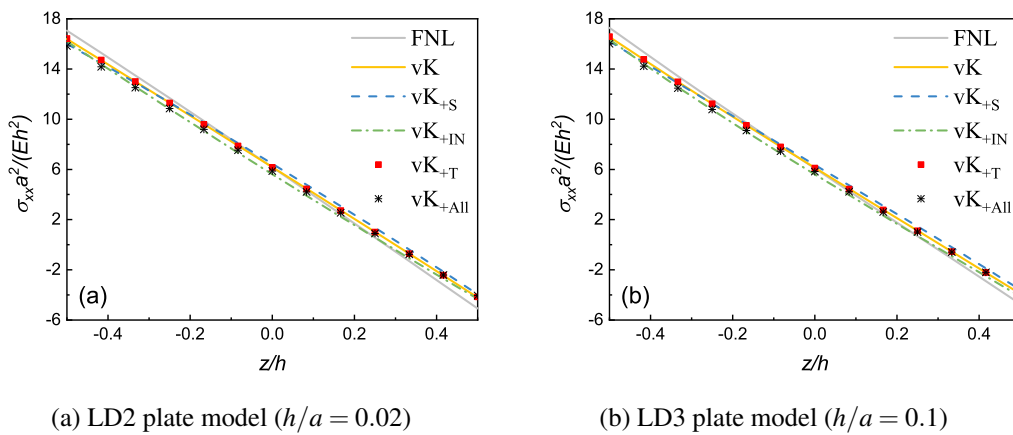


Fig. 6.6 The distributions of the dimensionless in-plane normal stress through the thickness of CCCC moderately thick square plate at the middle point  $(x = a/2, y = b/2)$  and fixed load of  $\frac{P_z a^4}{Eh^4} = 200$

Through-the-thickness distributions of the dimensionless transverse shear stress  $\sigma_{xz}a^2/(Eh^2)$  at the point  $(x = a/6, y = b/2)$  of CCCC square plates based on different geometrically nonlinear plate models at a fixed load of  $\frac{P_z a^4}{Eh^4} = 200$  are shown in Fig. 6.7 according to the LD2 and LD3. The findings demonstrate that the LD3 nonlinear plate model satisfies the traction-free boundary condition ( $\sigma_{xz} = 0$ ) for the shear stress at the bottom surface ( $z = -h/2$ ).

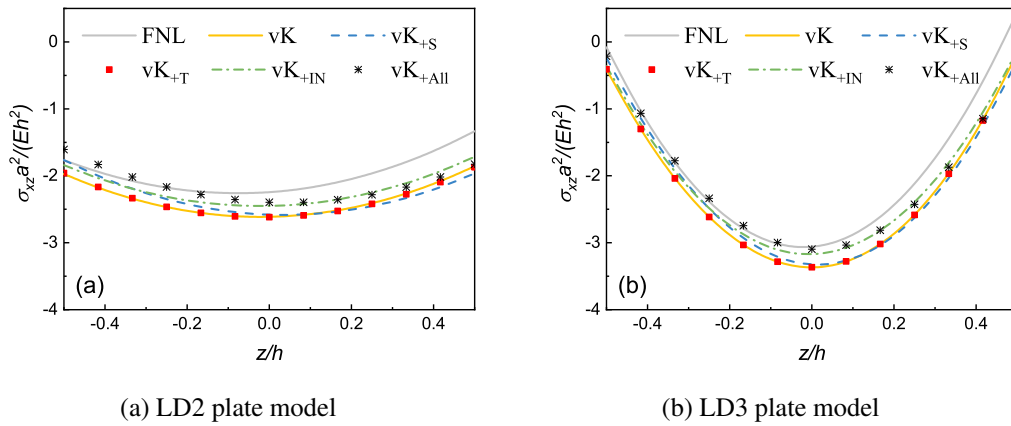


Fig. 6.7 The distributions of the dimensionless transverse shear stress through the thickness of moderately thick square plate at the point  $(x = a/6, y = b/2)$  and fixed load of  $\frac{P_z a^4}{Eh^4} = 200$

Afterwards, the influence of various approximation orders and nonlinear geometric assumptions on the stress distributions is explored in the case of a fixed displacement of  $\frac{u_z}{h} = 1.5$ . The through-the-thickness distributions of the dimensionless in-plane normal stress  $\frac{10\sigma_{xx}}{E}$  at the middle point  $(x = a/2, y = b/2)$  of CCCC square plates based on different geometrically nonlinear plate models at the fixed displacement of  $\frac{u_z}{h} = 1.5$  are depicted in Fig. 6.8 according to the LD2 and LD3 plate models. This figure illustrates the fact that the linear theory and the full nonlinear theories without von Kármán terms have the most substantial discrepancies when compared to the other analyzed theories. Moreover, it can be inferred from this figure that, in this particular case of the plate subjected to bending, there would be a few differences between the predictions of shear stress made by the von Kármán theory, the full nonlinear theory, and also various modifications that contain the von Kármán terms.

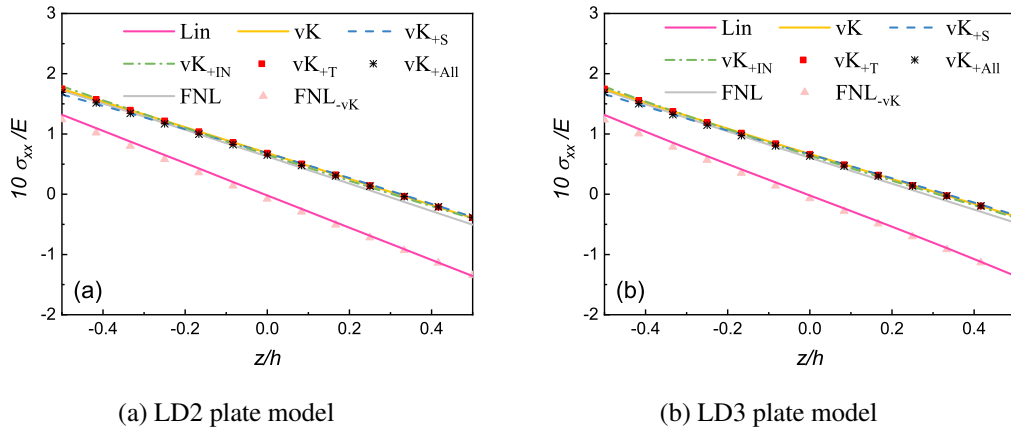


Fig. 6.8 The distributions of the dimensionless in-plane normal stress through the thickness of CCCG moderately thick square plate at the middle point ( $x = a/2, y = b/2$ ) and fixed displacement of  $\frac{u_z}{h} = 1.5$

Fig. 6.9 depicts the through-the-thickness distributions of the dimensionless transverse shear stress  $\frac{100\sigma_{xz}}{E}$  measured at the point ( $x = a/6, y = b/2$ ) of CCCG square plates based on different geometrically nonlinear plate models at the fixed displacement of  $\frac{u_z}{h} = 1.5$ . The findings demonstrate that the LD3 nonlinear plate model satisfies the traction-free boundary condition ( $\sigma_{xz} = 0$ ) of the shear stress at the bottom surface ( $z = -h/2$ ). Furthermore, with the exception of the full nonlinear theory, the differences between the shear stress predictions of the other studied nonlinear theories are not substantial.

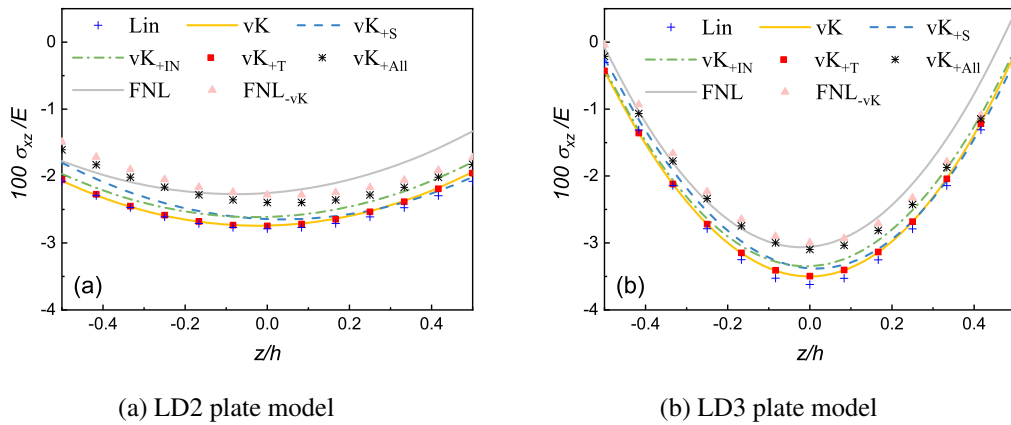


Fig. 6.9 The distributions of the dimensionless transverse shear stress through the thickness of CCCG moderately thick square plate at the point ( $x = a/6, y = b/2$ ) and fixed displacement of  $\frac{u_z}{h} = 1.5$

## 6.3 Post-buckling analysis of slender isotropic plates

Post-buckling analysis of slender plates is discussed in this section, which takes into consideration a variety of edge and loading conditions for different nonlinear strain-displacement relationships. When considering the first example, the dimensions of the slender plates are  $a = 30$  cm,  $b = 6$  cm, and  $h = 0.6$  cm, and the clamped edge condition is in such a way that  $u = v = w = 0$  at  $x = 0$ . The immovable simply-supported edge condition satisfies  $u = v = w = 0$  at  $z = 0$  and  $x = 0$ , and movable simply-supported edge condition ‘S<sub>1</sub>’ satisfies  $v = w = 0$  at  $z = 0$  and  $x = a$ . The compression load is applied at the point  $(x = a, y = b/2, z = 0)$ , and a small deflection load is utilized to provide a stable post-buckling nonlinear response. The material is isotropic, with a Young’s modulus of  $E = 75$  GPa and a Poisson’s ratio of  $\nu = 0.316$ .

### 6.3.1 Validation

The comparison of post-buckling equilibrium curves is presented here for the LD2 full nonlinear and von Kármán models with the validated CUF beam models in [43, 44, 70]. The first plate case has one clamped edge and three free edges (CFFF), while the second one has two immovable simply-supported and movable simply-supported edges in the opposite direction and two other free edges (SFS<sub>1</sub>F). As depicted in Fig. 6.10, the equilibrium curves for both beams and slender plates are seen to be accurate and highly correlated. Additionally, the figure shows that the von Kármán theory is incapable of accurately predicting equilibrium curves in the beam or plate LD2 models.

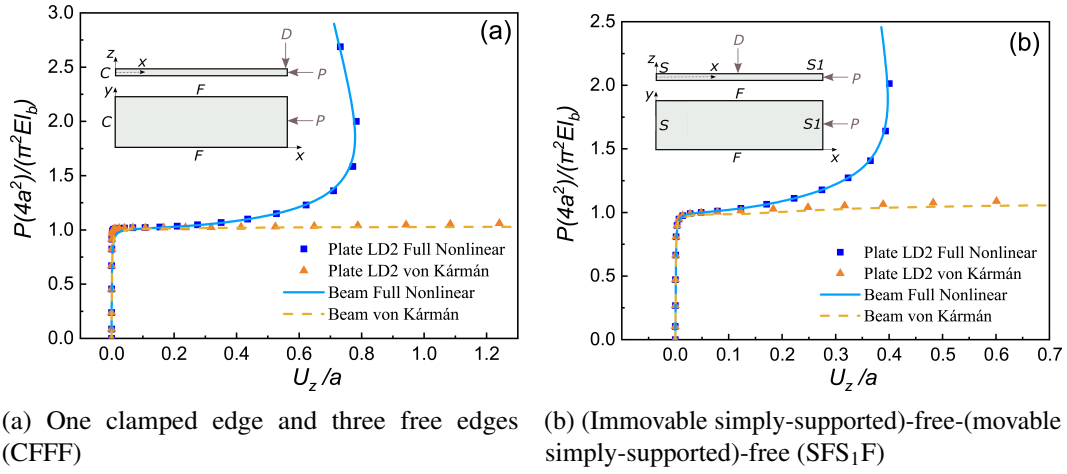


Fig. 6.10 Post-buckling equilibrium curves for slender plates subjected to an in-plane compressive point load  $P$  based on plate and beam models

### 6.3.2 Post-buckling of slender plates with the (movable simply-supported)-free-(movable simply-supported)-free ( $S_1FS_1F$ ) edge conditions

In this section, the post-buckling equilibrium curves and stress distributions of the slender plate under the in-plane compressive point loads are investigated. The slender plate has the length, width and thickness of  $a = 20$  cm,  $b = 5$  cm, and  $h = 0.4$  cm, respectively. The edge conditions for this case are (movable simply-supported)-free-(movable simply-supported)-free ( $S_1FS_1F$ ). The post-buckling equilibrium curves of this case are shown in Fig. 6.11 based on different geometrically nonlinear CUF plate models. The post-buckling equilibrium curves and stress distributions of the slender plate under in-plane compressive loads are studied in this section. The slender plate dimensions are  $a = 20$ cm (length),  $b = 5$ cm (width), and  $h = 0.4$ cm (thickness) with the edge conditions (movable simply-supported)-free-(movable simply-supported)-free ( $S_1FS_1F$ ). Fig. 6.11 illustrates the post-buckling equilibrium curves for this example using several geometrically nonlinear CUF plate models. The findings demonstrate that only the full nonlinear model is capable of providing dependable and accurate results for this example. In fact, the von Kármán theory and all other modifications are unable to accurately estimate the post-buckling equilibrium curves.

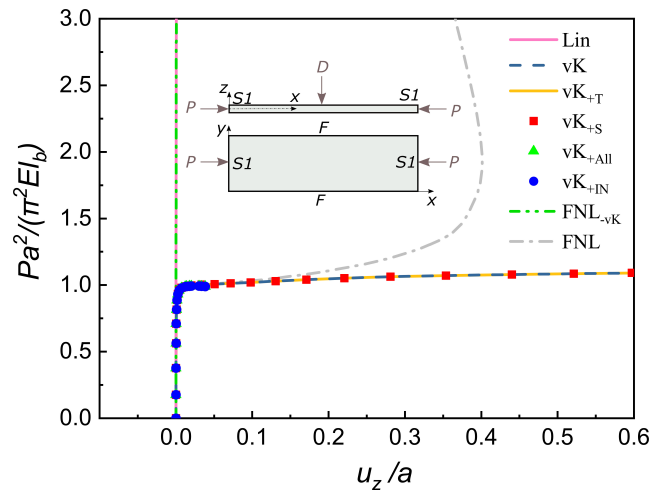


Fig. 6.11 Post-buckling equilibrium curves of  $S_1FS_1F$  slender plates under the in-plane compressive point loads based on the different geometrically nonlinear CUF plate models

A comparison of the stress distributions for this case based on the various nonlinear theories is carried out in order to get a better understanding of the influence of different nonlinear strain-displacement relations on the axial and shear stresses. Fig. 6.12 depicts the through-the-thickness distribution of the dimensionless in-plane normal stress  $\sigma_{xx}bh^2/(Pa)$  at the point  $(x = a/4, y = b/4)$  of  $S_1FS_1F$  slender plates based on various geometrically nonlinear plate models at the fixed load of  $\frac{Pa^2}{\pi^2El_b} = 1.1$ . This study's findings demonstrate that only the full nonlinear model can provide dependable and precise results in this particular example of post-buckling. As a matter of fact, based on the von Kármán theory and its modifications, the axial stress distributions cannot be predicted precisely in this case. According to the graphs, it is also clear that the choice of LD2 or LD3 has a negligible impact on the outcomes of the axial stress evaluations.



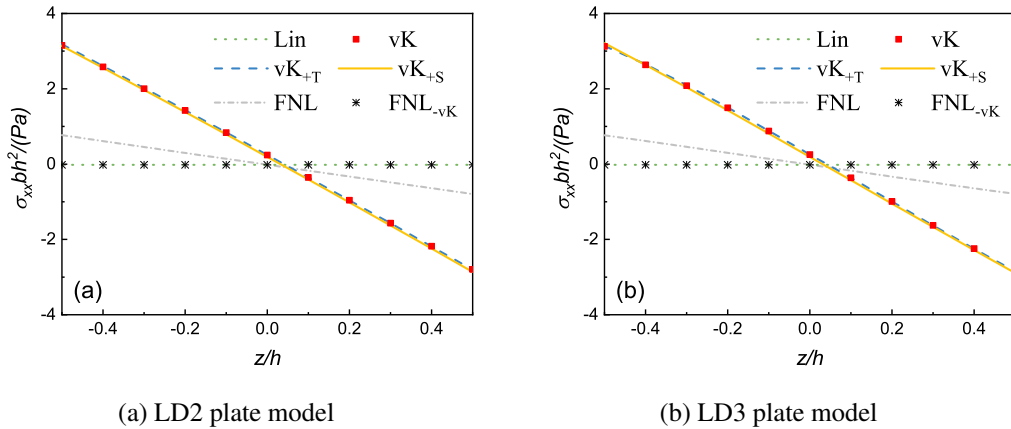


Fig. 6.12 The distributions of the dimensionless in-plane normal stress through the thickness of  $S_1FS_1F$  slender plate at the point  $(x = a/4, y = b/4)$  and fixed load of  $\frac{Pa^2}{\pi^2 EI_b} = 1.1$

Fig. 6.13 depicts the through-the-thickness distributions of the dimensionless transverse shear stress  $\sigma_{xz} h^2 / P$  at the point  $(x = a/4, y = b/4)$  of  $S_1FS_1F$  slender plates based on different geometrically nonlinear plate models at a fixed load of  $\frac{Pa^2}{\pi^2 EI_b} = 1.1$  for the LD2 plate model. The findings demonstrate that there is a significant difference between the shear stress results estimated by the full nonlinear theory and those obtained by other nonlinear plate theories such as the von Kármán and its modifications. Furthermore, neither the linear theory nor the full nonlinear theory without von Kármán terms can accurately assess the shear stress distributions for the LD2 or LD3 plate models, regardless of the plate model.

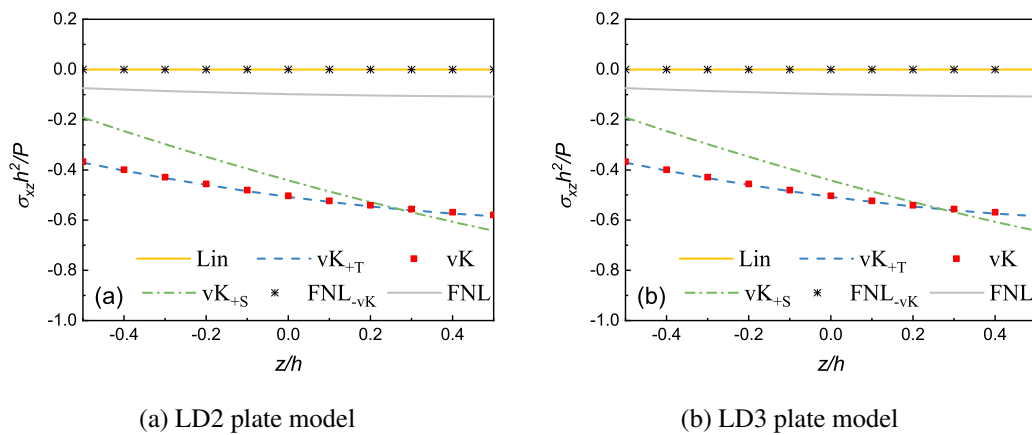


Fig. 6.13 The distributions of the dimensionless transverse shear stress through the thickness of  $S_1FS_1F$  slender plate at the point  $(x = a/4, y = b/4)$  and fixed load of  $\frac{Pa^2}{\pi^2 EI_b} = 1.1$

### 6.3.3 Post-buckling of slender plates with all edges simply-supported ( $S_1S_2S_1S_2$ )

For this example, a line compression load is applied to the plate edges in order to evaluate the influence of the edge and loading conditions on the post-buckling analysis of plates. All the plate edges are simply-supported, and a line compression load as shown in Fig. 6.14 is applied. The resultant force of  $P$  is applied to the middle line of the cross-section. It should be noted that the edge conditions along the length fulfill  $w = 0$  at  $z = 0$  and  $y = 0, b$ . Refer to Fig. 6.14 for a representation of the post-buckling nonlinear response of the thin plate based on several nonlinear strain-displacement relationships for this example.

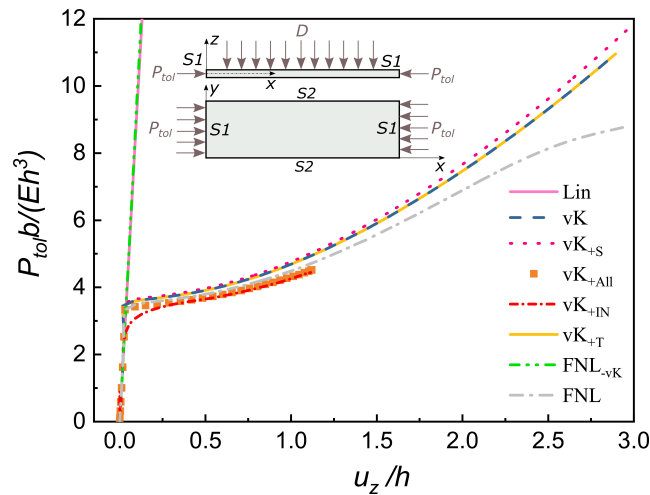


Fig. 6.14 Post-buckling equilibrium curves of slender plates with all edges simply-supported ( $S_1S_2S_1S_2$ ) under the in-plane compressive line loads based on the different geometrically nonlinear CUF plate models

As a consequence of these findings, it is clear that only the full nonlinear model provides dependable and correct results for this case. Nevertheless, the difference between the von Kármán theory and other modifications is not as substantial as the difference between the two nonlinear theories discussed in Section 6.3.2 (see Fig. 6.11). The von Kármán theory and all other modifications are unable to estimate the post-buckling equilibrium curves as correctly and precisely as the full nonlinear theory in this particular plate example. According to mentioned points, the proper assumption of nonlinear geometric relations based on the edge and loading conditions

of the plate structure should be taken into account carefully in order to assess the accurate and precise post-buckling curves of the structure.

## 6.4 Large-deflection of composite plates subjected to transverse pressure

In this section, the large-deflection of composite plates under uniform transverse pressure is evaluated. In this regard, cross-ply laminate  $[0/90]_s$  with different edge conditions, angle-ply laminate  $[45/-45/0/0/45/-45/90/90]_s$  with clamped edge conditions, and cross-ply laminates  $[0/90]$  with clamped edge conditions are investigated.

### 6.4.1 Cross-ply $[0/90]_s$ laminate with different edge conditions

For this plate example, a 4-layer  $[0/90]_s$  square composite plate is considered. The plate has a width of  $a = b = 30.48$  cm and the thickness of  $h = 7.62$  mm. The plate is under the large-deflection due to a transverse uniform pressure. Two kinds of edge conditions are taken for this case: (a) all edges fully clamped that satisfies  $u = v = w = 0$  at  $x = 0, a$  and  $y = 0, b$ , (b) all edges simply-supported that fulfills  $u = v = w = 0$  at  $x = 0, a, z = 0$  and  $y = 0, b, z = 0$ . The material properties for this composite plate are reported in Table 6.1.

Table 6.1 Material properties of the investigated 4-layer  $[0/90]_s$  composite plate [224]

$E_1$ (GPa)	$E_2=E_3$ (GPa)	$G_{12}=G_{13}$ (GPa)	$\nu_{12}=\nu_{13}$
12.60	12.62	2.15	0.2395

Convergence studies, as seen in Fig. 6.15, are used to assess the impacts of mesh approximation and kinematic expansion in this study. To begin, the finite plate elements are  $4 \times 4Q9$ ,  $8 \times 8Q9$ , and  $12 \times 12Q9$ , respectively, with each layer having a fixed LD1 theory approximation order. Then, using the  $12 \times 12Q9$  in-plane mesh approximation, the order of kinematic expansion along the thickness direction is altered from LD1 to LD3. Additionally, the transverse displacement values for different models and loads are presented in Table 6.2, along with the total degrees of freedom (DOF).

As seen in Fig. 6.15 and Table 6.2, convergence is obtained for nonlinear response curves based on the  $12 \times 12\text{Q9-LD1}$  model, which will be utilized to analyze the equilibrium curves of the aforementioned composite plate. Additionally, the findings indicate that the difference between the equilibrium curves for the analyzed CUF plate models with different expansion orders along the thickness is negligible.

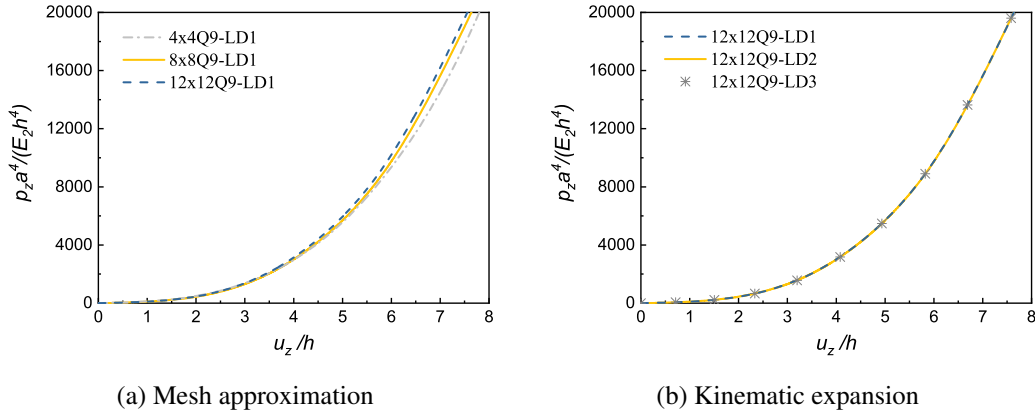


Fig. 6.15 Convergence analysis for a 4-layer  $[0/90]_s$  composite plate under uniform transverse pressure with clamped edge conditions at the center of the composite plate

Table 6.2 Equilibrium points of nonlinear response curves of a 4-layer  $[0/90]_s$  composite plate under transverse pressure with clamped edge conditions

CUF plate model	DOF	$u_z/h$	
		$p_z a^4 / E_2 h^4 = 4000$	$p_z a^4 / E_2 h^4 = 16000$
$4 \times 4\text{Q9-LD1}$	1215	4.44	7.16
$8 \times 8\text{Q9-LD1}$	4335	4.42	7.03
$12 \times 12\text{Q9-LD1}$	9375	4.41	6.98

Fig. 6.16 depicts the equilibrium curves for this composite plate with boundary conditions of clamped or simply-supported. The figure shows the normalized values of the displacement at the central point of the plate versus the normalized values of the applied transverse pressure. The figure shows that the equilibrium curves predicted by the CUF linear and full nonlinear plate models are consistent with those found in the published literature utilizing the first-order shear deformation theory (FSDT) [224]. Furthermore, the difference between linear and nonlinear models

becomes more substantial when the magnitude of the transverse pressure is increased. It should be noted that the load-carrying capability of the composite plate under the clamped edge conditions is greater than that of the composite plate under the simply-supported edge conditions.

The displacement values based on different CUF 2D models and solutions in the available literature [224] are reported in Table 6.3 at a fixed load of  $\frac{P_z a^4}{E_2 h^4} = 100$  for the clamped edge conditions, and at a fixed load of  $\frac{P_z a^4}{E_2 h^4} = 25$  for the simply-supported edge conditions. As shown in this table, the displacement values of the CUF 2D full nonlinear and linear models match well with the corresponding values of the FSDT nonlinear and linear models, respectively.

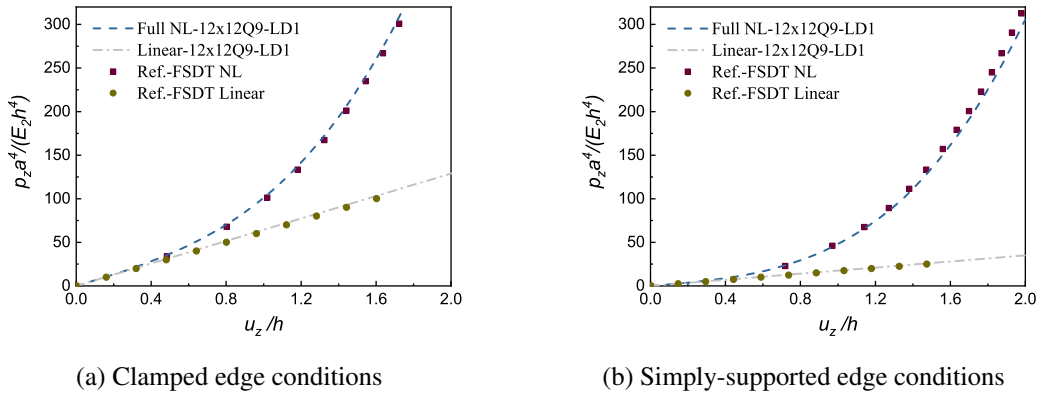


Fig. 6.16 The equilibrium curves for a 4-layer  $[0/90]_s$  composite plate under uniform transverse pressure with different edge conditions based on the CUF 2D and Ref. [224]

Table 6.3 The comparison of displacement values for the 4-layer  $[0/90]_s$  composite plates under transverse pressure at the fixed load of  $\frac{P_z a^4}{E_2 h^4} = 100$  with clamped edge conditions, and at the fixed load of  $\frac{P_z a^4}{E_2 h^4} = 25$  with simply-supported edge conditions

Model	Clamped	Simply-supported
	$u_z$ (mm)	$u_z$ (mm)
Full NL 12×12Q9-LD1	7.57	5.62
Ref. [224] - FSDT NL	7.71	5.67
Linear 12×12Q9-LD1	11.81	10.86
Ref. [224] - FSDT Linear	12.19	11.21

### 6.4.2 $[45/-45/0/0/45/-45/90/90]_s$ laminate with clamped edge conditions

A square composite plate with 16 layers  $[45/-45/0/0/45/-45/90/90]_s$  is considered for this analysis case. The plate has a width of  $a = b = 25.4$  cm and the thickness of  $h = 2.11$  mm. A schematic view of this composite plate is shown in Fig. 6.17. The plate is subjected to large-deflection due to a transverse uniform pressure, and the edges are fully clamped that  $u = v = w = 0$  at  $x = 0, a$  and  $y = 0, b$ . In Table 6.4, the material properties for this composite plate are reported.

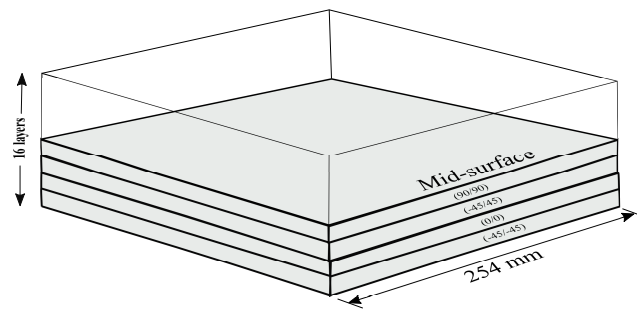


Fig. 6.17 Schematic view of a 16-layer  $[45/-45/0/0/45/-45/90/90]_s$  composite plate

Table 6.4 Material properties of the 16-layer  $[45/-45/0/0/45/-45/90/90]_s$  composite plate [240]

$E_1$ (GPa)	$E_2=E_3$ (GPa)	$G_{12}=G_{13}$ (GPa)	$G_{23}$ (GPa)	$\nu_{12}=\nu_{13}$
131	13.03	6.41	4.72	0.38

Fig. 6.18 shows the convergence analysis for this case. First, the plate FEs are  $4 \times 4Q9$ ,  $8 \times 8Q9$ , and  $12 \times 12Q9$  with the fixed LD1 theory approximation order. Then, the theory order along the thickness direction is changed from LD1 to LD3, while the plate FEs are fixed at  $12 \times 12Q9$ . As can be seen in this figure, the convergence is achieved for the  $12 \times 12Q9$ -LD1 model. Furthermore, the results show that the difference between the equilibrium curves for the investigated theory approximations is not significant for the case of the plate under bending. Furthermore, the transverse displacement values for different CUF plate models and the related DOF are listed in Table 6.5.

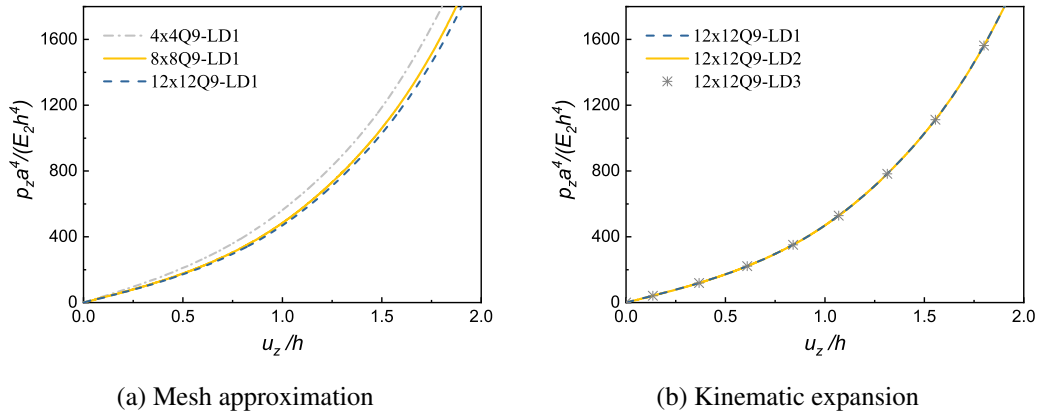


Fig. 6.18 Convergence analysis for a 16-layer  $[45/-45/0/0/45/-45/90/90]_s$  composite plate under uniform transverse pressure with clamped edge conditions

Table 6.5 Equilibrium points of nonlinear response curves of a 16-layer  $[45/-45/0/0/45/-45/90/90]_s$  composite plate under uniform transverse pressure with clamped edge conditions

CUF plate model	DOF	$u_z/h$	
		$p_z a^4 / E_2 h^4 = 400$	$p_z a^4 / E_2 h^4 = 1600$
$4 \times 4Q9-LD1$	4131	0.81	1.71
$8 \times 8Q9-LD1$	14739	0.89	1.80
$12 \times 12Q9-LD1$	31875	0.90	1.82

For this composite plate, the equilibrium curves are shown in Fig. 6.19, which plots the normalized values of the displacement in the middle point of the plate versus the normalized values of the applied transverse pressure. As shown in this figure, the equilibrium curves obtained by the CUF linear and full nonlinear models match well with the corresponding values from the available literature [240–242]. As can be seen in the figure, the difference between linear and nonlinear models is more significant as the transverse pressure value is increased.

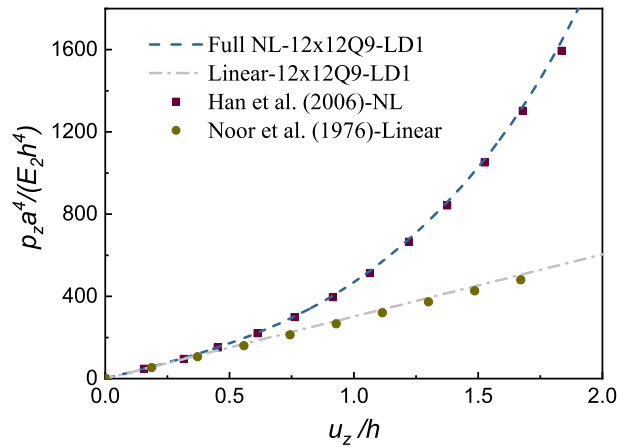


Fig. 6.19 The equilibrium curves for the 16-layer  $[45/-45/0/0/45/-45/90/90]_s$  composite plate based on the CUF 2D and the available literature [240, 242]

### 6.4.3 Cross-ply $[0/90]$ and $[0/90]_3$ laminates with clamped edge conditions

The last large-deflection cases are 2-layer  $[0/90]$ , and 6-layer  $[0/90]_3$  square composite plates with the width of  $a = b = 30.48$  cm and the thickness of  $h = 2.44$  mm. The plates are subjected to the large-deflection due to a uniform transverse pressure, and the edges are fully clamped such that  $u = v = w = 0$  at  $x = 0, a$  and  $y = 0, b$ . The material properties for the two composite plates are shown in Table 6.6.

The large-deflection examples in this section correspond to 2-layer  $[0/90]$  and 6-layer  $[0/90]_3$  square composite plates with a width of  $a = b = 30.48$  cm and a thickness of  $h = 2.44$  mm. A uniform transverse pressure causes the large-deflection in the plates, and the edges are fully clamped such that  $u = v = w = 0$  at  $x = 0, a$  and  $y = 0, b$  and  $u = v = w = 0$ . The material properties of the two composite plates are listed in Table 6.6.

Table 6.6 Material properties of a 2-layer  $[0/90]$  composite plate [224]

$E_1$ (GPa)	$E_2=E_3$ (GPa)	$G_{12}=G_{13}$ (GPa)	$G_{23}$ (GPa)	$\nu_{12}=\nu_{13}$
275.79	6.89	4.13	3.44	0.25



The convergence study seen in Fig. 6.20 is used to assess the impact of in-plane mesh and kinematic expansion approximations. To begin, the finite plate elements are  $2 \times 2Q9$ ,  $4 \times 4Q9$ , and  $8 \times 8Q9$  in size, with each layer having a fixed LD1 kinematic approximation order. The theoretical expansion order is then altered from LD1 to LD3, but the finite plate elements remain fixed at  $8 \times 8Q9$ . Additionally, the transverse displacement values for several CUF plate models are included in Table 6.7, along with the DOF associated with each model. As seen in Fig. 6.20, convergence is obtained at least for the  $4 \times 4Q9$  plate model with LD1 kinematic approximations.

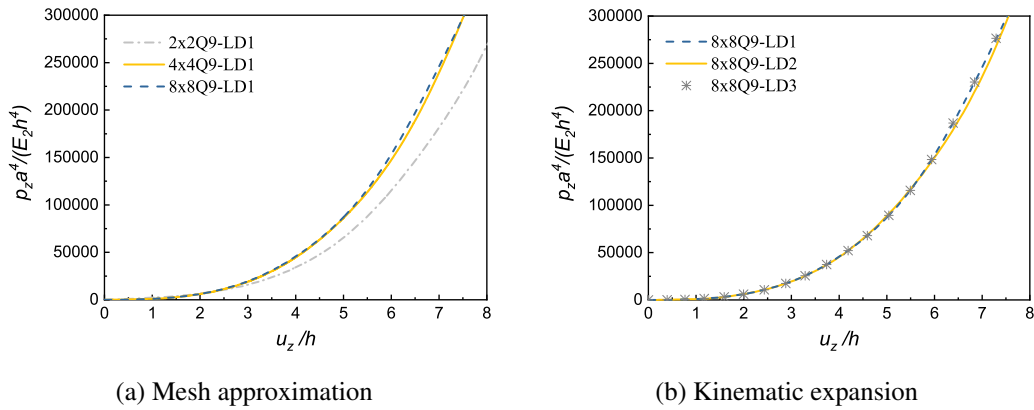


Fig. 6.20 Convergence analysis for a 2-layer  $[0/90]$  composite plate under uniform transverse pressure with clamped edge conditions

Table 6.7 Equilibrium points of nonlinear response curves of a 2-layer  $[0/90]$  composite plate under uniform transverse pressure with clamped edge conditions

CUF plate model	DOF	$u_z/h$	
		$p_z a^4 / E_2 h^4 = 50000$	$p_z a^4 / E_2 h^4 = 250000$
$2 \times 2Q9-LD1$	225	4.61	7.80
$4 \times 4Q9-LD1$	729	4.18	7.07
$8 \times 8Q9-LD1$	2601	4.17	7.05

The equilibrium curves for 2-layer  $[0/90]$  and 6-layer  $[0/90]_3$  composite plates subjected to clamped edge conditions are shown in Fig. 6.21, which plots the normalized values of the displacement at the center of the plate versus the normalized values

of the applied transverse pressure. It is evident in this figure that the equilibrium curves obtained by the CUF linear and full nonlinear plate models provide excellent predictions compared with the solutions in the available literature using the FSDT theory [224]. In addition, the load-carrying capacity of the composite plate with 6 layers is higher than that of the composite plate with 2 layers.

Fig. 6.21 depicts the equilibrium curves for the 2-layer [0/90] and 6-layer [0/90]<sub>3</sub> composite plates subjected to clamped edge conditions. The equilibrium curve for the 2-layer [0/90] and 6-layer [0/90]<sub>3</sub> composite plates subjected to clamped edge conditions. This figure clearly illustrates that the equilibrium curves provided by the CUF linear and full nonlinear plate models give good predictions when compared to the solutions in the available literature obtained by the FSDT theory [224]. Furthermore, the load-carrying capacity of the composite plate with 6 layers is greater than that of the composite plate with 2 layers. In Table 6.3 the displacement values based on the different CUF 2D plate models are compared with the results in the available literature [224] for the 2-layer [0/90] composite plate at the fixed load of  $\frac{P_z a^4}{E_2 h^4} = 500$ , and for the 6-layer [0/90/0/90/0/90] composite plate at the fixed load of  $\frac{P_z a^4}{E_2 h^4} = 1500$ . Based on Table 6.3, the displacement values of the CUF linear and Full nonlinear plate models correlate reasonably well with those obtained by the FSDT nonlinear and linear models, respectively.

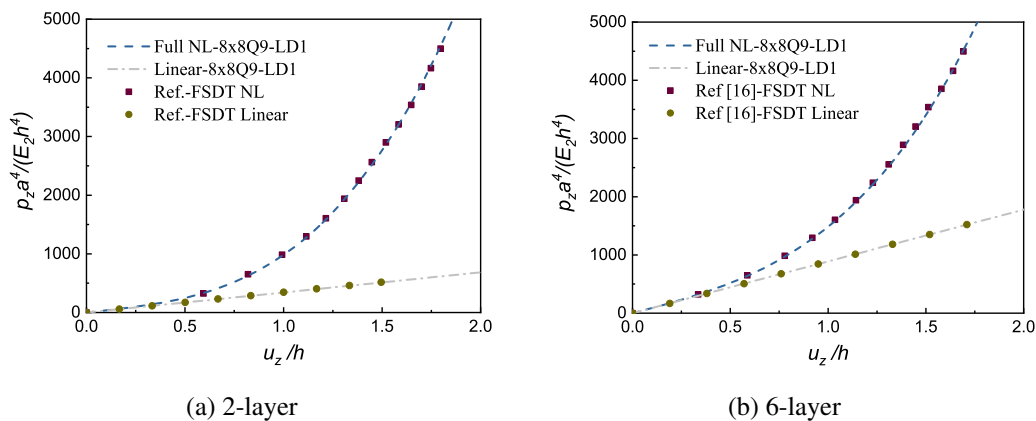


Fig. 6.21 The equilibrium curves for 2-layer [0/90] and 6-layer [0/90]<sub>3</sub> composite plates under uniform transverse pressure with clamped edge conditions based on the CUF 2D and Ref. [224]

Table 6.8 The displacement values based on different methods at the fixed load of  $\frac{P_z a^4}{E_2 h^4} = 500$  for the 2-layer [0/90] composite plate, and at the fixed load of  $\frac{P_z a^4}{E_2 h^4} = 1500$  for the 6-layer [0/90]<sub>3</sub> composite plate

Model	2-layer [0/90]	6-layer [0/90/0/90/0/90]
	$u_z$ (mm)	$u_z$ (mm)
Full NL 8×8Q9-LD1	1.79	2.45
Ref. [224] - FSDT NL	1.78	2.43
Linear 8×8Q9-LD1	3.57	4.12
Ref. [224] - FSDT Linear	3.52	4.11

## 6.5 Post-buckling of composite plates under in-plane compressive loads

In this section, the post-buckling behavior of composite plates under in-plane compressive loads is investigated. In this regard, the cross-ply rectangular laminate [0/90/0/90], cross-ply laminates [0/90...], angle-ply laminate [45/-45/-45/45], and cross-ply laminate [0/90] with different edge and loading conditions are evaluated, and the post-buckling responses of composite plates are compared in different states.

### 6.5.1 Cross-ply [0/90]<sub>2</sub> rectangular laminate with simply-supported edge conditions

This post-buckling example corresponds to a 4-layer [0/90]<sub>2</sub> rectangular composite plate. The structure dimensions are  $a = 20$  cm (length),  $b = 5$  cm (width), and  $h = 2$  mm (thickness). The plate is compressed along the  $x$ -axis,  $N_x$  (force per unit width), as shown in Fig. 6.23. The edges are simply-supported in such a manner that one set of opposite edges along width  $x = 0, a$  satisfies  $v = w = 0$  (S1 in Fig. 6.23), while the other set of opposite edges along the length  $y = 0, b$  satisfies  $w = 0$  at  $z = 0$  (S2 in Fig. 6.23). Additionally, a constraint condition fulfilling  $u = v = 0$  at the plate's center point is employed to prevent the plate's rigid-body motion. Table 6.9

and Fig. 6.23 show the material properties, loading, and edge conditions for this composite plate example.

Table 6.9 Material properties of a 4-layer  $[0/90]_2$  composite plate

$E_1$ (GPa)	$E_2=E_3$ (GPa)	$G_{12}=G_{13}$ (GPa)	$G_{23}$ (GPa)	$\nu_{12}=\nu_{13}$
220	5.5	3.3	2.75	0.25

The convergence analysis of the equilibrium curves for this composite plate is shown in Fig. 6.22. To assess the influence of in-plane mesh and kinematic expansion approximations, the finite plate elements are first assumed to be  $10 \times 2Q9$ ,  $20 \times 5Q9$ , and  $40 \times 10Q9$  with a fixed LD1 kinematic expansion for each layer. The expansion order is then altered from LD1 to LD3, with the finite plate element set at  $20 \times 5Q9$ . Additionally, Table 6.10 presents transverse displacement data for several CUF plate models and loads. It can be understood from the figure that the convergence is obtained at least for the  $20 \times 5Q9$ -LD1 plate model. Thus, as seen in Fig. 6.22 and Table 6.10, the nonlinear response curves are converged when the  $20 \times 5Q9$ -LD1 plate model is employed.

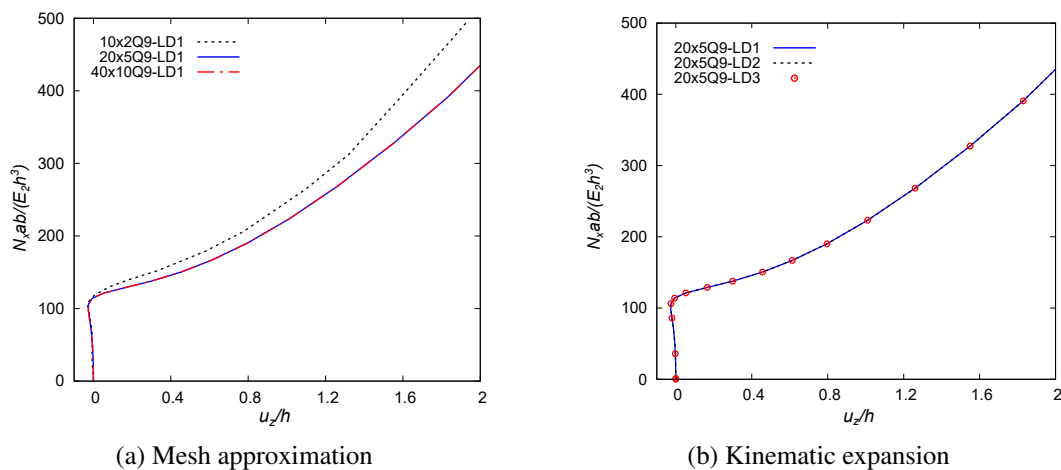


Fig. 6.22 Convergence analysis for a cross-ply  $[0/90]_2$  laminate under in-plane compressive line loads in the  $x$ -axis direction with simply-supported edge conditions

Table 6.10 Equilibrium points of nonlinear response curves of a cross-ply  $[0/90]_2$  laminate under in-plane compressive line loads in the  $x$ -axis direction with simply-supported edge conditions

CUF plate model	DOF	$u_z/h$	
		$N_x ba/E_2 h^3 = 200$	$N_x ba/E_2 h^3 = 400$
$10 \times 2Q9$ -LD1	1575	0.731	1.618
$20 \times 5Q9$ -LD1	6765	0.859	1.865
$40 \times 10Q9$ -LD1	25515	0.859	1.865

For a cross-ply  $[0/90]_2$  composite plate, the equilibrium curves derived using the CUF 2D full nonlinear model, the ABQ 2D shell model, and the ABQ 3D solid model are shown in Fig. 6.23. As seen in this figure, the equilibrium curves calculated using the CUF 2D full nonlinear model match well with those obtained using the ABQ 3D solid model. On the contrary, the ABQ 2D shell model predicts accurate results only for small or moderate displacements, whereas the discrepancy becomes more evident for high displacements. It should be noted that a fine mesh utilizing C3D20R elements is employed in the nonlinear analysis using the ABQ 3D solid model.

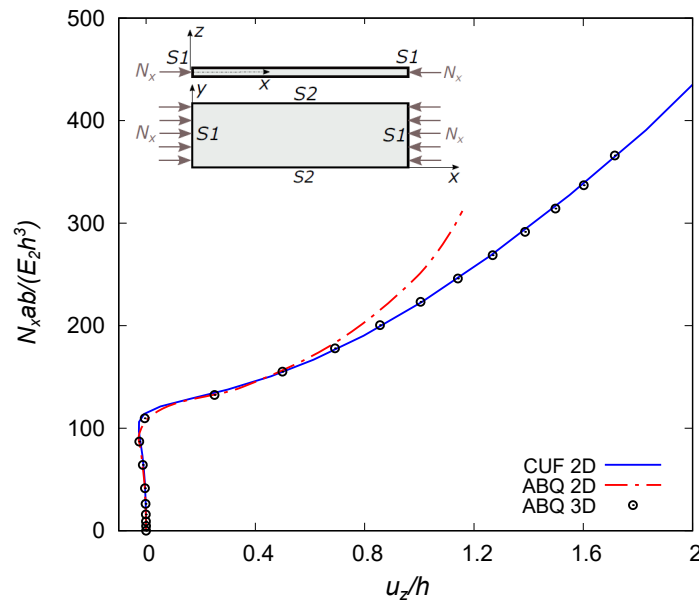


Fig. 6.23 The comparison of equilibrium curves for the cross-ply  $[0/90]_2$  laminate based on the CUF 2D full nonlinear model ( $20 \times 5Q9$ -LD1), ABQ 2D NL model ( $60 \times 15$  S8R) and ABQ 3D NL model ( $60 \times 15 \times 4$  C3D20R)

The deformed configurations for the mentioned rectangular composite plate at the fixed load of  $\frac{N_x b a}{E_2 h^3} = 300$  are shown in Fig. 6.24. The results are obtained based on the CUF 2D full nonlinear model (20×5Q9-LD1), the ABQ 2D shell model (60×15 S8R), and the ABQ 3D solid model (60×15×4 C3D20R). This figure demonstrates that the buckling pattern and displacement values indicated by the CUF 2D model are consistent with those predicted by the ABQ models. Table 6.11 reports the displacement values at the mentioned load and the corresponding linear buckling loads evaluated by each one of the three models. It can be comprehended that although the DOF and the computational costs of the problem are reduced significantly using the current CUF 2D model, it offers reliable and accurate results that match well with the ABQ models.

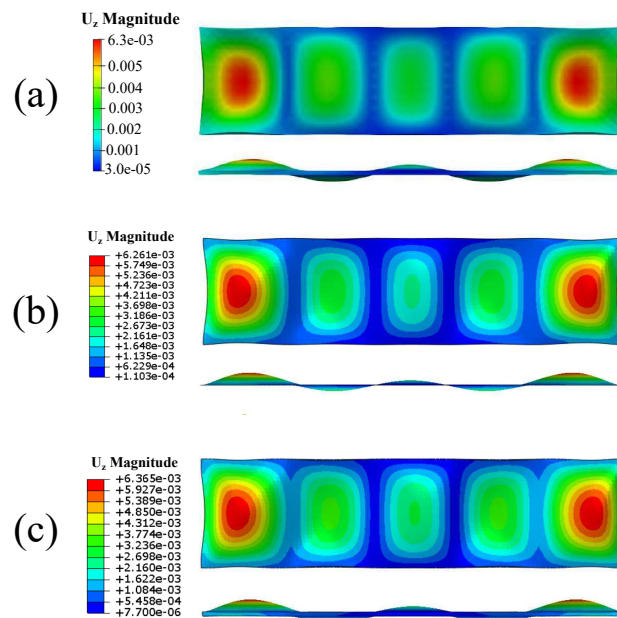


Fig. 6.24 The comparison of displacement contours at the fixed load of  $\frac{N_x b a}{E_2 h^3} = 300$  for a cross-ply  $[0/90]_2$  laminate based on (a) CUF 2D full nonlinear 20×5Q9-LD1 model, (b) ABQ 2D NL 60×15 S8R model and (c) ABQ 3D NL 60×15×4 C3D20R model

Table 6.11 The comparison of displacement values at the fixed load of  $\frac{N_x b a}{E_2 h^3} = 300$  and the normalized linear buckling loads for a cross-ply  $[0/90]_2$  laminate

Model	DOF	$u_z$ (mm)	Linear Buckling Load (N/m)
CUF 2D Full NL 20×5Q9-LD1	6765	1.422	503360
ABQ 2D NL 60×15 S8R	17106	1.134	497658
ABQ 3D NL 60×15×4 C3D20R	24993	1.428	498976

### 6.5.2 Cross-ply $[0/90]_n$ square laminates with simply-supported edge conditions

In this section, the cross-ply  $[0/90]_n$  composite square plates are evaluated [224]. Note that the number of  $[0/90]$  layers are denoted by subscript  $n$ . This structure has the dimensions of  $a = b = 1$  m and  $h = 2$  mm. The plate is under a uniformly distributed in-plane compressive line load  $N_y$  (force per unit length). As can be seen in Fig. 6.26, the edge conditions are simply-supported in such a way that one set of opposite edges  $x = 0, a$  satisfy  $v = w = 0$ , and the other set of opposite edges  $y = 0, b$  fulfill  $u = w = 0$ . The material properties of this composite plate are reported in Table 6.12.

Table 6.12 Material properties of a  $[0/90]_n$  composite plate [224]

$E_1$ (GPa)	$E_2=E_3$ (GPa)	$G_{12}=G_{13}$ (GPa)	$G_{23}$ (GPa)	$\nu_{12}=\nu_{13}$	$\nu_{23}$
250	6.25	5.125	3.25	0.24	0.49

The convergence analysis of the equilibrium curves for this composite plate structure is provided in Fig. 6.25. In addition, the transverse displacement values for different CUF plate models and loads are listed in Table 6.13. It can be noted from Fig. 6.25 and Table 6.13 that the convergence is obtained at least for the  $12 \times 12$ Q9-LD1 model.

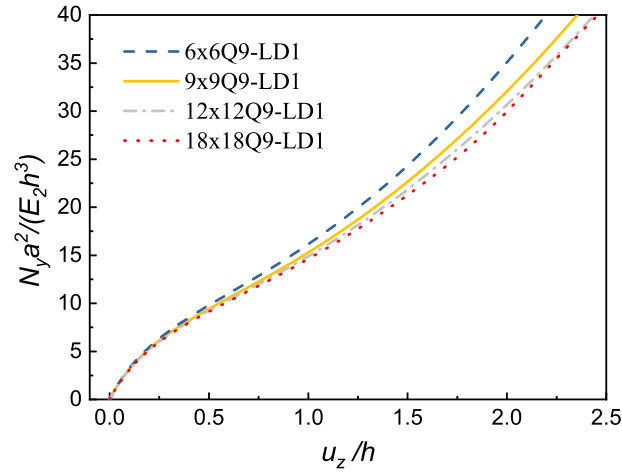


Fig. 6.25 Convergence analysis of the in-plane mesh approximation for a cross-ply [0/90] laminate under in-plane compressive line loads in the  $y$ -axis direction with simply-supported edge conditions

Table 6.13 Equilibrium points of nonlinear response curves of a cross-ply [0/90] laminate under in-plane compressive line loads in the  $y$ -axis direction with simply-supported edge conditions

CUF plate model	DOF	$u_z/h$	
		$N_y a^2 / E_2 h^3 = 15$	$N_y a^2 / E_2 h^3 = 35$
$6 \times 6Q9-LD1$	1521	0.90	1.97
$9 \times 9Q9-LD1$	3249	0.97	2.11
$12 \times 12Q9-LD1$	5625	1.01	2.19
$18 \times 18Q9-LD1$	12321	1.03	2.20

In Fig. 6.26, the equilibrium curves found using the CUF 2D full nonlinear model and solutions from the existing literature are compared. The horizontal lines in this figure represent the relevant linear buckling load calculated using the CUF. It can be noticed from Fig. 6.26 that the equilibrium curves obtained by the CUF 2D full nonlinear model correlate well with those available in the literature [224]. The findings demonstrate that when the plate thickness is kept constant, increasing the layers number of the composite plate structure increases the structural stiffness and the load-carrying capability of the plate structure. Additionally, the linear buckling



strength of the  $[0/90]_4$  plate with 8 layers is dramatically higher than the one for  $[0/90]_1$  plate with 2 layers.

It is noted from Fig. 6.26 that no exact buckling load exists for the  $[0/90]_n$  composite plate structure based on the CUF full nonlinear plate model. This is because the antisymmetric composite laminate is under in-plane compressive loads. The buckling load predicted by the linear buckling analysis is much higher than that based on the full nonlinear plate model. Therefore, the linear buckling analysis cannot be utilized to calculate the buckling load of the antisymmetric plate structure due to the curvature introduced by the in-plane compressive loads. Additionally, it is clear that the linear buckling strength of the  $[0/90]$  composite plate is much less than that of all other composite plates studied. As seen in Fig. 6.26, there is no exact buckling load for the  $[0/90]_n$  composite plate structure. As a result of the curvature introduced by the in-plane compressive loads for this antisymmetric composite laminate, the linear buckling analysis predicts a substantially larger buckling load than the full nonlinear plate model.

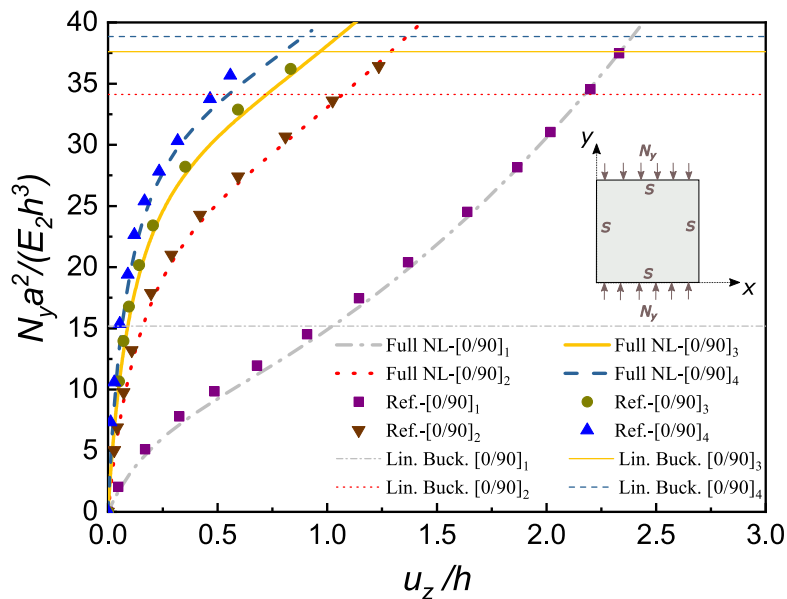


Fig. 6.26 The equilibrium curves for different cross-ply  $[0/90]_n$  laminated plates based on the CUF 2D full nonlinear  $12 \times 12$ Q9-LD1 model and Ref. [224]

### 6.5.3 Angle-ply $[45/-45]_s$ laminate with simply-supported edge conditions

In this section, a composite square plate  $[45/-45]_s$  subjected to the combined loading [240] is investigated. The plate width and thickness are  $a = b = 0.25$  m and  $h = 2.5$  mm, respectively. The composite plate is assumed to have different loading conditions including the combination of uniformly distributed in-plane compressive biaxial line loads of  $N_x$  and  $N_y$  ( $N_x = N_y$ ), the in-plane shear load of  $N_{xy} = N_x$ , and the uniform transverse pressure of  $P_z = 0.1N_x$ . For this plate example, the edge conditions are assumed to restrain all the transverse deflections at the edges. A schematic view of the loading conditions and the material properties of the investigated composite plate are shown in Fig. 6.27 and Table 6.14, respectively.

Table 6.14 Material properties of a 4-layer  $[45/-45]_s$  composite plate [240]

$E_1$ (GPa)	$E_2=E_3$ (GPa)	$G_{12}=G_{13}$ (GPa)	$\nu_{12}=\nu_{13}$
206.9	5.2	2.6	0.25

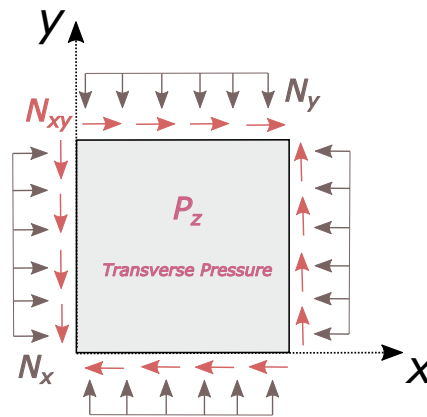


Fig. 6.27 Combined loading of a laminated composite plate: negative in-plane shear, in-plane compression, and the uniform transverse pressure [240]

In Fig. 6.28, the convergence analysis of the equilibrium curves is given, which plots the normalized values of the displacement in the middle point of the plate against the values of the loading factor ( $\lambda$ ). Fig. 6.28 shows that the convergence is achieved at least for the  $12 \times 12$ Q9-LD1 plate model. As can be seen in Fig. 6.29, the deflection in the center of the laminate is increased with the load after the bifurcation

point. The findings demonstrate that the direction of the applied shear loading has a significant impact on the post-buckling behavior of the angle-ply composite plate; for instance, the plate with negative shear loading shows higher stiffness and load-carrying capability.

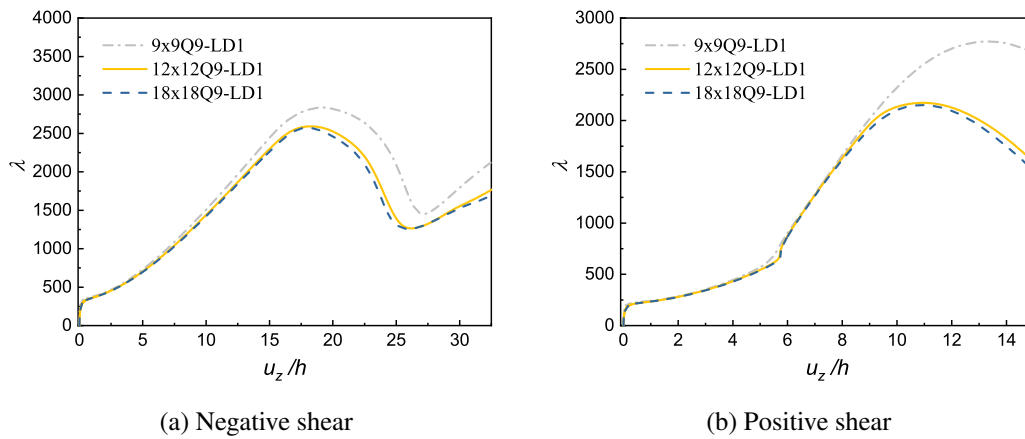


Fig. 6.28 Convergence analysis for an angle-ply  $[45/-45]_s$  laminate under the combined loading with simply-supported edge conditions

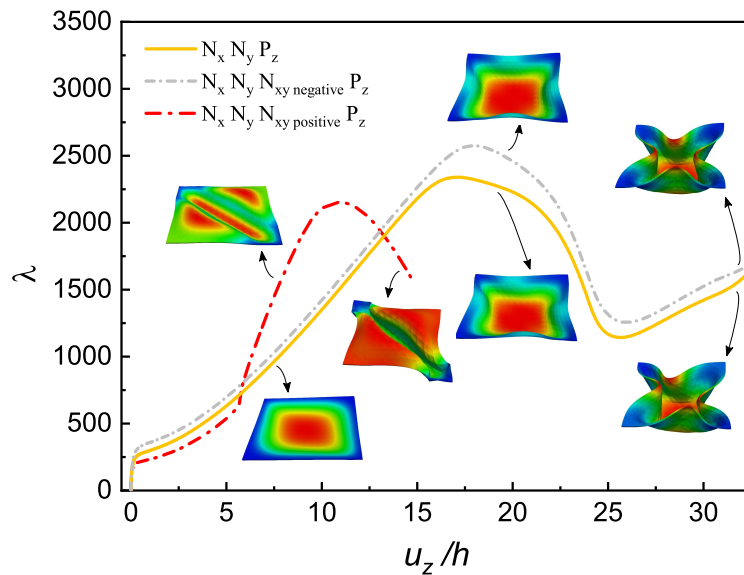


Fig. 6.29 The equilibrium curves based on the values of loading factor  $\lambda$  for an angle-ply  $[45/-45]_s$  laminate under different combined loadings with simply-supported edge conditions

Fig. 6.30 depicts the equilibrium curves for this angle-ply composite plate under various combined loadings. This graph plots the normalized values of the displace-

ment in the middle point of the plate versus the normalized values of the applied compressive line load in the  $x$ -axis direction. The associated linear buckling loads calculated by the CUF are shown by the horizontal lines in this figure. Based on the results of the linear buckling analysis shown in Fig. 6.30, it can be concluded that, for this symmetric composite structure, the buckling loads predicted by the linear buckling analysis are nearly identical to those predicted by the CUF full nonlinear plate model. Hence the linear buckling analysis can be used to predict the buckling load of the symmetric composite structure, which can then be used to design the composite plate structure. The linear buckling load of the angle-ply plate with negative shear is also greater than the load of the other examples, demonstrating the previously indicated fact that the angle-ply plate with negative shear loading has more stiffness and load-carrying capacity. Finally, it should be underlined that while the transverse pressure is relatively small in comparison with the in-plane loads, the equilibrium curves with transverse pressure eventually approach those without transverse pressure when the loading is increased continuously.

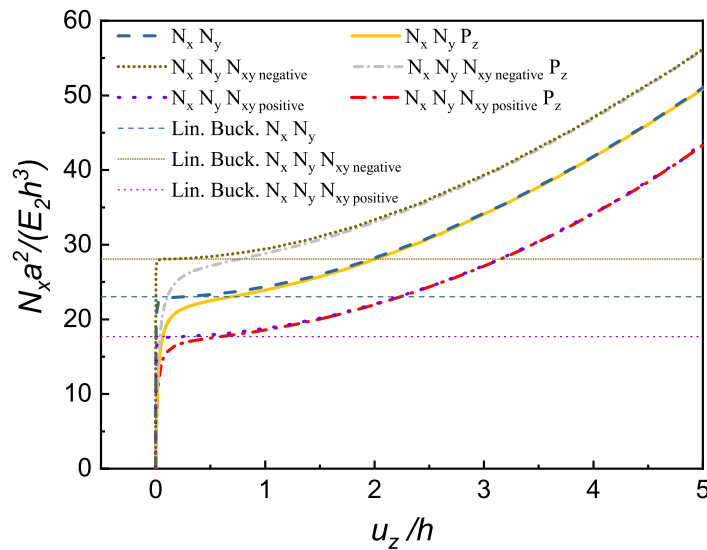


Fig. 6.30 The equilibrium curves for an angle-ply  $[45/-45]_s$  laminate under different combined loadings with simply-supported edge conditions

### 6.5.4 Cross-ply [0/90] square laminate with different edge conditions

For the last post-buckling example, the influence of different edge conditions on the post-buckling nonlinear response of the cross-ply composite plate under in-plane compressive loads is shown. This problem corresponds to a cross-ply [0/90] square plate with different edge conditions [237]. This dimensions of the plate structure are  $a = b = 1$  m and  $h = 1$  cm. Firstly, a uniformly distributed in-plane compressive line load in the  $x$ -axis direction  $N_x$  is applied to the plate. Then, for the other analysis case, a uniformly distributed in-plane compressive line load in the  $y$ -axis direction  $N_y$  is applied to the plate structure. The assumed edge conditions include SSSS, SSCC, SSSC, SSFC, and SSFS. Note that the letters "S", "C", and "F" for the edge conditions represent simply-supported, clamped, and free edge conditions, respectively. In addition, the third and fourth letters of the mentioned boundary condition refer to  $y = b$  and  $y = 0$ , respectively. Also, it is worth noting that the clamped edge conditions fulfill  $u = v = w = 0$  at the associated edge and the simply-supported edge conditions fulfill  $v = w = 0$  at  $x = 0, a$ , or  $u = w = 0$  at  $y = 0, b$ . In Table 6.15, the material properties of this composite plate are provided.

Table 6.15 Material properties of a 2-layer [0/90] composite plate [237]

$E_1$ (GPa)	$E_2=E_3$ (GPa)	$G_{12}=G_{13}$ (GPa)	$G_{23}$ (GPa)	$\nu_{12}=\nu_{13}$
220	5.5	3.3	2.75	0.25

The convergence analysis of the equilibrium curves for the in-plane compressive loads in the  $x$ -axis direction is shown in Fig. 6.31 for this cross-ply composite plate with simply-supported edge conditions. This figure demonstrates that convergence is achieved at least for the 12×12Q9-LD1. In Figs. 6.32 and 6.33, the equilibrium curves based on this plate model are studied for SSSS, SSCC, SSSC, SSFC, and SSFS edge conditions to determine the influence of various edge conditions on the cross-ply composite plate's nonlinear response. The horizontal lines in the magnified views of these two figures depict the associated linear buckling loads calculated using the CUF. The findings indicate that the load-carrying capability of the composite plate under clamped edge conditions is greater than other studied edge conditions. Additionally, it is understandable that the presence of a free edge considerably affects

the buckling strength, and results in the reduction of that. It can be concluded that the present method can be used efficiently to investigate the composite plate's nonlinear behavior beyond the limit load and snap-through instability.

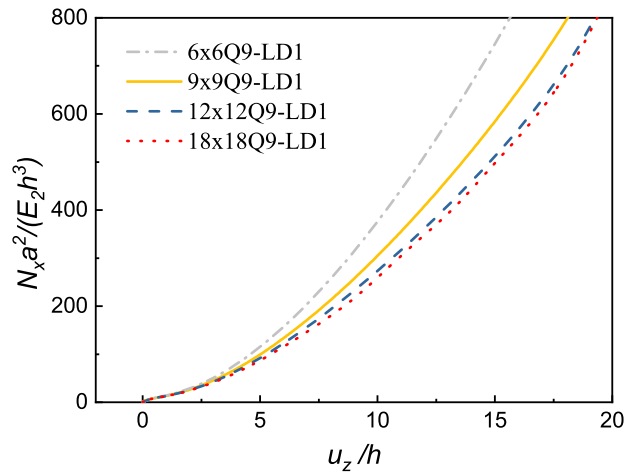


Fig. 6.31 Convergence analysis of the in-plane mesh approximation for a cross-ply [0/90] laminate under in-plane compressive loads in the  $x$  axis direction with simply-supported edge conditions

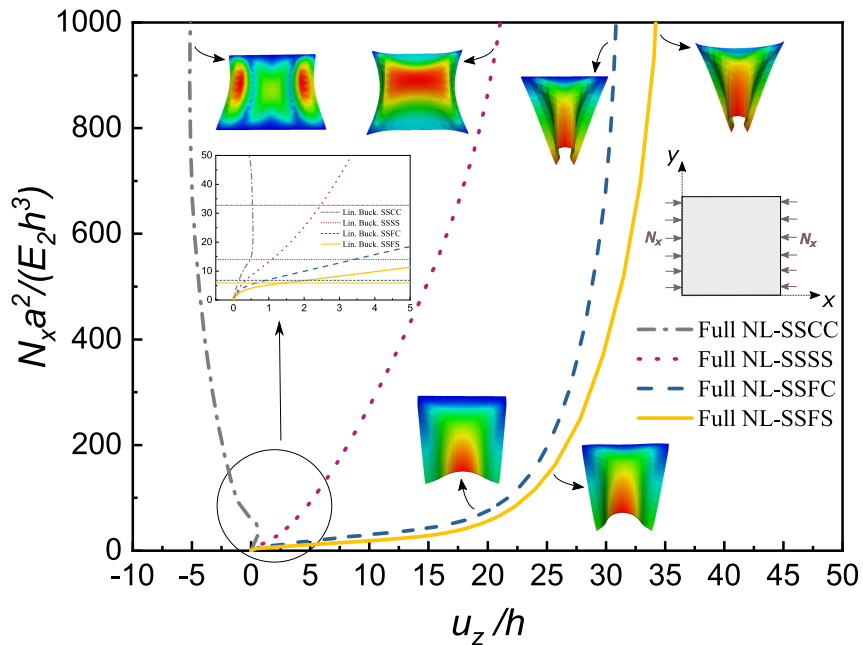


Fig. 6.32 The equilibrium curves for a cross-ply [0/90] laminate under in-plane compressive line loads in the  $x$ -axis direction with different edge conditions based on CUF 2D full nonlinear  $12 \times 12$ Q9-LD1 model

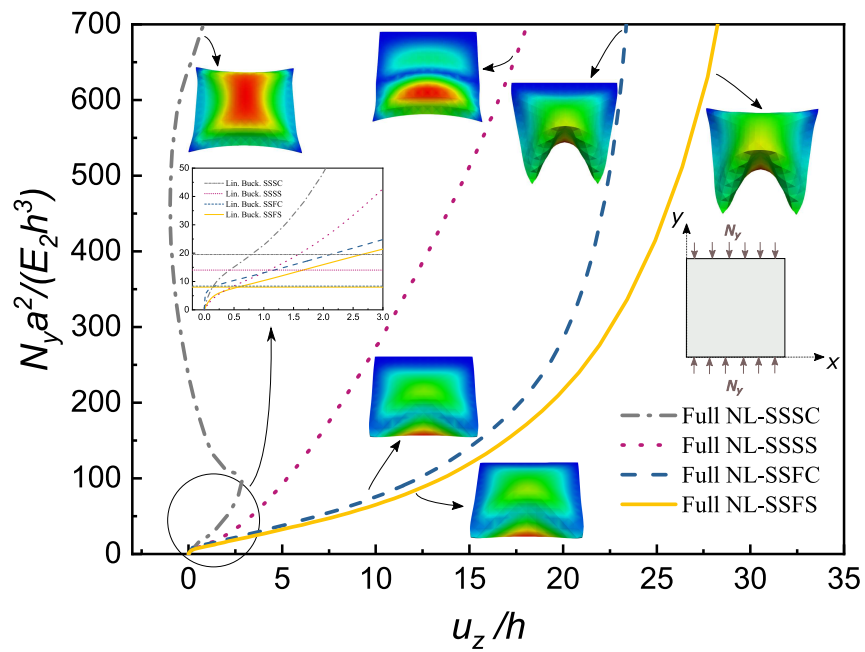


Fig. 6.33 The equilibrium curves for a cross-ply [0/90] laminate under in-plane compressive line loads in the y-axis direction with different edge conditions based on CUF 2D full nonlinear  $12 \times 12$  Q9-LD1 model

## 6.6 Conclusions

It has been shown in this chapter that the CUF and layer-wise approaches may be used to investigate the large-deflection and post-buckling of rectangular isotropic and composite plates. Because of this approach, we have been able to explore a variety of geometric nonlinear relationships. Hence, the well-known von Kármán theory for nonlinear deformations of plates has been evaluated with several modifications, including thickness stretching and shear deformations owing to transverse deflection. In this context, equilibrium curves and stress distributions for each of the cases have been provided and analyzed in detail. Moreover, the linear buckling load of the composite plates has been estimated for the post-buckling examples. Different factors influencing the nonlinear response of plates, including the stacking sequence, number of layers, loading and edge conditions, have been thoroughly studied. The results have demonstrated that:

- Inaccuracies in the nonlinear response of plate structures by von Kármán displacement-strain relations are more evident in the case of moderately thick and thick plates, and this effect could be more significant in the very large displacements/rotations fields. Hence, the full nonlinear Green-Lagrange relations are preferred for these cases.
- A reasonable estimation for the in-plane normal stresses of plates under the uniform pressure is provided by the von Kármán theory; however, when transverse shear stress assessments in the nonlinear range are required, on the other hand, the von Kármán theory it is not exact enough to be useful.
- The selection of proper geometrically nonlinear assumption is dependent on the structure and loading conditions. Among all the investigated theories, the full nonlinear model is more reliable in order to investigate the correct equilibrium curves and stress distributions in the very large displacements and far post-buckling regime. Nevertheless, the von Kármán approximation overestimates the effect of post-buckling stresses.
- The results of nonlinear analysis of plates obtained by the CUF linear and full nonlinear models match well with those found in the available literature as well as the ABQ 3D solid models



- 
- The buckling strength and load-carrying capacity of composite plate structures are increased when the number of layers in the composite plates is increased.
  - Angle-ply laminate subjected to combined loading (in-plane shear and biaxial compression) exhibits post-buckling behavior that is dependent on the direction of the applied shear. The angle-ply laminate subjected to negative shear loading exhibits higher rigidity and load-carrying capacity than the other loading conditions.
  - The buckling strength of the composite plates with clamped edge conditions is greater than those of the composite plates with other studied edge conditions. Moreover, the presence of a free edge, considerably reduces the buckling strength of the composite plates.

# Chapter 7

## Stiffeners and boundary conditions effects on the compressed flexible plates

### 7.1 Introduction

Due to the availability of novel components and production technologies, composite laminated structures are rapidly being employed in various fields of aeronautics, automotive, and construction engineering. Composite materials are becoming ever more important to designers and academic researchers. Attachments or stiffeners around the borders of a plate or panel structure impose load or displacement boundary conditions according to the stiffness of these stiffeners in their practical applications. According to this, designers and engineers need to pay more attention to this effect because stiffeners enforce a uniform displacement to the edges based on their stiffness. A panel enclosed by longerons in aerospace applications or a wing structure, as schematically shown in Fig. 7.1, might be seen as examples of these surrounding effects. The fact that BC1 to BC4 in this figure enforce constant load or displacement boundary conditions, or a combination of both, is highly dependent on the stiffness of the attached components.

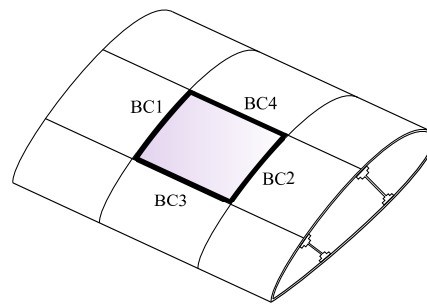


Fig. 7.1 The effects of attachments on the boundary conditions of a panel in the sample wing structure

Wang et al. [243] proposed a theoretical solution for the post-buckling response of orthotropic plates under combined in-plane biaxial compression and shear. Carrera and Villani [244] analyzed the post-buckling of compressed symmetrically laminated thick plates with different boundary conditions by employing a shear deformable plate FE of Reissner-Mindlin type. Fan and Wang studied [245] the post-buckling of hybrid laminated plates in thermal environments. The compressive post-buckling of sandwich plates with temperature-dependent properties was investigated by Shen et al. [246]. The same authors analyzed the post-buckling response of graphene-reinforced composite plates in thermal conditions [247, 248].

As previously noted, engineers and designers need to precisely determine the effect of boundary conditions on the mechanical response of plate structures. Additionally, adopting proper strain-displacement assumptions is critical for evaluating plate structures' geometrically nonlinear behavior. For example, under certain loading and edge conditions, the well-known von Kármán theory may exhibit considerable inconsistencies when compared to the full nonlinear analysis. Numerous theoretical analyses have neglected these facets. The post-buckling behavior of rectangular laminated composite plates is investigated in this chapter by employing the CUF. The Newton-Raphson linearization method is used in conjunction with the arc-length method. A stiffener model is provided to illustrate the geometrically nonlinear behavior of composite plates under various load and displacement boundary conditions. On the basis of various strain-displacement assumptions, the nonlinear equilibrium curves and stress distributions of post-buckled laminated composite plates corresponding to many stiffener models are evaluated. The von Kármán theory and certain modified strain-displacement relationships incorporating various

nonlinear components are compared to the full Green-Lagrange nonlinear model based on the CUF plate model.

## 7.2 Square composite plate with SFSF edge conditions

Different numerical evaluations are provided in this section in order to evaluate the effect of stiffeners in the post-buckling of composite plate structures under compressive loads. SFSF edge conditions are studied for the first analysis case, which is a cross-ply square composite plate with a  $[0/90/0/90]$  lamination. This composite plate has a width of  $a = b = 1$  m and a thickness of  $h = 2$  mm. Fig. 7.2 shows a composite plate that is subjected to in-plane compressive line load in the  $y$ -axis direction  $N_y$  (force per unit length). Simply-supported edge conditions fulfill  $u = w = 0$  at  $y = 0, b$ . The material properties of the composite plate under investigation are shown in table 7.1.

Table 7.1 Material properties of the investigated composite plate [224]

$E_1$ (GPa)	$E_2 = E_3$ (GPa)	$G_{12} = G_{13}$ (GPa)	$G_{23}$ (GPa)	$\nu_{12} = \nu_{13}$	$\nu_{23}$
250	6.25	5.125	3.25	0.24	0.49

### 7.2.1 Evaluation of different stiffeners

In this chapter, stiffeners with a variety of material properties are utilized to describe the load and displacement boundary conditions. In particular, one row of Q9 plate elements is added to every loaded edge of the plate structure. It is assumed that the stiffeners are isotropic with Young's modulus of  $E_s$ . Changing the values of the ratio  $\frac{E_s}{E_1}$  allows us to enforce the loaded edges to have a consistent distribution of displacements or loads. Fig. 7.2 depicts nonlinear equilibrium curves for a variety of  $\frac{E_s}{E_1}$  ratios ranging from 0.0001 to 100. These graphs illustrate the normalized values of the displacement in the middle point of the laminate against the normalized values of the applied compressive load. It should be noted that for the purpose of simplicity, the stiffeners are not displayed in the deformed configurations of this chapter. To be more specific, the principal deformations of interest in this chapter are those that occur in the main composite plate rather than those related to the stiffeners.

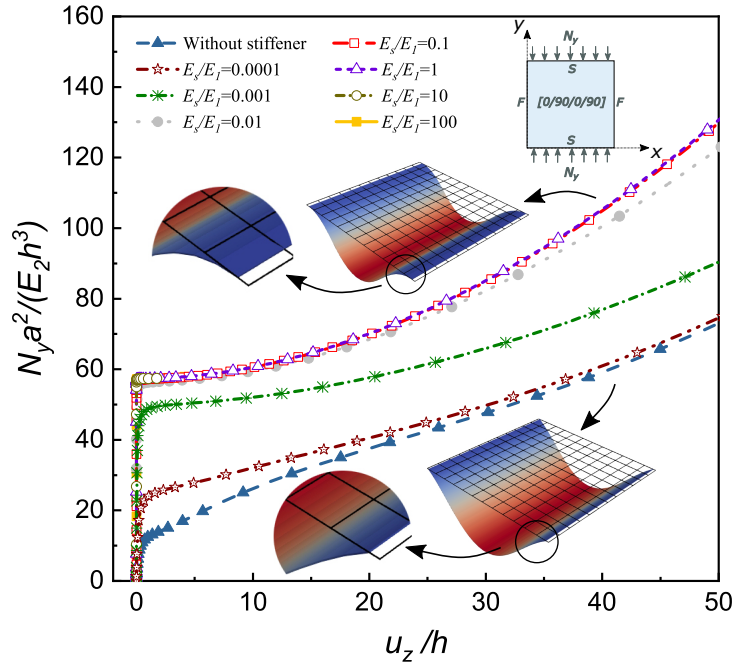


Fig. 7.2 The comparison of equilibrium curves for the composite plate [0/90/0/90] with different load and displacement boundary conditions based on the full nonlinear CUF plate model  $12 \times 12Q9$ -LD1

As seen in Fig. 7.2, the material properties of the stiffeners have a significant effect on both prebuckling and post-buckling behaviors. As seen in the figure, the case of  $\frac{E_s}{E_1} = 0.0001$  exhibits a post-buckling behavior that is identical to that of an SFSF plate without any stiffener. However, increasing this ratio leads to an increase in the buckling load of the composite plate structure until the ratio  $\frac{E_s}{E_1} = 0.1$  or more is attained, at which point the graphs almost coincide and the maximum load-carrying capacity of the plate structure. Indeed, raising the  $\frac{E_s}{E_1}$  ratio enforces the loaded edges a more uniform displacement distributions along the y axis ( $u_y$ ) until the constant displacement boundary condition is achieved. Additionally, the stiffeners impose restrictions on the rotations of loaded edges (see the detailed contour plots of Fig. 7.2). As a result, when stiffeners with high stiffness are used, the boundary conditions at the loaded edges tend to be more clamped. As a consequence, the boundary conditions for the loaded edges become more constrained. Additionally, for the remainder of this section's analyses, the case with stiffener  $\frac{E_s}{E_1} = 1$  will be referred to as *BC displacement*, and the case without stiffener will be referred to as *BC load*.

## 7.2.2 Convergence analysis

The convergence analysis of the equilibrium curves for the cross-ply laminated composite plate [0/90/0/90] is displayed in Fig. 7.3. This figure illustrates the normalized displacement in the laminate's central point against the normalized compressive load. The influence of in-plane mesh size on the equilibrium curves for the load and displacement boundary conditions is investigated in this figure.  $6 \times 6Q9$ ,  $8 \times 8Q9$ ,  $12 \times 12Q9$ , and  $15 \times 15Q9$  finite plate elements are analyzed using the LD1 theory approximation order for each layer. Additionally, the DOF for each model is presented in Table 7.2 with the normalized values of the applied compressive load corresponding to the transverse displacements at the middle point. One can note that the convergence is reached for the nonlinear response curve of the  $12 \times 12Q9$ -LD1 model. As a result, this model will be utilized to explore the equilibrium curves and stress distributions of this composite plate in the following assessments.

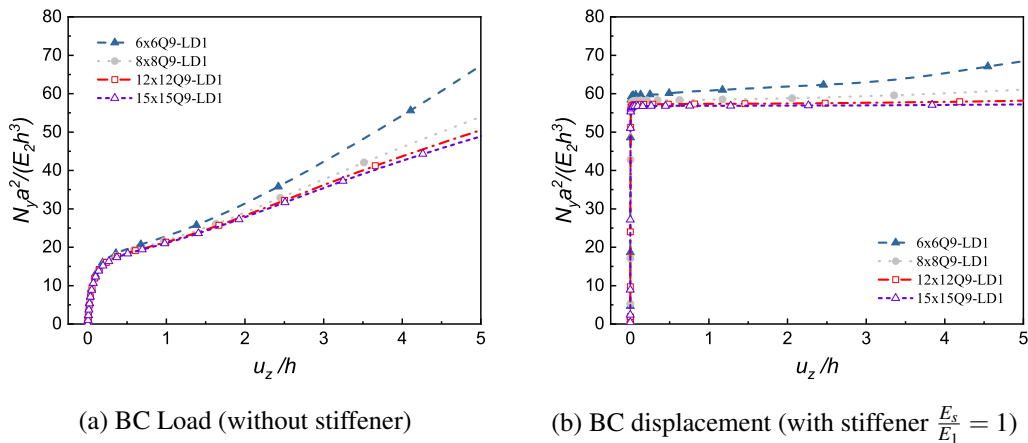


Fig. 7.3 Convergence analysis of the in-plane mesh size for SFSF composite plate based on the full nonlinear CUF plate model

Table 7.2 Equilibrium points for different in-plane mesh size in SFSF composite plate based on the full nonlinear CUF plate model

CUF plate model	DOF	BC Load (without stiffener)		BC displacement (with stiffener $\frac{E_2}{E_1} = 1$ )	
		$\frac{N_y a^2}{E_2 h^3}$		$\frac{N_y a^2}{E_2 h^3}$	
		$\frac{u_z}{h} = 1$	$\frac{u_z}{h} = 4$	$\frac{u_z}{h} = 1$	$\frac{u_z}{h} = 4$
$6 \times 6$ Q9-LD1	2535	23.08	54.45	60.85	65.37
$8 \times 8$ Q9-LD1	5415	21.96	46.16	58.39	60.08
$12 \times 12$ Q9-LD1	9375	21.28	43.62	57.38	57.94
$15 \times 15$ Q9-LD1	14415	21.07	42.88	56.93	57.15

### 7.2.3 Lamination angles and equilibrium curves

The effects of various lamination angles on the equilibrium curves for the composite plate with SFSF edge conditions are studied in this section. In this context, Fig. 7.4 compares the nonlinear equilibrium curves for the various lamination angles. As seen in Fig. 7.4, the lamination angles and stacking sequence have a significant effect on the buckling and post-buckling behaviors of the composite plate structure under load and displacement boundary conditions. As a consequence, lamination angles  $[0,45,45,0]$  and  $[0,90,90,0]$  exhibit increased buckling strength and load-carrying capacity, while  $[45,90,90,45]$  exhibits lower stiffness and buckling strength. Additionally, comparing nonlinear equilibrium curves for the load and displacement boundary conditions indicates that stiffeners greatly enhance buckling strength and load-bearing capacity. In fact, the clamped edge condition is more likely to occur in the presence of stiffeners because the plate structure becomes more constrained.

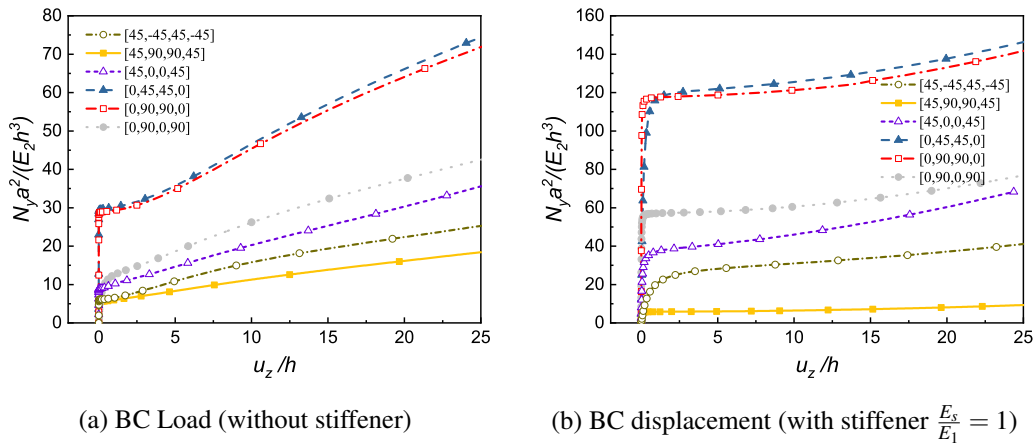


Fig. 7.4 The comparison of equilibrium curves for SFSF composite plates with different lamination angles based on the full nonlinear CUF plate model

### 7.2.4 Geometrically nonlinear assumptions and equilibrium curves

As shown in Fig. 7.5, for the previously discussed composite plate with SFSF edge conditions, the nonlinear equilibrium curves corresponding to the various nonlinear strain-displacement assumptions of Table 2.3 are shown side by side and evaluated. The normalized values of the applied compressive load related to the transverse displacements at the middle point are also presented in Table 7.3, which is a reference to the previous table. The findings of Fig. 7.5 reveal that the linear and  $FNL_{-vK}$  models are unable to accurately estimate the equilibrium curves for both load and displacement boundary conditions. Additionally, only the full nonlinear model can provide trustworthy and correct results for the load boundary conditions seen in Fig. 7.5a. On the contrary, the von Kármán nonlinear theory and its modifications are incapable of accurately predicting deflections and equilibrium paths. On the other hand, for the displacement boundary conditions (see Fig. 7.5b), the full nonlinear model, the von Kármán model, and its modifications are almost identical and may provide satisfactory results. Thus, under load boundary conditions for this composite plate, it is critical to analyze the full nonlinear model in order to correctly study the geometrically nonlinear response.



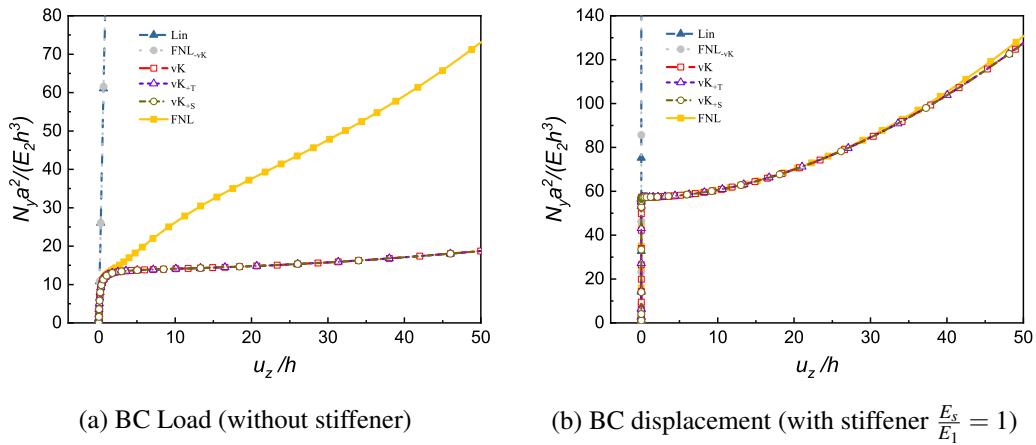


Fig. 7.5 The comparison of equilibrium curves for the composite plate [0/90/0/90] with SFSF edge conditions with different geometrically nonlinear assumptions of Table 2.3 based on the 12×12Q9-LD1 model

Table 7.3 Equilibrium points for SFSF composite plate based on the different geometrically nonlinear assumptions of Table 2.3

Strain-displacement assumption	BC Load (without stiffener)		BC displacement (with stiffener $\frac{E_s}{E_1} = 1$ )	
	$\frac{N_y a^2}{E_2 h^3}$		$\frac{N_y a^2}{E_2 h^3}$	
	$\frac{u_z}{h} = 5$	$\frac{u_z}{h} = 40$	$\frac{u_z}{h} = 5$	$\frac{u_z}{h} = 40$
vK	13.70	17.07	58.28	104.16
vK <sub>+T</sub>	13.85	17.21	58.49	104.39
vK <sub>+S</sub>	13.78	17.16	58.37	104.28
FNL	18.87	59.32	58.51	105.54

### 7.2.5 Geometrically nonlinear assumptions and stress distributions

The impact of utilizing various strain-displacement assumptions on the assessments of stress distributions is provided for this composite plate with SFSF edge conditions. The Fig. 7.6 illustrates the through-the-thickness distributions of dimensionless in-plane normal stresses at different points ( $x = 0.5a, y = 0.7b$ ) through the laminate’s thickness. It is worth noting that the stress assessments are based on the post-buckling

equilibrium curves with a fixed displacement of  $\frac{u_z}{h} = 20$ . The findings of Fig. 7.6 demonstrate that only the full nonlinear model can provide valid distributions of normal stresses for the load boundary conditions. Indeed, neither the von Kármán theory nor any of its modifications can reliably predict the normal stress distributions in this example. For the displacement boundary conditions, on the other hand (see Figs. 7.6b and 7.6d), the full nonlinear model, the von Kármán, and its modifications are almost identical and provide correct stress distributions. Additionally, Fig. 7.6 reveals the fact that the choice of LD1 or LD3 CUF plate models seems to have no significant effect on the normal stress distributions.

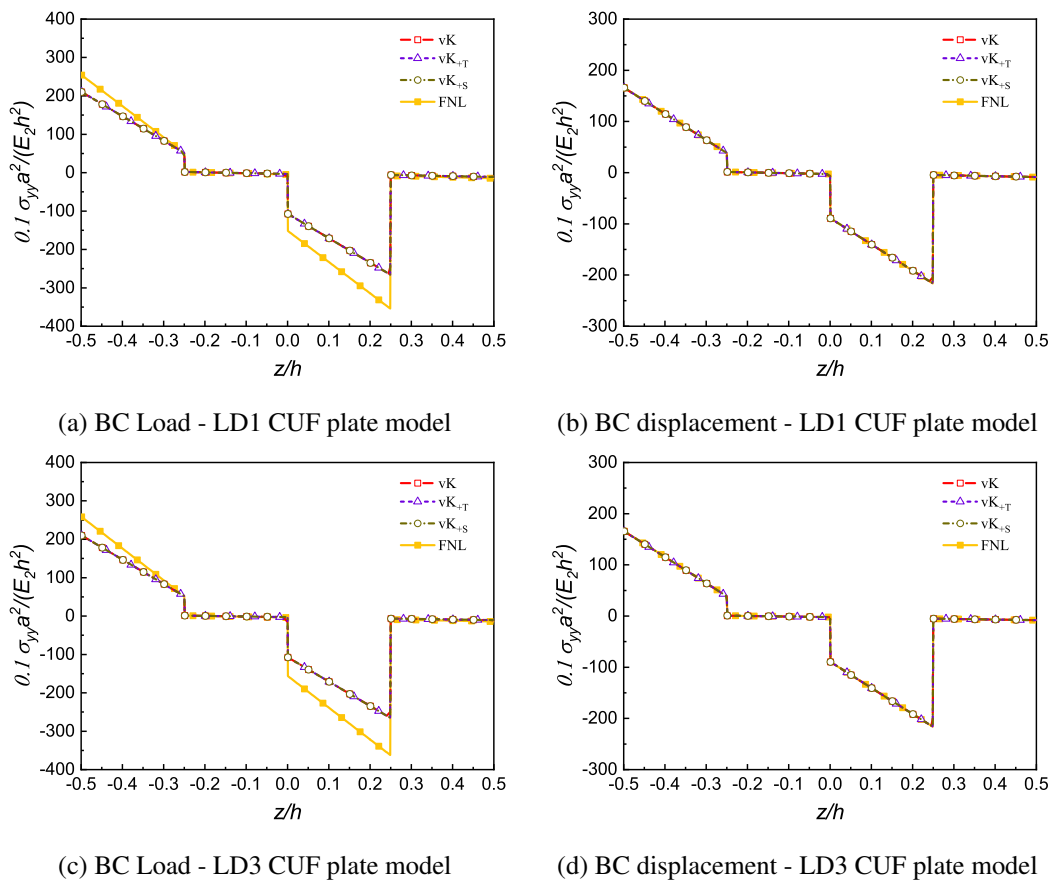


Fig. 7.6 The distributions of dimensionless in-plane normal stress through the thickness of plate at the point  $(x = 0.5a, y = 0.7b)$  of SFSF [0/90/0/90] square composite plate at the fixed displacement of  $\frac{u_z}{h} = 20$

The impacts of various strain-displacement assumptions on the shear stress assessments in the aforementioned composite plate with SFSF edge conditions are examined in Fig. 7.7. This figure depicts the through-the-thickness distributions

of the dimensionless transverse shear stress at the composite plate's points located at  $x = 0.5a$  and  $y = 0.7b$ . The findings reveal that the LD1 CUF plate models are incapable of maintaining shear stress continuity throughout the thickness of the laminated composite plate, which is physically unsatisfactory. However, the cubic LD3 CUF plate model with four nodes per layer can accurately predict quadratic shear stress distributions. It can be concluded that, while using LD1 or LD3 models has almost no effect on the normal stress distributions in Fig 7.6, they are critical in evaluating shear stresses in Fig. 7.7 by establishing the correct physical conditions for the problem.

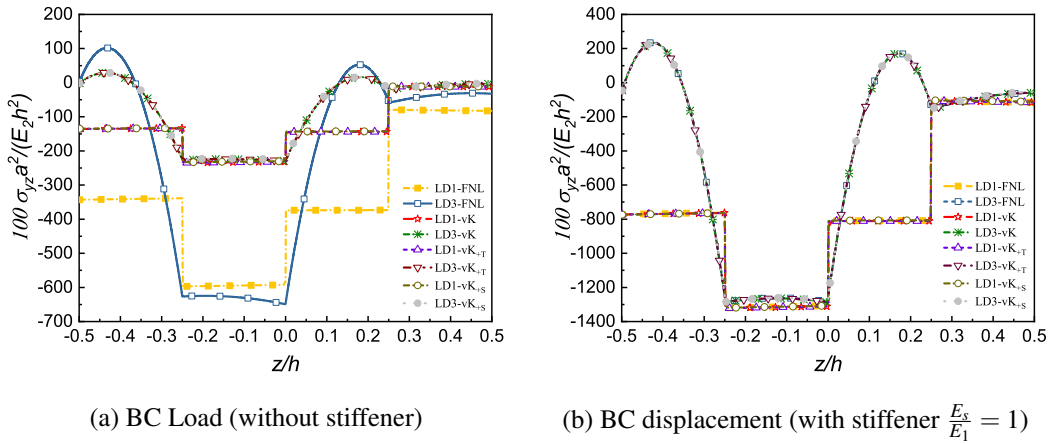


Fig. 7.7 The distributions of dimensionless transverse shear stress through the thickness of plate at the point ( $x = 0.5a$ ,  $y = 0.7b$ ) of SFSF [0/90/0/90] square composite plate at the fixed displacement of  $\frac{u_z}{h} = 20$

### 7.3 Square composite plate with SSSS edge conditions

This numerical assessment deals with the composite plate discussed in Section 7.2. For this plate example, the loading conditions and material properties are similar to the previous composite plate, except for the boundary conditions of SSSS, which include an extra set of opposite edge conditions along the  $x$ -axis direction satisfying  $v = w = 0$  at  $x = 0, a$ . The edge conditions in this case are SSSS, such that one set of opposite edges along the  $x$ -axis direction  $x = 0, a$  fulfill  $v = w = 0$ , while another set of simply-supported opposite edges along the  $y$ -axis direction  $y = 0, b$  satisfy  $u = w = 0$ .

### 7.3.1 Evaluations of different stiffeners

The nonlinear equilibrium curves for various  $\frac{E_s}{E_1}$  ratios ranging from 0.0001 to 100 are compared in Fig. 7.8, as well as for the case of a plate without stiffeners. Additionally, data from the existing literature [224] for the case of the plate without a stiffener are included to demonstrate the suggested CUF plate models' consistency. The deformation contour plots of the composite plate are shown in Table 7.4 at selected positions on the post-buckling equilibrium curves.

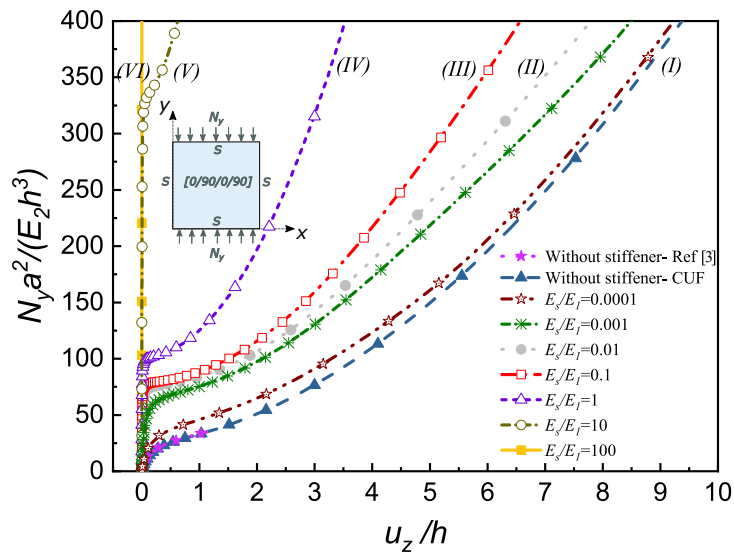
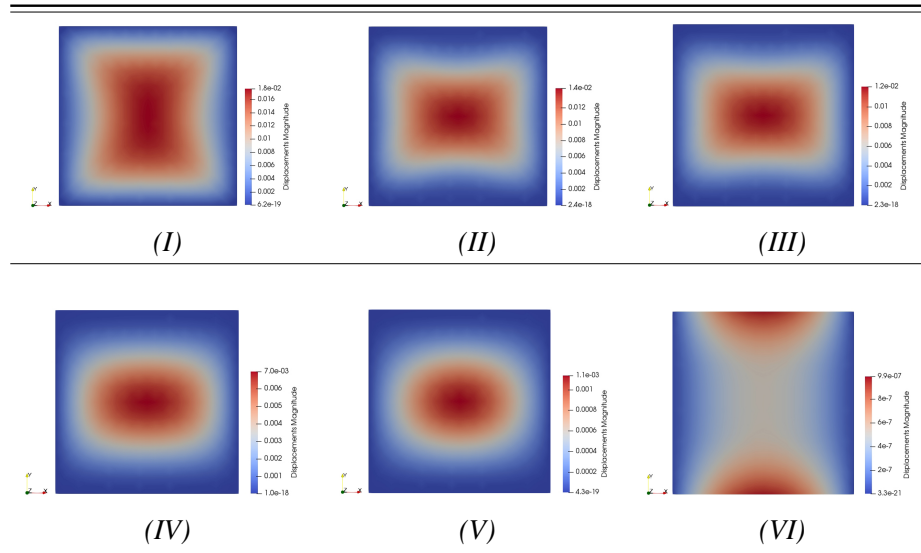


Fig. 7.8 The comparison of equilibrium curves for the composite plate [0/90/0/90] with SSSS edge conditions with different load and displacement boundary conditions based on the full nonlinear CUF plate model 12×12Q9-LD1

Table 7.4 The deformation contour plots of composite plate [0/90/0/90] with SSSS edge conditions with different load and displacement boundary conditions based on the full nonlinear CUF plate model  $12 \times 12$ Q9-LD1



As seen in Fig. 7.8, the results obtained by the present CUF-based method match well with findings derived from the literature. As seen in Fig. 7.8, increasing the ratio of  $\frac{E_s}{E_1}$  has a considerable effect on both prebuckling and post-buckling behaviors. It is observed that when  $\frac{E_s}{E_1} = 0.0001$ , the post-buckling behavior of the SSSS plate is identical to that of the plate without any stiffener. Nonetheless, raising this ratio leads to an increase in the composite plate structure's buckling strength and load-carrying capability. While this behavior in the composite plate with SSSS edge conditions is similar to that in the first numerical example of this chapter with SFSF edge conditions, it is quite different in this case because there is no ultimate curve where the constant displacement boundary condition is reached (for comparison, see Figs. 7.2 and 7.8). Indeed, since the previously free edge conditions are simply-supported here, additional rotations are restricted in the loaded edges. This results in a greater influence of ratio  $\frac{E_s}{E_1}$  on the buckling strength and load-carrying capacity of the plate structure. Furthermore, by comparing the graphs in 7.2 and 7.8, it is apparent that the composite plate with SSSS edge conditions exhibits much greater rigidity and buckling strength than the plate with SFSF edge conditions.

### 7.3.2 Convergence analysis

The convergence analysis of the equilibrium curves for a composite plate with SSSS edge conditions is shown in Fig. 7.9. The influence of in-plane mesh size on the load and displacement boundary conditions is explored in this figure. It is noted that the convergence is reached at least for the nonlinear response curve of the  $12 \times 12$ Q9-LD1 model. As a result, this model will be utilized to analyze the equilibrium curves and stress distributions of this composite plate in the following evaluations. The normalized values of the applied compressive load related to some specific transverse displacements at the middle point of the plate structure, along with the DOF for each model, are presented in Table 7.5. Additionally, as seen in Fig. 7.9a for the load boundary conditions, no precise buckling load exists for this composite plate with SSSS edge conditions [224].

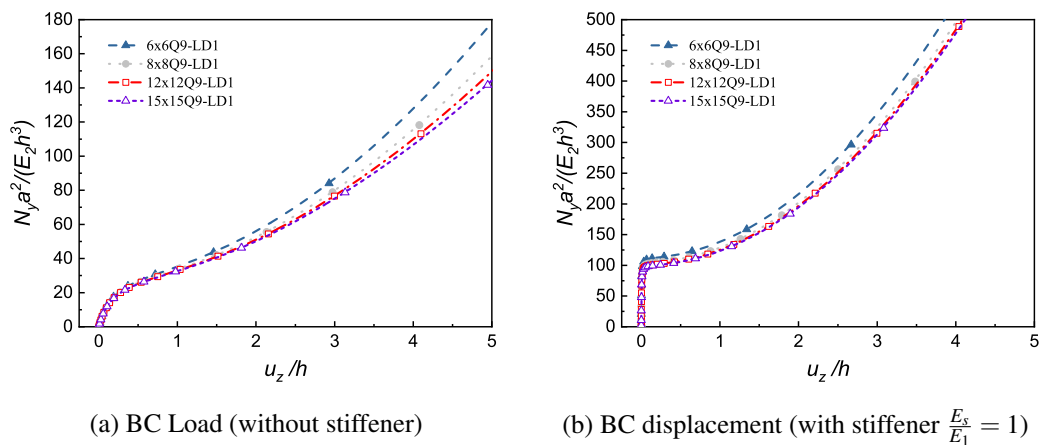


Fig. 7.9 Convergence analysis of the in-plane mesh size for SSSS composite plate based on the full nonlinear CUF plate model

Table 7.5 Equilibrium points for different in-plane mesh size in SSSS composite plate based on the full nonlinear CUF plate model

CUF plate model	DOF	BC Load (without stiffener) $\frac{N_y a^2}{E_2 h^3}$		BC displacement (with stiffener $\frac{E_2}{E_1} = 1$ ) $\frac{N_y a^2}{E_2 h^3}$	
		$\frac{u_z}{h} = 1$	$\frac{u_z}{h} = 4$	$\frac{u_z}{h} = 1$	$\frac{u_z}{h} = 4$
$6 \times 6Q9-LD1$	2535	35.39	127.92	137.95	533.70
$8 \times 8Q9-LD1$	5415	33.62	115.02	128.83	494.43
$12 \times 12Q9-LD1$	9375	33.11	109.22	124.33	481.80
$15 \times 15Q9-LD1$	14415	32.87	107.14	122.72	477.59

### 7.3.3 Lamination angles and equilibrium curves

In Fig. 7.10, various lamination angles and their related nonlinear equilibrium curves are analyzed for the given composite plate with SSSS edge conditions. As seen in Fig. 7.10, the lamination angles and stacking sequence have a significant effect on the buckling and post-buckling responses of the composite plate structure for both load and displacement boundary conditions. As a result, the lamination angles  $[0/90/0/90]$  and  $[0/90/90/0]$  exhibit decreased stiffness and load-bearing capability. On the other hand, for this composite plate with SSSS edge conditions, snap-through instability is found for certain lamination angles, which shows complete contradiction to the behavior previously reported for the SFSF composite plate in Fig. 7.4. The findings of Fig. 7.10 reveal that the proposed CUF plate model is capable of evaluating the composite plate's nonlinear behavior beyond the limit load and snap-through instability.

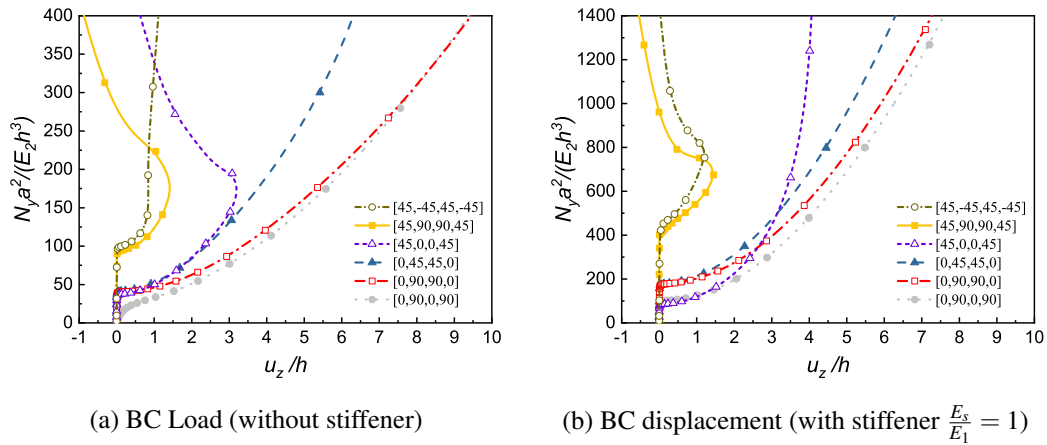


Fig. 7.10 The comparison of equilibrium curves for the composite plate [0/90/0/90] with SSSS edge conditions with different geometrically nonlinear assumptions of Table 2.3 based on the  $12 \times 12$ Q9-LD1 model

### 7.3.4 Geometrically nonlinear assumptions and equilibrium curves

For the case of composite plate with SSSS edge conditions, the nonlinear equilibrium curves related to the various nonlinear strain-displacement assumptions in Table 2.3 are assessed in Fig. 7.11. Additionally, Table 7.6 contains the normalized values of the applied compressive load relevant to the specific transverse displacements at the middle point of the plate structure. The findings of Fig. 7.11 reveal that the linear and  $FNL_{-vK}$  models cannot accurately estimate the equilibrium curves for both load and displacement boundary conditions. There are some inconsistencies between the full nonlinear model, the von Kármán theory and its modifications for load boundary conditions. Take note that these nonlinear assumptions deviate less from the full nonlinear model than the SFSF plate in Fig. 7.5a. For the displacement boundary conditions in Fig. 7.11b, on the other hand, the full nonlinear model, the von Kármán, and its modifications are almost identical and provide reliable results.



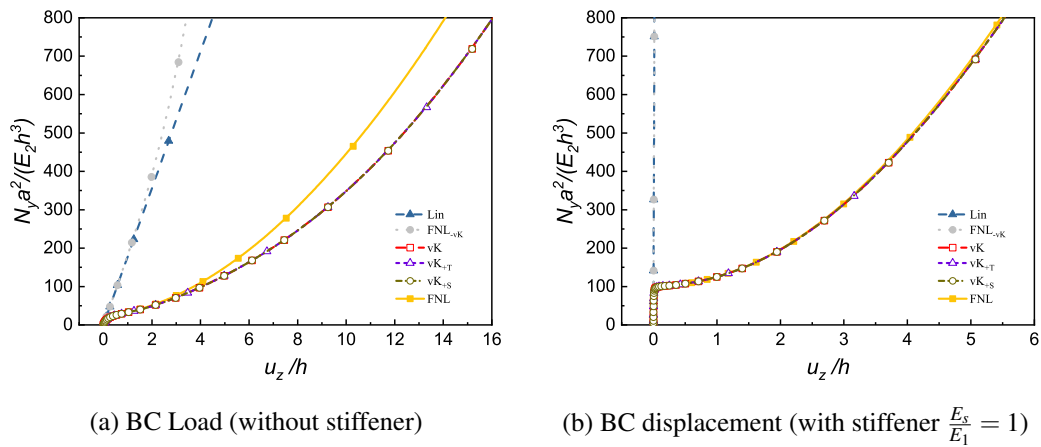


Fig. 7.11 The comparison of equilibrium curves for the composite plate [0/90/0/90] with SSSS edge conditions with different geometrically nonlinear assumptions of Table 2.3 based on the  $12 \times 12Q9$ -LD1 model

Table 7.6 Equilibrium points for SSSS composite plate based on the different geometrically nonlinear assumptions of Table 2.3

Strain-displacement assumption	BC Load (without stiffener)		BC displacement (with stiffener $\frac{E_s}{E_1} = 1$ )	
	$\frac{N_y a^2}{E_2 h^3}$		$\frac{N_y a^2}{E_2 h^3}$	
	$\frac{u_z}{h} = 1$	$\frac{u_z}{h} = 5$	$\frac{u_z}{h} = 1$	$\frac{u_z}{h} = 5$
vK	31.41	130.15	122.47	674.35
vK <sub>+T</sub>	31.62	130.44	122.80	677.91
vK <sub>+S</sub>	31.54	130.27	122.64	676.12
FNL	32.04	149.35	123.11	385.39

### 7.3.5 Geometrically nonlinear assumptions and stress distributions

Fig. 7.12 shows through-the-thickness distributions of the dimensionless in-plane normal stresses for the point located in  $(x = 0.5a, y = 0.7b)$  of the SSSS composite plate. It should be noted that the stress evaluations are on the post-buckling equilibrium curves at the fixed load of  $\frac{N_y a^2}{E_2 h^3} = 400$ . The results of Fig. 7.12 confirm the fact that for both load and displacement boundary conditions, the linear and

FNL<sub>-vK</sub> models cannot have an accurate prediction of the stress distributions. In fact, For the load boundary conditions, only the full nonlinear model can present reliable distributions of normal stresses. Similar to the previous SFSF plate example, for the load boundary conditions, the nonlinear theories of von Kármán and other modifications cannot accurately predict the normal stress distributions. On the other hand, for the displacement boundary conditions (see Fig. 7.12b), the full nonlinear model, the von Kármán, and its modifications are almost similar, and predict accurate stress distributions. Note that the graphs of normal stresses based on the LD3 CUF plate model are not presented here for the sake of brevity. In fact, for the mentioned SSSS composite plate, similar to the previous SFSF plate example, the selection of LD1 or LD3 CUF plate models does not affect the normal stress distributions considerably.

Fig. 7.12 illustrates the through-the-thickness distributions of dimensionless in-plane normal stresses for the points of SSSS composite plate located in  $x = 0.5a$ ,  $y = 0.7b$  coordinates at a fixed load of  $\frac{N_y a^2}{E_2 h^3} = 400$ . The findings of this figure demonstrate that the linear and FNL<sub>-vK</sub> models cannot precisely estimate the stress distributions for both load and displacement boundary conditions. In addition, one can note that for the case of load boundary conditions, only the full nonlinear model can provide valid distributions of normal stresses. On the other hand, with displacement boundary conditions (see Fig. 7.12b), the full nonlinear model, the von Kármán, and its modifications are almost identical and present reliable stress distributions. For the sake of brevity, the normal stress graphs based on the LD3 CUF plate model are not provided in this figure because, as with the preceding SFSF plate example, selecting LD1 or LD3 CUF plate models had no effect on the normal stress distributions.

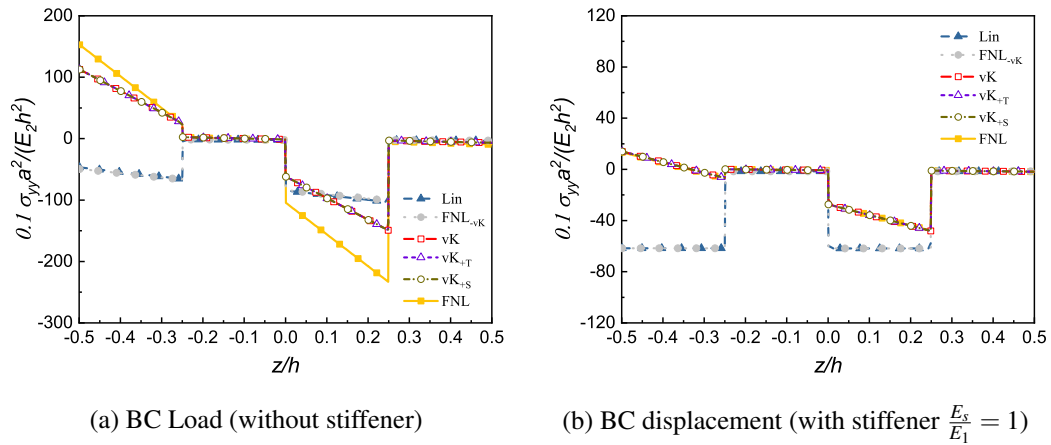


Fig. 7.12 The distributions of dimensionless in-plane normal stress through the thickness of plate at the point  $(x = 0.5a, y = 0.7b)$  of SSSS  $[0/90/0/90]$  square composite plate at the fixed load of  $\frac{N_y a^2}{E_2 h^3} = 400$

In Fig. 7.13, the impacts of various strain-displacement assumptions on the assessments of shear stresses in the aforementioned composite plate with SSSS edge conditions are studied. This figure depicts the through-the-thickness distributions of the dimensionless transverse shear stress at the composite plate's points located in  $x = 0.5a, y = 0.7b$  coordinates. The findings of Fig. 7.13 demonstrate that the linear and  $FNL_{-vK}$  models cannot provide a credible estimation of shear stress distributions for both load and displacement boundary conditions. Additionally, as seen in Fig. 7.13a, only the full nonlinear model can properly estimate the shear stresses for the case of load boundary conditions. Moreover, the findings reveal that the LD1 CUF plate models are incapable of maintaining shear stress continuity across the thickness of the laminated composite plate, which is physically unsatisfactory. The cubic LD3 CUF plate model with four nodes in each layer, on the other hand, can properly predict quadratic shear stress distributions.

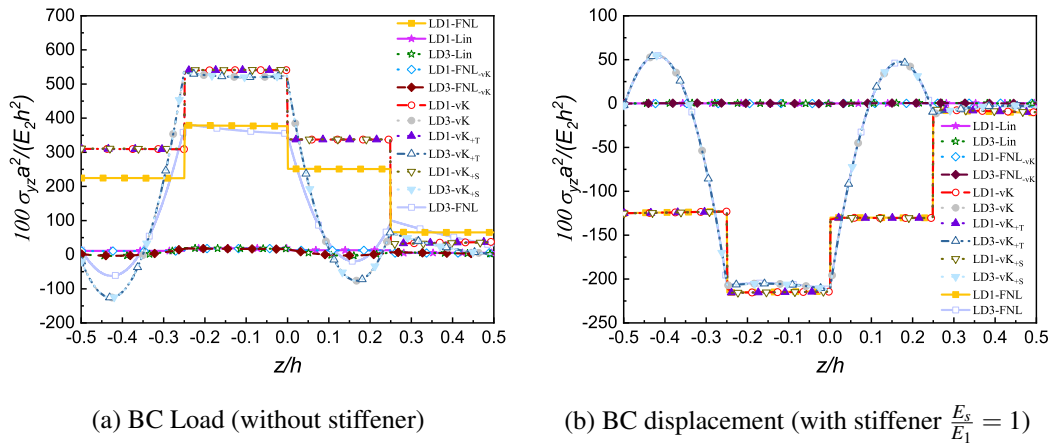


Fig. 7.13 The distributions of dimensionless transverse shear stress through the thickness of plate at the point  $(x = 0.5a, y = 0.7b)$  of SSSS  $[0/90/0/90]$  square composite plate at the fixed load of  $\frac{N_y a^2}{E_2 h^3} = 400$

## 7.4 Angle-ply lamintaed composite plate with SSSS edge conditions

Finally, for the sake of completeness, this numerical evaluation deals with the identical composite plate indicated in Section 7.3 with a different  $[45/-45/-45/-45]$  layup. It is discussed in detail in the following sections how different stiffeners affect the nonlinear response of this angle-ply laminated composite plate, as well as how alternative geometrically nonlinear assumptions can be used for that.

### 7.4.1 Evaluation of different stiffeners

Fig. 7.14 illustrates the nonlinear equilibrium curves for various  $\frac{E_s}{E_1}$  ratios and the case of the plate without stiffeners for the angle-ply laminated composite plate with SSSS edge conditions. In comparison with earlier numerical evaluations, this figure illustrates a significantly different geometrically nonlinear behavior with snap-through instabilities for many  $\frac{E_s}{E_1}$  ratios. As previously stated, raising the value of this ratio results in an increase in the composite plate structure’s buckling strength and load-bearing capacity. Due to the fact that all boundary conditions are simply

supported in the absence of any free edge conditions, the rotations are more limited than the plate with SFSF edge conditions.

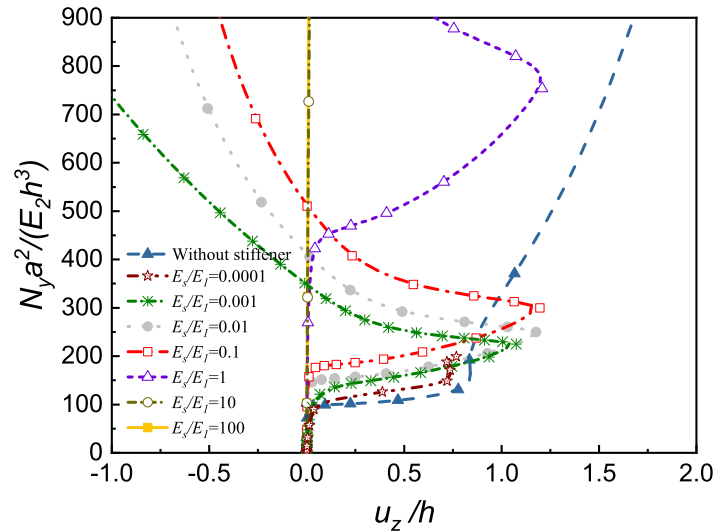


Fig. 7.14 The comparison of equilibrium curves for the composite plate [45/-45/45/-45] with SSSS edge conditions with different load and displacement boundary conditions based on the full nonlinear CUF plate model 12×12Q9-LD1

## 7.4.2 Geometrically nonlinear assumptions and equilibrium curves

In Fig. 7.15, the nonlinear equilibrium curves related to the various nonlinear strain-displacement assumptions of Table 2.3 are compared for the angle-ply laminated composite plate with SSSS edge conditions. The findings of Fig. 7.15 reveal that the linear and  $FNL_{-vK}$  models cannot accurately estimate the equilibrium curves for both load and displacement boundary conditions. Additionally, only the full nonlinear model can properly determine the post-buckling equilibrium curves for the load boundary conditions shown in Fig. 7.15a. Moreover, Fig. 7.15 reveals that the provided CUF plate model is capable of detecting the nonlinear equilibrium paths of composite plate structures beyond the snap-through instability.

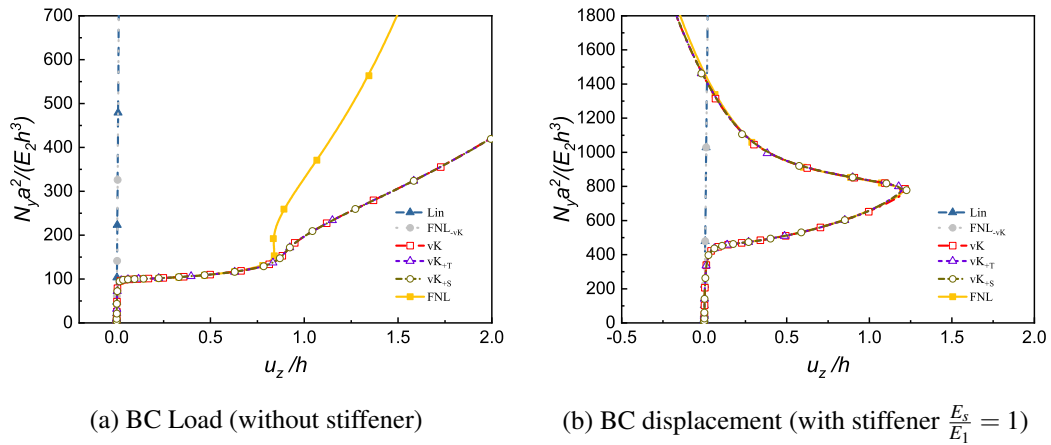


Fig. 7.15 The comparison of equilibrium curves for the composite plate [45/-45/45/-45] with SSSS edge conditions with different geometrically nonlinear assumptions of Table 2.3 based on the  $12 \times 12$ Q9-LD1 model

## 7.5 Conclusions

This chapter investigates the influence of load and displacement boundary conditions on the geometrically nonlinear response of laminated composite plates under various strain-displacement assumptions. The CUF and layer-wise methods based on LE have been used to determine the post-buckling equilibrium curves and stress distributions of laminated composite plates. To evaluate nonlinear equilibrium curves for the cases, different stiffeners have been modeled, and the effect of boundary conditions imposed by them has been investigated. Different nonlinear strain-displacement assumptions have been compared to the full Green-Lagrange nonlinear model based on the CUF. Various numerical analyses of post-buckling in laminated composite plates have been carried out to determine the effect of load and displacement boundary conditions on the equilibrium curves and stress distributions of post-buckled laminated composite plates. The following observations may be made in light of the findings:

- The stiffeners’ material properties have a significant impact on the nonlinear post-buckling behaviors. The presence of stiffeners limits the rotations at the loaded edges of the plate structure by enforcing uniform edge displacement.

- Lower values of the stiffener's material properties result in a post-buckling behavior that is similar to the response of the plate in the absence of the stiffener. Higher values of material properties for the stiffener, on the other hand, result in rotational limitations in the loaded edges that are more comparable to the clamped edge conditions, resulting in the boundary conditions being more similar to the clamped edge conditions.
- Lamination angles and stacking sequence have a major effect on the composite plate structure's buckling and post-buckling behaviors. When the edge conditions of a composite plate are varied, the post-buckling equilibrium curve may exhibit a dramatic change.
- The CUF plate models LD1 and LD3 might provide accurate and promising findings when evaluating nonlinear equilibrium curves and normal stress distributions. The LD1 models, on the other hand, cannot guarantee the continuation of the shear stress across the laminated composite plate's thickness, which is unsatisfactory physically. The quadratic shear stress distributions may be predicted with high accuracy using the cubic LD3 CUF plate model, which has four nodes at each layer.
- The nonlinear response of the composite plate above the limit load and snap-through instability may be predicted using the CUF plate model that has been provided.
- The von Kármán theory and its modifications proved to be capable of providing correct nonlinear equilibrium curves and stress distributions for the analyzed structural problems with displacement boundary conditions. However, for many examples, given the load boundary conditions, these theories do not offer a reasonable assessment of the displacements and stresses.
- For many geometrically nonlinear investigations, the full nonlinear Green-Lagrange relations should be used since they provide a foundation for comparing the efficiency of various structural theory approximation orders and geometrically nonlinear assumptions.

# Chapter 8

## Modeling in-plane shear and combined loadings in flexible plates

### 8.1 Introduction

Highly flexible plate and panel structures are subjected to in-plane shear and combined loadings in many engineering applications such as aerospace and civil industries. The accurate investigation of buckling and post-buckling behavior of these structures is vital for engineers and designers. Shear buckling of plate and panel structures has been studied by many researchers [249–253]. Hui [254] and Kosteletos [255] worked on the shear buckling of rectangular laminated plates using theoretical methods. Loughlan [256, 257] investigated the effect of bend-twist coupling on the shear buckling behavior of thin composite plates by employing the finite strip method. Three-dimensional cubic B-spline FE for the shear buckling of orthotropic heterogeneous plates with functionally graded materials was developed by Shariyat and Asemi [258]. Employing the assumed natural strain method, Jung and Han [259] proposed a modified eight-node shell element to study the initial shear buckling of laminated composite plates and shells. Chen and Qiao [260] analyzed the shear buckling of rotationally-restrained laminated plates semi-analytically based on the Galerkin method. Atashipour and Girhammar [261] proposed a closed-form method in order to predict the critical buckling load of clamped narrow rectangular orthotropic plates under uniformly distributed shear load around the edges. The



research on shear buckling of bending-twisting coupled finite length plates with simply-supported edge conditions was conducted by Lee and York [262].

In some research studies of the plate and panel structures, the combination of axial and shear loadings has been focused [263–267]. Zhang and Matthews [268] worked on the initial buckling of cylindrically curved composite panels subjected to axial compressive and shear forces. The buckling behaviors of stiffened composite panels under combined in-plane compression and shear loadings were investigated by Loughlan [269]. Nemteh [270, 271] presented parametric analytical analysis on the buckling of long anisotropic Plates subjected to combined loads. Featherston [272] investigated the effect of imperfection on the initial buckling load of curved panels subjected to combined compression and shear. Utilizing the assumed strain method, Kim et al. [273] developed a co-rotational eight-node shell element for post-buckling analysis of composite plates and shells under different loadings. Featherston and Watson [274] conducted a series of experiments in order to analyze the buckling and post-buckling of flat composite plates under shear and in-plane bending.

In the research studies focused on shear buckling and combined loadings of plate structures, the effects of boundary conditions imposed by stiffeners and surrounding components are ignored in many cases. This is more important when considering the plate in real conditions with surroundings. In addition, in the large displacements and rotations, modeling real shear loading and edge conditions could be challenging by FE methods. This is in fact because all plate edges should be free to have in-plane displacements. In this chapter, an artificial surrounding area is modeled in order to address this issue. Accordingly, the effects of stiffeners and this surrounding area on the post-buckling equilibrium curves of laminated plates are evaluated. Then numerous problems of shear and combined loadings are investigated accurately using the efficient CUF framework. The layer-wise refined plate models are implemented by employing the LE functions through the laminate thickness. Different equilibrium curves are assessed by using the Newton-Raphson linearization scheme with the path-following method based on the arc-length constraint.

## 8.2 Modeling technique

The boundary conditions play a pivotal role in the geometrically nonlinear analysis of plates subjected to shear and combined loadings. In this chapter, the effects of

boundary conditions imposed by the plate surroundings are investigated precisely. In this regard, a modeling technique based on the surrounding area and stiffeners is employed, which will be further discussed and validated in the following sections.

### 8.2.1 The surrounding area

According to the displacements of exact equilibrium point, one can note that when the plate is subjected to pure shear, all the edges need to be able to move in any in-plane direction. This free-body moving could cause issues in the convergence of nonlinear solution in the large displacements and rotations. Here, in order to address this issue, the artificial surrounding area, as shown in Fig. 8.1 is modeled. As can be seen in this figure, the outside boundary conditions of this area are completely fixed. The surrounding area is assumed to be isotropic with Young's modulus of  $E_{surrounding}$  which is significantly lower than the main plate  $E_1$ . The effect of material properties of the surrounding area on the equilibrium curves for  $[45/-45]_s$  composite plates without stiffeners subjected to negative pure shear loading conditions based on the 12x12Q9-LD1 model is depicted in the graph of Fig. 8.1. This plot shows the normalized values of displacement in the middle point of plate versus the normalized values of applied in-plane shear load. It can be noticed from Fig. 8.1 that the convergence of nonlinear equilibrium curves is achieved at least for  $E_{surrounding}/E_1$  ratio 0.0001. Therefore, in the following sections, this ratio  $E_{surrounding}/E_1$  will be assumed for the surrounding area. Moreover, for the sake of brevity and due to the fact that equilibrium curves and deformed configurations of the main plate are of interest, the surrounding area deformations will not be shown in the following sections. The material properties of the investigated composite plates are provided in Table 8.1.

Table 8.1 Material properties of the investigated composite plates [240]

Material	$E_1$ (GPa)	$E_2 = E_3$ (GPa)	$G_{12}=G_{13}=G_{23}$ (GPa)	$\nu_{12}=\nu_{13}=\nu_{23}$
Carbon Epoxy	206.9	5.2	2.6	0.25
Baron Epoxy	206.9	20.7	5.2	0.3

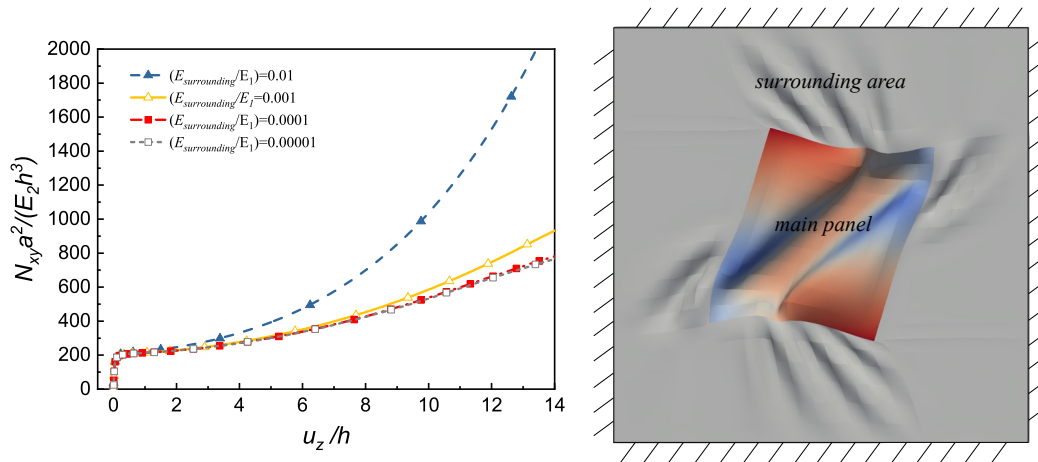


Fig. 8.1 The effect of material properties of surrounding area on the equilibrium curves for  $[45/-45]_s$  composite plates without stiffeners subjected to negative pure shear loading conditions based on the 12x12Q9-LD1 model

## 8.2.2 The stiffeners

In practical applications such as the wing or longeron aerospace structures, plates and panels are bounded by some attachments or stiffeners along their edges (See Fig. 8.2). In fact, these stiffeners impose the load or displacement boundary conditions on the main plate because they can enforce the edges a uniform displacement according to their stiffness. In this chapter, the stiffeners are modeled using one row of Q9 plate elements, and are assumed to be isotropic with Young's modulus of  $E_{stiffener}$ . The equilibrium curves corresponding to the models with different material properties of stiffeners are illustrated in the graph of Fig. 8.2. This graph shows different nonlinear responses of  $[45/-45]_s$  plate structures subjected to negative pure shear loading with the values of  $E_{stiffener}/E_1$  ratio changing from 0.1 to 100. Fig. 8.2 shows that the post-buckling response of the main plate is influenced remarkably as the material properties of the stiffeners are changed. Increasing the values of  $E_{stiffener}/E_1$  ratio results in higher rigidity and load-carrying capacity of the main plate structure. In fact, the stiffeners impose constraints on the rotations of edges, and enforce more uniform distributions of displacements on them. It should be noted that for the subsequent analysis of this chapter, the case with stiffener  $\frac{E_s}{E_1} = 10$  will be employed, and will be referred to as *with stiffener* plates.

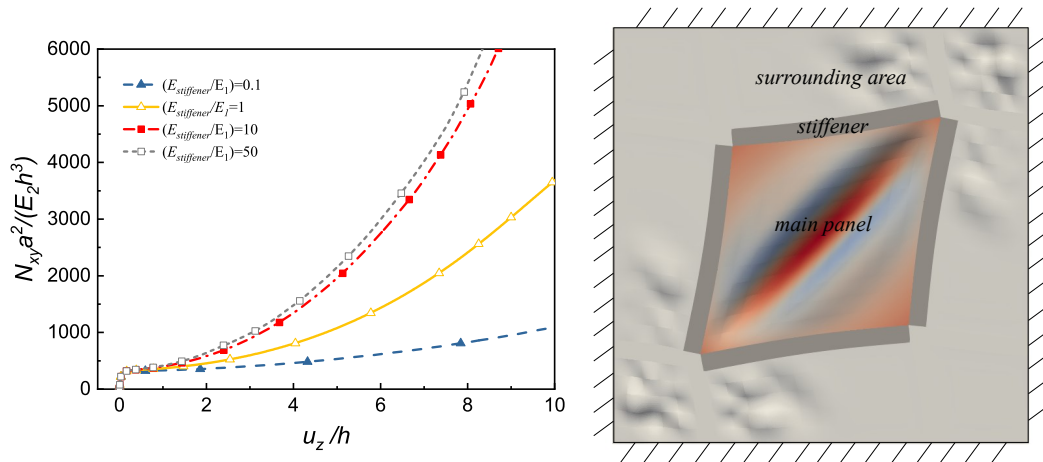


Fig. 8.2 The effect of material properties of the stiffeners on the equilibrium curves for  $[45/-45]_s$  composite plates with stiffeners subjected to negative pure shear loading conditions based on the 12x12Q9-LD1 model

### 8.2.3 Validation of models

In order to demonstrate the consistency of the proposed method, in this section, the nonlinear equilibrium curves obtained by the CUF and the presented modeling technique are compared with the available literature [226, 240]. Fig. 8.3 illustrates the comparison of equilibrium curves for Baron Epoxy composite plates subjected to pure shear loading based on the 12x12Q9-LD1 CUF model and the available literature. It is shown that for different lamination angles and loading conditions, the results obtained by the CUF correlate well with the ones reported in the references. For the sake of completeness, some of the equilibrium points for Baron Epoxy composite plates subjected to pure shear loading based on the 12x12Q9-LD1 CUF model and the available literature are also compared in Table 8.2 .

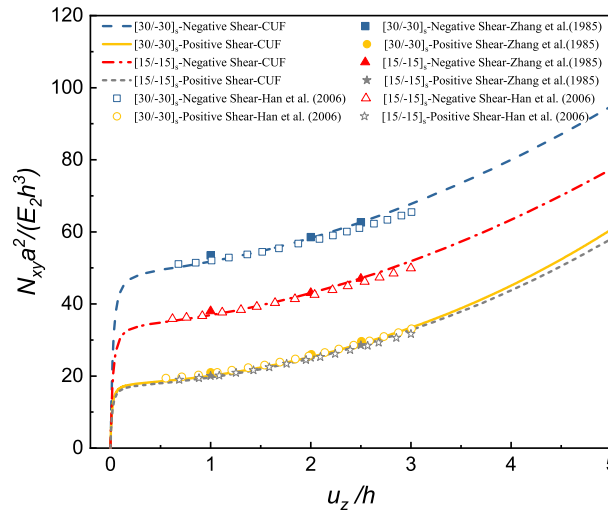


Fig. 8.3 The comparison of equilibrium curves for Baron Epoxy composite plates subjected to pure shear loading based on the 12x12Q9-LD1 CUF model and the available literature [226, 240]

Table 8.2 Equilibrium points for Baron Epoxy composite plates subjected to pure shear loading based on the 12x12Q9-LD1 CUF model and the available literature

Lamination angles	Negative shear		Positive shear	
	$\frac{N_{xy}a^2}{E_2h^3}$		$\frac{N_{xy}a^2}{E_2h^3}$	
	$\frac{u_z}{h} = 1$	$\frac{u_z}{h} = 2.5$	$\frac{u_z}{h} = 1$	$\frac{u_z}{h} = 2.5$
[30/ - 30] <sub>s</sub> -CUF	51.87	62.59	20.23	28.87
[30/ - 30] <sub>s</sub> -Ref. [226]	53.49	62.30	20.98	29.31
[30/ - 30] <sub>s</sub> -Ref. [240]	52.05	61.20	20.70	28.98
[15/ - 15] <sub>s</sub> -CUF	37.34	47.11	19.71	28.35
[15/ - 15] <sub>s</sub> -Ref. [226]	38.02	47.01	20.03	28.74
[15/ - 15] <sub>s</sub> -Ref. [240]	37.63	46.48	19.87	27.96

A similar comparison is presented in Fig. 8.4 for Carbon Epoxy composite plates with various lamination angles. In Table 8.3, some of the equilibrium points are reported for Carbon Epoxy composite plates subjected to pure negative shear loading based on the 12x12Q9-LD1 CUF model and the available literature. It is observed that the results obtained by the CUF are in good agreement with the available literature. Furthermore, the results are consistent with the fact that the load-carrying

capacity and rigidity of the composite plate with four layers  $[45/-45]_2$  are increased in comparison with the plate with only two layers  $[45/-45]$ . Also, it should be noted that the proposed method can predict larger displacement and rotations compared to the available literature. Note that the equilibrium curves of composite plates with larger deflections will be completely reported in the following sections.

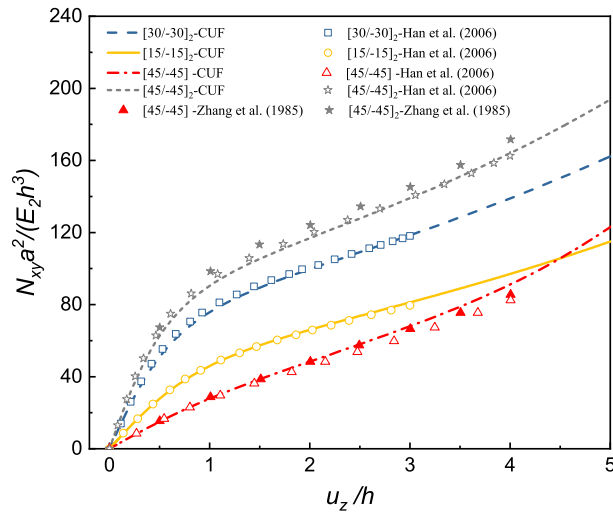


Fig. 8.4 The comparison of equilibrium curves for Carbon Epoxy composite plates subjected to pure negative shear loading based on the 12x12Q9-LD1 CUF model and the available literature [226, 240]

Table 8.3 Equilibrium points for Carbon Epoxy composite plates subjected to pure negative shear loading based on the 12x12Q9-LD1 CUF model and the available literature

Lamination angles	CUF 2D		Ref. [226]		Ref. [240]	
	$\frac{N_{xy}a^2}{E_2h^3}$		$\frac{N_{xy}a^2}{E_2h^3}$		$\frac{N_{xy}a^2}{E_2h^3}$	
	$\frac{u_z}{h} = 1$	$\frac{u_z}{h} = 3$	$\frac{u_z}{h} = 1$	$\frac{u_z}{h} = 3$	$\frac{u_z}{h} = 1$	$\frac{u_z}{h} = 3$
$[45/-45]_2$	92.11	139.02	98.48	145.31	94.06	139.71
$[45/-45]$	28.35	68.47	28.70	66.46	27.66	64.33
$[30/-30]_2$	76.08	119.30	-	-	77.81	118.92
$[15/-15]_2$	45.99	81.26	-	-	45.64	8.14

### 8.3 Pure shear loading

In this section, numerical assessments are provided in order to investigate the geometrically nonlinear response of composite plate structures subjected to pure shear loading. Then, the effects of stiffeners and surroundings on the equilibrium curves of composite plates are evaluated meticulously according to Section 8.2. For the first analysis cases, four-layer composite plates with different lamination angles  $[30/-30]_s$ ,  $[45/-45]_s$ , and  $[0/90]_s$  are studied. The height and width of the plate structures are  $a = b = 25$  cm, and the thickness is assumed to be  $h = 2.5$  mm. The plate structures are subjected to negative and positive in-plane shear loadings  $N_{xy}$ . The edge conditions are simply-supported that only the transverse deflections are restrained at the edges. The material properties for the Carbon Epoxy composite plates are reported in Table 8.1 [240]. In Fig. 8.5, the normalized values of displacements in the middle point of plate versus the normalized values of applied in-plane shear loads are plotted. In this figure, the equilibrium curves are compared for the composite plates without stiffeners subjected to pure shear loading based on the 12x12Q9-LD1 model.

The deformed composite plates without stiffeners subjected to pure shear loading in correspondence with Fig. 8.5b are shown in Table 8.4. Moreover, in Table 8.5, some of the equilibrium points are compared for composite plates without stiffeners subjected to pure shear loading based on the 12x12Q9-LD1 model. Note that, according to the results, the direction of the applied shear loading plays an important role in the geometrically nonlinear response of composite plates. Here, the plate with lamination angles  $[45/-45]_s$  under negative shear shows higher rigidity and load-carrying capacity compared to the other investigated cases.

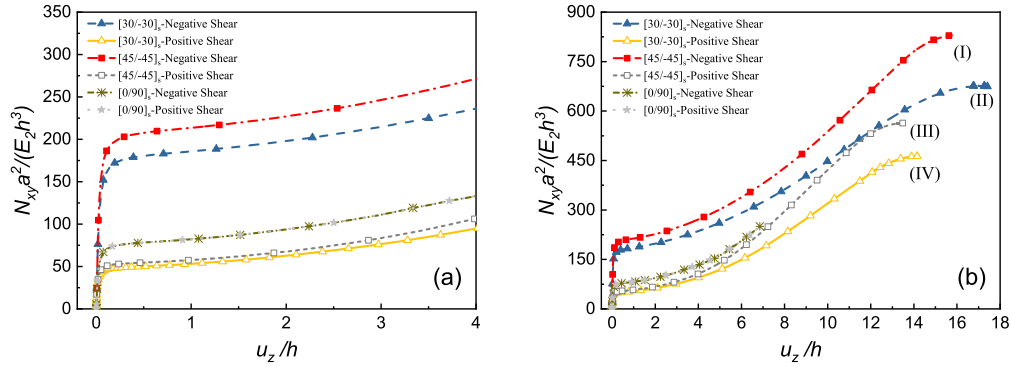


Fig. 8.5 The comparison of equilibrium curves for composite plates without stiffeners subjected to pure shear loading based on the 12x12Q9-LD1 model (a) prebuckling and buckling (b) post-buckling in large deflections

Table 8.4 The deformation contour plots based on Fig. 8.5(b) for composite plates without stiffeners subjected to pure shear loading

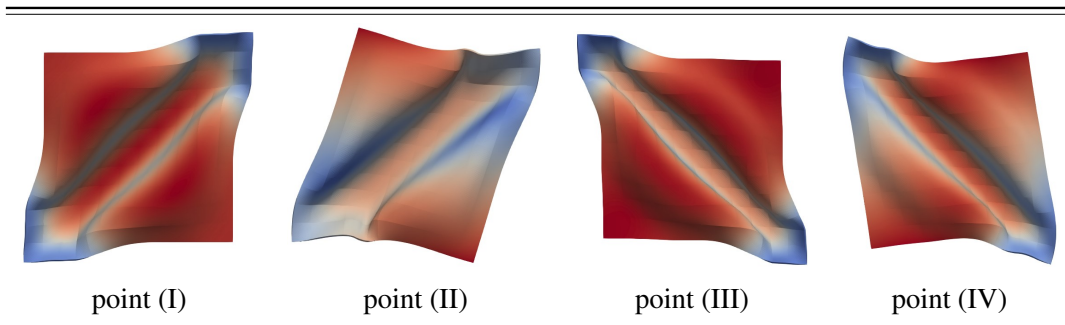


Table 8.5 Equilibrium points for composite plates without stiffeners subjected to pure shear loading based on the 12x12Q9-LD1 model

Lamination angles	Negative shear		Positive shear	
	$\frac{N_{xy}a^2}{E_2h^3}$		$\frac{N_{xy}a^2}{E_2h^3}$	
	$\frac{u_z}{h} = 3$	$\frac{u_z}{h} = 10$	$\frac{u_z}{h} = 3$	$\frac{u_z}{h} = 10$
$[30/-30]_s$	215.22	447.31	76.79	319.70
$[45/-45]_s$	246.56	539.87	84.10	421.79
$[0/90]_s$	111.79	416.41	111.79	416.41



In Fig. 8.6, similar assessments are carried out for the composite plates with stiffeners under pure shear loading. The deformed composite plates with stiffeners subjected to pure shear loading in correspondence with Fig. 8.6b are shown in Table 8.6. Furthermore, in Table 8.7, some of the equilibrium points are compared for composite plates with stiffeners subjected to pure shear loading based on the 12x12Q9-LD1 model. Comparing the geometrically nonlinear response of composite plates without stiffeners and the ones with stiffeners (see Figs. 8.5 and 8.6) demonstrates that the plates with stiffeners show significantly higher load-carrying capacity in comparison with the plates without stiffeners. This could be due to the fact that in the presence of stiffeners, the plate structure becomes more constrained and more likely tends towards clamped edge conditions. Also, it should be noted that for the prebuckling and buckling states, the composite plates with lamination angles  $[45/-45]_s$  under negative shear show higher load-carrying capacity. However, in the large deflections ( $\frac{u_z}{h} > 4$ ), the plate with similar lamination angles under positive shear shows higher rigidity.

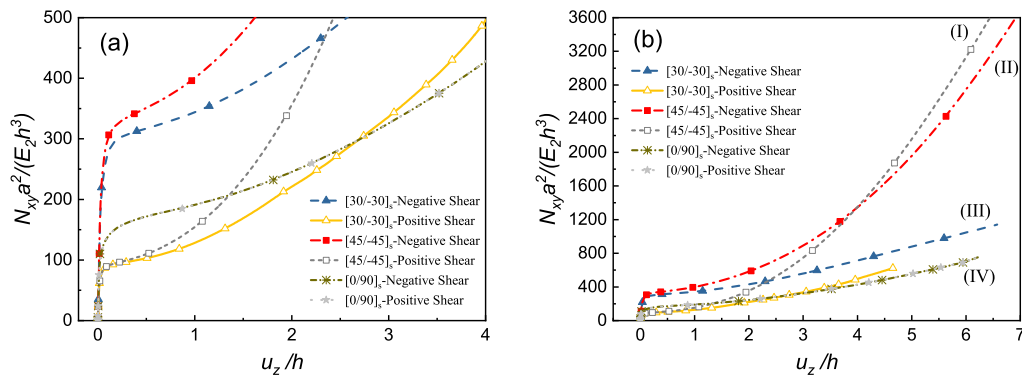


Fig. 8.6 The comparison of equilibrium curves for composite plates with stiffeners subjected to pure shear loading based on the 12x12Q9-LD1 model (a) prebuckling and buckling (b) post-buckling in large deflections

Table 8.6 The deformation contour plots based on Fig. 8.6(b) for composite plates with stiffeners subjected to pure shear loading

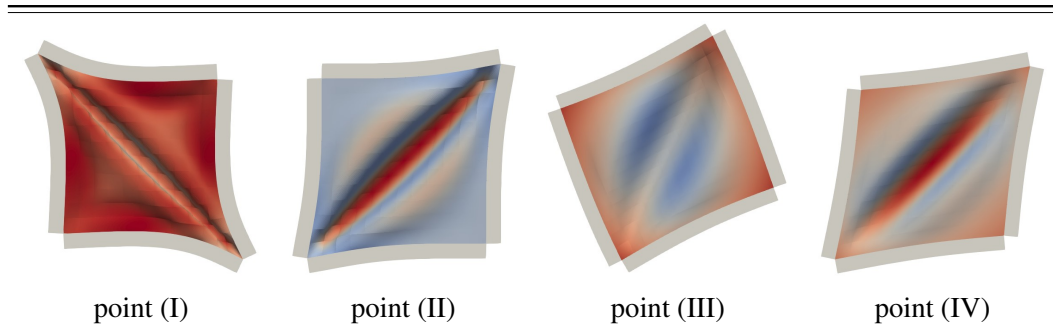


Table 8.7 Equilibrium points for composite plates with stiffeners subjected to pure shear loading based on the 12x12Q9-LD1 model

Lamination angles	Negative shear		Positive shear	
	$\frac{N_{xy}a^2}{E_2h^3}$		$\frac{N_{xy}a^2}{E_2h^3}$	
	$\frac{u_z}{h} = 1$	$\frac{u_z}{h} = 4$	$\frac{u_z}{h} = 1$	$\frac{u_z}{h} = 4$
$[30/-30]_s$	343.33	711.46	128.33	490.91
$[45/-45]_s$	400.85	1344.66	155.04	1351.78
$[0/90]_s$	191.66	419.76	191.66	419.76

## 8.4 Shear and biaxial compressive loading

Fig. 8.7 shows the comparison of equilibrium curves for the same four-layer composite plates with different lamination angles  $[30/-30]_s$ ,  $[45/-45]_s$ , and  $[0/90]_s$  subjected to in-plane shear and biaxial compressive loading. This figure plots the normalized values of displacements in the middle point of plate versus the normalized values of applied in-plane shear loads. Here, the applied compressive load is assumed to be equal to the in-plane shear load ( $N_x = N_y = N_{xy}$ ). The deformed composite plates without stiffeners subjected to pure shear and biaxial compressive loading in correspondence with Fig. 8.7b are depicted in Table 8.8. It is evident that the deformed configurations of composite plates are strongly dependent on the loading conditions. For instance, here, the presence of biaxial compressive loading results in the different

nonlinear responses of plates (see Figs. 8.8 and 8.4 for comparison). Moreover, in Table 8.9, some of the equilibrium points are compared for the mentioned composite plates. Similar to the previous section, the direction of the applied shear loading influences the geometrically nonlinear response of composite plates significantly. In addition, the plate with lamination angles  $[45/-45]_s$  under negative shear shows higher buckling strength.

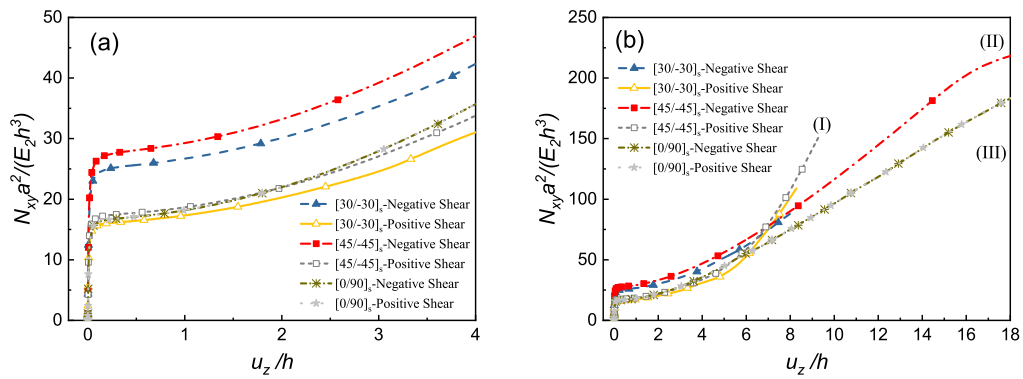


Fig. 8.7 The comparison of equilibrium curves for composite plates without stiffeners subjected to pure shear and biaxial compressive loading based on the 12x12Q9-LD1 model (a) prebuckling and buckling (b) post-buckling in large deflections

Table 8.8 The deformation contour plots based on Fig. 8.7(b) for composite plates without stiffeners subjected to pure shear and biaxial compressive loading

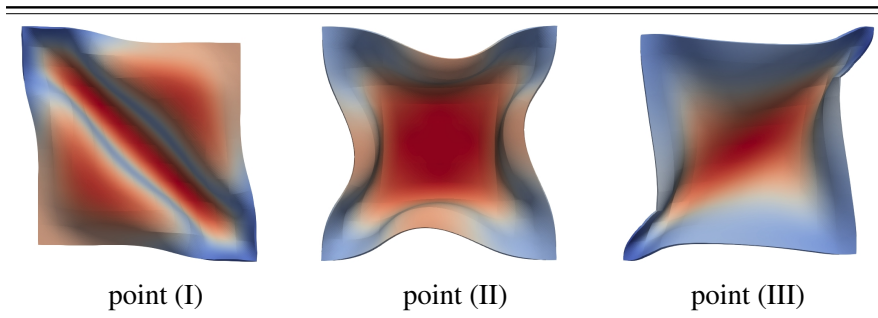


Table 8.9 Equilibrium points for composite plates without stiffeners subjected to pure shear and biaxial compressive loading based on the 12x12Q9-LD1 model

Lamination angles	Negative shear		Positive shear	
	$\frac{N_{xy}a^2}{E_2h^3}$		$\frac{N_{xy}a^2}{E_2h^3}$	
	$\frac{u_z}{h} = 2$	$\frac{u_z}{h} = 8$	$\frac{u_z}{h} = 2$	$\frac{u_z}{h} = 8$
$[30/-30]_s$	29.98	87.74	20.25	101.41
$[45/-45]_s$	33.25	89.94	21.85	108.02
$[0/90]_s$	22.17	74.95	22.17	74.95

Fig. 8.8 shows how the deflection at the middle point of laminate varies by increasing the loading after the bifurcation point for composite plates with stiffeners subjected to in-plane shear and biaxial compressive loading. The deformation contour plots of these composite plates based on the 12x12Q9-LD1 model are provided in Table 8.10. For some specific displacement values, the normalized loads are reported in Table 8.11. Similar to the previous cases, the  $[45/-45]_s$  plate subjected to negative shear loading shows higher buckling loads. It can also be noticed that in the large deflections, the same composite plate under negative shear loading exhibits somehow a similar nonlinear response to the one subjected to the positive shear (see Fig. 8.8b). The comparison of equilibrium curves for the composite plates without stiffeners and the ones with stiffeners (see Figs. 8.7 and 8.8) confirms the fact that the plates with stiffeners show significantly higher load-carrying capacity compared to the plates without stiffeners. Actually, in the presence of stiffeners, the plate structure becomes more constrained and more likely tends towards clamped edge conditions which results in higher load-carrying capacity.

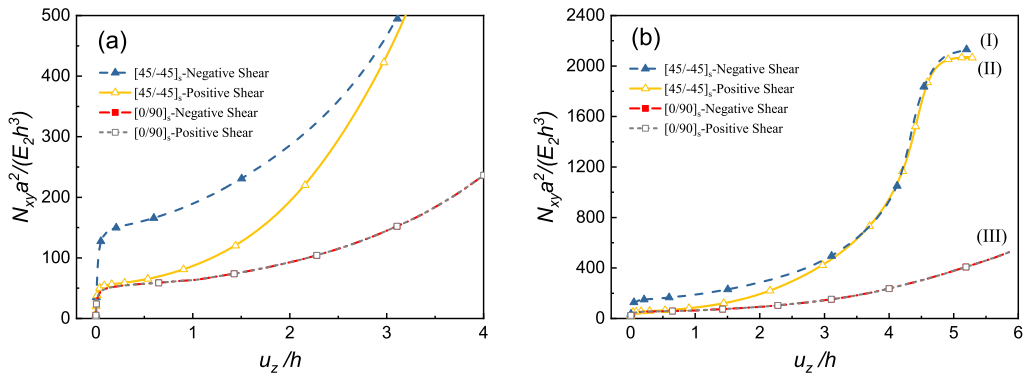


Fig. 8.8 The comparison of equilibrium curves for composite plates with stiffeners subjected to pure shear and biaxial compressive loading based on the 12x12Q9-LD1 model (a) pre-buckling and buckling (b) post-buckling in large deflections

Table 8.10 The deformation contour plots based on Fig. 8.8(b) for composite plates with stiffeners subjected to pure shear and biaxial compressive loading

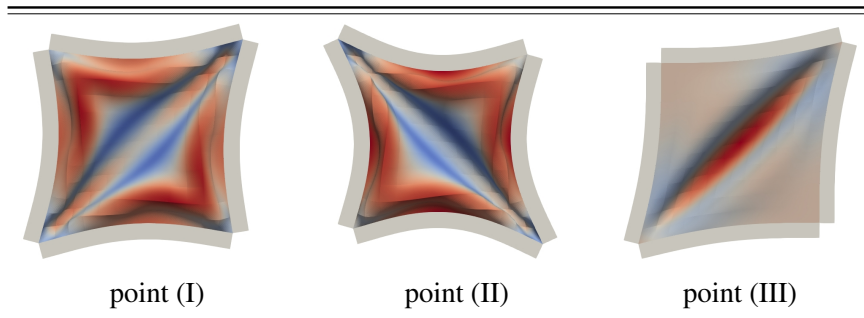


Table 8.11 Equilibrium points for composite plates with stiffeners subjected to pure shear and biaxial compressive loading based on the 12x12Q9-LD1 model

Lamination angles	Negative shear		Positive shear	
	$\frac{N_{xy}a^2}{E_2h^3}$		$\frac{N_{xy}a^2}{E_2h^3}$	
	$\frac{u_z}{h} = 1$	$\frac{u_z}{h} = 4$	$\frac{u_z}{h} = 1$	$\frac{u_z}{h} = 4$
$[45/-45]_s$	189.59	938.54	86.41	956.42
$[0/90]_s$	63.49	236.87	63.49	236.87

## 8.5 Shear and biaxial tensile loading

The final loading assessment corresponds to the same composite plates subjected to in-plane shear and biaxial tensile loading. Two different states of  $N_x = N_y = N_{xy}$  and  $N_x = N_y = 0.5 N_{xy}$  for the values of the applied tensile loading are assumed. The comparison of equilibrium curves for composite plates  $[45/-45]_s$  with stiffeners are provided in Fig. 8.9. It is observed that the loading condition with lower tensile load ( $N_x = N_y = 0.5 N_{xy}$ ) shows lower rigidity and buckling strength compared to the loading condition  $N_x = N_y = N_{xy}$ . This is due to the fact that tensile loading could somehow decrease the effects of deflections induced by the shear loading. Thus, the more tensile loads are applied, the more load-carrying capacity of the structure is increased. Additionally, the deformation contour plots of the mentioned composite plates corresponding to Fig. 8.9b are displayed in Table 8.12. It is indicated that in the large deflections, the case with positive shear and biaxial tensile loading  $N_x = N_y = N_{xy}$  exhibits higher rigidity and load-carrying capacity, which is because of the formation of wrinkles on the deformed plate (see first deformed configuration (I) of Table 8.12).

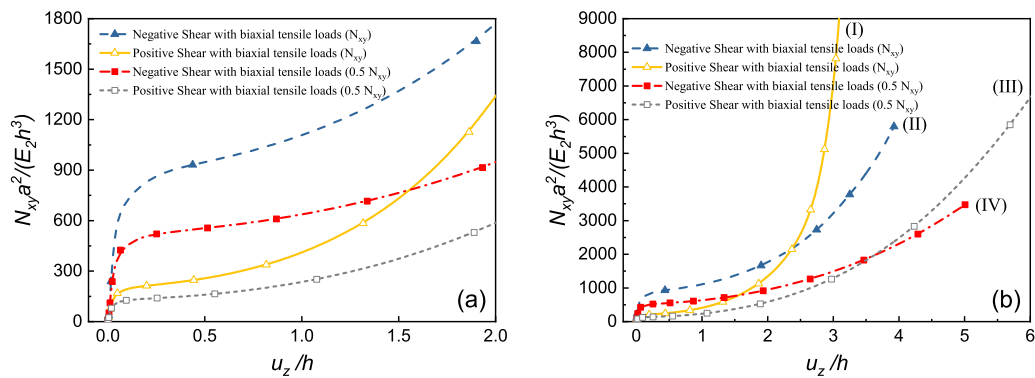
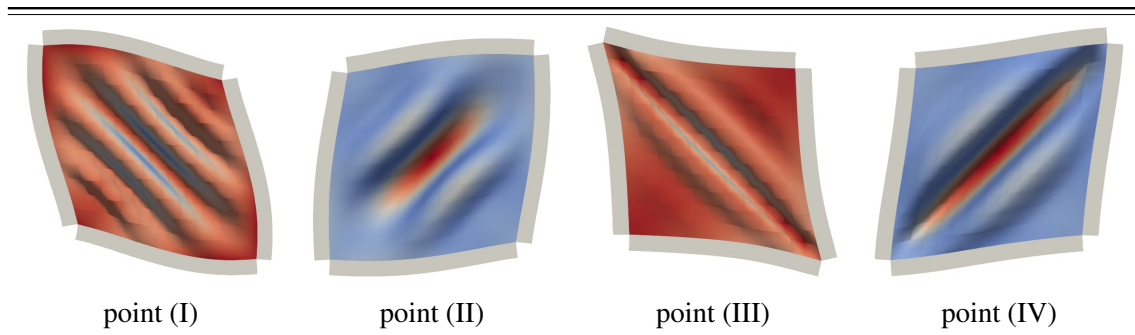


Fig. 8.9 The comparison of equilibrium curves for composite plates  $[45/-45]_s$  with stiffeners subjected to pure shear and biaxial tensile loading based on the  $12 \times 12 Q9$ -LD1 model (a) prebuckling and buckling (b) post-buckling in large deflections

Table 8.12 The deformation contour plots based on Fig. 8.9(b) for composite plates  $[45/-45]_s$  with stiffeners subjected to pure shear and biaxial tensile loading



## 8.6 Comparison of loading conditions

In this section, the geometrically nonlinear response of the previously-mentioned composite plates under different loading conditions is presented. The comparison of equilibrium curves for composite plates without stiffeners and the ones with stiffeners subjected to different loading conditions are compared in Figs. 8.10 and 8.11, respectively. The results demonstrate the fact that the biaxial compressive loading decreases the buckling strength and the rigidity of structure because of the intensification effects on the induced deflections by the shear loading. On the other hand, biaxial tensile loading lowers the induced deflections by the shear loading, resulting in the higher load-carrying capacity and rigidity of the plate structure.

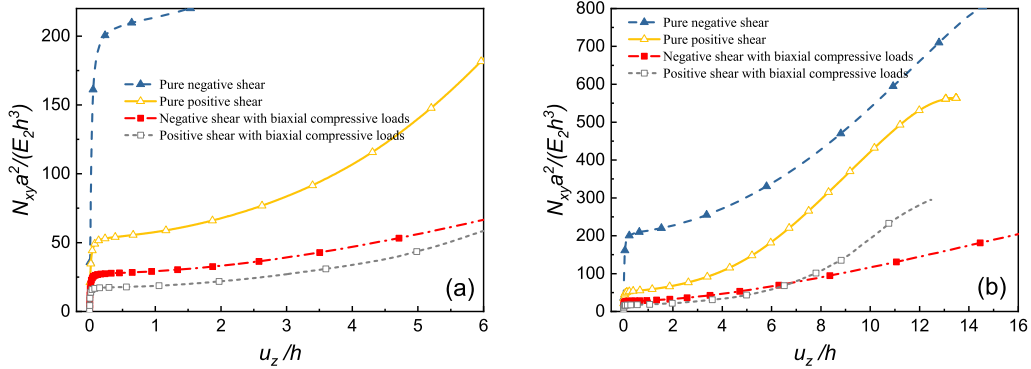


Fig. 8.10 The comparison of equilibrium curves for composite plates without stiffeners subjected to different loading conditions based on the 12x12Q9-LD1 model (a) prebuckling and buckling (b) post-buckling in large deflections

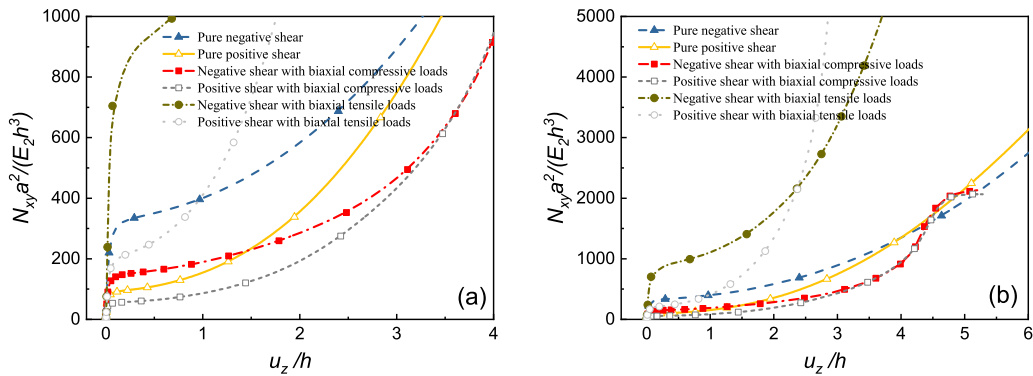


Fig. 8.11 The comparison of equilibrium curves for composite plates with stiffeners subjected to different loading conditions based on the 12x12Q9-LD1 model (a) prebuckling and buckling (b) post-buckling in large deflections

## 8.7 Conclusions

In this chapter, a modeling technique based on the CUF, layer-wise theory, and full Green–Lagrange nonlinear relations has been proposed in order to model the real shear conditions, and investigate the nonlinear response of composite plates subjected to shear and combined loadings. In this regard, the effects of boundary conditions imposed by the stiffeners and surrounding components have been con-



sidered and evaluated precisely. The layer-wise refined plate models have been implemented, employing the efficient LE functions through the laminate thickness. Various geometrically nonlinear assessments have been successfully carried out using the Newton-Raphson linearization scheme with the path-following method based on the arc-length constraint. The following points can be made according to the results:

- The use of layer-wise kinematics with Lagrange polynomial expansions provides the possibility of easily imposing interface compatibility conditions between different layers, and results in accurate evaluation of equilibrium curves and nonlinear response of the plates.
- Compared to some other strain-displacement assumptions such as von Kármán, the CUF-based full Green-Lagrange nonlinear model presented here can be efficiently used in very large displacements/rotations fields.
- For both Baron Epoxy and Carbon Epoxy composite plates with different lamination angles and shear loading conditions, the results obtained by the presented CUF-based method match well with the results reported in the available literature. In addition, the proposed method can be efficiently employed for the nonlinear analysis of plates under very large deflections.
- The lamination angles of the composite plates influence the post-buckling equilibrium curves remarkably. Among the investigated lamination angles, composite plate  $[45/-45]_s$  showed higher buckling strength.
- The direction of applied shear plays an important role in the geometrically nonlinear response of angle-ply composite plates. As a result, the plates under negative shear show higher buckling strength. On the other hand, in the large deflections, this effect might be changed according to the loading conditions and deformed configurations
- The plates with stiffeners show significantly higher load-carrying capacity compared to the plates without stiffeners. Actually, in the presence of stiffeners, the plate structure becomes more constrained and more likely tends towards clamped edge conditions.
- The deformed configurations of composite plates are strongly dependent on the loading conditions. For instance, in many cases, the plates subjected to

in-plane shear and biaxial compressive loading exhibit different nonlinear responses compared to the plates subjected to in-plane shear and biaxial tensile loading.

- Biaxial compressive loading decreases the buckling strength and the rigidity of structure because of the intensification effects on the induced deflections by the shear loading. On the other hand, biaxial tensile loading decreases the effects of induced deflections by the shear loading, resulting in the higher load-carrying capacity and rigidity of plate structure.

# Chapter 9

## Conclusions and perspectives

### 9.1 Summary

The dissertation has been focused on the refined structural and nonlinear theories in order to investigate the free vibration and post-buckling response of thin-walled beam and flexible plate structures. In this regard, the CUF has been employed to obtain nonlinear governing equations of the finite beam and plate elements. Then, various assessments have been conducted related to the thin-walled beam and flexible plate structures. The free vibration response of thin-walled isotropic and composite beams has been accurately evaluated, and the Vibration Correlation Technique has been used in order to investigate the variations of natural frequencies in thin-walled laminated isotropic and composite beam structures under compression. The physically and geometrically nonlinear analysis of thin-walled beams has been investigated using Newton–Raphson linearization scheme with the path-following method based on the arc-length constraint. The large-deflection and post-buckling of isotropic and composite plates under axial, in-plane shear and combined loadings considering different strain-displacement assumptions has been analyzed, and the corresponding equilibrium curves and stress distributions have been presented. Furthermore, the effects of stiffeners and displacement boundary conditions in the post-buckled laminated composite plates have been studied. The results have shown that the present method based on the CUF can be efficiently used for accurate structural analysis, including the free vibration and post-buckling of the thin-walled beam and flexible plate structures.

## 9.2 Concluding remarks

In Chapters 1 and 2, the details of implementation of the CUF framework, and the nonlinear governing equations have been provided. In Chapter 3, higher-order vibration modes in a series of open-section thin-walled beams have been investigated as benchmark problems. Detailed comparisons have been made between the classical beam theories, refined ones based on the CUF, shell models obtained using commercial FE software, and data from the literature. It has been shown that the natural frequencies and mode shapes found using the suggested efficient framework correlate well with those obtained using shell models, which require significantly more computational efforts. The importance of developing models capable of detecting cross-sectional deformations has been demonstrated. The MAC has been successfully used to compare the free vibration modes obtained by various structural theories, and it has been suggested that additional refinement is required for the TE when applied to the complicated cross-section geometries. It has been shown that the selected structural theory has a greater influence in higher-order modes.

In Chapter 4, the vibrations and buckling of thin-walled isotropic and composite beams under compression with different open cross-sections has been evaluated. The effects of axial loads on the variations of the beam structure's natural frequencies have been assessed. The MAC analysis has revealed that the number of related modes for classical models such as Taylor order 1 is much less than that for other Lagrange models. Indeed, classical beam theories eliminate a large number of modes in favor of never-existing rigid cross-section modes. As long as the initial buckling and vibration modes are similar; the VCT may be used to estimate buckling loads based on the decrease in the natural frequencies of the beam under progressive compressive loads. The advantages of the CUF 1D method with efficient LE have been shown for a more complex structural problem involving a channel-shaped composite beam subjected to compression with different number of transverse stiffeners. It been demonstrated that adding transverse stiffeners alters the mode shapes and natural frequencies of the beam structure significantly.

In Chapter 5, the CUF 1D model in combination with a Newton–Raphson linearization scheme based on the path-following method with arc-length constraint has been used to solve physically and geometrically nonlinear beam problems. Numerical results have been presented for square, channel-shaped, and T-shaped beam structures with elastic and elastoplastic materials subjected to large deformations and

rotations. It has been demonstrated that for the beams with different cross-sections, the equilibrium curves obtained by CUF 1D elastic and elastoplastic LE models match well with the results of available literature and 3D solid models. The stress distributions have been investigated based on the different LE models, and the results have been compared with 3D FE models. For the elastoplastic material, the plastic zones have been initiated near the top and bottom surfaces of the beam near the clamped edge, where the values of equivalent plastic strain have been increased due to the larger load factor values. Although the DOF and the computational costs of the problems have been reduced significantly using the current method, it can predict the equilibrium curves and the stress distributions of the structure accurately and precisely.

In Chapter 6, it has been shown that the CUF and layer-wise approaches may be used to investigate the large-deflection and post-buckling of rectangular isotropic and composite plates. The well-known von Kármán theory for nonlinear deformations of plates has been evaluated with several modifications. The equilibrium curves and stress distributions for different isotropic and composite plates have been provided and analyzed in detail. Different factors influencing the nonlinear response of plates, including the stacking sequence, number of layers, loading and edge conditions, have been thoroughly studied. In comparison with the von Kármán theory and its modifications, the full nonlinear model has been proved to be more reliable in order to investigate the correct equilibrium curves and stress distributions in the very large displacements and far post-buckling regime. It has been indicated that the buckling strength of the composite plates with clamped edge conditions is greater than those of the composite plates with other studied edge conditions, and the presence of a free edge, considerably reduces the buckling strength of the plate structures.

In Chapter 7, the stiffeners and boundary conditions effects on the geometrically nonlinear response of laminated composite plates under various strain-displacement assumptions have been studied. It has been demonstrated that the stiffeners' material properties have a significant impact on the nonlinear post-buckling behaviors, and the presence of stiffeners limits the rotations at the loaded edges of the plate structure by enforcing uniform edge displacement. Lower values of the stiffener's material properties have resulted in a post-buckling behavior that is similar to the response of the plate in the absence of the stiffener. On the other hand, higher values of material properties for the stiffener have resulted in rotational limitations in the loaded edges. Lamination angles and stacking sequence have shown to be important

in the composite plate structure's buckling and post-buckling behaviors. It has been shown that the quadratic shear stress distributions can be predicted with high accuracy using the cubic LD3 CUF plate models. The nonlinear response of the composite plate above the limit load and snap-through instability has been predicted using the presented CUF plate model.

In Chapter 8, a modeling technique based on the CUF, layer-wise theory, and full Green–Lagrange nonlinear relations has been proposed in order to model the real shear conditions, and investigate the nonlinear response of composite plates subjected to shear and combined loadings. It has been indicated that for both Baron Epoxy and Carbon Epoxy composite plates with different lamination angles and shear loading conditions, the results obtained by the presented CUF-based method match well with the results reported in the available literature. It has been demonstrated that the direction of applied shear plays an important role in the geometrically nonlinear response of angle-ply composite plates. As a result, the plates under negative shear show higher buckling strength. Biaxial compressive loading has resulted in the decrease of buckling strength and the rigidity of structure because of the intensification effects on the induced deflections by the shear loading. Nonetheless, biaxial tensile loading has resulted higher load-carrying capacity of the plate structure.

### 9.3 Future directions

Due to the reliable and accurate results of the CUF in solving geometrically and physically nonlinear problems of structures, further developments of the proposed methodology could be focused on a nonlinear local analysis and a localized buckling with the advantage of coupling the global/local approach with optimization tools to reduce computation time. Furthermore, the same nonlinear methodology will also be adopted to perform dynamic analyses. Other important topics that could be further developed could be the extension of CUF-based nonlinear finite elements for the analysis of deployable space structures, elastomers and mechanical meta-materials. Furthermore, Hyperelastic models could be implemented in the CUF 1D or CUF 2D frameworks in order to be used in the complex materials such as biological soft tissues and organs. For instance, the soft materials are susceptible to the occurrence of instability and failure that needs to be accurately predicted; therefore, using the

---

CUF, the constitutive relations of soft tissues or complex structures using continuum approaches could be investigated, and in-depth study on the material behavior of soft matters could be presented. In addition, future extensions could be focused on high-velocity impact problems and progressive failure of composite structures. Also, the effects of transverse stiffeners nonlinearities on the dynamic response of the beam and plate structures under compression deserve special attention.

# References

- [1] S. Brischetto and E. Carrera. Free vibration analysis for layered shells accounting of variable kinematic and thermo-mechanical coupling. *Shock and Vibration*, 19(2):151–169, 2012.
- [2] A. Varello and E. Carrera. Free vibration response of thin and thick nonhomogeneous shells by refined one-dimensional analysis. *Journal of Vibration and Acoustics*, 136(6), 2014.
- [3] M. Cinefra, S. Valvano, and E. Carrera. A layer-wise mitc9 finite element for the free-vibration analysis of plates with piezo-patches. *International Journal of Smart and Nano Materials*, 6(2):85–104, 2015.
- [4] E. Zappino, T. Cavallo, and E. Carrera. Free vibration analysis of reinforced thin-walled plates and shells through various finite element models. *Mechanics of Advanced Materials and Structures*, 23(9):1005–1018, 2016.
- [5] E. Carrera, M. Petrolo, and P. Nali. Unified formulation applied to free vibrations finite element analysis of beams with arbitrary section. *Shock and Vibration*, 18(3):485–502, 2011.
- [6] E. Carrera, F. Miglioretti, and M. Petrolo. Computations and evaluations of higher-order theories for free vibration analysis of beams. *Journal of Sound and Vibration*, 331(19):4269–4284, 2012.
- [7] M. Petrolo, E. Zappino, and E. Carrera. Refined free vibration analysis of one-dimensional structures with compact and bridge-like cross-sections. *Thin-Walled Structures*, 56:49–61, 2012.
- [8] A. Pagani, M. Boscolo, J.R Banerjee, and E. Carrera. Exact dynamic stiffness elements based on one-dimensional higher-order theories for free vibration analysis of solid and thin-walled structures. *Journal of Sound and Vibration*, 332(23):6104–6127, 2013.
- [9] A. Pagani, F. Zangallo, and E. Carrera. Influence of non-structural localized inertia on free vibration response of thin-walled structures by variable kinematic beam formulations. *Shock and Vibration*, 2014, 2014.



- [10] E. Carrera, M. Filippi, P.K Mahato, and A. Pagani. Advanced models for free vibration analysis of laminated beams with compact and thin-walled open/closed sections. *Journal of Composite Materials*, 49(17):2085–2101, 2015.
- [11] M. Filippi, A. Pagani, M. Petrolo, G. Colonna, and E. Carrera. Static and free vibration analysis of laminated beams by refined theory based on chebyshev polynomials. *Composite Structures*, 132:1248–1259, 2015.
- [12] A. Pagani, E. Carrera, M. Boscolo, and J.R Banerjee. Refined dynamic stiffness elements applied to free vibration analysis of generally laminated composite beams with arbitrary boundary conditions. *Composite Structures*, 110:305–316, 2014.
- [13] A. Pagani, E. Carrera, and A.J.M Ferreira. Higher-order theories and radial basis functions applied to free vibration analysis of thin-walled beams. *Mechanics of Advanced Materials and Structures*, 23(9):1080–1091, 2016.
- [14] M. Dan, A. Pagani, and E. Carrera. Free vibration analysis of simply supported beams with solid and thin-walled cross-sections using higher-order theories based on displacement variables. *Thin-Walled Structures*, 98:478–495, 2016.
- [15] Y. Yan, A. Pagani, and E. Carrera. Exact solutions for free vibration analysis of laminated, box and sandwich beams by refined layer-wise theory. *Composite Structures*, 175:28–45, 2017.
- [16] A. Pagani, R. Augello, and E. Carrera. Frequency and mode change in the large deflection and post-buckling of compact and thin-walled beams. *Journal of Sound and Vibration*, 432:88–104, 2018.
- [17] E. Carrera, A. Pagani, and R. Augello. Effect of large displacements on the linearized vibration of composite beams. *International Journal of Non-Linear Mechanics*, 120:103390, 2020.
- [18] X. Xu, N. Fallahi, and H. Yang. Efficient cuf-based fem analysis of thin-wall structures with lagrange polynomial expansion. *Mechanics of Advanced Materials and Structures*, pages 1–22, 2020.
- [19] X. Xu, E. Carrera, R. Augello, E. Daneshkhah, and H. Yang. Benchmarks for higher-order modes evaluation in the free vibration response of open thin-walled beams due to the cross-sectional deformations. *Thin-Walled Structures*, 166:107965, 2021.
- [20] R. Augello, E. Daneshkhah, X. Xu, and E. Carrera. Efficient cuf-based method for the vibrations of thin-walled open cross-section beams under compression. *Journal of Sound and Vibration*, page 116232, 2021.
- [21] H. Yang, E. Daneshkhah, R. Augello, X. Xu, and E. Carrera. Numerical vibration correlation technique for thin-walled composite beams under compression based on accurate refined finite element. *Composite Structures*, In Press, 2021.

- [22] B. Wu, A. Pagani, M. Filippi, W.Q. Chen, and E. Carrera. Accurate stress fields of post-buckled laminated composite beams accounting for various kinematics. *International Journal of Non-Linear Mechanics*, 111:60–71, 2019.
- [23] O.O. Ochoa and J.N. Reddy. Finite element analysis of composite laminates. In *Finite Element Analysis of Composite Laminates*, pages 37–109. Springer, 1992.
- [24] E. Carrera, M. Cinefra, M. Petrolo, and E. Zappino. *Finite element analysis of structures through unified formulation*. John Wiley & Sons, 2014.
- [25] K. J. Bathe. *Finite Element Procedure*. Prentice Hall, Upper Saddle River, New Jersey, USA, 1996.
- [26] Erasmo Carrera and Enrico Zappino. Carrera unified formulation for free-vibration analysis of aircraft structures. *AIAA Journal*, 54(1):280–292, 2016.
- [27] E. Carrera, A. Pagani, and M. Petrolo. Classical, refined and component-wise theories for static analysis of reinforced-shell wing structures. *AIAA Journal*, 51(5):1255–1268, 2013.
- [28] E. Carrera, A. Pagani, and M. Petrolo. Refined 1D finite elements for the analysis of secondary, primary, and complete civil engineering structures. *Journal of Structural Engineering*, 141:04014123/1–14, 2015.
- [29] E. Carrera and A. Pagani. Free vibration analysis of civil engineering structures by component-wise models. *Journal of Sound and Vibration*, 333(19):4597–4620, 2014.
- [30] J.N Reddy. On locking-free shear deformable beam finite elements. *Computer methods in applied mechanics and engineering*, 149(1-4):113–132, 1997.
- [31] E. Carrera, G. Giunta, P. Nali, and M. Petrolo. Refined beam elements with arbitrary cross-section geometries. *Computers & structures*, 88(5-6):283–293, 2010.
- [32] O.C Zienkiewicz, R.L Taylor, and J. Too. Reduced integration technique in general analysis of plates and shells. *International Journal for Numerical Methods in Engineering*, 3(2):275–290, 1971.
- [33] O.C Zienkiewicz and E. Hinton. Reduced integration, function smoothing and non-conformity in finite element analysis (with special reference to thick plates). *Journal of the Franklin Institute*, 302(5-6):443–461, 1976.
- [34] D.S Malkus and T.R Hughes. Mixed finite element methods—reduced and selective integration techniques: a unification of concepts. *Computer Methods in Applied Mechanics and Engineering*, 15(1):63–81, 1978.

- [35] T.R Hughes, M. Cohen, and M. Haroun. Reduced and selective integration techniques in the finite element analysis of plates. *Nuclear Engineering and design*, 46(1):203–222, 1978.
- [36] E.N Dvorkin and K.J Bathe. A continuum mechanics based four-node shell element for general non-linear analysis. *Engineering computations*, 1984.
- [37] R.H Macneal. Derivation of element stiffness matrices by assumed strain distributions. *Nuclear Engineering and Design*, 70(1):3–12, 1982.
- [38] E. Carrera, A.G de Miguel, and A. Pagani. Extension of mitc to higher-order beam models and shear locking analysis for compact, thin-walled, and composite structures. *International Journal for Numerical Methods in Engineering*, 112(13):1889–1908, 2017.
- [39] A. Pagani and E. Carrera. Large-deflection and post-buckling analyses of laminated composite beams by carrera unified formulation. *Composite Structures*, 170:40–52, 2017.
- [40] A. Pagani and E. Carrera. Unified formulation of geometrically nonlinear refined beam theories. *Mechanics of Advanced Materials and Structures*, 25(1):15–31, 2018.
- [41] M. Petrolo, M.H. Nagaraj, I. Kaleel, and E. Carrera. A global-local approach for the elastoplastic analysis of compact and thin-walled structures via refined models. *Computers & Structures*, 206:54–65, 2018.
- [42] E. Carrera, I. Kaleel, and M. Petrolo. Elastoplastic analysis of compact and thin-walled structures using classical and refined beam finite element models. *Mechanics of advanced materials and structures*, 26(3):274–286, 2019.
- [43] B. Wu, A. Pagani, M. Filippi, W.Q. Chen, and E. Carrera. Large-deflection and post-buckling analyses of isotropic rectangular plates by carrera unified formulation. *International Journal of Non-Linear Mechanics*, 2019.
- [44] A. Pagani and E. Carrera. Unified formulation of geometrically nonlinear refined beam theories. *Mechanics of Advanced Materials and Structures*, 25(1):15–31, 2018.
- [45] E. Carrera. Multilayered shell theories accounting for layerwise mixed description, Part 1: governing equations. *AIAA Journal*, 37(9):1107–1116, 1999.
- [46] E. Carrera. Multilayered shell theories accounting for layerwise mixed description, Part 2: Numerical evaluations. *AIAA Journal*, 37(9):1117–1124, 1999.
- [47] I. Kaleel, E. Carrera, and M. Petrolo. Progressive delamination of laminated composites via 1d models. *Composite Structures*, page 111799, 2019.

- [48] I. Kaleel, M. Petrolo, E. Carrera, and A.M. Waas. On the effectiveness of higher-order one-dimensional models for physically nonlinear problems. In *Advances in Predictive Models and Methodologies for Numerically Efficient Linear and Nonlinear Analysis of Composites*, pages 67–81. Springer, 2019.
- [49] M.H. Nagaraj, I. Kaleel, E. Carrera, and M. Petrolo. Nonlinear analysis of compact and thin-walled metallic structures including localized plasticity under contact conditions. *Engineering Structures*, 203:109819, 2020.
- [50] M. Petrolo, M.H. Nagaraj, E. Daneshkhah, R. Augello, and E. Carrera. Static analysis of thin-walled beams accounting for nonlinearities. *Proceedings of the Institution of Mechanical Engineers, Part C: Journal of Mechanical Engineering Science*, page 09544062211032997, 2021.
- [51] A. Pagani, E. Carrera, and R. Augello. Evaluation of various geometrical nonlinearities in the response of beams and shells. *AIAA Journal*, 57(8):3524–3533, 2019.
- [52] A. Pagani, E. Daneshkhah, X. Xu, and E. Carrera. Evaluation of geometrically nonlinear terms in the large-deflection and post-buckling analysis of isotropic rectangular plates. *International Journal of Non-Linear Mechanics*, 121:103461, 2020.
- [53] X. Xu, E. Carrera, H. Yang, E. Daneshkhah, and R. Augello. Evaluation of stiffeners effects on buckling and post-buckling of laminated panels. *Aerospace Science and Technology*, page 107431, 2022.
- [54] E. Carrera, R. Azzara, E. Daneshkhah, A. Pagani, and B. Wu. Buckling and post-buckling of anisotropic flat panels subjected to axial and shear in-plane loadings accounting for classical and refined structural and nonlinear theories. *International Journal of Non-Linear Mechanics*, 133:103716, 2021.
- [55] E. Carrera, A. Pagani, R. Azzara, and R. Augello. Vibration of metallic and composite shells in geometrical nonlinear equilibrium states. *Thin-Walled Structures*, 157:107131, 2020.
- [56] B. Wu, A. Pagani, W.Q. Chen, and E. Carrera. Geometrically nonlinear refined shell theories by Carrera Unified Formulation. *Mechanics of Advanced Materials and Structures*, pages 1–21, 2019.
- [57] A. Pagani, R. Azzara, R. Augello, E. Carrera, and B. Wu. Accurate through-the-thickness stress distributions in thin-walled metallic structures subjected to large displacements and large rotations. *Vietnam Journal of Mechanics*, 42(3):239–254, 2020.
- [58] K. Washizu. *Variational Methods in Elasticity and Plasticity*. Pergamon, Oxford, 1968.
- [59] E. Carrera, G. Giunta, and M. Petrolo. *Beam Structures: Classical and Advanced Theories*. John Wiley & Sons, 2011.

- [60] J.N. Reddy. *An Introduction to Nonlinear Finite Element Analysis: with applications to heat transfer, fluid mechanics, and solid mechanics*. Oxford University Press, Oxford, 2014.
- [61] E. Carrera. A study on arc-length-type methods and their operation failures illustrated by a simple model. *Computers & Structures*, 50(2):217–229, 1994.
- [62] M. A. Crisfield. *Non-Linear Finite Element Analysis of Solid and Structures*. John Wiley & Sons, Chichester, England, 1991.
- [63] J.-L Batoz and G. Dhatt. Incremental displacement algorithms for nonlinear problems. *International Journal for Numerical Methods in Engineering*, 14(8):1262–1267, 1979.
- [64] M.A. Crisfield. A fast incremental/iterative solution procedure that handles “snap-through”. *Computers & Structures*, 13(1):55–62, 1981.
- [65] M.A. Crisfield. An arc-length method including line searches and accelerations. *International Journal for Numerical Methods in Engineering*, 19(9):1269–1289, 1983.
- [66] K. H. Schweizerhof and P. Wriggers. Consistent linearization for path following methods in nonlinear fe analysis. *Computer Methods in Applied Mechanics and Engineering*, 59(3):261–279, 1986.
- [67] P. Wriggers and J. C. Simo. A general procedure for the direct computation of turning and bifurcation points. *International Journal for Numerical Methods in Engineering*, 30(1):155–176, 1990.
- [68] E. Oñate. On the derivation and possibilities of the secant stiffness matrix for non linear finite element analysis. *Computational Mechanics*, 15(6):572–593, 1995.
- [69] O. C. Zienkiewicz and R. L. Taylor. *The Finite Element Method for Solid and Structural Mechanics*. Butterworth-Heinemann, Washington, 6th edition, 2005.
- [70] A. Pagani, E. Carrera, and R. Augello. Evaluation of various geometrically nonlinear terms in the static response of beams and thin-walled shell-like structures. *Submitted*, 2019.
- [71] T. von Kármán. Festigkeitsprobleme in maschinenbau. *Enzyklopaedie der Mathematischen Wissenschaften*, 4:311–385, 1910.
- [72] A. H. Nayfeh and P. F. Pai. *Linear and nonlinear structural mechanics*. John Wiley & Sons, 2008.
- [73] Leonhard Euler. Additamentum i: De curvas elasticis. *Leonhardi Euleri Opera omnia*, 1(24):231–297, 1911.

- [74] D. Bernoulli. De vibrationibus et sono laminarum elasticarum. *Commentarii Academiae Scientiarum Imperialis Petropolitanae*, 13(1741-3):105–20, 1751.
- [75] S.P. Timoshenko. Lxvi. on the correction for shear of the differential equation for transverse vibrations of prismatic bars. *The London, Edinburgh, and Dublin Philosophical Magazine and Journal of Science*, 41(245):744–746, 1921.
- [76] S.P. Timoshenko. X. on the transverse vibrations of bars of uniform cross-section. *The London, Edinburgh, and Dublin Philosophical Magazine and Journal of Science*, 43(253):125–131, 1922.
- [77] V. Z. Vlasov. Thin-walled elastic beams. *PST Catalogue*, 428, 1959.
- [78] V. Z. Vlasov. Thin-walled elastic rods. *Fizmatgiz, Moscow*, 1959.
- [79] J.W. Jaworski and E.H. Dowell. Free vibration of a cantilevered beam with multiple steps: Comparison of several theoretical methods with experiment. *Journal of sound and vibration*, 312(4-5):713–725, 2008.
- [80] S. Xu and X. Wang. Free vibration analyses of timoshenko beams with free edges by using the discrete singular convolution. *Advances in Engineering Software*, 42(10):797–806, 2011.
- [81] M.S. Choi, T. Kondou, and Y. Bonkobara. Development of free vibration analysis algorithm for beam structures by combining sylvester’s inertia theorem and transfer stiffness coefficient method. *Journal of mechanical science and technology*, 26(1):11–19, 2012.
- [82] S.K Jang and C.W Bert. Free vibration of stepped beams: exact and numerical solutions. *Journal of sound and vibration*, 130(2):342–346, 1989.
- [83] S.K Jang and C.W Bert. Free vibration of stepped beams: higher mode frequencies and effects of steps on frequency. *Journal of sound and vibration*, 132(1):164–168, 1989.
- [84] M.J Maurizi and P.M Belles. Free vibration of stepped beams elastically restrained against translation and rotation at one end. *Journal of sound and vibration*, 163(1):188–191, 1993.
- [85] F. Ju, H.P. Lee, and K.H. Lee. On the free vibration of stepped beams. *International journal of solids and structures*, 31(22):3125–3137, 1994.
- [86] W.L. Li. Free vibrations of beams with general boundary conditions. *Journal of Sound and Vibration*, 237(4):709–725, 2000.
- [87] P. Dey and S. Talukdar. Influence of warping on modal parameters of thin-walled channel section steel beam. *Procedia Engineering*, 144:52–59, 2016.

- [88] H.H. Chen and K.M. Hsiao. Quadruply coupled linear free vibrations of thin-walled beams with a generic open section. *Engineering Structures*, 30(5):1319–1334, 2008.
- [89] Li Jun, Shen Rongying, Hua Hongxing, and Jin Xianding. Coupled bending and torsional vibration of axially loaded bernoulli–euler beams including warping effects. *Applied Acoustics*, 65(2):153–170, 2004.
- [90] F. Mohri, L. Azrar, and M. Potier-Ferry. Vibration analysis of buckled thin-walled beams with open sections. *JSV*, 275(1-2):434–446, 2004.
- [91] A. Prokić. On triply coupled vibrations of thin-walled beams with arbitrary cross-section. *Journal of Sound and Vibration*, 279(3-5):723–737, 2005.
- [92] J. Murin, M. Aminbaghai, J. Hrabovsky, G. Balduzzi, M. Dorn, and H.A. Mang. Torsional warping eigenmodes of fgm beams with longitudinally varying material properties. *Engineering Structures*, 175:912–925, 2018.
- [93] R. Schardt. Generalized beam theory—an adequate method for coupled stability problems. *Thin-walled structures*, 19(2-4):161–180, 1994.
- [94] N. Silvestre and D. Camotim. Generalized beam theory to analyze the vibration of open-section thin-walled composite members. *Journal of Engineering Mechanics*, 139(8):992–1009, 2013.
- [95] C. Basaglia, D. Camotim, and H.B. Coda. Generalised beam theory (gbt) formulation to analyse the vibration behaviour of thin-walled steel frames. *Thin-Walled Structures*, 127:259–274, 2018.
- [96] Rui AS Bebiano, Dinar RZ Camotim, and Rodrigo M Gonçalves. Local and global vibration analysis of thin-walled members subjected to internal forces—application of generalised beam theory.
- [97] G. Piana, E. Lofrano, A. Manuello, and G. Ruta. Natural frequencies and buckling of compressed non-symmetric thin-walled beams. *Thin-Walled Structures*, 111:189–196, 2017.
- [98] F.A. Fazzolari. A beam formulation with 3d capabilities for the free vibration analysis of thin-walled metallic and composite structures. *Thin-Walled Structures*, 146:106441, 2020.
- [99] St. Kugler, PA Fotiu, and J. Murin. Analysis of shells, plates, and beams: A state of the art report [ch. beam dynamics using a generalized beam theory based on the solution of a reference beam problem]. 2020.
- [100] St. Kugler, PA Fotiu, and J. Murin. A novel gbt-formulation for thin-walled fgm-beam-structures based on a reference beam problem. *Composite Structures*, 257:113158, 2021.
- [101] W. Jrad. *Dynamic behavior of thin-walled beams: Analytical, numerical and experimental approaches*. PhD thesis, Université de Lorraine, 2019.

- [102] W. Jrad, F. Mohri, G. Robin, E.M. Daya, and J. Al-Hajjar. Analytical and finite element solutions of free and forced vibration of unrestrained and braced thin-walled beams. *Journal of Vibration and Control*, 26(5-6):255–276, 2020.
- [103] D.J. Gorman. *Free Vibration Analysis of Beams and Shafts*. A Wiley-Interscience publication. Wiley, 1975.
- [104] R.D. Blevins. *Formulas for natural frequency and mode shape*. 1979.
- [105] G.W. Wei, Y.B. Zhao, and Y. Xiang. A novel approach for the analysis of high-frequency vibrations. *Journal of Sound and Vibration*, 257(2):207–246, 2002.
- [106] R.S. Langley and N.S. Bardell. A review of current analysis capabilities applicable to the high frequency vibration prediction of aerospace structures. *The Aeronautical Journal*, 102(1015):287–297, 1998.
- [107] J.I. Ding, R.x. Wu, J. Wang, L.T. Xie, and J.k. Du. A new theory for high frequency vibrations of beams from displacements of trigonometric functions of thickness. In *2017 Symposium on Piezoelectricity, Acoustic Waves, and Device Applications (SPAWDA)*, pages 372–379. IEEE, 2017.
- [108] P. Reddy Sudalagunta, C. Sultan, R.K. Kapania, L.T. Watson, and P. Raj. Accurate computing of higher vibration modes of thin flexible structures. *AIAA Journal*, 54(5):1704–1718, 2016.
- [109] X. Wang. Novel discrete singular convolution for high-frequency vibration analysis of structural elements. *AIAA Journal*, 55(12):4364–4375, 2017.
- [110] Z. Lin, X. Chen, and B. Zhang. Energy finite element analysis of vibrating beams at high frequency. In *2017 IEEE International Conference on Information and Automation (ICIA)*, pages 1033–1038. IEEE, 2017.
- [111] R.J. Allemang and D.L. Brown. A correlation coefficient for modal vector analysis. In *Proceedings of the 1st international modal analysis conference*, volume 1, pages 110–116. SEM Orlando, 1982.
- [112] R.J. Allemang. The modal assurance criterion—twenty years of use and abuse. *Sound and vibration*, 37(8):14–23, 2003.
- [113] M. Pastor, M. Binda, and T. Harčarik. Modal assurance criterion. *Procedia Engineering*, 48:543–548, 2012.
- [114] J. Singer, J. Arbocz, and T. Weller. *Buckling experiments*. Second Edition, 2002.
- [115] P. H. Cabral, E. Carrera, H.E. dos Santos, P.H. Galeb, A. Pagani, D. Peeters, and A.P. Prado. Experimental and numerical vibration correlation of prestressed laminated reinforced panel. *Mechanics of Advanced Materials and Structures*, pages 1–13, 2020.



- [116] Haim Abramovich. The vibration correlation technique—a reliable nondestructive method to predict buckling loads of thin walled structures. *Thin-Walled Structures*, page 107308, 2020.
- [117] G. Piana. *Vibrations and stability of axially and transversely loaded structures*. PhD thesis, Turin: Polytechnic University Turin, 2013.
- [118] S. Fässler. Axial load determination using modal analysis. 2014.
- [119] G. Piana, E. Lofrano, A. Manuello, G. Ruta, and A. Carpinteri. Compressive buckling for symmetric twb with non-zero warping stiffness. *Engineering Structures*, 135:246–258, 2017.
- [120] X.Y. Li, X.H. Wang, Y.Y. Chen, Y. Tan, and H.J. Cao. Bending, buckling and free vibration of an axially loaded timoshenko beam with transition parameter: Direction of axial force. *International Journal of Mechanical Sciences*, 176:105545, 2020.
- [121] A. Prokić and D. Lukić. Flexural-torsional vibration analysis of axially loaded thin-walled beam. *Journal of the Brazilian Society of Mechanical Sciences and Engineering*, 34(3):262–268, 2012.
- [122] H. Abramovich. Natural frequencies of timoshenko beams under compressive axial loads. *Journal of Sound and Vibration*, 157(1):183–189, 1992.
- [123] A. Carpinteri, R. Malvano, A. Manuello, and G. Piana. Fundamental frequency evolution in slender beams subjected to imposed axial displacements. *Journal of Sound and Vibration*, 333(11):2390–2403, 2014.
- [124] Y.Q. Zhang, Y. Lu, S.L. Wang, and X. Liu. Vibration and buckling of a double-beam system under compressive axial loading. *Journal of Sound and Vibration*, 318(1-2):341–352, 2008.
- [125] X. Zhao, B. Chen, Y.H. Li, W.D. Zhu, F.J. Nkiegaing, and Y.B. Shao. Forced vibration analysis of timoshenko double-beam system under compressive axial load by means of green’s functions. *Journal of Sound and Vibration*, 464:115001, 2020.
- [126] G. Piana, A. Carpinteri, E. Lofrano, and G. Ruta. Vibration and buckling of open twbs with local weakening. *Procedia engineering*, 199:242–247, 2017.
- [127] Ł. Żmuda-Trzebiatowski. Investigation of natural frequencies of axially loaded thin-walled columns. In *MATEC Web of Conferences*, volume 219, page 02018. EDP Sciences, 2018.
- [128] G. Aquaro. *Torsional instability of open thin-walled beams: Numerical and experimental investigation*. PhD thesis, Politecnico di Torino, 2018.

- [129] A. Pagani, R. Augello, and E. Carrera. Virtual vibration correlation technique (vct) for nonlinear analysis of metallic and composite structures. In *ASME 2018 International Mechanical Engineering Congress and Exposition*. American Society of Mechanical Engineers Digital Collection, 2018.
- [130] Ahmed Elkaimbillah, Bouazza Braikat, Foudil Mohri, and Noureddine Damil. A one-dimensional model for computing forced nonlinear vibration of thin-walled composite beams with open variable cross-sections. *Thin-Walled Structures*, page 107211, 2020.
- [131] M.R. Forouzan, M.R. Hosseini A., and E. Daneshkhah. Damage and residual bending strength in glass-polyester molded grating composite panels after low-velocity impact. *Composite Structures*, 227:111290, 2019.
- [132] E. Daneshkhah, R.J. Nedoushan, D. Shahgholian, and N. Sina. Cost-effective method of optimization of stacking sequences in the cylindrical composite shells using genetic algorithm. *European Journal of Computational Mechanics*, pages 115–138, 2020.
- [133] O. Song and L. Librescu. Structural modeling and free vibration analysis of rotating composite thin-walled beams. *Journal of the American Helicopter Society*, 42(4):358–369, 1997.
- [134] J.R. Banerjee, H. Su, and C. Jayatunga. A dynamic stiffness element for free vibration analysis of composite beams and its application to aircraft wings. *Computers & Structures*, 86(6):573–579, 2008.
- [135] R.A. Jafari-Talookolaei, M.H. Kargarnovin, and M.T. Ahmadian. Free vibration analysis of cross-ply layered composite beams with finite length on elastic foundation. *International Journal of Computational Methods*, 5(01):21–36, 2008.
- [136] L.L. Ke, J. Yang, and S. Kitipornchai. Nonlinear free vibration of functionally graded carbon nanotube-reinforced composite beams. *Composite Structures*, 92(3):676–683, 2010.
- [137] J. Liu, S. Huang, J. Li, and Y.F. Chen. Vibration serviceability of large-span steel–concrete composite beam with precast hollow core slabs under walking impact. *Engineering*, 2021.
- [138] O. Song and L. Librescu. Free vibration of anisotropic composite thin-walled beams of closed cross-section contour. *Journal of Sound and Vibration*, 167(1):129–147, 1993.
- [139] A.S. Sayyad and Y.M. Ghugal. Bending, buckling and free vibration of laminated composite and sandwich beams: A critical review of literature. *Composite Structures*, 171:486–504, 2017.
- [140] M. Karama, B. Abou Harb, S. Mistou, and S. Caperaa. Bending, buckling and free vibration of laminated composite with a transverse shear stress continuity model. *Composites Part B: Engineering*, 29(3):223–234, 1998.

- [141] A.A. Khdeir and J.N. Reddy. Buckling of cross-ply laminated beams with arbitrary boundary conditions. *Composite Structures*, 37(1):1–3, 1997.
- [142] A.A. Khdeir and J.N. Reddy. An exact solution for the bending of thin and thick cross-ply laminated beams. *Composite Structures*, 37(2):195–203, 1997.
- [143] M.T. Piovan, C.P. Filipich, and V.H. Cortínez. Exact solutions for coupled free vibrations of tapered shear-flexible thin-walled composite beams. *Journal of Sound and Vibration*, 316(1-5):298–316, 2008.
- [144] V.H. Cortínez and M.T. Piovan. Vibration and buckling of composite thin-walled beams with shear deformability. *Journal of Sound and Vibration*, 258(4):701–723, 2002.
- [145] N. Silvestre and D. Camotim. Gbt-based local and global vibration analysis of loaded composite open-section thin-walled members. *International Journal of Structural Stability and Dynamics*, 6(01):1–29, 2006.
- [146] N. Silvestre and D. Camotima. Vibration analysis of composite folded-plate members. *International Journal of Vehicle Structures & Systems (IJVSS)*, 1, 2009.
- [147] A.H. Sheikh, A. Asadi, and O.T. Thomsen. Vibration of thin-walled laminated composite beams having open and closed sections. *Composite Structures*, 134:209–215, 2015.
- [148] L. Jun, H. Hongxing, and S. Rongying. Dynamic stiffness analysis for free vibrations of axially loaded laminated composite beams. *Composite Structures*, 84(1):87–98, 2008.
- [149] L. Jun, H. Xiang, and L. Xiaobin. Free vibration analyses of axially loaded laminated composite beams using a unified higher-order shear deformation theory and dynamic stiffness method. *Composite Structures*, 158:308–322, 2016.
- [150] L. Jun and H. Hongxing. Free vibration analyses of axially loaded laminated composite beams based on higher-order shear deformation theory. *Meccanica*, 46(6):1299–1317, 2011.
- [151] J.R. Banerjee. Free vibration of axially loaded composite timoshenko beams using the dynamic stiffness matrix method. *Computers & structures*, 69(2):197–208, 1998.
- [152] T.P. Vo and H.T. Thai. Free vibration of axially loaded rectangular composite beams using refined shear deformation theory. *Composite Structures*, 94(11):3379–3387, 2012.
- [153] T.P. Vo, J. Lee, and K. Lee. On triply coupled vibrations of axially loaded thin-walled composite beams. *Computers & structures*, 88(3-4):144–153, 2010.

- [154] A. Asadi and A.H. Sheikh. Buckling of thin-walled laminated composite beams having open and closed sections subjected to axial load and end moment. In *9th Australasian Congress on Applied Mechanics (ACAM9)*, page 70. Engineers Australia, 2017.
- [155] T.P. Vo and J. Lee. Free vibration of axially loaded thin-walled composite box beams. *Composite structures*, 90(2):233–241, 2009.
- [156] T.P. Vo and J. Lee. Vibration and buckling of thin-walled composite i-beams with arbitrary lay-ups under axial loads and end moments. *Mechanics of Advanced Materials and Structures*, 20(8):652–665, 2013.
- [157] T.P. Vo, J. Lee, K. Lee, and N. Ahn. Vibration analysis of thin-walled composite beams with i-shaped cross-sections. *Composite structures*, 93(2):812–820, 2011.
- [158] N.I. Kim, D.K. Shin, and Y.S. Park. Dynamic stiffness matrix of thin-walled composite i-beam with symmetric and arbitrary laminations. *Journal of Sound and Vibration*, 318(1-2):364–388, 2008.
- [159] T.P. Vo and J. Lee. Free vibration of thin-walled composite box beams. *Composite Structures*, 84(1):11–20, 2008.
- [160] T.P. Vo and J. Lee. Flexural–torsional buckling of thin-walled composite box beams. *Thin-walled structures*, 45(9):790–798, 2007.
- [161] T.P. Vo and J. Lee. Interaction curves for vibration and buckling of thin-walled composite box beams under axial loads and end moments. *Applied Mathematical Modelling*, 34(10):3142–3157, 2010.
- [162] T.P. Vo, J. Lee, and N. Ahn. On sixfold coupled vibrations of thin-walled composite box beams. *Composite structures*, 89(4):524–535, 2009.
- [163] N. D. Duc, P. H. Cong, and V. D. Quang. Nonlinear dynamic and vibration analysis of piezoelectric eccentrically stiffened fgm plates in thermal environment. *International Journal of Mechanical Sciences*, 115:711–722, 2016.
- [164] P. H. Cong, N. D. Khanh, N. D. Khoa, and N. D. Duc. New approach to investigate nonlinear dynamic response of sandwich auxetic double curved shallow shells using tsdt. *Composite Structures*, 185:455–465, 2018.
- [165] D. D. Nguyen, Q. Q. Tran, and D. K. Nguyen. New approach to investigate nonlinear dynamic response and vibration of imperfect functionally graded carbon nanotube reinforced composite double curved shallow shells subjected to blast load and temperature. *Aerospace Science and Technology*, 71:360–372, 2017.
- [166] N. D. Duc and T. Q. Quan. Nonlinear response of imperfect eccentrically stiffened fgm cylindrical panels on elastic foundation subjected to mechanical loads. *European Journal of Mechanics-A/Solids*, 46:60–71, 2014.

- [167] T.X. Yu and W. Johnson. The plastica: the large elastic-plastic deflection of a strut. *International Journal of Non-linear Mechanics*, 17(3):195–209, 1982.
- [168] F. Gruttmann, R. Sauer, and W. Wagner. Theory and numerics of three-dimensional beams with elastoplastic material behaviour. *International Journal for Numerical Methods in Engineering*, 48(12):1675–1702, 2000.
- [169] B. Štok and M. Halilovič. Analytical solutions in elasto-plastic bending of beams with rectangular cross section. *Applied Mathematical Modelling*, 33(3):1749–1760, 2009.
- [170] M. Saje, G. Turk, A. Kalagasiđu, and B. Vratanař. A kinematically exact finite element formulation of elastic-plastic curved beams. *Computers & structures*, 67(4):197–214, 1998.
- [171] M.S. Park and B. C. Lee. Geometrically non-linear and elastoplastic three-dimensional shear flexible beam element of von-mises-type hardening material. *International Journal for Numerical Methods in Engineering*, 39(3):383–408, 1996.
- [172] P. Mata, S. Oller, and A.H. Barbat. Static analysis of beam structures under nonlinear geometric and constitutive behavior. *Computer methods in applied mechanics and engineering*, 196(45-48):4458–4478, 2007.
- [173] S. Pajunen. Large deflection elasto-plastic analysis of beams using kinematically exact elements. *Communications in numerical methods in engineering*, 16(7):497–504, 2000.
- [174] J.M. Battini and C. Pacoste. Plastic instability of beam structures using co-rotational elements. *Computer Methods in Applied Mechanics and Engineering*, 191(51-52):5811–5831, 2002.
- [175] N. Challamel, C. Lanos, and C. Casandjia. On the propagation of localization in the plasticity collapse of hardening–softening beams. *International Journal of Engineering Science*, 48(5):487–506, 2010.
- [176] R. Gonalves and D. Camotim. Generalised beam theory-based finite elements for elastoplastic thin-walled metal members. *Thin-Walled Structures*, 49(10):1237–1245, 2011.
- [177] N. Silvestre, M. Abambres, and D. Camotim. Influence of the deformation mode nature on the 1st order post-yielding strength of thin-walled beams. *Thin-Walled Structures*, 128:71–79, 2018.
- [178] M. Abambres, D. Camotim, N. Silvestre, and K.J. Rasmussen. Gbt-based structural analysis of elastic–plastic thin-walled members. *Computers & Structures*, 136:1–23, 2014.
- [179] M. Abambres, D. Camotim, and N. Silvestre. Gbt-based elastic–plastic post-buckling analysis of stainless steel thin-walled members. *Thin-Walled Structures*, 83:85–102, 2014.

- [180] M. Abambres, D. Camotim, and N. Silvestre. Physically non-linear gbt analysis of thin-walled members. *Computers & Structures*, 129:148–165, 2013.
- [181] G. Shi and S.N. Atluri. Elasto-plastic large deformation analysis of space-frames: A plastic-hinge and stress-based explicit derivation of tangent stiffnesses. *International Journal for Numerical Methods in Engineering*, 26(3):589–615, 1988.
- [182] G. Turkalj, J. Brnic, and J. Prpic-Orsic. Esa formulation for large displacement analysis of framed structures with elastic–plasticity. *Computers & structures*, 82(23-26):2001–2013, 2004.
- [183] M. Shugyo. Elastoplastic large deflection analysis of three-dimensional steel frames. *Journal of Structural Engineering*, 129(9):1259–1267, 2003.
- [184] R. He and H. Zhong. Large deflection elasto-plastic analysis of frames using the weak-form quadrature element method. *Finite Elements in Analysis and Design*, 50:125–133, 2012.
- [185] E.A. de Souza Neto, D. Peric, and D.R. Owen. *Computational Methods for Plasticity: Theory and Applications*. Wiley, 2008.
- [186] M. Amabili. *Nonlinear Mechanics of Shells and Plates in Composite, Soft and Biological Materials*. Cambridge University Press, New York, USA, 2018.
- [187] S. Levy, D. Goldenberg, and G. Zibritosky. Simply supported long rectangular plate under combined axial load and normal pressure. *National Advisory Committee for Aeronautics, Technical Note*, No. 949, 1944.
- [188] A. G. Striz, S. K. Jang, and C. W. Bert. Nonlinear bending analysis of thin circular plates by differential quadrature. *Thin-Walled Structures*, 6(1):51–62, 1988.
- [189] E. Carrera and M. Villani. Large deflections and stability FEM analysis of shear deformable compressed anisotropic flat panels. *Composite Structures*, 29(4):433–444, 1994.
- [190] D. W. Murray and E. L. Wilson. Finite-element large deflection analysis of plates. *Journal of the Engineering Mechanics Division*, 95(1):143–166, 1969.
- [191] G. J. Turvey and M. Y. Osman. Elastic large deflection analysis of isotropic rectangular Mindlin plates. *International Journal of Mechanical Sciences*, 32(4):315–328, 1990.
- [192] K. R. Rushton. Large deflection of variable-thickness plates. *International Journal of Mechanical Sciences*, 10(9):723–735, 1968.
- [193] S. Levy. Bending of rectangular plates with large deflections. *NACA Technical Note*, No. 737, 1942.

- [194] S. Levy. Square plate with clamped edges under normal pressure producing large deflections. *NACA Technical Note*, No. 740, 1942.
- [195] F. Alijani and M. Amabili. Non-linear static bending and forced vibrations of rectangular plates retaining non-linearities in rotations and thickness deformation. *International Journal of Non-linear Mechanics*, 67:394–404, 2014.
- [196] M. Amabili, I.D. Breslavsky, and J.N. Reddy. Nonlinear higher-order shell theory for incompressible biological hyperelastic materials. *Computer Methods in Applied Mechanics and Engineering*, 346:841–861, 2019.
- [197] F. Alijani and M. Amabili. Effect of thickness deformation on large-amplitude vibrations of functionally graded rectangular plates. *Composite Structures*, 113:89–107, 2014.
- [198] A. W. Leissa. Buckling of laminated composite plates and shell panels. *Flight Dynamics Laboratory Report*, AFWAL-TR-85-3069, 1985.
- [199] G. J. Turvey and I. H. Marshall. *Buckling and postbuckling of composite plates*. Springer Science & Business Media Dordrecht, 1995.
- [200] L. Librescu and M.Y. Chang. Imperfection sensitivity and postbuckling behavior of shear-deformable composite doubly-curved shallow panels. *International Journal of Solids and Structures*, 29(9):1065–1083, 1992.
- [201] A.K. Kaw. *Mechanics of composite materials*. CRC press, 2005.
- [202] A. Pagani, E. Carrera, A. Hasanyan, and S. Pellegrino. Advanced simulation and testing of composite TRAC longerons. In *71st International Astronautical Congress (IAC)*, pages 12–14, 2020.
- [203] J. N. Reddy and W. C. Chao. Non-linear bending of thick rectangular, laminated composite plates. *International Journal of Non-Linear Mechanics*, 16(3-4):291–301, 1981.
- [204] C. Y. Chia. Large deflection of unsymmetric laminates with mixed boundary conditions. *International Journal of Non-Linear Mechanics*, 20(4):273–282, 1985.
- [205] B.N. Singh, A. Lal, and R. Kumar. Nonlinear bending response of laminated composite plates on nonlinear elastic foundation with uncertain system properties. *Engineering Structures*, 30(4):1101–1112, 2008.
- [206] Y. Urthaler and J. N. Reddy. A mixed finite element for the nonlinear bending analysis of laminated composite plates based on FSDT. *Mechanics of Advanced Materials and Structures*, 15(5):335–354, 2008.
- [207] P. Dash and B.N. Singh. Static response of geometrically nonlinear laminated composite plates having uncertain material properties. *Mechanics of Advanced Materials and Structures*, 22(4):269–280, 2015.

- [208] E. Carrera and B. Kröplin. Zigzag and interlaminar equilibria effects in large-deflection and postbuckling analysis of multilayered plates. *Mechanics of Composite Materials and Structures*, 4(1):69–94, 1997.
- [209] P. Dash and B. N. Singh. Geometrically nonlinear bending analysis of laminated composite plate. *Communications in Nonlinear Science and Numerical Simulation*, 15(10):3170–3181, 2010.
- [210] K. K. Shukla and Y. Nath. Nonlinear analysis of moderately thick laminated rectangular plates. *Journal of Engineering Mechanics*, 126(8):831–838, 2000.
- [211] Y.X. Zhang and C.H. Yang. Recent developments in finite element analysis for laminated composite plates. *Composite Structures*, 88(1):147–157, 2009.
- [212] Y.X. Zhang and K.S. Kim. A simple displacement-based 3-node triangular element for linear and geometrically nonlinear analysis of laminated composite plates. *Computer Methods in Applied Mechanics and Engineering*, 194(45-47):4607–4632, 2005.
- [213] W. Han, M. Petyt, and K.M. Hsiao. An investigation into geometrically nonlinear analysis of rectangular laminated plates using the hierarchical finite element method. *Finite Elements in Analysis and Design*, 18(1-3):273–288, 1994.
- [214] Y.X. Zhang and K.S. Kim. Geometrically nonlinear analysis of laminated composite plates by two new displacement-based quadrilateral plate elements. *Composite Structures*, 72(3):301–310, 2006.
- [215] C. Sridhar and K.P. Rao. Large deformation finite element analysis of laminated circular composite plates. *Computers & Structures*, 54(1):59–64, 1995.
- [216] L.V. Tran, J. Lee, H. Nguyen-Van, H. Nguyen-Xuan, and M.A. Wahab. Geometrically nonlinear isogeometric analysis of laminated composite plates based on higher-order shear deformation theory. *International Journal of Non-Linear Mechanics*, 72:42–52, 2015.
- [217] F. Alijani and M. Amabili. Non-linear dynamic instability of functionally graded plates in thermal environments. *International Journal of Non-Linear Mechanics*, 50:109–126, 2013.
- [218] K.M. Liew, J. Wang, M.J. Tan, and S. Rajendran. Nonlinear analysis of laminated composite plates using the mesh-free kp-Ritz method based on FSDT. *Computer Methods in Applied Mechanics and Engineering*, 193(45-47):4763–4779, 2004.
- [219] B.S. Reddy, A.R. Reddy, J.S. Kumar, and K.V.K. Reddy. Bending analysis of laminated composite plates using finite element method. *International Journal of Engineering, Science and Technology*, 4(2):177–190, 2012.



- [220] A.K. Baltacıoğlu, Ö. Civalek, B. Akgöz, and F. Demir. Large deflection analysis of laminated composite plates resting on nonlinear elastic foundations by the method of discrete singular convolution. *International Journal of Pressure Vessels and Piping*, 88(8-9):290–300, 2011.
- [221] H. B. Coda. Continuous inter-laminar stresses for regular and inverse geometrically nonlinear dynamic and static analyses of laminated plates and shells. *Composite Structures*, 132:406–422, 2015.
- [222] H. B. Coda, R. R. Paccola, and R. Carrazedo. Zig-zag effect without degrees of freedom in linear and nonlinear analysis of laminated plates and shells. *Composite Structures*, 161:32–50, 2017.
- [223] M. Amabili. *Nonlinear Vibrations and Stability of Shells and Plates*. Cambridge University Press, New York, USA, 2008.
- [224] J.N. Reddy. *Mechanics of Laminated Composite Plates and Shells: Theory and Analysis*. CRC press, 2003.
- [225] M. Gorji. On large deflection of symmetric composite plates under static loading. *Proceedings of the Institution of Mechanical Engineers, Part C: Journal of Mechanical Engineering Science*, 200(1):13–19, 1986.
- [226] Y. Zhang and F.L. Matthews. Large deflection behavior of simply supported laminated panels under in-plane loading. *Journal of Applied Mechanics*, 52(3):553–558, 1985.
- [227] S. Hui-Shen. Buckling and postbuckling behavior of antisymmetrically angle-ply laminated composite plates. *Applied Mathematics and Mechanics*, 11(12):1155–1165, 1990.
- [228] S. Hui-shen. *Postbuckling Behavior of Plates and Shells*. World Scientific, 2017.
- [229] Y. Zhang and F.L. Matthews. Postbuckling behaviour of curved panels of generally layered composite materials. *Composite Structures*, 1(2):115–135, 1983.
- [230] P. Dash and B.N. Singh. Buckling and post-buckling of laminated composite plates. *Mechanics Research Communications*, 46:1–7, 2012.
- [231] A.W. Leissa. A review of laminated composite plate buckling. *Applied Mechanics Reviews*, 40(5):575–591, 1987.
- [232] G.J. Turvey and I.H. Marshall. *Buckling and postbuckling of composite plates*. Springer Science & Business Media, 2012.
- [233] L. Librescu and M. Stein. A geometrically nonlinear theory of transversely isotropic laminated composite plates and its use in the post-buckling analysis. *Thin-Walled Structures*, 11(1-2):177–201, 1991.

- [234] P. Sundaresan, G. Singh, and G.V. Rao. Buckling and post-buckling analysis of moderately thick laminated rectangular plates. *Computers & Structures*, 61(1):79–86, 1996.
- [235] S.S. Wang, S. Srinivasan, H.T. Hu, and R. HajAli. Effect of material nonlinearity on buckling and postbuckling of fiber composite laminated plates and cylindrical shells. *Composite Structures*, 33(1):7–15, 1995.
- [236] M. Amabili and M.R.S. Tajahmadi. Thermal post-buckling of laminated and isotropic rectangular plates with fixed edges: Comparison of experimental and numerical results. *Proceedings of the Institution of Mechanical Engineers, Part C: Journal of Mechanical Engineering Science*, 226(10):2393–2401, 2012.
- [237] K.M. Liew, J. Wang, M.J. Tan, and S. Rajendran. Postbuckling analysis of laminated composite plates using the mesh-free kp-Ritz method. *Computer Methods in Applied Mechanics and Engineering*, 195(7-8):551–570, 2006.
- [238] P. Dash and B.N. Singh. Buckling and post-buckling response of laminated composite plate with random system properties. *Mechanics of Advanced Materials and Structures*, 21(6):516–529, 2014.
- [239] Q. Chen and P. Qiao. Post-buckling analysis of composite plates under combined compression and shear loading using finite strip method. *Finite Elements in Analysis and Design*, 83:33–42, 2014.
- [240] S.C. Han, S.Y. Lee, and G. Rus. Postbuckling analysis of laminated composite plates subjected to the combination of in-plane shear, compression and lateral loading. *International Journal of Solids and Structures*, 43(18-19):5713–5735, 2006.
- [241] S.J. Lee and W. Kanok-Nukulchai. A nine-node assumed strain finite element for large-deformation analysis of laminated shells. *International Journal for Numerical Methods in Engineering*, 42(5):777–798, 1998.
- [242] A.K. Noor and M.D. Mathers. Anisotropy and shear deformation in laminated composite plates. *AIAA Journal*, 14(2):282–285, 1976.
- [243] H. Wang, M. Ou, and T. Wang. Post-buckling behaviour of orthotropic rectangular plates. *Computers & structures*, 41(1):1–5, 1991.
- [244] E. Carrera and M. Villani. Effects of boundary conditions on postbuckling of compressed, symmetrically laminated thick plates. *AIAA Journal*, 33(8):1543–1546, 1995.
- [245] Y. Fan and H. Wang. Nonlinear bending and postbuckling analysis of matrix cracked hybrid laminated plates containing carbon nanotube reinforced composite layers in thermal environments. *Composites Part B: Engineering*, 86:1–16, 2016.

- [246] H.S. Shen and S.R. Li. Postbuckling of sandwich plates with fgm face sheets and temperature-dependent properties. *Composites Part B: Engineering*, 39(2):332–344, 2008.
- [247] H.S. Shen, Y. Xiang, F. Lin, and D. Hui. Buckling and postbuckling of functionally graded graphene-reinforced composite laminated plates in thermal environments. *Composites Part B: Engineering*, 119:67–78, 2017.
- [248] Y. Yu, H.S. Shen, H. Wang, and D. Hui. Postbuckling of sandwich plates with graphene-reinforced composite face sheets in thermal environments. *Composites Part B: Engineering*, 135:72–83, 2018.
- [249] I.T. Cook and K.C. Rockey. Shear buckling of rectangular plates with mixed boundary conditions. *Aeronautical Quarterly*, 14(4):349–356, 1963.
- [250] S.B. Biggers and S.S. Pageau. Shear buckling response of tailored composite plates. *AIAA journal*, 32(5):1100–1103, 1994.
- [251] C. Dou, Z.Q. Jiang, Y.L. Pi, and Y.L. Guo. Elastic shear buckling of sinusoidally corrugated steel plate shear wall. *Engineering Structures*, 121:136–146, 2016.
- [252] Y. Kiani. Shear buckling of fg-cnt reinforced composite plates using chebyshev-ritz method. *Composites Part B: Engineering*, 105:176–187, 2016.
- [253] C.H. Pham. Shear buckling of plates and thin-walled channel sections with holes. *Journal of Constructional Steel Research*, 128:800–811, 2017.
- [254] D. Hui. Shear buckling of anti-symmetric cross ply rectangular plates. *Fibre Science and Technology*, 21(4):327–340, 1984.
- [255] S. Kosteletos. Shear buckling response of laminated plates. *Composite structures*, 20(3):147–154, 1992.
- [256] J. Loughlan. The influence of bend–twist coupling on the shear buckling response of thin laminated composite plates. *Thin-walled structures*, 34(2):97–114, 1999.
- [257] J. Loughlan. The shear buckling behaviour of thin composite plates with particular reference to the effects of bend–twist coupling. *International Journal of Mechanical Sciences*, 43(3):771–792, 2001.
- [258] M. Shariyat and K. Asemi. Three-dimensional non-linear elasticity-based 3d cubic b-spline finite element shear buckling analysis of rectangular orthotropic fgm plates surrounded by elastic foundations. *Composites Part B: Engineering*, 56:934–947, 2014.
- [259] W.Y. Jung and S.C. Han. Shear buckling responses of laminated composite shells using a modified 8-node ans shell element. *Composite Structures*, 109:119–129, 2014.

- [260] Q. Chen and P. Qiao. Shear buckling of rotationally-restrained composite laminated plates. *Thin-Walled Structures*, 94:147–154, 2015.
- [261] S.R. Atashipour and U.A. Girhammar. On the shear buckling of clamped narrow rectangular orthotropic plates. *Mathematical Problems in Engineering*, 2015, 2015.
- [262] H.S.J. Lee and C.B. York. Compression and shear buckling performance of finite length plates with bending-twisting coupling. *Composite Structures*, 241:112069, 2020.
- [263] N.G.R. Iyengar and A. Chakraborty. Study of interaction curves for composite laminate subjected to in-plane uniaxial and shear loadings. *Composite structures*, 64(3-4):307–315, 2004.
- [264] I. Shufrin, O. Rabinovitch, and M. Eisenberger. Buckling of symmetrically laminated rectangular plates with general boundary conditions—a semi analytical approach. *Composite Structures*, 82(4):521–531, 2008.
- [265] C. Bedon and C. Amadio. Buckling analysis of simply supported flat glass panels subjected to combined in-plane uniaxial compressive and edgewise shear loads. *Engineering structures*, 59:127–140, 2014.
- [266] Q. Liu, P. Qiao, and X. Guo. Buckling analysis of restrained orthotropic plates under combined in-plane shear and axial loads and its application to web local buckling. *Composite Structures*, 111:540–552, 2014.
- [267] E. Daneshkhah, E. Carrera, X. Xu, and H. Yang. The effects of surroundings and stiffeners in the cuf-based post-buckling analysis of composite panels under in-plane shear. *Mechanics of Advanced Materials and Structures*, 2022.
- [268] Y. Zhang and F.L. Matthews. Initial buckling of curved panels of generally layered composite materials. *Composite Structures*, 1(1):3–30, 1983.
- [269] J. Loughlan. The buckling performance of composite stiffened panel structures subjected to combined in-plane compression and shear loading. *Composite Structures*, 29(2):197–212, 1994.
- [270] M.P. Nemeth. Buckling behavior of long anisotropic plates subjected to combined loads. In *36th Structures, Structural Dynamics and Materials Conference*, page 1455, 1995.
- [271] M.P. Nemeth. *Buckling behavior of long symmetrically laminated plates subjected to shear and linearly varying axial edge loads*, volume 3659. National Aeronautics and Space Administration, Langley Research Center, 1997.
- [272] C.A. Featherston. Imperfection sensitivity of curved panels under combined compression and shear. *International Journal of Non-Linear Mechanics*, 38(2):225–238, 2003.

- 
- [273] K.D. Kim, G.R. Lomboy, and S.C. Han. A co-rotational 8-node assumed strain shell element for postbuckling analysis of laminated composite plates and shells. *Computational Mechanics*, 30(4):330–342, 2003.
- [274] C.A. Featherston and A. Watson. Buckling of optimised flat composite plates under shear and in-plane bending. *Composites science and technology*, 65(6):839–853, 2005.